DEFECTS IN HIGH-ENTROPY ALLOYS STUDIED BY ATOMIC SCALE COMPUTER SIMULATIONS

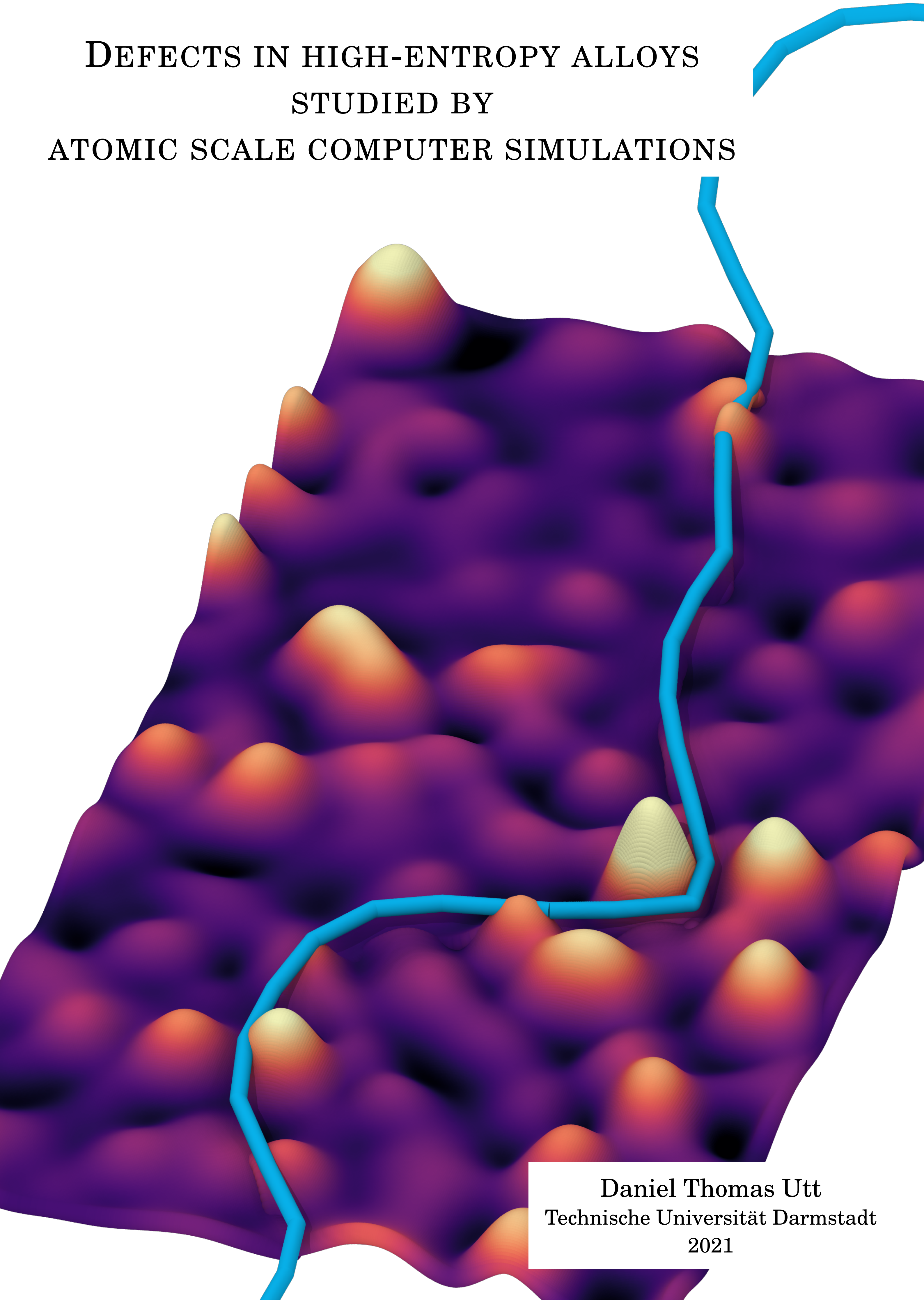

Daniel Thomas Utt
Technische Universität Darmstadt
2021

On the cover: Dislocation (blue) during glide in the CoCrFeMnNi high-entropy alloy. The calculated atomic scale pinning point strength is shown as schematic *energy landscape* where strong pinning points are shown as tall obstacles. Pinning of the dislocation line on the highest obstacle can be seen.

Defects in high-entropy alloys studied by atomic scale computer simulations

Zur Erlangung des akademischen Grades Doktor-Ingenieur (Dr.-Ing.)
genehmigte Dissertation vorgelegt
von Daniel Thomas Utt
geboren in Marburg

Fachgebiet:	Materialmodellierung
Fachbereich:	Material- und Geowissenschaften Technische Universität Darmstadt

Berichter:	Prof. Dr. rer. nat. Karsten Albe, Technische Universität Darmstadt
Mitberichter:	Asst. Prof. Francesco Maresca, PhD, Rijksuniversiteit Groningen
1. Prüfer:	Prof. Dr.-Ing. Karsten Durst, Technische Universität Darmstadt
2. Prüfer:	Prof. Dr. rer. nat. Wolfgang Donner, Technische Universität Darmstadt

Tag der Einreichung:	20.07.2021
Tag der Prüfung:	27.09.2021
Jahr der Veröffentlichung:	2022

Darmstadt 2021
D17

Please cite this document as:
URN: `urn:nbn:de:tuda-tuprints-209296`
URL: `https://tuprints.ulb.tu-darmstadt.de/20929`

Utt, Daniel Thomas: Defects in high-entropy alloys studied by atomic scale computer simulations
Darmstadt, Technische Universität Darmstadt
Jahr der Veröffentlichung auf TUprints: 2022
URN: `urn:nbn:de:tuda-tuprints-209296`
URL: `https://tuprints.ulb.tu-darmstadt.de/20929`
Tag der mündlichen Prüfung: 27.09.2021

Erklärung laut Promotionsordnung

§8 Abs. 1 lit. c PromO

Ich versichere hiermit, dass die elektronische Version meiner Dissertation mit der schriftlichen Version übereinstimmt.

§8 Abs. 1 lit. d PromO

Ich versichere hiermit, dass zu einem vorherigen Zeitpunkt noch keine Promotion versucht wurde. In diesem Fall sind nähere Angaben über Zeitpunkt, Hochschule, Dissertationsthema und Ergebnis dieses Versuchs mitzuteilen.

§9 Abs. 1 PromO

Ich versichere hiermit, dass die vorliegende Dissertation selbstständig und nur unter Verwendung der angegebenen Quellen verfasst wurde.

§9 Abs. 2 PromO

Die Arbeit hat bisher noch nicht zu Prüfungszwecken gedient.

Darmstadt, March 16, 2022

Daniel Thomas Utt

Abstract

High-entropy alloys (HEAs) are a new class of metal alloys containing multiple principal elements in concentrations between 5 % and 35 %. Due to their inherent chemical complexity, they possess a wide range of interesting properties, which we explore in greater detail throughout this thesis.

Reduced or *sluggish* diffusion has been discussed for HEAs since their inception. We perform time-scale bridging simulations on the pseudo-binary $(\mathrm{CoCrFeMn})_{1-x}\mathrm{Ni}_x$ HEA, combining atomistic simulations of the vacancy migration energies and equilibrium vacancy concentrations with kinetic Monte Carlo simulations of tracer diffusion trajectories. Here, we extend the established random alloy model to account for the local chemical fluctuations within the complex alloy matrix. The results compare favorably to experimental tracer diffusion measurements.

Dislocations in HEAs also interact with chemical fluctuations in the random matrix. This leads to a meandering dislocation line shape and localized pinning during dislocation glide. We find a physically motivated descriptor for these pinning sites in the form of a per-atom Peierls force. This descriptor shows good spatial correlation with observed dislocation pinning sites during glide. Furthermore, we show that the density of strong pinning sites in an alloy correlates not only with the critical shear required to initiate dislocation glide but also the dislocation mobility.

We report on the grain growth properties of a CoCuFeNi model HEA. Atomistic simulations give unique insights into the effects of random chemical fluctuations by comparison of the HEA to its average-atom counterpart. The average-atom is a virtual element which has the same long-range properties as the alloy but consists only of a single element. Additionally, solute segregation to grain boundaries (GBs) is considered. The comparison of two different samples, namely a $\Sigma 11$ GB and a large-scale nanocrystalline sample, reveals that while grain growth is reduced in the HEA compared to other pure metals, this does not stem from the chemical randomness. Instead, solute segregation is necessary to pin GBs up to high temperatures.

Zusammenfassung

Hoch-Entropie Legierungen (engl. *high-entropy alloy*, HEA) sind eine neue Klasse von Metalllegierungen, die mehrere Hauptelemente in Konzentrationen zwischen 5 % und 35 % enthalten. Aufgrund dieser chemischen Komplexität besitzen sie eine breite Palette interessanter Eigenschaften, die wir in dieser Arbeit näher untersuchen.

Seit den ersten Experimenten wird für HEAs eine reduzierte Diffusivität im Vergleich zu klassischen Legierungen diskutiert. Wir kombinieren atomistisch berechneten Leerstellenmigrationsenergien und Leerstellenkonzentrationen zu Mehrskalensimulation verschiedener pseudo-binärer $(\mathrm{CoCrFeMn})_{1-x}\mathrm{Ni}_x$ HEA. Hierfür werden kinetische Monte Carlo Simulationen genutzt, um die Diffusionspfade von Traceratomen durch die HEA zu bestimmen. Hier erweitern wir das klassische Zufallslegierungsmodell, sodass die lokalen chemischen Fluktuationen der komplexen Legierung explizit berücksichtigt werden. Die berechneten Diffusivitäten zeigen gute Übereinstimmung mit experimentellen Tracerdiffusionsmessungen.

Versetzungen interagieren ebenfalls mit den chemischen Fluktuationen in HEAs. Dies führt zu einer geschlängelten Versetzungslinie und lokalisiertem anhaften der Versetzung während des Gleitens. Wir entwickeln einen physikalisch motivierten Deskriptor für diese Verankerungspositionen im Material. Diese zeigen sich in Form einer atomaren Peierls-Kraft. Dieser Deskriptor zeigt eine räumliche Korrelation mit den während der Verformung beobachteten Versetzungsverankerungsstellen. Darüber hinaus zeigen wir, dass die Dichte der starken Haftstellen in einer Legierung nicht nur mit der kritischen Scherkraft korreliert, die erforderlich ist, um die Versetzung in Bewegung zu versetzen, sondern auch mit ihrer Mobilität.

Abschließend, berichten wir über die Kornwachstumseigenschaften einer CoCuFeNi Modell-HEA. Atomistische Simulationen geben einzigartige Einblicke in die Effekte der chemischen Fluktuationen in der HEA. Dies wird durch den Vergleich der vier Komponenten Legierung mit ihrem Durchschnittsatom Gegenstück ermöglicht. Dieses sogenannte Durchschnittsatom ist ein virtuelles Element mit den gleichen makroskopischen Eigenschaften wie die vollständige HEA, obwohl es lediglich aus einer Atomsorte besteht. Des Weiteren wird der Einfluss von Seigerung zu den Korngrenzen (KG) untersucht. In beiden studierten Probengeometrien, einer $\Sigma 11$ KG und einer nanokristallinen Probe, zeigt sich, dass das Kornwachstum in der HEA im Vergleich zu anderen reinen Metallen zwar reduziert ist, dass dies jedoch nicht auf die chemische Komplexität zurückzuführen ist. Die Seigerung von Cu zu den KG ist essenziell, um Kornwachstum bis zu hohen Einsatztemperaturen zu unterbinden.

Acknowledgements — Danksagung

Als Erstes möchte ich Prof. Dr. Karsten Albe, sowohl für sein Vertrauen, als auch die Möglichkeiten, die er mir über die Jahre eröffnet hat, danken. Ohne diese wäre diese Arbeit nicht zustande gekommen.

Special thanks go to professor Francesco Maresca, PhD, who volunteered his time and expertise to co-referee this thesis. In gleicher Weise möchte ich auch den weiteren Mitgliedern meiner Prüfungskommission, Prof. Dr. Karsten Durst und Prof. Dr. Wolfgang Donner für ihre Zeit und Expertise danken.

Des Weiteren möchte ich mich bei meinen Kollaboratoren und Co-Autoren für die spannende und ertragreiche Zusammenarbeit bedanken. Hier möchte ich besonders Josua Kottke und Dr. Sergiy Divinskiy der Westfälische Wilhelms-Universität Münster für Messungen und Diskussionen zur Diffusion in HEAs danken. Ihre Messergebnisse waren der Startpunkt unserer Simulationen und Überlegungen. Moreover, I would like to thank Dr. Subin Lee from Karlsruhe Institute of Technology, Prof. Dr. Gerhard Dehm from the Max-Planck-Institut für Eisenforschung, and Prof. Sang Ho Oh from Sungkyunkwan University for the many discussions we had on dislocations. Their meticulous experiments were the perfect starting point for our investigation on dislocation pinning. Außerdem Danke ich Tom Keil, Dr. Enrico Bruder und Prof. Dr. Karsten Durst der Technischen Universität Darmstadt, sowie Felix Thiel und Prof. Dr. Jens Freudenberger vom Leibniz-Institut für Festkörper- und Werkstoffforschung Dresden, für die Zusammenarbeit zu den mechanischen Eigenschaften von HEAs. Zwar haben es diese Ergebnisse nicht in diese Arbeit geschafft, sie haben mir dennoch enorm geholfen.

I am indebted to Prof. Maryam Ghazisaeidi, PhD, from The Ohio State University who has hosted me for an extended stay at her research group. I learned a lot about atomistic simulations and dislocations in these three months. Here, I would also like to thank everyone I met in these three month for welcoming me with open arms.

Mit dem Blick zurück nach Darmstadt möchte ich zuerst Gabriele Rühl danken, sie hat in den letzten 4 Jahren mit ihrem Einsatz viele organisatorische Probleme gelöst.

Außerdem Danke ich Arne Klomp, dem wahrscheinlich besten Bürokollegen den ich mir hätte wünschen können. Wir haben zusammen viele wissenschaftliche und unwissenschaftliche Probleme des Doktoranden Alltags gelöst und es bleibt eigentlich nur noch eine Frage: “*Warum werden Dinge kalt?*” Im gleichen Atemzug danke ich Dr. Constanze Kalcher für ihre tägliche Unterstützung und für Spaß und Freude über die Jahre! #GoTeamOVITO! Auch wenn aufgeben nie eine Option war, war euer Support doch essenziell. Vielen Dank richte ich an Dr. Leonie Koch, Dr. Alexander Stukowski, Dr. Jochen Roher, sowie Marcel Sadowski für Diskussion, Freundschaft und Unterstützung. Dies gilt natürlich auch für alle anderen MMs, die diese Arbeitsgruppe zur besten Arbeitsgruppe machen!

Besonderer Dank gilt außerdem meinen Freunden, An-Phuc Hoang, Elisa Tengan, Nicole Bein, Vivian Hsu, Alexander Kempf, David Kasdorf, Maximilian Geringer, Markus Frericks, Ryan Thompson, Thierry Kohl. Ihr seid eine großartige Gruppe, die sich gegenseitig nicht nur durchs Studium, sondern auch durch die jeweiligen Promotionen trägt / getragen hat. Außerdem danke ich dem Murder-Quartett und der Festival-Crew für viele Stunden Spaß und Ablenkung vom Ernst des Lebens.

Mein ganz besonderer Dank gilt meinen Eltern, denn ohne eure Unterstützung wäre ich heute nicht hier.

I also want to thank everyone not named above, who has enriched my scientific career with discussions, ideas and suggestions.

Zu guter Letzt bedanke ich mich bei der Deutschen Forschungsgesellschaft für finanzielle Unterstützung im Projekt STU 611/2-1 als Teil des SPP2006. Außerdem Danke ich der Technischen Universität Darmstadt, sowie dem Gauss Centre for Supercomputing e.V. für Rechenzeit auf dem Lichtenberg-Hochleistungsrechner, sowie dem GCS Supercomputer SuperMUC des Leibniz Supercomputing Centre.

Contents

1 Introduction

> *"There is a hype on HEAs, for sure. Indications are not only the exponential growth of publications on this topic [. . .], but also the many papers that are based on possibly unreliable and unreproducible experimental data from as-cast samples."*
>
> — W. Steurer, *2020*[1]

What are High-Entropy Alloys?

Conventional alloying strategies revolve around a primary element, which forms the matrix to which secondary elements are added to improve certain properties. One such example is iron to which up to 2 wt% of carbon can be added to increase its strength. The addition of 11 wt% to 18 wt% of Cr leads to a strong oxidation resistance of Fe-based alloys.[2] Even in Ni-superalloys, some of the most highly alloyed materials in use today, the main element Ni still makes up 50 wt% to 70 wt%.[3] This alloying paradigm of one main element with some added secondary elements, which has been followed for more than 4000 years[4] can only go so far. The combinatoric space of new alloys with ever-improving properties is obviously limited.

Therefore, a new approach, expanding the concept of alloying, was proposed in 2004. To put it in the words of Cantor et al.,[5] they set out *"to investigate the unexplored central region of multicomponent alloy phase space, concentrating particularly on multicomponent transition metal alloys which are found to exhibit a surprising degree of intersolubility in a single fcc phase."* This unexplored central region can be seen

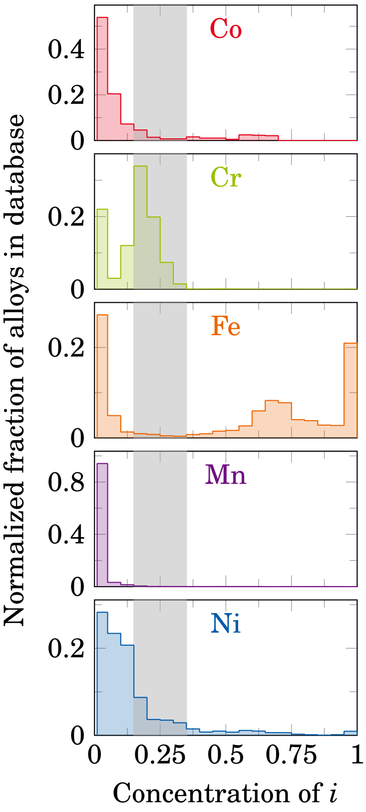

Figure 1.1: Co, Cr, Fe, Mn, and Ni concentrations in the alloys contained in the MATMATCH database.

in Figure 1.1, showing the concentration of Co, Cr, Fe, Mn, and Ni in the 24 000 commercially available alloys in the MATMATCH database.[*] Here, normalized histograms for the number alloys containing a given element are shown. The conventional alloying strategy can be seen most clearly in the case of Fe based alloys. Most of them either contain iron exceeding 70 %, encompassing stainless steels as well as conventional steels, or below 10 %. The central region of the multicomponent alloy phase space spanning concentrations from 15 % to 35 % shows almost now available alloys (shaded region in Figure 1.1). Similarly, we can see that Co, Mn, and Ni are usually added in concentrations below 15 %. Solely Cr is commonly found in this concentration window ($\approx 18\,\%$) to facilitate corrosion resistance in stainless steels.

Surprisingly, in 2004 two research groups independently published their work on concentrated solid solutions. Both Yeh et al.[6,7] and Cantor et al.[5] showed that alloys, containing five or more elements in equal ratio, can form stable random solid solutions. This came as a surprise, as conventional wisdom would expect such concentrated alloys to phase separate into multiple intermetallic phases. The two prototypical alloys initially reported were $(\mathrm{CuCoNiCrFe})\mathrm{Al}_x$[6] and CoCrFeMnNi.[5] The latter is often called *Cantor alloy*.

Yeh et al.[6] surmise that once there is a sufficient number of elements N, e.g., five, in an alloy the resulting configurational entropy, $S_{\mathrm{conf}} = k_{\mathrm{B}} \ln(N) = 1.609 k_{\mathrm{B}}$, is sufficient to stabilize the random solid solution against ordering or phase decomposition. Based on this assumption these alloys are often called *high-entropy alloys*. Further research since then has revealed that the configurational entropy, especially at low temperatures, is not sufficient to stabilize these alloys.[8,9] Therefore, other names like *complex concentrated alloy* or *multiple-principal element alloy* have been suggested and are used mostly interchangeably.[10] As noted by George et al.,[2] however, *"Judging by its popularity in the literature, we suspect that, despite entropy not being the prime factor responsible for the structure and properties of these alloys, the term high-entropy alloys is likely to be the name that endures."* Another material class, following in the footsteps of high-entropy alloys (HEAs) are medium-entropy alloys (MEAs). They contain three constituents in equimolar ratio. One commonly studied example is CoCrNi.[11,12] The origin and development of the first HEAs, spanning more than two decades, has recently been collected by Biswas et al.[13] and Cantor.[14]

Yeh[15] postulated four *core effects* present in HEA which sparked substantial research interest and shaped more than a decade of intensive HEA research.[8] Even though, all of these core effects have been subject to scientific scrutiny and debunking, they are still worth summarizing.[10,16]

I. The *high-entropy effect* is the eponymous HEA effect stating that the high configurational entropy, stemming from the different components, stabilizes a solid solution against intermetallic or secondary phase formation.

---

[*] `https://matmatch.com/` retrieved on Feb. 15, 2021

II. The *lattice distortion effect* stems from differently sized species occupying the HEA lattice, which leads to locally varying bond lengths and thereby modifies the properties of the alloy.

III. The *sluggish diffusion effect* claims that the diffusion in HEA is intrinsically reduced by the local chemical fluctuations compared to dilute alloys.

IV. The *cocktail effect* does not describe any specific physical effect present in HEAs, but instead tells us that concentrated alloys are a synergistic mix, where the resulting properties may be greater than the sum of its parts.[17]

Even though, this novel material class has only been around since 2004 the vast compositional flexibility has already produced alloys and compositions that show exceptional ductility at comparatively high strengths. Figure 1.2 outlines

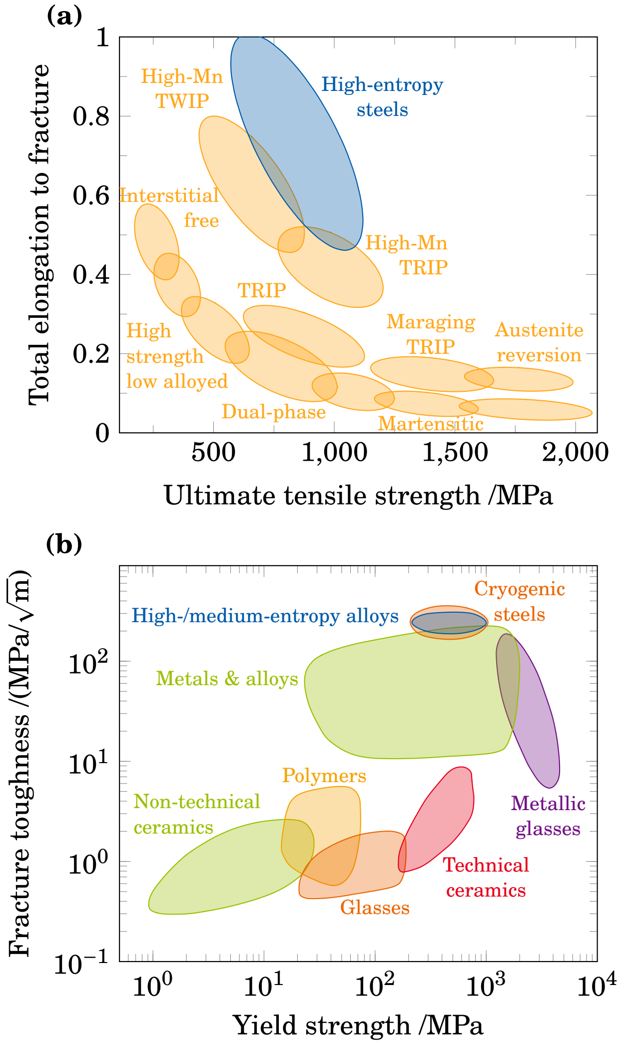

Figure 1.2: Ashby maps showing the exceptional strength and ductility of different HEAs in comparison to established material classes. They possess a comparatively high strength while retaining a high ductility. (a) Total elongation against ultimate tensile strength for a wide range of conventional steels (yellow) in comparison to high-entropy steels. Adapted from Ref. 18. (b) Yield strength against fracture toughness benchmarking MEAs and HEAs against many of material classes highlighting their exceptional performance. Adapted from Ref. 2. Some labels are omitted for clarity — refer to the original publications for further details. TWIP: Twinning induced plasticity, TRIP: Transformation induced plasticity.

how selected HEAs can maintain a much higher ductility and fracture toughness at a given strength compared to a wide range of established steels, polymers, and ceramics. As shown in (a), they can rise above the *steel banana* and overcome the strength-ductility trade-off seen in conventional steels. Comparing the fracture toughness against yield stress data (b) confirms these trends. Even though, the shown HEAs cannot rival the strongest available steels and metallic glasses in yield strength, they still show excellent fracture toughness at comparatively high strength. Given these promising results MEA and HEA research has exploded with recent reviews by Miracle et al.[10] and George et al.[2,19] outlining their prospects and challenges. While most of the research and also this thesis is focused on the mechanical properties of HEAs, there have also been advances using them as functional materials.[20,21]

The multi-component concentrated matrix challenges conventional theories of materials science and metallurgy, where a material is typically described as a host system which get additional, often beneficial, properties from dilute defects dispersed throughout this host material. In HEAs the notion of host *matrix* and *defect* atoms becomes intrinsically ambiguous. Every atom acts as defect and matrix at the same time. This leads to the interesting question how defects, like dislocations or vacancies, interact with this new form of inhomogeneous matrix.[22] Some authors even call the HEA matrix a *defective reference state*,[13] to highlight this difference to conventional materials.

Given this interest in the defect-matrix interaction in HEAs we decided to investigate point, line, and planar defects in the form of vacancies, dislocations, and grain boundaries (GBs), respectively, throughout this thesis. The remainder of this chapter provides a brief introduction to each of these three topics. Subsequently, Chapter 2 gives a literature review and outlines the research questions answered in Chapters 4 to 6 using the methodology described in Chapter 3.

Vacancies

High temperature applications, which have long been envisioned for HEAs,[2,19,23] require knowledge of diffusional properties. Opposite to what was believed initially, HEAs are not thermodynamically stable single phase solid solutions at ambient or even elevated temperatures.[9] Instead, they are kinetically frozen in their metastable state, but given sufficient time or temperature, they are prone to phase separation or short-range ordering.[9,24–30] While these effects are not necessarily bad for applications, as both precipitation[27,31–35] and short-range order (SRO)[36–39] can lead to enhanced mechanical properties, precise knowledge of the diffusion kinetics is required to tailor these strengthening mechanisms.[40]

The most important failure mechanism that occurs in high temperature structural application is diffusive creep.[41] Here, the creep rate depends not only on the applied stress but also on the vacancy concentration and their diffusivity.[42–44] A reduced or sluggish diffusion rate has been suggested as a *core effect* in HEAs for many years.[6,15,45] Even though this effect has been scrutinized recently[16,46] it would make HEAs good candidates for creep resistant alloys.

Lastly, HEAs have been suggested as structural materials for fusion and fission reactors[10,47] due to their high irradiation resistance.[48–63] Here the vacancy formation energy and vacancy kinetics are of great interest as they govern void formation and swelling,[64,65] two main failure mechanisms in irradiated metals.[66]

Vacancies and their migration are intimately linked to diffusion, as all diffusion mechanism in densely packed metals rely on vacancy mediated mechanisms. Therefore, we investigate the effects of the random multi-component matrix on these zero-dimensional point defects in Chapter 4, *'Vacancies'*, of this thesis. Here, our atomic scale computer simulations give unique insights into the interaction of individual point defects with their environment. These interactions cannot only be calculated in equilibrium, but also during a diffusive jump, where vacancy and neighboring atom exchange positions.

Dislocations

The yield strength and initial stages of plastic deformation in a ductile face-centered cubic (FCC) metal are governed by planar slip, facilitated by the glide of dislocations.[67,68] Dislocation glide in highly pure FCC metals can occur at applied stresses as low as 10 MPa.[69–71] This very low strength can easily be increased by alloying, i.e., the addition of solutes into the metal matrix. Each solute acts as a pinning point for gliding dislocations, thereby hindering slip up to applied stresses in the hundreds of MPa.[72]

While it is relatively easy to point towards the dislocation pinning points in a dilute alloy where the distinction between solute and matrix is obvious, the atomic scale origin of the dislocation pinning sites in concentrated alloys remains elusive.[19,73] There have been a large number of experimental[74–77] and computer simulation results[36,38,74,78–82] observing the meandering dislocation lines in MEAs and HEAs. Their atomic scale origin, however, has not been considered in great depth by the HEA community. Li et al.[36] take a first step in this direction, investigating dislocation lines in CoCrNi and finding increased dislocation pinning in regions with increased Co and Cr concentration. Meanwhile, George et al.[19] suggest that dislocation pinning cannot be understood as a process on the atomic scale as dislocation glide involves at least 100 atoms inside the so-called *activation volume*.

Based on the classical theories of solute strengthening two pictures come to mind. In the strong-pinning model by Fleischer[83,84] and Friedel,[85] the dislocation line gets pinned on discrete obstacles which require an additional shear stress for the dislocation to pass. Weak-pinning models by Mott[86] and Labusch[87,88] treat the solutes within the host matrix as solute field with energetically favorable fluctuations in which the dislocation gets pinned. The most commonly used solid solution strengthening model for concentrated alloys by Varvenne et al.[72,89] builds on this Labusch model.

Chapter 5, *'Dislocations'*, aims to improve understanding of dislocations in concentrated alloys and show how these one-dimensional line defects interact with the complex matrix. Compared to both experiment and continuum modeling of dislocations our atomistic simulations can give unique insights in the trajectories and energetics of each atom as it is displaced by a gliding dislocation. The dislocation line can be tracked with a high temporal and spatial resolution unmatched by other simulation and experimental approaches.

Grain Boundaries

Even though, the high-temperature mechanical properties of HEAs can currently not compete with established Ni-based superalloys there are still prospects for future high temperature application.[2,10,19,23] While strength at high temperatures is most important in this regard, a stable microstructure is equally important to allow for long-term use of a part without changes in its properties.[90] To this end, the grain growth kinetics in HEAs need to be understood to allow for alloy design resilient against high temperature grain growth. The application of HEAs as structural materials in fission or fusion reactors[10,47] could be further improved by a decreased grain growth rate. In conventional metals and alloys, nanocrystalline (NC) microstructures possess an increased irradiation tolerance compared to their coarse-grained counterparts.[91–93] This makes NC microstructures desirable for application, but the irradiation of such grain structures can lead a rapid coalescence of grains and grain coarsening.[63] This unwanted grain growth needs to be prevented for the lifetime the reactor. Reduced grain growth in FCC 3*d* transition metal HEAs has been reported widely, however, there is still debate over its origin.

Some authors[94,95] suggest that the grain growth rate in HEAs might be reduced by the intrinsic lattice distortions, one of the four aforementioned core effects. Others attribute the reduced grain growth rate to the sluggish diffusion[94,96–98] or solute drag.[11,97,99–102] There are also examples, where the increased resistance against grain growth has been attributed to deliberate or accidental secondary phase formation at GBs.[102–107] While the initial research interest, especially in the simulation community, in GB thermodynamics and kinetics was low, a recent spike in interest can be seen.[108–110]

Chapter 6, *'Grain Boundaries'*, reports on the migration behavior of a planar symmetrical tilt grain boundary (STGB) as a case study of grain boundary migration in HEAs. These results are later generalized by means of isothermal grain growth simulations of nanocrystalline samples. Here atomistic simulations offer unique insights in the GB migration mechanism which governs the GB mobility on the smallest scale. Moreover, we have access to a virtual element, the so-called average-atom (avg.-atom),[111] which possesses the same long-range properties as the full HEA, without any chemical inhomogeneity. This unique tool allows for disentanglement of the intrinsic properties of the HEA matrix and solute-drag effects caused by its chemical randomness.

2 Literature Review

2.1 Vacancies

2.1.1 Thermodynamics of Vacancy Formation

Knowledge of the vacancy formation energies and the resulting vacancy concentrations are essential to understand (secondary) phase formation kinetics,[40,112] creep,[41] or transport phenomena[43] in metals and alloys. From a theoretical standpoint, one would expect the vacancy formation energy in a concentrated alloy (independent of the number of constituents) to follow a binomial distribution around a given mean vacancy formation energy. Importantly, said energy is independent of the removed atom — the vacancy formation energy only depends on the atoms surrounding the vacancy, *"unless a ghost of the removed atom is still in the site. Although in reality nobody is certain about ghosts, they cannot exist in the well-determined first-principles calculations."*[113]

To our knowledge, there are only two experimental studies on the vacancy formation energy in the CoCrFeMnNi Cantor alloy. Huang et al.[114] measure the thermal lattice expansion to determine vacancy concentration at a given temperature and then extrapolate the vacancy formation energy.[115] They report a vacancy formation energy of 0.64 eV.[114] This value is substantially lower than the one measured by Sugita et al.[116] who measure a vacancy formation energy of 1.69(13) eV or 1.72(18) eV using positron lifetime spectroscopy.

There are different approaches in modeling vacancy formation energies. A recent CALPHAD calculation reports a vacancy formation energy of 1.7 eV in the equimolar Cantor alloy.[117] At the time of writing, there are only two density functional theory (DFT) calculations of the vacancy formation energies in the full five component Cantor alloy. One by Mizuno et al.[118] who report a mean vacancy formation energy averaged over 125 lattice sites between 1.93 eV (Cr)[†] and 2.06 eV (Ni). Guan et al.[119] find similar values between 1.899 eV (Co) and 2.187 eV (Cr). Both compare favorably to the aforementioned measurements by Sugita et al.[116]

There are other calculations on different subsystems of the Cantor alloy: Chen et al.,[120] Zhao et al.,[121] and Guan et al.[119] investigate the equimolar

---

[†] The element in the parenthesis denotes the species of the atom originally occupying the vacancy site.

four component CoCrFeNi system. They find comparable vacancy formation energies of 1.58 eV (Fe) to 1.89 eV (Ni),[120] 1.8 eV,[121] or 1.81 eV,[119] respectively. Li et al.[122] calculate a mean vacancy formation energy of 1.95 eV in CrFeNiMn. Meanwhile, Middleburgh et al.[123] report a negative vacancy formation energy of −0.3 eV (Cr) and positive energies (1.7 eV to 2 eV) for the other constituents of the CoCrFeNi alloy. Reports on the CoCrNi medium-entropy alloy (MEA) find values of comparable magnitude of 1.8 eV[121] and 1.82 eV.[119] All authors show substantial scatter in their calculated vacancy formation energies suggesting a strong site, i.e., chemical environment, dependency of the vacancy formation energy in high-entropy alloys (HEAs).

Vacancy Concentration Models for Concentrated Alloys

To apply these calculated vacancy formation energies to diffusion problems, the vacancy concentration at a given temperature needs to be known. Fundamentally, there are two different methods of linking vacancy formation energies to vacancy concentrations. Either by means of grand canonical Monte Carlo (MC) simulations[124] or using established thermodynamical models. In monoatomic materials these models boil down to an Arrhenius law,[43,125] but for concentrated alloys this relation is less obvious. In the following, three different approaches will be presented.

Model by Ruban

For equimolar binary alloys Ruban[113] suggests the following method to calculate the vacancy concentration c_{Vac} considering the excess free energy ΔG_{Vac} of a system containing a given vacancy concentration, with respect to the configurational entropy of the vacancy and the configurational entropy of the defect-free host matrix. Initially, ΔG_{Vac} can be written as,

$$\Delta G_{\mathrm{Vac}} = c_{\mathrm{Vac}} \overline{G}_{\mathrm{f}} - T S_{\mathrm{Conf}}, \tag{2.1}$$

where $\overline{G}_{\mathrm{f}}$ is the effective vacancy formation free energy and S_{Conf} is the configurational entropy of the alloy containing vacancies. S_{Conf} can be readily computed under the assumption of randomly dispersed vacancies and constant concentrations of the alloy's constituents,

$$S_{\mathrm{Conf}} = -k_{\mathrm{B}}(c_{\mathrm{Vac}} \ln c_{\mathrm{Vac}} + c_1 \ln c_1 + c_2 \ln c_2), \tag{2.2}$$

where:

$$c_1 = c(1 - c_{\mathrm{Vac}}), \quad c_2 = (1-c)(1-c_{\mathrm{Vac}}), \quad \text{and} \quad c = \frac{c_1}{c_1 + c_2}. \tag{2.3}$$

Here, $c_1 + c_2 + c_{\mathrm{Vac}} = 1$ and indices 1 and 2 denote the two different species in the binary alloy. As per usual, k_{B} is the Boltzmann constant. Further, using the single-site approximation and assuming small vacancy concentrations the minimization of ΔG_{Vac} with respect c_{Vac} to yields,

$$c_{\mathrm{Vac}} = \exp\left(-\frac{\overline{G}_{\mathrm{f}} + TS_{\mathrm{All}}}{k_{\mathrm{B}}T}\right) \equiv \exp\left(-\frac{\widetilde{G}_{\mathrm{f}}}{k_{\mathrm{B}}T}\right), \tag{2.4}$$

where S_{All} is the configurational entropy of the defect-free host alloy equal to,

$$S_{\mathrm{All}} = -k_{\mathrm{B}}(c\ln c + (1-c)\ln(1-c)). \tag{2.5}$$

Given the difference in chemical environments in concentrated alloys, the vacancy formation energy is not a single value but instead follows a distribution g. To account for this distribution Equation 2.4 needs to be integrated over all vacancy formation energies,

$$c_{\mathrm{Vac}} = \int g \exp\left(-\frac{\widetilde{G}_{\mathrm{f}}}{k_{\mathrm{B}}T}\right) d\widetilde{G}_{\mathrm{f}}, \tag{2.6}$$

neglecting vacancy-vacancy interactions and assuming that non-configurational entropy contributions to the vacancy formation entropy S_{f} are independent of the vacancy environment this equation can be simplified to,

$$c_{\mathrm{Vac}} = \exp\left(\frac{S_{\mathrm{f}} - S_{\mathrm{All}}}{k_{\mathrm{B}}}\right) \int g \exp\left(-\frac{H_{\mathrm{f}}}{k_{\mathrm{B}}T}\right) dH_{\mathrm{f}}, \tag{2.7}$$

knowing that $\overline{G}_{\mathrm{f}} = H_{\mathrm{f}} - TS_{\mathrm{f}}$, where H_{f} is the vacancy formation enthalpy. Note, the distribution g needs to be normalized,

$$g = \sum_i g_i x_i \quad \text{and} \quad \int g_i dH_i = 1, \tag{2.8}$$

where c is the concentration and i is the index denoting the different species in the alloy. In the special case of an equimolar alloy of N components which ideally mix the S_{All} term in Equation 2.7 maybe be solved explicitly,

$$c_{\mathrm{Vac}} = \frac{1}{N} \exp\left(\frac{S_{\mathrm{f}}}{k_{\mathrm{B}}}\right) \int g \exp\left(-\frac{H_{\mathrm{f}}}{k_{\mathrm{B}}T}\right) dH_{\mathrm{f}}, \tag{2.9}$$

as $S_{\mathrm{All}} = -k_{\mathrm{B}} \sum_i c_i \ln c_i$ in this case. Notably, this means that a random equimolar alloy always has a $1/N$ times lower vacancy concentration compared to a monoatomic metal with the same vacancy formation energy. The is not an intuitive result but it follows directly from the configurational entropy of the HEA host matrix S_{Conf} in Equation 2.1. Moreover, as outlined in the next section, there is substantial doubt on the validity of this model and the assumptions made therein.

Model by Morgan and Zhang

The model by Ruban[113] has since been disputed by Morgan and Zhang.[126] They state that the vacancy concentration in a concentrated alloy is independent of the number of constituents in the host matrix. They state that the error in Ruban's derivation shown above is introduced at Equation 2.4 as it corresponds to the minimization of the *Gibbs free energy per site*, but not the total Gibbs free energy G_{Total}, i.e., the *Gibbs free energy per atom*, of the whole system. While the difference of *energy per lattice site* or *energy per atom* is usually insignificant, it matters for the case of vacancy formation, as this process creates lattice sites at constant particle numbers. In the following their reasoning will be shown. The number of sites N_{Sites} in an alloy containing n species i is related to the number of atoms N_{Atoms} in the following way,

$$N_{\mathrm{Atoms}} = \sum_i^n N_i \quad \text{and} \quad N_{\mathrm{Sites}} = N_{\mathrm{Atoms}} + N_{\mathrm{Vac}}, \tag{2.10}$$

where N_{Vac} is the number of vacancies. Starting from a system with N_{Sites} occupied lattice sites, $N_{\mathrm{Vac}} = 0$ the following quantities can be defined,

$$c_i = \frac{N_i}{N_{\mathrm{Sites}}}, \quad c'_{i\neq 1} = \frac{N_i}{\sum_{j=2}^n N_j} \quad \text{and} \quad c_{i\neq 1} = (1-c_1)c'_{i\neq 1}. \tag{2.11}$$

The configurational entropy in this system may be written as,

$$\begin{aligned} S_{\mathrm{Conf}} &= -k_{\mathrm{B}} \sum_i^n (c_i \ln c_i) \\ &= -k_{\mathrm{B}} \Bigg[\underbrace{c_1 \ln c_1}_{1} + \underbrace{(1-c_1)\ln(1-c_1)}_{\text{'not 1'}} + \underbrace{(1-c_1)\sum_{i=2}^n c'_i \ln c'_i}_{\text{mixing of 'not 1'}} \Bigg]. \end{aligned} \tag{2.12}$$

Equation 2.12 is a way to formulate the ideal mixing entropy per site of a multicomponent system in terms of a binary system containing species 1 and fictitious species 'not 1' and the ideal mixing entropy of all 'not 1' species on the 'not 1' lattice sites. Armed with this knowledge of the configurational entropy, the total Gibbs free energy can be written under the condition that all species except '1' mix ideally and are taken from an unmixed reference state,

$$\begin{aligned} G_{\mathrm{Total}} = N_1 \mu_1^0 &+ k_{\mathrm{B}} T N_{\mathrm{Sites}} [c_1 \ln c_1 + (1-c_1)\ln(1-c_1)] \\ &+ k_{\mathrm{B}} T N_{\mathrm{Sites}} (1-c_1) \sum_{i=2}^n c'_i \ln c'_i, \end{aligned} \tag{2.13}$$

where μ_1^0 is the standard chemical potential of species '1'. The last term in Equation 2.13 is only related to the number of atoms in the system not of type '1'. Therefore, it becomes independent of N_1. Now defining type '1' as vacancies in the alloy, one can see that if the system is only open to species '1', i.e., vacancies can be created and destroyed, while the number of all other species remains constant, $N_{\mathrm{Sites}}(1-c_1)$ and $c'_{i\neq 1}$ = constant. From here it follows that the total free energy of a multicomponent alloy can be written in the form of a binary alloy containing species '1', fictitious species 'not 1', and some constant term. The equilibrium concentration of species '1' or in this case vacancies can now be determined by setting their chemical potential to some external value μ_1^*,

$$\left(\frac{\partial G_{\mathrm{Total}}}{\partial N_1}\right)_{T,P,N_{i\neq 1}} = \mu_1^*. \tag{2.14}$$

Since all complications of the multicomponent alloy are encapsulated in the constant term, this derivative takes the well-known form, established for binary alloys,

$$\frac{c_1}{1-c_1} = \exp\left(-\frac{\mu_1^0-\mu_1^*}{k_{\mathrm{B}}T}\right). \tag{2.15}$$

As mentioned before, type 1 corresponds to the vacancies in the alloy. Per convention, μ_1^* is set to 0 and $\mu_1^0 = \overline{G}_f$, where $\overline{G}_f$ is again the free vacancy formation energy. Lastly, assuming $c_1 \ll 1$ the established expression for the vacancy concentration may be obtained,

$$c_1 = c_{\mathrm{Vac}} = \exp\left(-\frac{\overline{G}_f}{k_{\mathrm{B}}T}\right). \tag{2.16}$$

This equation derived by Morgan and Zhang[126] now gives identical vacancy concentrations for multicomponent and monoatomic alloys if they have the same vacancy formation energy. Moreover, this equation is independent of the number of constituents in an alloy and therefore generalizes to all multicomponent alloys, as long as ideal mixing of the elements can be guaranteed. Lastly, all complications of the distribution of the vacancy formation energies due to local chemical fluctuations and the effect of other entropic contributions in the form of S_{f} can be treated analogous to Equation 2.7.

Model by Wang et al.

The last thermodynamic model established in literature is derived by Wang et al.[127] Compared to the previous authors, they do not provide an in-depth theoretical derivation. Therefore, we will present their derivation in its entirety, without expressed or implied agreement or full understanding. Moreover, they do not consider a distribution of vacancy formation energies; instead, they only take a single mean vacancy formation energy into account. Similar to Ruban[113] and Morgan and Zhang,[126] they start from molar free energy of a vacancy containing system ΔG,[128]

$$\Delta G = c_1 N_{\mathrm{A}} G_{\mathrm{f}} - N_{\mathrm{A}} k_{\mathrm{B}} T[c_1 \ln c_1 + (1-c_1)\ln(1-c_1)], \tag{2.17}$$

here c_1 is the molar vacancy concentration, G_f is the free energy of vacancy formation, N_A is the Avogadro constant, and k_B is the Boltzmann constant. The equilibrium vacancy concentration can be determined from the equilibrium condition,

$$\frac{\partial \Delta G}{\partial c_1} = N_\mathrm{A} G_\mathrm{f} - N_\mathrm{A} k_\mathrm{B} T[c_1 \ln c_1 + (1-c_1)\ln(1-c_1)] = 0, \tag{2.18}$$

which gives,

$$c_1 = c_\mathrm{Vac} = \frac{\exp\left(-\frac{G_\mathrm{f}}{k_\mathrm{B}T}\right)}{1+\exp\left(-\frac{G_\mathrm{f}}{k_\mathrm{B}T}\right)} \approx \exp\left(-\frac{G_\mathrm{f}}{k_\mathrm{B}T}\right), \tag{2.19}$$

under the assumption of a vacancy concentration significantly smaller than 1. Wang et al.[127] extend this approach for an equimolar HEA containing n elements (subsequently indicated by sub/superscript), stating that the free vacancy formation energy is given by,

$$\Delta G_\mathrm{f}^n = c_n N_\mathrm{A} G_\mathrm{f}^n - N_\mathrm{A} k_\mathrm{B} T\left[c_n \ln c_n + (1-c_n)\ln\left(\frac{1-c_n}{n}\right)\right] - \ln\frac{1}{n}, \tag{2.20}$$

which leads to the following equilibrium condition,

$$\frac{\partial \Delta G_\mathrm{f}^n}{\partial c_n} = N_\mathrm{A} G_\mathrm{f}^n - N_\mathrm{A} k_\mathrm{B} T\left[1 + \ln c_n - n - \ln\left(\frac{1-c_n}{n}\right)\right] = 0, \tag{2.21}$$

and the resulting vacancy concentration in the n-component system is given by,

$$c_n = c_\mathrm{Vac} = \frac{\exp\left(n-1-\frac{G_\mathrm{f}^n}{k_\mathrm{B}T}\right)}{n+\exp\left(n-1-\frac{G_\mathrm{f}^n}{k_\mathrm{B}T}\right)}. \tag{2.22}$$

If one is only interested in the ratio of vacancies for the n component alloy compared to a monoatomic alloy of the same vacancy formation energy their ratio may be written as,

$$\frac{c_n}{c_1} = \frac{\exp(n-1)\left(1+\exp\left(-\frac{G_\mathrm{f}^n}{k_\mathrm{B}T}\right)\right)}{n+\exp\left(n-1-\frac{G_\mathrm{f}^n}{k_\mathrm{B}T}\right)} \approx \frac{\exp(n-1)}{n}. \tag{2.23}$$

From here, it can be seen that opposite to Ruban,[113] Wang et al.[127] predict an increased vacancy concentration in the multicomponent alloy compared to a monoatomic alloy with the same vacancy formation energy. This increase is equal to a factor 11 in a five component alloy and rises to 25 in a six component HEA.

2.1.2 Kinetics of Vacancy Migration

Tracer diffusivity D^* via the vacancy mechanism, can be described by the following equation,[43]

$$D^* = c_{\mathrm{Vac}} \lambda^2 \nu_0 f \exp\left(-\frac{\overline{G}_{\mathrm{Mig}}}{k_{\mathrm{B}} T}\right), \tag{2.24}$$

where c_{vac} is the vacancy concentration at a given temperature, λ is the length of a diffusional jump, ν_0 is the attempt frequency, $\overline{G}_{\mathrm{Mig}}$ is the effective free energy of vacancy migration, and f is the tracer correlation factor, the latter two will be described in more detail in the following sections.

Atomistic computer simulations in this field remain rare due to the chemical complexity in HEAs requiring large simulation cells and many independent simulations to obtain statistically representative results. To our knowledge, there are only two computational studies of the vacancy migration energy on the full five component Cantor alloy; Mizuno et al.[118] used DFT to calculate the vacancy migration energy in the Cantor alloy for all species in six different chemical environments. They find the lowest migration barrier for Cr (0.57 eV) and the highest one for Ni (0.97 eV). Other results are published by Choi et al.[129] who report vacancy migration barriers calculated based on their interatomic potential. Sampling 390 different vacancy jumps, they find the lowest migration energy for Mn (0.67 eV) and the highest one for Ni (1.21 eV). The direct comparison between both studies reveals substantial differences not only in the quantitative migration energy barriers, but also in the elemental hierarchies (Cr < Mn < Fe < Co < Ni[118] compared to Mn < Fe < Cr < Co < Ni[129]). Disagreement seems to be related to the position of Cr in this row. Note, while Mizuno et al.[118] use nudged elastic band (NEB) calculations to determine the minimum energy path for diffusion, Choi et al.[129] only sample a direct and linear transition path. Therefore, the latter study most likely overestimates the migration energy as they do not allow for structural relaxation. There are two more DFT studies reporting on the migration energies in different four component subsystems of the Cantor alloy. Even though, these might not be immediately comparable, they show different hierarchies compared to the five component alloy (Cr < Fe < Ni < Co[121] and Mn < Cr < Ni < Fe[122])

2.1.3 Tracer Diffusion Correlation Factor

The next ingredient required to connect the atomistic calculations to the experimentally measured tracer diffusivities is the so-called correlation factor. Intuitively one would expect diffusing atoms in a crystal to perform a random walk on the lattice. Tracking atomic trajectories through a solid reveals deviations from this ideal behavior as the atoms take a correlated walk. The difference between these walks is described by a so-called *correlation factor*. There are two different origins for these correlations. If one marks only a small subset of atoms (e.g., using radioactive isotopes), their exchange frequencies with vacancies in the material will not be random. Instead, after a single vacancy exchange jump the probability for the reverse jump will be increased leading to a correlation.[130] Even in dilute alloys containing more than one species, there is a second effect, as there are different jump frequencies associated to different directions based on the chemical environment of the vacancy.[130] In an alloy containing multiple solutes, or in the case of concentrated alloys, more than two main constituents, a different correlation factor may be found for each species.[131,132]

The correlation factor in random alloys is usually determined from the so-called *random alloy model*.[131,132] This model allows for the determination of the correlation factors from lattice MC simulations. The main approximation of this model is the assumption that each atom has a single jump frequency, i.e., a single vacancy migration energy, only depending on its species and independent of its chemical environment or its specific lattice site. These frequencies are used as probabilities for an atom to exchange lattice site with a neighboring vacancy. Here, higher frequencies correspond to a higher exchange probability. Constructing the vacancy and atom trajectories based on these frequencies can be used to determine the correlation factors (cf. Section 4.3 for further details). Manning,[132] the developer of the model, states that the error introduced by these assumptions should be small in any reasonably random alloy.

The random alloy model has been used extensively over the years to derive different analytical models for the tracer correlation factor in random alloys and compare them to MC simulations.[133–143] Unfortunately, many of these MC simulations are not converged or otherwise limited due to the constrained computational resources at their time of writing.[143,144]

Paul et al.[145] reported first results on MC simulations for the tracer correlation factor within the framework of the random alloy model for HEAs. In their work, however, they are not describing a *real* material; instead they construct a multicomponent alloy made up of species of differing jump frequencies. This setup is used to compare predictions of theoretical models against these simulations. An important conclusion from this paper is their finding that the random alloy model approximates real HEAs sufficiently well. Multiple authors have since stated the importance of correlated diffusion in HEAs.[146–149] Gärtner et al.[150] recently used MC simulations within the random alloy model to fit the tracer correlation factors to experimentally measured single crystalline tracer diffusion coefficients.

2.1.4 Sluggish Diffusion

Sluggish diffusion was postulated as one of the four core effects of HEAs by Yeh[15] in 2006. Sluggish diffusion here means that the diffusion in HEAs is systematically reduced compared to pure metals or dilute alloys.[15] This effect is often attributed to strong fluctuations in activation energies based on the local chemical environment decreasing overall diffusion rates.[16] As diffusion itself is not an easy phenomenon to measure, early experimental confirmation[6,15,151–157] came from secondary observations like the appearance of nanocrystalline microstructures, the absence of low temperature phases even after slow furnace cooling[8,10] or a reduced creep rate.[157] Critical assessment of these results noted that these results are not conclusive as especially phase transformations are influenced by other parameters like chemical potential differences and concentration gradients and not only the diffusive properties.[8] Moreover, there are a multitude of counterexamples[8] where precipitation is observed after casting[6,152,158–170], rapid cooling[171–173], or quenching.[170,174,175]

After these initial reports of sluggish diffusion in HEAs, the first detailed diffusion study on a five component alloy, namely CoCrFeMn$_{0.5}$Ni, was published by Tsai et al.[45] in 2013. They studied different diffusion couples using a quasi-binary sample setup (in each diffusion couple only two species had a concentration gradient) and concluded that this alloy has reduced diffusivities and higher activation energies compared to its pure constituents. Hence, they took this as confirmation of the sluggish diffusion hypothesis. Further, they conjectured that this reduction in diffusivities is caused by the fluctuations in the potential energy landscape in HEAs which features local low energy sites in which the diffusing atoms or vacancies get trapped. In the following years, this study has been widely criticized; Pickering and Jones[8] state that the small differences found in the activation energies for diffusion in the CoCrFeMn$_{0.5}$Ni HEA and conventional alloys[179] are not sufficient to confirm sluggish diffusion. While this criticism is directed at the interpretation of the obtained results, the calculations of Tsai et al.[45] have been doubted as well. Paul[180] reveals

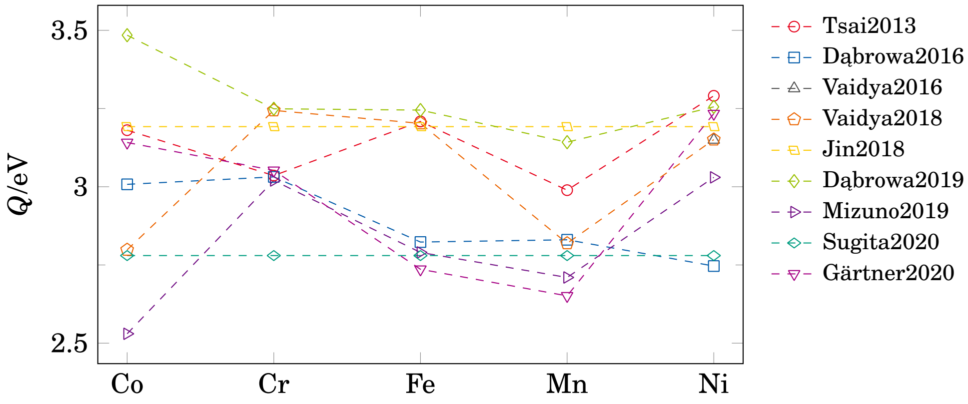

Figure 2.1: Comparison of the activation energies Q for bulk diffusion in the 5 component Cantor alloy system from different references: Tsai2013,[45] Dąbrowa2016,[176] Vaidya2016,[148] Vaidya2018,[149] Jin2018,[177] Dąbrowa2019,[178] Mizuno2019,[118] Sugita2020,[116] and Gärtner2020.[150] Tsai et al.[45] and Dąbrowa et al.[176] investigated the CoCrFeMn$_{0.5}$Ni HEA. Sugita et al.[116] and Jin et al.[177] only reported a single Q value for the full alloy.

multiple errors in their data treatment which could not be dispelled[16] even after a response by the original authors.[181]

Since 2013 many more diffusion studies have been published, and there are two main methods from which atomic diffusivities have been obtained: Measurement of concentration gradients in diffusion couples[45,176–178,182–190] or tracking the diffusion of radioactive tracer isotopes into the HEA.[148–150,191–195] Only Sugita et al.[116] report on a third method, namely positron lifetime spectroscopy. Meaningful comparison of these diffusivities, especially across alloy systems, is nigh on impossible. Therefore, we restrict our comparison on the CoCrFeMnNi Cantor alloy system. Figure 2.1 shows the activation energy Q calculated for the different species in this HEAs. It can be seen that even though these experiments determine the same quantity their scatter is large. As Q enters the diffusivity calculation in the exponential term,[43]

$$D = D_0 \exp\left(-\frac{Q}{k_\mathrm{B}T}\right), \tag{2.25}$$

where D_0 is an exponential pre-factor and $k_\mathrm{B}T$ has its usual meaning. The observed differences of ±0.5 eV can lead to changes of multiple orders of magnitude in the resulting D. If one also considers the experimental uncertainties of up to 0.23 eV,[149] interpretation becomes even more difficult.

The conclusion on sluggish diffusion in HEAs remains divisive. Refs. 45,146, 176,178,182,185–187,190,192,196 conclude that diffusion in HEA can be called sluggish, while Refs. 148,149,177,178,184,189,191,193,195 report that diffusion is either non-sluggish or that there is not enough evidence to confirm sluggish diffusion. There are two approaches of consolidating these different conclusions. Firstly, there appears to be a split where the inter-diffusion in HEAs seems to be sluggish, while tracer diffusion appears to be *normal*, i.e., non-sluggish.[185–187] Unfortunately, this correlation remains unexplained.

Secondly, recent findings suggest that it is not the number of constituents in an alloy that is responsible for sluggish diffusion but the type of elements which are mixed.[177,196,197] Durand et al.[196] report that the diffusivity is relatively high in pure elements and concentrated binary alloys but decreases substantially once a third element is added, while the addition of a fourth element does not influence the diffusion constants further. Dąbrowa et al.[178] find that Mn seems to be responsible for the sluggish diffusion cited so often. They compared the diffusion in the Cantor alloy and its subsystems. Here, the Mn-free alloys show normal diffusion kinetics, while the Mn containing alloys show a pronounced reduction in diffusivity. Both agree that the species of added elements is more important than their absolute number.

2.2 Dislocations and Strengthening Mechanisms

Dislocations in concentrated alloys have been of great interest ever since their inception. This stems not only from the great potential for solid solution strengthening in these alloys but also from their meandering shape in equilibrium and during glide. The following sections summarize established literature of solid solution strengthening and the discrepancies of stable stacking fault energies observed in the Cantor alloy system. This is followed by a review on dislocations in face-centered cubic (FCC) HEAs in equilibrium and during glide. Here, different origins for the localized pinning of dislocations in these materials are summarized in detail.

2.2.1 Solid Solution Strengthening Models

Even after their exhaustive search, George et al.[19] and others[2,10,198] conclude that there is currently no HEA that can compete with the strongest steels or superalloys available today. Therefore, eyes have turned towards other methods to improve the mechanical properties of HEAs. A lot of work[18,199–205] has been put into the development of HEAs showing transformation induced plasticity or twinning induced plasticity (compare conventional steels[206]). While others[27,31–35,207–209] worked on precipitation hardening, a method commonly used in Al[210] or Mg[211] alloys (details summarized in Subsection 2.2.6). A relatively new approach is the incorporation of short-range order (SRO) to hinder dislocation glide and improve strength of the alloy (see Subsection 2.2.5 for detailed review).[36–39,212]

Nevertheless, the strength of FCC single phase HEAs remains of interest as they form the backbone for all further strengthening mechanism mentioned above[213] or as a matrix in HEA-matrix composites.[214–216] Here, much of the vast design space has been left unexplored.[2,9,10,19] Comprehensive and parameter free solid solution strengthening models can be used to rapidly screen this design space and guide experiments. The following brief historical overview of solid solution strengthening models is based on the review by LaRosa et al.[213] For dilute alloys there are two different approaches to describe solid solution strengthening. Fleischer[83,84] and Friedel[85] suggest strong-pinning models, where the dislocation line gets pinned on individual solutes in a monoatomic matrix. Once the dislocation is pinned by such an obstacle, an additional shear stress is required to bow out the dislocation line until it can detach and glide further. The weak-pinning models derived by Mott[86] and Labusch,[87,88] on the other hand, do not model solutes as individual atoms in a matrix but instead treats them as a stochastic field of randomly distributed solutes. Within this field, there are positions which are energetically favorable for the dislocation line. Once trapped in such a position, an additional force is required to detach the dislocation thereby reducing its mobility and increasing the strength of an alloy. Comparison of the two models reveals that the Labusch model better describes strengthening at temperatures and solute concentrations relevant for real-world structural applications.[217] Leyson et al.[218,219] further improved the Labusch model removing the need for ad hoc assumptions. Nevertheless, the model still relies on a well-defined host matrix in which solutes are dissolved.

For obvious reason, the definition of host and added solute atoms breaks down for concentrated alloys like MEAs or HEAs. Knowing these limitations, Senkov et al.[220] described their TaNbHfZrTi body-centered cubic (BCC) refractory HEA as a pseudo-binary system and estimated its strength based on the conventional Labusch model. They report a moderate error of 18 % between model and experiment.

More recently, solid solution strengthening models directly designed to describe concentrated alloys have been developed. Toda-Caraballo and Rivera-Díaz-del-Castillo have formally extended the Labusch model to account for arbitrary compositions.[221,222] Further, they linked the strengthening coefficients in the Labusch model to the intrinsic lattice distortions to concentrated alloys, as they can be measured or calculated directly.[223–229] This model has successfully been applied to different concentrated alloys.[221,222,230–233]

Instead of augmenting the Labusch model with further theory, Walbrühl et al. assumed a non-linear concentration dependence of strengthening parameters on alloy composition. They fit these strengthening parameters to a large database of experimental hardness measurements, thereby training the model, and obtain an accuracy of ±13 % over a broad range of elements and compositions.[234] While this model can be used to predict the Vickers hardness in a material system, it does not offer new insights into the physical origin of said strength. Compared to other strengthening models, this formalism cannot only account for hardness in a single-phase FCC solid solution but also models multiphase materials with different phase factions and even interstitial atoms.

A similar, less broad, fitting approach has recently been outlined for the hardness in the Cantor alloy system by Shafiei.[235] They fit the experimental hardness measurements by Bracq et al.[236] using a second-order polynomial. Similar to Walbrühl et al.,[234]they provide a parameter set for the best fit.

Zhang et al.[37,237] derive a stochastic Peierls-Nabarro model which can be applied to near equiatomic single-phase HEAs. The chemical fluctuations in this statistical continuum model are described by the standard deviation of the local concentration and a correlation length. Including this correlation length allows for a correct treatment of chemical short- or long-range order which might be present in HEAs. Something that is impossible with the previously mentioned models.

The Model by Varvenne et al.

Lastly, the most commonly used[38,72,231,236,238–245] solid solution strengthening model for concentrated alloys is derived by Varvenne et al.[72,89] Their two main publications describing the model currently tally a combined citation count of 350.[72,89] It deviates from other theories by describing any HEA as a monoatomic effective medium matrix, where each lattice site hosts a solute species embedded into this average matrix. For each species in the HEA an interaction between dislocation, average matrix (solvent), and this species acting as solute are responsible for the strengthening. The Varvenne model can be seen as a direct extension of the Leyson model[218,219] to which it reduces in the dilute limit.[213]

While there is a full model, featuring chemical binding energies of the dislocation and the solutes, a reduced version of the model, where all dislocation-solute interactions are of elastic nature is most commonly used. In the following, this reduced model will be introduced. Here, the solutes are characterized by their misfit volume ΔV, the effective size difference between a solute and the alloy matrix. This corresponds not necessarily to a *physical* size difference but also accounts for the chemical interactions of the different species.[19] The resulting elastic energy contribution considered here stems from the interaction of the dislocation stress field with the misfit strain created by each solute embedded into the average *solvent* matrix.[213] The finite temperature yield stress in the Varvenne model has two ingredients: The zero-temperature flow shear stress $\tau_{\mathrm{y},0}$ and the potential energy barrier ΔE_{b} the dislocation faces during glide. These are given by,[72]

$$\tau_{\mathrm{y},0} = 0.051\alpha^{-\frac{1}{3}}\mu\left(\frac{1+\nu}{1-\nu}\right)^{\frac{4}{3}} f_1 \left[\frac{\sum_i x_i\left(\Delta V_i^2 + \sigma_{\Delta V_i}^2\right)}{b^6}\right]^{\frac{2}{3}}, \tag{2.26}$$

$$\Delta E_{\mathrm{b}} = 0.247\alpha^{\frac{1}{3}}\mu b^3\left(\frac{1+\nu}{1-\nu}\right)^{\frac{2}{3}} f_2 \left[\frac{\sum_i x_i\left(\Delta V_i^2 + \sigma_{\Delta V_i}^2\right)}{b^6}\right]^{\frac{1}{3}}, \tag{2.27}$$

where α is the dimensionless line tension parameter taken as 0.123,[72] μ is the shear modulus, ν is Poisson's ratio, x_i the molar fraction of species i, ΔV_i is the misfit volume and its standard deviation $\sigma_{\Delta V_i}$, and b is the Burgers vector. The two minimized dislocation core coefficients f_1 and f_2 are reported to be $f_1 = 0.35$ and $f_2 = 5.70$ for typical FCC HEAs with typical elastic constants and stacking fault energies below $100\,\mathrm{mJ\,m^{-2}}$.[72]

In the low temperature and high stress regime the finite temperature critical shear stress τ_{y} is equal to,[72,219]

$$\tau_{\mathrm{y}} = \tau_{\mathrm{y},0}\left[1 - \left(\frac{k_{\mathrm{B}}T}{\Delta E_{\mathrm{b}}}\ln\frac{\dot{\varepsilon}_0}{\dot{\varepsilon}}\right)^{\frac{2}{3}}\right], \tag{2.28}$$

in the high temperature low stress regime, on the other hand,[72,219]

$$\tau_{\mathrm{y}} = \tau_{\mathrm{y},0}\exp\left(-\frac{1}{0.51}\frac{k_{\mathrm{B}}T}{\Delta E_{\mathrm{b}}}\ln\frac{\dot{\varepsilon}_0}{\dot{\varepsilon}}\right). \tag{2.29}$$

Here, $k_{\mathrm{B}}T$ has its usual meaning, $\dot{\varepsilon}_0$ is a references strain rate which may be obtained from the Orowan relationship[68] as its value only enters logarithmically a value of $\dot{\varepsilon}_0 = 1\times 10^4\,\mathrm{s}^{-1}$ is usually sufficiently accurate.[72,219] Using the Taylor factor[246] $M = 3.06$ for FCC metals the calculated critical shear stress can be related to a macroscopic yield strength,[68]

$$\sigma_{\mathrm{y}} = M\tau_{\mathrm{y}}. \tag{2.30}$$

This model is steadily improved, and the strengthening effects of SRO[38] or solute-solute interactions[247] have recently been added.

We have applied these solid solution strengthening models to explain the experimentally measured strengthening in the AuCuNiPdPt noble metal HEA system in cooperation with Felix Thiel from IFW Dresden.[248,249] Similarly, in cooperation with Tom Keil of TU Darmstadt, we applied different solid solution strengthening models to describe the solid solution hardening observed in the Cantor alloy system.[250] These publications do not relate to the main body of this thesis; therefore they will not be discussed in detail.

2.2.2 Stacking Fault Energies

One important quantity in FCC metals is the stable stacking fault (SF) energy and, more general, the planar fault energy surface of the $\{1\,1\,1\}$ plane.[67,68] While these energies are fully accessible from atomistic simulations using standard methodology,[251,252] only the stable intrinsic stacking fault (ISF) energy is measurable, experimentally.[252] These experimental measurements are either based on TEM measurements of partial dislocations[253,254] or interpretation of X-ray diffraction data.[255] Sun et al.[256] recently reviewed SF energy data for different metastable metals and alloys which have a stable hexagonal close-packed (HCP) and metastable FCC phase. They report two problems with the established experimental techniques. First, the experimental resolution and uncertainties mean that there is a constant lower limit of measurable ISF energies at about $20\,\mathrm{mJ\,m^{-2}}$. Moreover, these methods are based on the force balance of the repulsive Peach-Koehler force of two partial dislocations and the attractive force from the positive SF energy. They state that this force balance does not exist anymore if an alloy has a negative SF energy, as this reverses the sign of the forces associated with the SF invalidating this force balance.

This becomes important for the Cantor alloy family HEAs as both the CoCrNi and the CoCrFeMnNi alloy are only metastable in the FCC phase with a stable HCP phase at room temperature.[257–260] As outlined above, this invalidates experimental results of the room temperature SF energy. Computational determination of the planar fault energies in these concentrated alloys is difficult as well, as it requires sampling of many chemical environments. It has been shown that the planar fault energies vary greatly not only with the local chemical environment[260–262] but also with SRO.[261] The following paragraphs give an overview over existing literature data, while they all agree on the fact, that the CoCrFeMnNi family of HEAs has a comparatively low ISF energy, the absolute values still scatter substantially. Figure 2.2 shows a graphical summary of the different references and their disagreement on the ISF energies. For the five component Cantor alloy experimental measurements[*] based on transmission electron microscopy (TEM) report stacking fault energies in the

---

[*] All planar fault energies given in the following are rounded to the nearest multiple 5. Artifacts from this rounding are smaller than commonly reported uncertainties.

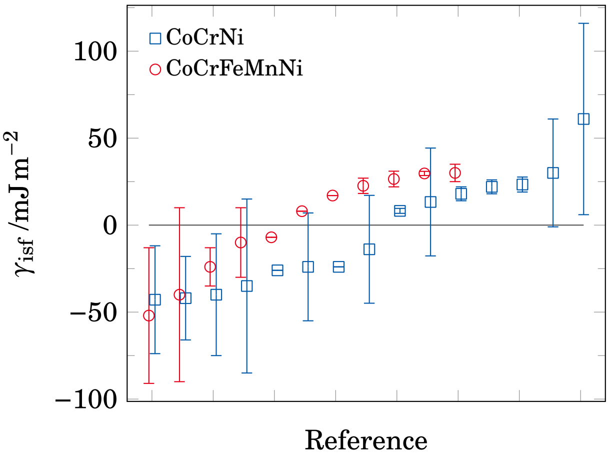

Figure 2.2: Summary of the stable ISF energies γ_{isf} extracted from the references presented in Subsection 2.2.2. The data points are shown in ascending order. It can be seen that there is no consensus on the sign or magnitude of the SF energy within these alloy systems.

range of 30 mJ m^{-2},[263,264] whereas the X-ray diffraction method gives a slightly lower value of 20 mJ m^{-2}.[265] DFT calculations give a much less clear picture. While some authors report stacking fault energies in the range of 15 mJ m^{-2} to 30 mJ m^{-2},[266,267] others report values slightly above[268] or below[269] 0 mJ m^{-2}. Lastly, there are several publications reporting ISF energies in the range of −40 mJ m^{-2} to −55 mJ m^{-2}.[258,260]

In the CoCrNi MEA the experimental results show quite a large scatter. TEM measurements of the partial dislocation spacing give stacking fault energies between 15 mJ m^{-2} to 25 mJ m^{-2} for the presumably random alloy.[264,270] Zhang et al.[39] intentionally prepared random samples and samples featuring SRO. They report an ISF energy of 10 mJ m^{-2} for the random CoCrNi and a significantly higher one of 25 mJ m^{-2} for the SRO sample. This trend, even though there is a stark difference in absolute values, is in agreement with DFT calculations by Ding et al.,[261] who report a lower mean ISF energy of −45 mJ m^{-2} for their random samples compared to 30 mJ m^{-2} for the most ordered samples. Other DFT simulations of the random MEA all report negative stacking fault energies between −20 mJ m^{-2} and −60 mJ m^{-2}.[258,260,269,271,272]

2.2.3 Dislocations in High-Entropy Alloys

Dislocations in FCC 3d transition metal HEAs initially appear to behave similarly to dislocations in conventional FCC metals or alloys. The perfect $1/2\langle 1\,1\,0\rangle$ dislocations gliding on $\{1\,1\,1\}$ planes dissociate into $\langle 1\,1\,2\rangle$ Shockley partial dislocations,[76,263,273,274] as expected from Frank's energy criterion.[67,68,275] The dislocation mobilities of screw and edge dislocations have been reported to be of similar magnitude[80,263] and dissociated partials have been found to be more mobile compared their perfect counterpart.[76]

The main difference between dislocations in concentrated MEAs and HEAs is the equilibrium dislocation line arrangement. Dislocations in pure metals form straight lines under static equilibrium conditions to minimize the dislocation line energy.[67,68] The local chemical fluctuations in the HEAs, however, can stabilize longer, i.e., meandering, dislocation lines if this enables favorable dislocation-solute interactions.[72,213,276] These lead to a strengthening of the resulting alloy, as moving the dislocation away from these favorable solute arrangements requires additional energy.[72] Moreover, partial dislocation spacing is dictated by the elastic constants and the SF energy.[67,68] In pure metals, both quantities are spatially invariant leading to two straight partial dislocations separated at a constant width. Suzuki has shown that in dilute alloys solutes can segregate to the SF and change its energy.[277,278] Ding et al.[261] and others[258,262] showed that the SF energy can vary strongly in HEAs depending on the local chemical environment of the planar fault. This means that as the SF energy varies along the dislocation line leading to locally fluctuating partial dislocation spacing and therefore encourages wavy dislocation arrangements. This effect has been reported for a variety of MEAs and HEAs.[36,74,78–80,279] A related discrete dislocation dynamics[68,280] simulation found that decreasing SF energies, while increasing their fluctuations leads to a strengthening of the alloy.[279]

The second factor leading to dislocation waviness is related to conventional strengthening theories. The dislocation does not glide smoothly through a concentrated alloy matrix as it would in a pure metal. Instead, it gets locally pinned in some positions while other line segments continue to glide, leading to an overall meandering dislocation line. Lee et al.[77] investigated dislocation glide in the equimolar Cantor alloy using TEM and report jerky motion of individual dislocations suggesting strong pinning of the dislocation at some sites followed by unpinning and rapid glide until the next obstacle is encountered. They compare the observed dislocation glide to nano-precipitate hardened, irradiated austenitic steels[281] or a 304 steel containing a high density of irradiation induced defects.[282] Zhai and Zaiser[276] incorporated local random forces into their discrete dislocation dynamics model to approximate the random chemical fluctuations in HEAs. Here, they find the dislocation pinning length as a good descriptor for an alloy's yield stress. These simulation results are in line with the solid solution strengthening models by Leyson et al.,[217–219] Varvenne et al.,[72,213] or Zhang et al.,[37] and the qualitative model by Péterffy et al.[283] They, however, treat the dislocation pinning sites as statistical quantity disregarding their exact atomic origin.

2.2.4 Dislocation Pinning on the Atomic Scale

In pure FCC metals, the energy barrier seen by a gliding dislocation is called *Peierls barrier*, while the stress required to overcome this barrier is called *Peierls stress*.[68] As outlined in a recent review by George et al.,[19] a similar approach is taken for the highly disordered HEAs where authors[12,284] attribute the high yield strength to a high average Peierls barrier without considering chemical fluctuations. According to their review,[19] this wording is erroneous as Varvenne et al.[111] have shown that the increased resistance against dislocation glide in concentrated alloys stems from the chemical disorder and should therefore be called *solid solution strengthening*. Their proof revolves around the so-called *average-atom (avg.-atom)*, which is a virtual element that can be used in atomistic simulations. It has the same long-range average properties as a concentrated alloy matrix, alas, only contains a single element. Varvenne et al.[111] report a dislocation glide stress below 10 MPa for the avg.-atom while the full, multi-component HEA has glide stresses between 200 MPa and 500 MPa.[111] Therefore, the resistance against dislocation glide in concentrated alloys stems from the *solutes* and not the matrix.

The review by George et al.[19] further states that the strengthening observed in MEAs and HEAs should not be seen as a phenomenon on the atomic scale as the activation volume for dislocation glide V_A in the Cantor alloy is in the range of $70b^3$ at 77 K.[285] To put this number into perspective, each activation volume contains $N \approx 100$ atoms.[*] Overall reports on the activation volume remain inconclusive as they scatter between $10b^3$ and $360b^3$ depending on measurement temperature (between 77 K and 300 K) and other experimental conditions.[285–289] Hong et al.,[286] who report low temperature activation volumes between $10b^3$ and $100b^3$, note that these activation volumes are about a factor of 10 smaller than the ones in pure FCC metals. Therefore, the question on the scale of dislocation pinning and strengthening remains contentious.

One possible atomic scale origin of dislocation pinning might be the degree of local lattice distortion. Multiple authors have reported a direct correlation between the Peierls stress[284] or the macroscopic yield strength[224,225,284,290,291] and the intrinsic lattice distortions. Even though, this observation is not motivated by theory[19] it would give an atomistic descriptor for dislocation pinning. Recently, however, Nöhring and Curtin[292] have shown that this correlation is spurious and agrees with the HEA solid solution strengthening model by Varvenne et al.[72] as the lattice distortions and the misfit volume, one of the main input quantities of the model, are directly correlated.

2.2.5 The Effect of Short-Range Order

Another option for atomic scale dislocation pinning conceivable is the effect of preferred bonds. During glide, the dislocation shifts the atomic layers in the glide plane against each other, replacing two of three nearest neighbor bonds (in the case of an FCC {1 1 1} glide plane).[68,293] This means that in an ordered material, a dislocation passing through the material destroys the local order which carries an additional energy cost as many preferential bonds are broken. In a random alloy this effect is supposedly small, as the atoms and their bonds are spatially uncorrelated on average. On the local scale, however, the dislocation advancement could be hindered, i.e., the dislocation line is pinned,

---

[*] Assuming that $N = V_A/\Omega$, where $V_A = 70b^3 = 70(a_0/\sqrt{2})^3$ and $\Omega = a_0^3/4$, gives $N = 70\sqrt{2}$.

if it encounters an energetically favorable random arrangement of atoms that would be broken up. In HEA samples with some degree of SRO the fraction of energetically favorable bonds is increased, leading to a higher degree of pinning.[293–295]

Antillon et al.[38] have performed large-scale atomistic simulations on a model FCC HEA. They created samples with different degrees of SRO from MC annealing at different temperatures and found two opposite effects. While the preferential SRO bonds lead to an increase in strength, the SRO samples also show a decreasing atomic size misfit, which leads to a decrease in solid solution strengthening, as described by the Varvenne et al.[72] solid solution strengthening model. These two effects balance for edge dislocations, whereas SRO increases the glide resistance for screw dislocations.

The final verdict on whether there is SRO in the Cantor alloy and its subsystems after high temperature homogenization and quenching is still out. In the following, arguments for both views are going to be presented. There is evidence for SRO in different MEAs and HEAs.[39,208,261,286,296–300] Zhang et al.[297] performed extended X-ray absorption fine structure measurements on the NiCoCr alloy and found preferential bonding of Cr-Co and Cr-Ni pairs. This SRO, where Cr-Cr bonds in the first neighbor shell are energetically unfavorable while all other elements i in the alloy tend to form Cr-i bonds, has been reported for CoCrNi[261] and CoCrFeNi[296] based on DFT calculations. Using similar techniques, Pei et al.[301] report a transition in SRO at $\approx 1000\,\mathrm{K}$, where the Co-Cr and Co-Ni SRO disappears while the Co-Ni preference remains. Note that while these DFT based MC simulations can predict the thermodynamically stable SRO in an alloy, kinetics can still limit its formation, especially at lower temperatures.[261] Additionally, Zang et al.[39] find diffuse superlattice streaks in TEM diffraction patterns after heat treatment of CoCrNi samples which are taken as evidence of SRO. They show a pronounced strength increase stemming from this SRO. Similarly, Hong et al.[286] take an increase in dislocation activation volume and strength after annealing as an evidence for SRO formation. Another indirect evidence for SRO is the planar slip often reported for the Cantor alloy.[263,270,273,274] This has been attributed to a *glide softening mechanism*,[302] where dislocation activity on a given lattice plane becomes easier after the first dislocation has destroyed any pre-existing SRO.[212] Therefore, the prevalence of planar slip could be a sign of SRO. A common counterpoint to this argument is based on the great dissociation width in the Cantor alloy. Dissociated partial dislocations cannot cross-slip and thereby wide dissociation promotes planar slip.[263,270,273]

There is, on the other hand, ample of counter evidence as well. Many atom probe tomography (APT) studies find MEAs and HEA in a random solid solution state.[27,77,149,191,200,208,224,303–306] Laurent-Brocq et al.[306] report a true random solid solution down to the atomic scale in the equimolar Cantor alloy after their APT investigation. This was later confirmed down to a resolution limit of 1 nm by Lee et al.[77] Based on the works by Marceau et al.[307,308] the combination of limited spatial resolution as well as detector efficiency in APT can hide SRO and lead to a more randomized atomic matrix. An effect that needs to be considered in the assessment of chemical randomness of HEAs.[286]

A different method was chosen by Smith et al.[74] who use high resolution energy-dispersive X-ray spectroscopy to confirm the chemical homogeneity of their sample. Using positron annihilation spectroscopy, Ren et al.[208] report no significant segregation in CoCrFeMnNi HEA samples after annealing or after irradiation at temperatures between 300 K and 773 K. Opposite to these experimental results, their DFT based MC simulations show a reduction in Cr-Cr pairs and an increase in Ni-Cr bond count at 500 K, in line with the other DFT studies. These simulations yield an almost perfectly random alloy at a MC temperature of 1200 K. This suggests that the chemical randomness in the experimental samples is kinetically stabilized during cooling and the added energy from irradiation does not facilitate its ordering.

2.2.6 $L1_2$ Precipitation Strengthening in High-Entropy Alloys

The strengthening effect of coherent precipitates, already well established for conventional alloys,[309,310] has been investigated for different MEAs and HEAs of the Cantor alloy family.[32–34,207,209] These studies agree that the main premise of precipitation strengthening remains true in HEAs — it can lead to a substantial increase in strength without critically compromising the ductility of the alloy.

The literature overview presented in the following shows experimental measurements in different $L1_2$ precipitation strengthened HEA, the main takeaway is that in all cases, the strength of the material could be increased more than two-fold.

Qi et al.[209] investigated a $(FeCoNiCr)_{0.89}Ti_{0.06}Al_{0.05}$ alloy with a relatively low volume fraction 18 % of $L1_2$ precipitates finely dispersed within each grain. Here, the mean precipitate radius is reported to be 10.3 nm. Even this low number of small precipitates leads to a substantial yield strength increase of 275 MPa compared to the 165 MPa yield strength of the host matrix. He et al.[32] find $Ni_3(Al,Ti)$ precipitates in a similar FeCoNiCr base alloy with added Al and Ti. They report slightly higher volume fractions of secondary phase, around 25 %, leading to a strength increase of 327 MPa for particles in the 40 nm to 100 nm radius range. Starting from a non-equimolar HEA, Liang et al.[34] developed the $Al_{0.5}Cr_{0.9}FeNi_{2.5}V_{0.2}$ HEA. It contains a higher concentration of Ni and Al to facilitate the formation of $L1_2$ phases with a volume fraction greater than 50 %. Moreover, these initial concentrations ensure an almost equimolar ternary CrFeNi FCC matrix after the formation of the Ni_3Al precipitates. The increase in strength from these 30 nm radius particles is found to be 752 MPa. Looking at ternary base alloys, Zhao et al.[33] and Yang et al.[207] investigate the ternary CoCrNi and CoFeNi with added Al and Ti, respectively. They both find chemically more complex $L1_2$ phases of $(Ni,Co,Cr)_3(Ti,Al)$ and $(Ni,Co,Fe)_3(Ti,Al,Fe)$. Zhao et al.[33] report a total strength increase from these precipitates of 388 MPa, while

Yang et al.[207] report a much greater strength gain of 788 MPa. This stems from the differences in volume fraction of the secondary phase. Here, the former only have 11 %, while the latter find volume fractions of 50 % with mean radii around 40 nm.

The $L1_2$ secondary phase investigated by the aforementioned authors is coherent with the FCC matrix and therefore assumed to be sheared by the dislocation line as it passes this obstacle. While this assumption is made by all the authors, only Yang et al.[207] provide direct evidence in the form of TEM images showing the dislocation line cutting a $L1_2$ particle. The effect of incoherent BCC $L2_1$ precipitates has recently started to become of interest as well,[209] but it remains out of scope for the following sections.

2.3 Grain Boundaries

HEAs have been suggested for high-temperature applications[2,19,23] even though their mechanical properties can currently not compete with established Ni-based superalloys.[2,10,19] While their strength at high temperatures is most important for future applications, a stable microstructure is equally important to allow for long-term use of a part without changes in its material properties.[90] To this end, the grain growth kinetics of HEAs need to be understood to allow for alloy design resilient against high temperature grain growth. Another proposed application for HEAs is the use as structural material in fission or fusion reactors[10,47] due to their increased irradiation resistance.[48–63] In conventional metals and alloys, nanocrystalline (NC) microstructures possess an increased irradiation tolerance compared to their coarse-grained counterparts upon irradiation.[91–93] This makes NC microstructures desirable for applications but the irradiation of said grain structures can lead a rapid coalescence of grains and grain coarsening.[63] This unwanted grain growth needs to be prevented to ensure long-lasting parts.

Reduced grain growth in FCC 3*d* transition metal HEAs has been widely reported, however, there is still debate over its origin.[11,94–107]

There are different hypotheses on the origin of the reduced grain growth in HEAs. Bhattacharjee et al.[94] and others[95] suggest that the grain growth rate in HEAs might be intrinsically reduced due to the strong lattice distortions. Others state that the *sluggish diffusion*[94,96–98] and solute drag are reducing grain growth in complex alloys.[11,97,99–102] Lastly, the reduced grain growth rate has been attributed to secondary phase formation at grain boundaries (GBs).[102–107]

There are two different effects that can stabilize a microstructure against grain growth. Either by means of kinetic or thermodynamic stabilization (or a combination thereof).[311,312]

Kinetic Stabilization

Kinetic stabilization can be facilitated by solute drag,[313,314] which slows GB migration in a single phase solid solution, or due to Zener pinning,[315] which involves pinning of the GB at secondary phase particles. There is experimental indication that grain growth in HEAs is diffusion controlled. Liu et al.[97] determined the activation energy for thermally activated grain growth in the FCC Cantor (CoCrFeMnNi) HEA[5] to be 321.7 kJ mol^{-1}. The activation energies of self-diffusion reported by Tsai et al.[45] in said alloy are of a similar range between 288 kJ mol^{-1} and 318 kJ mol^{-1}.[*] The apparent similarity between these values suggests that a solute cloud forms at the GBs which subsequently needs to diffuse alongside the GB as it migrates through the alloy. Direct observation of this solute cloud remains elusive, with Vaidya et al.[191] reporting no excess concentration at GBs in the Cantor alloy after annealing. On the other hand, Barr et al.[316] report GB segregation of Co and Ni after irradiation in the same alloy. Moreover, the strong pinning force of secondary phases at the GBs has been observed in HEAs. These have been found to stabilize ultrafine-grained[104] and NC[103] microstructures up to 1173 K. Due to their vast compositional space and inherent metastability[9] HEAs have a very broad metallurgical design space to optimize these alloys for optimum secondary phase fraction and distribution.

Thermodynamic Stabilization

Thermodynamic stabilization of a microstructure is facilitated by reduction of the GB energy and thereby a reduction in driving force for grain growth due to solute segregation.[317,318] In conventional alloys, the reduction in GB energy is usually driven by segregation of an alloying element with low mixing but high segregation enthalpy.[319] In HEAs this effect could act on a local scale with chemical fluctuations providing favorable low energy arrangements for GBs in which they are pinned. This model image would translate the dislocation pinning argument by Varvenne et al.[72] to GBs.

Zhou et al.[98] used the combination of kinetic and thermodynamic stabilization to design an FCC HEA with exceptional resistance against grain growth. The alloy is based on the quaternary CoCrFeNi with small additions of Mo, Nb, and Zr, which stabilize nanosized grains up to very high temperatures of 1273 K.

---

[*] These values are possibly based on wrong assumptions[180] and correct treatment of the measured data leads to values from 272 kJ mol^{-1} to 293 kJ mol^{-1}.[176]

2.4 Research Questions

Based on the Introduction and this Literature Review the following research questions are raised and will be investigated throughout this thesis. They will serve as a guide summarizing our motivations.

Chapter 4 Vacancies

I. How does the vacancy formation energy change as function of chemical environment and HEA composition?

II. What is the resulting equilibrium vacancy concentration, and how does it depend on the configurational entropy of the host matrix?

III. How is the vacancy migration energy influenced by the local chemical fluctuations in the HEA matrix and the alloy's composition?

IV. Can we combine these ingredients to describe tracer diffusion in concentrated alloys from atomistic computer simulation?

Chapter 5 Dislocations

I. Is there strong Fleischer type pinning of the dislocation line on a distinct structural motive within the HEA matrix?

II. If not, can we characterize the pinning point strength and density of the whole solute field in the spirit of weak Labusch type pinning?

III. How do the atomic scale dislocation pinning points influence the critical stress for dislocation glide and its mobility?

IV. What is the effect of larger scale inhomogenieties, for example SRO or precipitates, on dislocation pinning and the dislocation line shape?

Chapter 6 Grain Boundaries

I. What is the magnitude of the intrinsic lattice distortions in the HEA and can they influence the GB structure or its migration?

II. Are there differences in the GB structure in the HEA compared to pure metals and its avg.-atom counterpart?

III. How does the GB mobility in the HEA compare to the avg.-atom and other metals?

IV. What is the effect of possible solute segregation in the HEA on its grain growth kinetics?

After a brief overview over the employed methods in Chapter 3 we will investigate and answer these questions based on large-scale atomistic computer simulations. Here, we climb the ladder of defect dimensionality, starting from zero-dimensional vacancies, going via one-dimensional dislocations, to two-dimensional grain boundaries. Special attention will always be given to the complex, multi-elemental matrix of HEAs which differentiates them from conventional alloys. To conclude, we will revisit the questions outlined above in Chapter 7 and give comprehensive answers.

3 Methodology

In the first part of this chapter, a brief overview over the computational methods and models used in all following chapters will be given. It is mostly based on the insightful books *'Modeling materials: continuum, atomistic, and multiscale techniques'* by Tadmore and Miller,[320] *'Understanding molecular simulation'* by Frenkel and Smit,[321] and *'Introduction to the kinetic Monte Carlo method'* by Voter.[322] The chapter starts with an introduction to molecular dynamics (MD) and molecular statics (MS) methods, continues with different Monte Carlo (MC) algorithms, and finishes with a section on interatomic potentials. The simulations within this thesis are mostly performed using the *Large-scale Atomic/Molecular Massively Parallel Simulator* (LAMMPS); it is available open-source under the GNU GPL at `http://lammps.sandia.gov`. Therefore, some details will be given in reference to this software. The second part of this chapter will provide a more detailed look in the simulation procedures used to derive the results presented throughout this thesis.

3.1 Molecular Dynamics

Molecular dynamics (MD) is the method of choice to study the dynamics of many interacting atoms. While this so-called *many-body problem* does not have an analytical solution, MD can be used to simulate its time evolution. Initially, a few assumptions about the simulated atoms need to be made. Firstly, the Born-Oppenheimer approximation,[323] which states that calculations of electrons and nuclei can be separated, due to their large difference in mass, is applied. Thereby, the electronic shell can always react instantly to the slow motion of the heavy nucleus, while the nucleus appears stationary to the electrons. For MD this means that only the motion of the atomic nuclei needs to be calculated explicitly, while the electrons tag along. Secondly, atoms are assumed to be heavy and slow moving so that they can be treated as classical particles following Newton's equation of motion. This means that both inner energy and heat capacities extracted from MD simulations give values predicted by the Dulong-Petit law.[324] Lastly, the size of the atomic nucleus is much smaller than the total size of the atom and realistic interatomic distances. Therefore, each nucleus can be treated as a point mass in space with associated position and velocity vectors.

Going back to the original question on the dynamic trajectories of these atomic nuclei in time and space, the classical equation of motion,

$$m_i \frac{d^2\vec{r}_i}{dt^2} = \vec{F}_i(r_1,\ldots,r_N) + \vec{F}_{\text{Ext},i}, \quad \text{where} \quad \frac{d^2\vec{r}_i}{dt^2} = \vec{a}_i, \tag{3.1}$$

needs to be integrated for all particles N. Here, m_i is the mass of particle i, $\vec{r}_i$ is its position, and t is time. The second time derivative of the position corresponds to the acceleration $\vec{a}$. The force acting on a particle i depends on the positions $(r_1,\ldots,r_N)$ of all other interacting particles in the system and, if applicable, an external applied force $\vec{F}_{\text{Ext}}$. These forces acting on each particle can be calculated from ab initio methods.[325] Even modern ab initio MD methods, however, scale $\approx \mathcal{O}(N^2)$, where N is the number of valence electrons.[326] This makes the simulation of many atoms or long time scales prohibitively expensive.

Alternatively, the atomic forces can be obtained from classical interatomic potentials, which lead to an $\mathcal{O}(N)$ scaling, where N is the number of simulated atoms, as all forces can be calculated from short-range particle interactions.[327] Moreover, classical interatomic potentials can be calculated from the atomic nuclei instead of individual electrons decreasing N compared to ab initio methods. A secondary benefit of the short-range interatomic potential is that parallel evaluation of the force calculation, the computationally most demanding step of the simulation, becomes *embarrassingly parallel*.[*] Meaning that doubling the number of CPUs running the simulation halves the execution time. This stems from the fact that the simulation volume can be split into chunks of atoms that are outside each other's interaction range for which forces become independent.

3.1.1 Velocity Verlet Algorithm

Knowing the forces and masses of the atoms Equation 3.1 can be integrated numerically. While there are many methods, usually the velocity Verlet integrator is used.[329,330] It calculates the forces $\vec{F}$, positions $\vec{r}$, and velocities $\vec{v}$ at discrete times which are separated by a short time interval Δt. Each of these time intervals corresponds to a single simulation step during which the algorithm performs three operations:

I. Calculate new positions: $\vec{r}(t+\Delta t) = \vec{r}(t) + \vec{v}(t)\Delta t + \frac{1}{2}\vec{a}(t)\Delta t^2$

II. Get $\vec{a}(t+\Delta t)$ from the interatomic potential using the new positions $\vec{r}(t+\Delta t)$[†]

III. Update the velocities: $\vec{v}(t+\Delta t) = \vec{v}(t)\frac{1}{2}(\vec{a}(t) + \vec{a}(t+\Delta t))\Delta t$

The total simulated time corresponds to the number of steps taken multiplied with the length of each time step. Therefore, longer time steps reduce the computational cost, while decreasing the integration accuracy. For metals time

---

[*] *'Some computational problems are "embarrassingly parallel": they can easily be divided into components that can be executed concurrently.'*, Herlihy and Shavit, 2012[328]

[†] $\vec{F} = -\vec{\nabla}E$ and $\vec{F} = m\vec{a}$, where E is the potential energy.

steps between 1 fs and 4 fs are commonly used. This algorithm requires initial velocities, which are usually initialized to a given temperature using the Maxwell-Boltzmann distribution.

The velocity Verlet algorithm has several benefits over other integration schemes. Without significant computational overhead, the error is reduced to $\mathcal{O}(\Delta t^2)$ compared to $\mathcal{O}(\Delta t)$ of the Euler method. This is necessary given the large number of integration steps required for a typical MD simulation, where errors readily propagate. Secondly, this algorithm is a so-called *symplectic integrator*.[331] This means that if one uses non-dissipative forces as an input, the energy will always oscillate around the exact solution of the differential equation making the integration energy conserving. Similarly, other physical quantities like linear and angular momentum are conserved as well.

3.1.2 Thermostat and Barostat

The MD methodology outlined above will conserve the number of particles number N, the volume V, and the total energy E, thereby simulating the microcanonical or NVE ensemble (if $\vec{F}_{\text{ext}} = 0$). Most of the time this is not the desired ensemble, instead constant temperature T or pressure p might be desired. These simulations become possible with the help of a thermostat or barostat, respectively.

Two different thermostats are commonly used. The Nosé–Hoover thermostat[332,333] couples the simulation to a virtual heat bath. This is done by means of a friction term which is added to the equations of motion. This friction term slows the particles if the temperature in the simulation is too high, while it accelerates the particles if the temperature is too low. The time needed for the thermostat to establish a selected temperature is defined by a damping parameter which is usually set to $100\Delta t$. Too small damping times can lead to unphysical behavior of the system while too high ones increase the time required for the system to reach equilibrium. The Nosé–Hoover thermostat generates temperature fluctuations consistent with the canonical (NVT) ensemble.

The second method of thermostating employed in this thesis is the Langevin thermostat.[334,335] It adds a frictional force proportional to the instantaneous velocity to each particle, accelerating or decelerating them depending on the current and target temperature. Physically, this corresponds to a solvent of constant target temperature randomly colliding with the simulated atoms, thereby exchanging energy with them. Due to the random nature of the interactions with the virtual solvent atoms, the Langevin thermostat efficiently removes shock waves and oscillations from the material.

Similar to the Nosé–Hoover thermostat, a Nosé–Hoover barostat,[332] also called Parrinello-Rahman barostat,[336] can be employed to dynamically change the size of the simulation cell. Thereby, this method can stabilize any desired stress state in the sample. This works again by a modification of the equations of motion. It preserves the fluctuations of the isobaric-isothermal (NPT) ensemble.

In general the equations of motion by Shinoda et al.[337] are implemented in LAMMPS, they allow for independent toggling of the thermostat and barostat during a simulation.

3.2 Molecular Statics

The MD methods outlined above simulate the dynamics of an atomic system at finite temperatures. Sometimes the 0 K ground state, i.e., local energy minimum, of a given configuration is of interest. This state can be found using local energy minimization techniques in a process called molecular statics (MS) simulations. The local energy minimization for a system containing N atoms corresponds to a minimization problem having $3N-6$ degrees of freedom.[338] There are different algorithms implemented in LAMMPS to solve this minimization problem, two of them will be described in more detail.

The first one is called *fast inertial relaxation engine* (FIRE)[338,339] and corresponds to a damped dynamics simulations. Here, the equations of motion for the particles are modified in a way such that they can only move towards lower potential energies. These modified equations of motion are then integrated using the velocity Verlet integrator leading to an atomic trajectory which minimizes the forces acting on the particles.

Secondly, the conjugate gradient (CG) algorithm,[340] in the formulation of Polak and Ribière[341] is implemented in LAMMPS. It directly minimizes the gradient of the potential energy, i.e., the forces, using an iterative line search approach following the directions of highest curvature on the energy landscape. CG minimization works best if the function to be minimized is quadratic towards the minimum. This is often the case for atoms in crystals, where each atom sits in a parabolic energy well (cf. harmonic approximation).[320] An important feature of the CG implementation in LAMMPS is that it cannot only optimize the atomic coordinates inside a simulation cell but also rescale and reshape the simulation cell to find the equilibrium simulation cell volume and shape.

Both methods find the closest local energy minimum of a given starting configuration. Examples comparing the minimization algorithms as implemented in LAMMPS can be seen in Figure 3.1. The trajectory of a single atom with its energy equal to Himmelblau's function[342] (a&b) or the Rosenbrock function[343] (c&d) is shown. The potential energy E and distances x and y are given in arbitrary units. Himmelblau's function is approximately quadratic close to its minima and both FIRE and CG converge well. The Rosenbrock function has a steep parabolic valley with a shallow minimum. Here, CG stops the minimization prematurely once the valley is reached, as the iterative line search cannot find a direction for further energy minimization. The FIRE method, on the other hand, converges to the minimum.

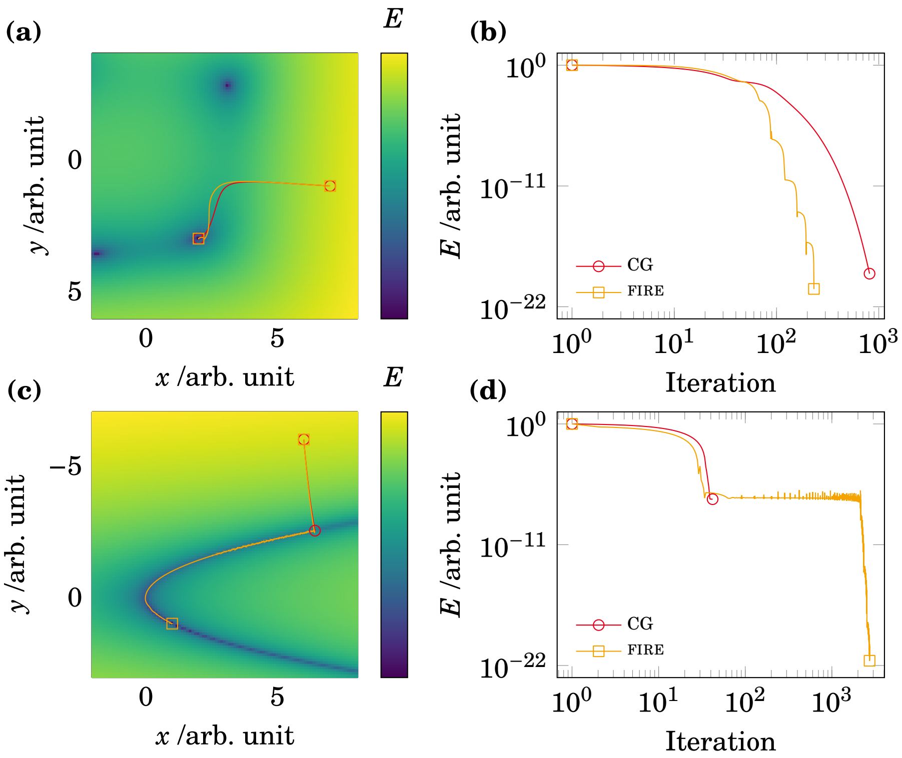

Figure 3.1: Potential energy landscapes following Himmelblau's function (a) or the Rosenbrock function (c). The minimization pathways for the CG and the FIRE methods are shown, initial and final positions are indicated. Local minima ($E = 0$) for both functions are located at $(3,2)$ and $(1,1)$, respectively. Note, the color scale is logarithmic. (b&d) show the progress of the energy minimization for both methods.

3.3 Nudged Elastic Band Method

The nudged elastic band (NEB) method is used to find the minimum energy path (MEP) between two metastable or stable states of a system.[344,345] It samples a discrete number of configurations along this minimum energy path and returns the atomic configurations and potential energies for each configuration.

The NEB algorithm works by creating a number of *replicas* along the estimated MEP. Each replica is a copy of the initial system, in some interpolated configuration between initial and final state. Each replica, except for the initial and final replicas are then subjected to MS energy minimization, taking not only the interatomic potential into account but also applying a cross-replica force. This force is an attractive spring force keeping the chain of replicas connected, so that not all replicas relax towards the two connected energy minima. Instead, this method allows this chain to relax towards the MEP. An example of such a NEB calculation can be seen in Figure 3.2, where (a) shows Himmelblau's function. Two of its minima are initially connected by a straight line (purple).

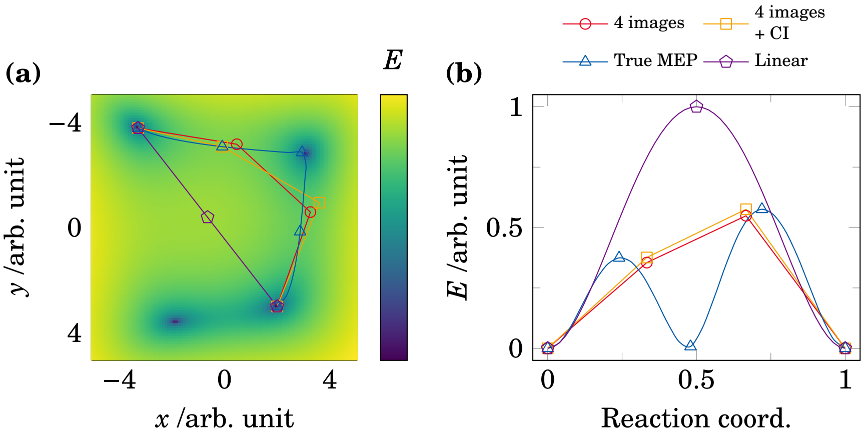

Figure 3.2: Energies along different paths connecting two local minima of Himmelblau's function. The energy along a linear path, and two different NEB calculations is compared to the true MEP. The color scale in (a) is logarithmic. For the linear and true MEP only a few data points are shown.

During NEB simulations the MEP is found via an intermediate energy minimum (blue). In (b), the large difference in saddle point energy between both paths can be seen.

Once the MEP is converged, the energy of all replicas is known. Normally, one is interested in the exact potential energy of the saddle point. If one uses many replicas, the saddle point energy corresponds to the energy of the highest replica. As each replica is expensive to calculate, only a small number of them can be used. To ensure that the maximum is found, a trick can be used. Once the MEP is converged, the NEB spring forces acting on the highest replica are reversed, thereby pushing it up to the saddle point. This two-step method is called climbing image (CI) NEB.[346,347] This can be seen in Figure 3.2 where we calculated the MEP with a tiny number of four replicas with and without CI. While the CI calculation finds the correct saddle point energy, the conventional NEB underestimates its energy by 5 %.

The LAMMPS implementation of the CI NEB follows the methodology given in Refs. 346–349.

3.4 Monte-Carlo Simulation

3.4.1 Canonical Ensemble

The canonical ensemble describes a chemically isolated system with constant particles counts N_i per species i, constant temperature T, and constant volume V. In a box containing N particles, the system can be described by two vectors: a $3N$-dimensional vector containing the position of each particle $\vec{r}^{3N}$ and a

N-dimensional vector $\vec{\sigma}^N$ storing the type of each particle. The potential energy of any configuration is a function of these two vectors $E\left(\vec{r}^{3N},\vec{\sigma}^N\right)$.

The resulting configurational integral $\mathscr{Z}_\mathrm{C}$ for a binary system within the canonical ensemble is,[350]

$$\begin{aligned}\mathscr{Z}_\mathrm{C}(N_1,\mathscr{N}) &= \frac{\Lambda_1^{-3N_1}\Lambda_2^{-3(N-N_1)}}{N_1!(N-N_1)!}\int \exp\left[\frac{-E\left(\vec{r}^{3N},\vec{\sigma}^N\right)}{k_\mathrm{B}T}\right] d^{3N}\vec{r}, \\ \text{where} \quad \Lambda_i &= \sqrt{\frac{h^2}{2\pi m_i k_\mathrm{B}T}}.\end{aligned} \tag{3.2}$$

k_B is the Boltzmann constant and m_i is the mass of particle i. $\mathscr{N}$ contains the three independent thermodynamic variables N, V, and T. Canonical Monte Carlo (MC) simulations therefore sample the probability distribution,[350]

$$\pi_\mathrm{C}\left(\vec{r}^{3N},\vec{\sigma}^N;N_1,\mathscr{N}\right) \propto \exp\left[\frac{-E\left(\vec{r}^{3N},\vec{\sigma}^N\right)}{k_\mathrm{B}T}\right]. \tag{3.3}$$

MC sampling of this probability distribution involves two different trial steps. Either random displacement of a single particle, or swapping the chemical identity of two particles of different types within the simulation cell. The canonical acceptance probability $\mathscr{A}_\mathrm{C}$, fulfilling detailed balance, for any trial moves is equal to,

$$\mathscr{A}_\mathrm{C} = \min\left\{1,\exp\left[\frac{-\Delta E}{k_\mathrm{B}T}\right]\right\}, \quad \text{with} \quad \Delta E = E\left(\vec{r}_t^{3N},\vec{\sigma}_t^N\right) - E\left(\vec{r}^{3N},\vec{\sigma}^N\right). \tag{3.4}$$

Here, E and $\vec{\sigma}$ denote the currently accepted system state, while the subscript t indicates the arrangement and energy after the trial move.

A canonical system modeled by this formalism converges relatively slowly. This can be improved if trial moves are biased towards the highest gradient in energy. One method providing such a bias is hybrid MC/MD sampling, where particle displacements are simulated by means of classical MD and only particle type exchanges are sampled using MC trial steps.[350]

3.4.2 Semi-Grand Canonical Ensemble

In the canonical ensemble, simulations can only be performed at constant particle numbers per species, i.e., constant concentration c. MC simulations in the semi-grand canonical ensemble overcome this limitation by allowing particle exchanges between the system of interest and an infinite reservoir of each species. Each reservoir is kept at a constant temperature and chemical potential $\Delta\mu$. MC simulations in this ensemble explore varying concentrations and particle arrangements, the overall sample concentration, however, is still imposed by the chemical potential.

The associated semi-grand canonical configurational integral $\mathcal{Z}_\mathrm{S}$ can be written as,[350]

$$\mathcal{Z}_\mathrm{S}(\Delta\mu, \mathcal{N}) = \int_0^1 \mathcal{Z}_\mathrm{C}(c, \mathcal{N}) \exp\left[\frac{-\Delta\mu N c}{k_\mathrm{B}T}\right] dc. \tag{3.5}$$

The resulting probability distribution is therefore given by,[350]

$$\pi_\mathrm{S}\left(\vec{r}^{3N}, \vec{\sigma}^N; \Delta\mu, \mathcal{N}\right) \propto \exp\left[-\frac{E\left(\vec{r}^{3N}, \vec{\sigma}^N\right) + \Delta\mu N c\left(\vec{\sigma}^N\right)}{k_\mathrm{B}T}\right]. \tag{3.6}$$

If we again assume that translational degrees of freedoms are sampled by means of MD, the only remaining trial move involves changes in concentration. Compared to the canonical ensemble, atoms are not swapped within the cell, instead a single particle is randomly selected and its type is exchanges with a different species taken from its respective reservoir. Obeying detailed balance, the acceptance probability for such a trial move is equal to,

$$\mathcal{A}_\mathrm{S} = \min\left\{1, \exp\left[-\frac{\Delta E + \Delta\mu N \Delta c}{k_\mathrm{B}T}\right]\right\}. \tag{3.7}$$

Compared to the canonical ensemble, the probability to accept a trial move does not only depend on the associated energy change. There is an additional driving energy $\Delta\mu N \Delta c$, steering the system in the direction of the desired composition.

The semi-grand canonical ensemble can stabilize single-phase equilibria, In systems featuring a miscibility gap, c becomes discontinuous function of $\Delta\mu$

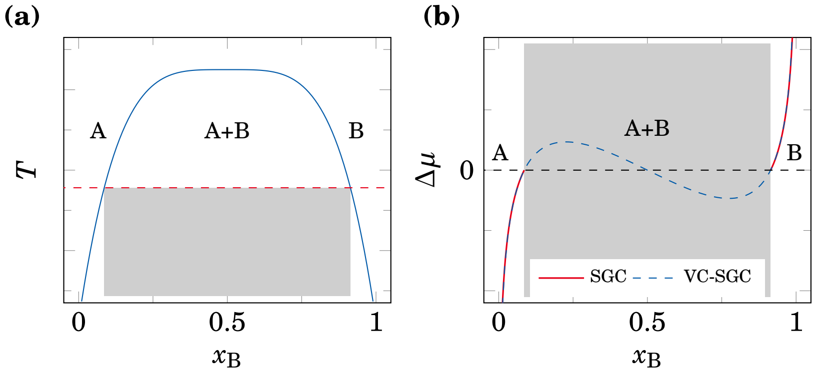

Figure 3.3: (a) Schematic phase diagram for a binary A-B system with miscibility gap. At the temperature of interest, marked by a horizontal line, the miscibility gap extends over the shaded concentration range. (b) Chemical potential over concentration at the same temperature. The semi-grand canonical (SGC) ensemble can only stabilize the two red branches outside the miscibility gap, while simulations in the variance-constrained semi-grand canonical ensemble can sample the whole concentration range. Adapted from Sadigh et al.[350]

meaning that concentrations in the gap cannot be reached. This is schematically shown in Figure 3.3. (a) gives a binary A-B phase diagram, while in (b) the corresponding chemical potential over concentration is shown. The semi-grand canonical ensemble cannot describe the miscibility gap, while the variance-constrained semi-grand canonical ensemble, which will be introduced in the following section can stabilize intermediate compositions.

3.4.3 Variance-Constrained Semi-Grand Canonical Ensemble

This restriction can be overcome if the variance-constrained semi-grand canonical ensemble is used.[350] It employs an additional constraint on the maximum concentration deviation, thereby stabilizing concentrations in the miscibility gap. Compared to the semi-grand canonical ensemble, the elemental reservoirs, with which particles from the simulation are exchanged are not infinite anymore, but become finite. They are, however, still kept at a constant temperature and their finiteness is regulated by two parameters ϕ and κ.

The configurational integral of this ensemble is similar to the semi-grand canonical ensemble,[350]

$$\mathcal{Z}_{\mathrm{V}}(\phi,\kappa,\mathcal{N}) = \int_0^1 \mathcal{Z}_{\mathrm{C}}(c,\mathcal{N})\exp\left[\frac{-Nc(\phi+\kappa Nc)}{k_{\mathrm{B}}T}\right]dc. \tag{3.8}$$

This configurational integral can be seen as a generalization of the canonical and the semi-grand canonical configurational integral. For the limiting case of $\kappa \to \infty$ and $\phi \to -2\kappa Nc$, Equation 3.8 reduces to $\mathcal{Z}_{\mathrm{C}}$. In the limit of $\kappa \to 0$, $\mathcal{Z}_{\mathrm{S}}$ is obtained.

The resulting probability density function is given by,[350]

$$\pi_{\mathrm{V}}\left(\vec{r}^{3N},\vec{\sigma}^{N};\phi,\kappa,\mathcal{N}\right) \propto \exp\left[-\frac{E\left(\vec{r}^{3N},\vec{\sigma}^{N}\right)+Nc(\phi+\kappa Nc)}{k_{\mathrm{B}}T}\right], \tag{3.9}$$

c obviously remains a function of $\vec{\sigma}^N$, the notation was abbreviated for clarity. The individual trial step in a hybrid MC/MD simulation is identical to the semi-grand canonical ensemble with acceptance probability,

$$\begin{aligned} \mathcal{A}_{\mathrm{V}} &= \min\left\{1,\exp\left[-\frac{\Delta E + N\Delta c\left(\phi+2\kappa N\tilde{c}\right)}{k_{\mathrm{B}}T}\right]\right\} \\ \text{with} \quad \tilde{c} &= \frac{1}{2}\left(c\left(\vec{\sigma}_t^N\right)+c\left(\vec{\sigma}^N\right)\right). \end{aligned} \tag{3.10}$$

Here, $\vec{\sigma}_t^N$ denotes the composition post swap attempt. Again, an additional driving force steering the system towards a desired concentration is imposed onto the energy change ΔE. Compared to the semi-grand canonical ensemble, this driving force is not constant anymore, but varies linearly with concentration.

3.5 Kinetic Monte Carlo Simulation

MD resolves the trajectories of each atom down to atomic vibrations. This requires short integration time steps and make the simulations on timescales greater than 1×10^{-6} s prohibitively expensive. The long-time dynamics of a system, however, are often not governed by the fast atomic vibrations but by the relatively rare transitions from one energy minimum to another one. One common example of such a rare event is a single diffusive jump, where an atom needs to cross an energy barrier multiple times higher than $k_{\mathrm{B}}T$ to move from one lattice site to the next one. Kinetic Monte Carlo (KMC) simulations can be used as a scale bridging method sampling these rare events directly allowing for simulated times on the order of seconds.

Rare or infrequent event in this context means that the atoms stay in a metastable stable state for many atomic vibrations. Hence, the system *forgets* how it reached this state and makes each subsequent event independent of the previous one. Therefore, all possible states for the system to explore form a Markarov chain and its state-to-state dynamics correspond to a Markarov walk. Within this walk, the probability or rate to transition out of state can be used to stochastically evolve the system and study its dynamics.

The probability distribution function p for the time t required for a system to escape state i depends on the total escape rate Γ_{tot},

$$p(t) = \Gamma_{\text{tot}} \exp(-\Gamma_{\text{tot}} t). \tag{3.11}$$

The resulting average escape time τ can be determined from this distribution,

$$\tau = \int t p(t) dt = \Gamma_{\text{tot}}^{-1}. \tag{3.12}$$

We are interested in the trajectory of the system; therefore, it is not the total escape rate from a given state that is required, but instead, the individual escape rates towards each available state j, Γ_{ij}, need to be accounted for,

$$p_{ij}(t) = \Gamma_{ij} \exp\left(-\Gamma_{ij} t\right), \quad \text{where} \quad \Gamma_{\text{tot}} = \sum_j \Gamma_{ij}. \tag{3.13}$$

Sampling these probabilities by means of computer (KMC) simulations now becomes straightforward if all escape rates from a state are known. In crystals, the rates are commonly determined from the harmonic transition state theory.[351,352] Here it is assumed that the energy landscape around (meta)stable minima is quadratic and in between adjacent minima there is a single saddle point in the energy landscape. The resulting rates,

$$\Gamma_{ij} = \frac{\prod_k^{3N} \nu_k^{\text{Min}_i}}{\prod_k^{3N-1} \nu_k^{\text{Sad}}} \exp\left(\frac{-\Delta E_{ij}}{k_{\mathrm{B}}T}\right) = \nu_0 \exp\left(\frac{-\Delta E_{ij}}{k_{\mathrm{B}}T}\right), \tag{3.14}$$

depend on the (non-imaginary) normal mode frequencies ν at the energy minimum (Min) and the saddle point (Sad) of the given $i \rightarrow j$ escape path. Here, ΔE_{ij} is the saddle point potential energy of the transition state which can be determined using NEB. As the determination of the pre-factor ν_0 is computationally costly, it is often taken as some constant value.

Given all rates in a system are known, the *direct*[353] or n-fold way[354] KMC algorithm can be implemented using the following steps,[354,355]

I. Determine the M rates (one for each escape path) leaving the current state.

II. Collect the rates of all events Γ_j and store the cumulative sum in Γ_{tot}.

III. Draw a random number $u \in (0,1)$ and select the event from the vector that fulfills,

$$\Gamma_{j-1} < u\Gamma_{\mathrm{tot}} \leq \Gamma_j. \tag{3.15}$$

IV. Evolve the system based on the selected rare event.

V. Advance the clock by the time interval Δt using a new random number $u' \in (0,1)$,

$$\Delta t = -\Gamma_{\mathrm{tot}}^{-1} \ln\left(u'\right). \tag{3.16}$$

Based on Equation 3.12 the time taken to leave a state i does not depend on the selected escape path but on all available escape paths.

3.6 Boundary Conditions

The atoms simulated in MD, MS, or MC simulations are contained within some finite volume called *simulation box* or *simulation cell*. For the simulation of solids, this volume usually has the shape of a parallelepiped to ensure a space-filling tessellation. The size of the simulation cell and thereby the number of atoms is limited by the available computational resources. While there are some really large simulations with more than a billion atoms,[356] most simulations use fewer than a million atoms. This means that simulations are tiny compared to experimental samples. One million Cu atoms in the face-centered cubic (FCC) phase only span a cube of edge length 22.5 nm which is equivalent to 1×10^{-16} g. This means that even the largest simulations have a high surface-to-volume ratio making the study of bulk properties impossible.

There is a simple workaround commonly used in atomistic simulations, so-called *periodic boundary conditions*. Here, the simulation cell is replicated along periodic directions and atoms in the original cell can interact with these periodic replications. This effectively creates a sample of infinite size as shown in Figure 3.4, where the particle in the original simulation cell (solid) can interact and bond with the atoms in the replicated cells (dashed). Even using periodic boundary conditions, a minimum sample size is required, to prevent finite size effects, e.g., the self-interaction of point defects across the cell boundaries.[357]

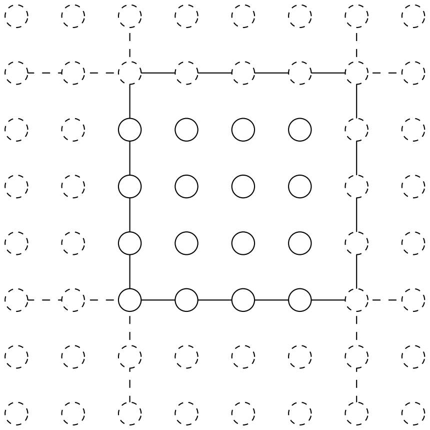

Figure 3.4: Schematic illustration showing the effect of periodic boundary conditions on a crystalline lattice. The original cell and its atoms are shown as solid lines, the periodic images are indicated by dashed lines. Atoms from the original cell can bond and interact with adjacent periodic images.

In LAMMPS the periodic boundary conditions can be toggled for each spatial dimension independently, allowing the simulation of infinitely long nanowires (1D periodic), infinite surface slabs (2D periodic), or infinite bulk (3D periodic).

3.7 Interatomic Potentials

All methods outlined above rely either on the energies or the forces acting on the atoms arranged in a particular configuration. These energy and force formulations are what brings real word physics into the algorithms. While there are ways to determine the forces from ab initio techniques,[325,358] ab initio MD is too computationally costly for simulations involving many atoms or long time scales. Instead, classical interatomic potentials need to be used for these large-scale simulations. They provide the potential energy per atom E_i and resulting forces $\vec{F}_i$ for each atom in the simulation at a fraction of the computation time. Classically, these interatomic potentials are based on a set of equations, relating the relative positions of atoms to their energy. There are many possible formulations,[359,360] for metals so-called embedded atom method (EAM) and modified embedded atom method (MEAM) potentials are commonly used. More recently, machine learning potentials have come into fashion. They do not follow the strict formulation of the conventional interatomic potentials but instead use structural descriptors and neural networks to determine the energy of atomic arrangements.[361,362]

3.7.1 Embedded Atom Method

The embedded atom method (EAM) is based on the Hohenberg and Kohn theorem[363] which states that the electron density determines the energy up to an additive constant. From this, Stott and Zaremba[364] concluded that the embedding energy of an impurity in a host can be determined from the electron density of the host system before said impurity is inserted. In mathematical form, this means that the energy potential E is a functional $\mathscr{F}$ of the electron density ρ_H of the host matrix and a function of the impurity type Z and its position $\vec{r}_\mathrm{I}$. The electron density of the host depends on the positions $\vec{r}_\mathrm{H}$ of all atoms in the host matrix. The general energy term can be written as,

$$E = \mathscr{F}_{\mathrm{Z},\vec{r}_\mathrm{I}}\left[\rho_\mathrm{H}(\vec{r}_\mathrm{H})\right]. \tag{3.17}$$

The quasi-atom approximation[365] states that this impurity experiences a locally uniform electron density.

Daw and Baskes[366,367] employed this formalism to determine the total energy of a system by treating each atom as an impurity embedded in the host lattice spanned by all other atoms. Equation 3.17 neglects core-core interactions which can easily be added in the form of an established pair potential ϕ_{ij} describing the energy of particles i and j as function of their distance r_{ij}. The total potential energy of this approach for any system is given as sum of all contributions,[366,367]

$$E = \frac{1}{2}\sum_{i,j}\phi_{ij}\left(r_{ij}\right) + \sum_{i} F\left[\overline{\rho}_i\right], \tag{3.18}$$

where the F is the embedding functional and $\overline{\rho}_i$ is the local electron density at position $\vec{r}_i$ without atom i. This electron density is taken as a superposition of the electron densities provided by the other atoms in the system,

$$\overline{\rho}_i = \sum_{j\neq i}\rho_j\left(r_{ij}\right). \tag{3.19}$$

Obviously, different formulations of ϕ_{ij}, F, and ρ_j can be used. Here, the local electron density ρ created by each particle has spherical symmetry, as it only depends on the distance r_{ij}.

The potentials used in this thesis are based on the formulation by Johnson[368] who postulated a set of functions and normalization conditions. These allow the analytical determination of cross-terms from elemental EAM potentials to describe random solid solution alloys. The parametrization of Zhou et al.[369] which can describe 16 different elements and their random alloys based on this mixing approach are included in LAMMPS. As the cross-terms in this potential pool are only calculated and not fit explicitly, they cannot account for intermetallic phases.

3.7.2 Average-Atom Method

The average-atom (avg.-atom) is a virtual element, which has the same average mechanical and material properties as a random alloy, but only consists of a single species. Schematically, this is shown in Figure 3.5 where the four elements of a random alloy get mixed into a single avg.-atom species. As it is a single virtual element, there is no chemical disorder in an avg.-atom sample. Therefore, comparison of avg.-atom and explicit random solid solution alloy

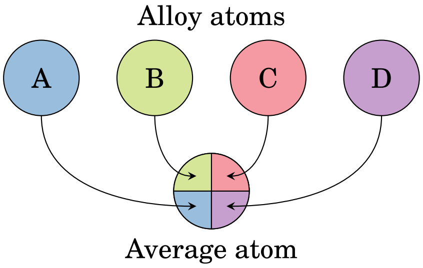

Figure 3.5: Schematic representation of the avg.-atom concept merging the four individual species in an alloy to a single virtual atom with average properties.

allows disentanglement of effects stemming from the chemical fluctuations in the alloy compared to its long-range mean field properties.

The concept was first introduced by Smith et al.[370] and from a theoretical standpoint it is comparable to the virtual crystal approximation or the coherent potential approximation.[371,372] This approach was used for example by Grujici and Zhou[373] who fit a single effective element to describe the properties of a CoCrNi alloy. Fitting a new avg.-atom interatomic potential to every multi-component alloy of interest is a tedious and difficult task.

Varvenne et al.[111] derived a way to analytical average appropriately normalized[368] EAM interatomic potentials using the following procedure. Taking an N component alloy with concentration c_X for each constituent X. Each possible atomic arrangement can be described by a vector of occupation variables σ_i^X. This vector is 1 if site i is occupied by X and 0 otherwise. The energy E in the EAM formalism of a configuration is then given by,

$$E\left(\left\{\sigma_i^X\right\}\right) = \sum_{i,X} \sigma_i^X F^X\left(\rho_i\right) + \frac{1}{2} \sum_{\substack{i,j\neq i\\ X,Y}} \phi_{ij}^{XY} \sigma_i^X \sigma_j^Y, \quad \text{with} \quad \rho_i = \sum_{j\neq i,X} \sigma_j^X \rho_{ij}^X. \tag{3.20}$$

Here i and j are the lattice sites, X, and Y indicate the different species in the alloy. Otherwise, the notation follows the standard EAM notation.

The average energy $\langle E\rangle$ of a given alloy composition can be determined by averaging over all possible configurations. In the ideally random alloy, the occupation of sites i and j is uncorrelated. Therefore,

$$\langle E\rangle = \sum_{i,X} c_X \left\langle F^X\left(\rho_i\right)\right\rangle + \frac{1}{2} \sum_{\substack{i,j\neq i\\ X,Y}} \phi_{ij}^{XY} c_X c_Y, \tag{3.21}$$

as $\left\langle \sigma_i^X \right\rangle = c_X$. Performing a Taylor expansion of $\left\langle F^X\left(\rho_i\right)\right\rangle$ and neglecting higher order terms, gives the following energy expression, where A denotes the derived functions for the avg.-atom,

$$\langle E\rangle = \sum_i F^A\left(\bar{\rho}_i\right) + \frac{1}{2} \sum_{i,j\neq i} \phi_{ij}^{AA}, \quad \text{with} \tag{3.22}$$

$$F^A\left(\bar{\rho}_i\right) = \sum_X c_X F^X\left(\bar{\rho}_i\right), \quad \bar{\rho}_i = \sum_{i,j}\sum_X c_X \rho_{ij}^X, \quad \text{and} \quad \phi_{ij}^{AA} = \sum_{X,Y} c_X c_Y \phi_{ij}^{XY}. \tag{3.23}$$

These equations again reproduce the EAM equations, which means, that the avg.-atom can be used as an EAM interatomic potential in LAMMPS.

We derived an avg.-atom potential for the CoCuFeNi model high-entropy alloy (HEA) described by the Zhou et al.[369] EAM interatomic potentials using the formalism outlined above. Table 3.1 shows different characteristic material properties of this avg.-atom in comparison to the full HEA.

		CoCuFeNi	Avg.-atom
a_0	Å	3.57	3.57
E_{coh}	eV	−4.14	−4.14
C_{11}	GPa	172	170
C_{12}	GPa	124	120
C_{44}	GPa	101	100
α	$\times 10^{-6}\,\mathrm{K}^{-1}$	21	21
T_{Melt}	K	1550	1425
γ_{isf}	$\mathrm{mJ\,m^{-2}}$	28.5	27.0
γ_{usf}	$\mathrm{J\,m^{-2}}$	127	130

Table 3.1: Comparison of the derived avg.-atom and the full CoCuFeNi alloy. The lattice constant a_0 and the cohesive energy E_{Coh} are calculated at 0 K. The elastic constants C_{ij} are calculated using Hooke's law.[374] The thermal expansion coefficient α is obtained from zero pressure NPT simulations. The melting temperature T_{Melt} is determined using the solid-liquid interface method,[375] stable and unstable stacking fault energies γ are obtained using standard methodology.[252] Adapted from Ref. 376.

3.7.3 Modified Embedded Atom Method

A direct extension to the EAM formalism is the modified embedded atom method (MEAM). Later, the second-nearest neighbor version of the MEAM interatomic potential will be applied.[377,378] It takes the same functional form as EAM interatomic potentials but augments the electron density by a three-body term and thereby incorporates an angular dependent electron density. The second-nearest neighbor MEAM is also a direct extension of the nearest neighbor MEAM[379,380] which works well for many material systems but fails for body-centered cubic (BCC) metals, where the difference in distance of first and second neighbor shell is small.

Mathematically, this difference is implemented in the following way. The total energy follows the equation already established for EAM:

$$E = \frac{1}{2}\sum_{i,j}\phi_{ij}(\vec{r}_{ij}) + \sum_{i} F[\overline{\rho}_i]. \tag{3.24}$$

There is, however, a change in the electron density $\overline{\rho}_i$. In the EAM formalism this was a single, spherical symmetric term only depending on the distance between two particles. In the MEAM formulation this is modified to,

$$\overline{\rho}_i = \overline{\rho}_i^{(0)} + \overline{\rho}_i^{(1)} + \overline{\rho}_i^{(2)} + \overline{\rho}_i^{(3)} + \overline{\rho}_i^{(4)}, \tag{3.25}$$

where $\overline{\rho}_i^{(0)}$ is the EAM electron density while the other three terms include the angular contributions.[360] There are again different mathematical forms for these angular terms, for more details, the reader is referred to the original works by Lee et al.[377,378]

3.8 Intrinsic Lattice Distortions

Figure 3.6 (a) schematically shows the lattice structure of a monoatomic material. All atoms sit on the high symmetry lattice sites maintaining an equal distance. In a random solid solution of multiple elements, this situation changes (b) as both the atomic size and their interactions change for the different species. This gives rise to a net displacement for each atom away from the high symmetry lattice sites leading to a distorted equilibrium atom arrangement. Based on the four HEA core effects proposed by Yeh[15] this phenomenon is called *lattice distortion effect*. One way of measuring these intrinsic lattice distortions is the radial distribution function (RDF) g. It measures the probability of finding two atoms at an interatomic distance r. For a perfect FCC lattice the RDF corresponds to Dirac delta functions at the distances of the atomic shells. For the first three FCC neighbor shells these are $a_0/\sqrt{2}$, a_0, and $a_0\sqrt{3/2}$, where a_0 is the lattice constant of the conventional unit cell, respectively. In a system with lattice distortions, these delta functions become broader, as the atoms are slightly displaced from their ideal lattice sites leading to a finite width distribution of interatomic distances. This effect is shown in Figure 3.6 (c).

Simulation Details

Atomistic simulations were performed using LAMMPS.[327] Samples were prepared using ATOMSK[381] and post-processing was performed using OVITO.[382] To quantify the intrinsic lattice distortions in the CoCuFeNi HEA cubes of 20^3 FCC unit cells, corresponding to 32 000 atoms, were simulated. The 0 K static

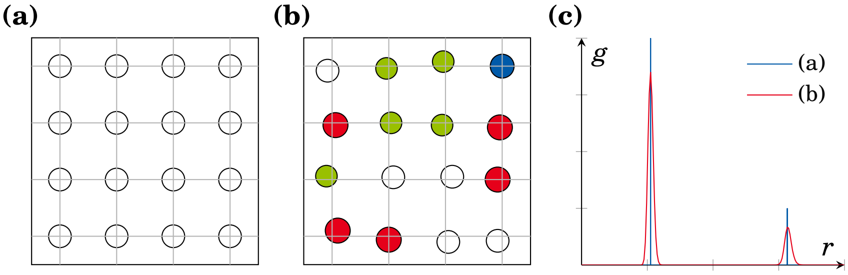

Figure 3.6: Schematic of the intrinsic lattice distortions found in concentrated alloys. Under static conditions, all atoms of a monoatomic metal can be found on their high symmetry sites (a). (b) In a concentrated alloy, the atoms are displaced from their ideal sites due to the interaction and size difference of the various species. (c) The RDF g can be used to measure the effect of the intrinsic lattice distortions on the interatomic distance r.

structures were obtained from CG energy minimization allowing for anisotropic volume changes to establish pressure-free conditions. The force tolerance was set to 1×10^{-10} eV atom^{-1}. Finite temperature MD simulations were run in the isobaric-isothermal (NPT) ensemble for 50 ps using a 1 fs time step. The sample was kept under pressure-free conditions at temperatures between 250 K and 1400 K. For comparison, the same methodology was repeated on Cu, Ni, and avg.-atom samples. These samples were all based on the interatomic EAM potential by Zhou et al.[369] and details on the avg.-atom interatomic potential are given in Subsection 3.7.2. The results are shown as part of Chapter 6.

3.9 Vacancies

As part of Chapter 4 the vacancy formation and vacancy migration energies of concentrated alloys were calculated using the following methodology and simulation setups. Both, the equimolar CoCrFeMnNi HEA and its Ni-rich subsystems were described by the second-nearest neighbor MEAM[377] interatomic potential parameterized by Choi et al.[129] MS and NEB calculations were performed using LAMMPS.[327] Samples were prepared using ATOMSK[381] and OVITO.[382] The latter one was also used for post-processing.

3.9.1 Vacancy Formation Energies

The employed methodology of calculating the vacancy formation energy is shown in Figure 3.7 (a). During this process, an atom is removed from the simulation cell, represented by solid lines, to create a vacant site (square). This atom is then placed in an infinite reservoir with chemical potential μ. In the case of a multicomponent alloy, this chemical potential also depends on the species i of the removed atom. The free vacancy formation energy G_f can be calculated from the energy difference of the initial and final state,[44]

$$G_\mathrm{f} = G_\mathrm{Def} + \mu_i - G_\mathrm{Ref}, \tag{3.26}$$

where index ‘Def’ denotes the sample containing the vacancy, index ‘Ref’ is the single crystalline reference. These simulations are usually performed using periodic boundary conditions. Therefore, removal of an atom from the main cell results in the removal of atoms in its periodic images (indicated by dashed lines) leading to the simulation of an infinite array of vacancies.

Simulation Details

Calculation of the vacancy formation energies required knowledge of the chemical potential μ for each species and each global alloy composition. These were obtained from samples with a varying number of lattice sites equal to $32\,000 \pm \Delta N$ atoms, with $\Delta N \leq 192$. Atoms were randomly distributed on the available lattice site based on the quasi-binary sum formula $(\mathrm{ABCD})_{4N}\mathrm{E}_{N\pm\Delta N}$. These samples

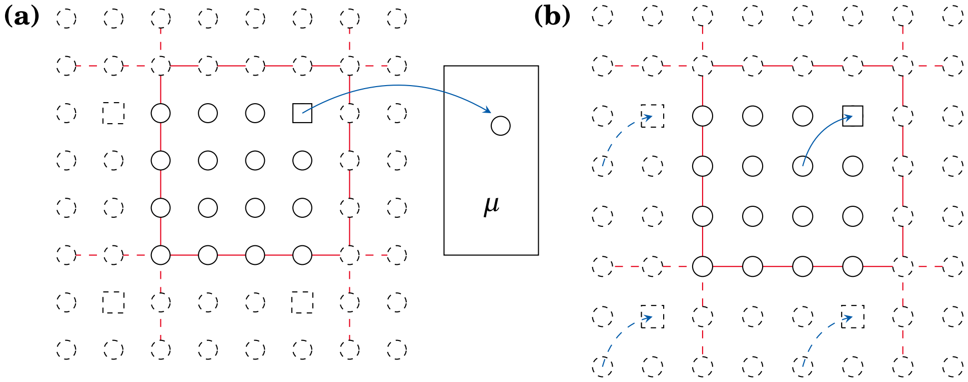

Figure 3.7: (a) Schematic representation of the method used to calculate the vacancy formation energy. An atom (circle) is removed from its lattice site and placed in an infinite reservoir with chemical potential μ leaving a vacancy (square) in its original position. The energy difference of the initial and final state corresponds to the vacancy formation energy. (b) Application of the NEB method to calculate a vacancy migration energy barrier. The vacancy exchanges site with one of its neighboring atoms and the energy is tracked along the MEP (see Section 3.3). Note that in both cases an infinite array of defects is simulated due to the periodic boundary conditions (periodic images are indicated by dashed lines).

were minimized using the CG algorithm allowing for an anisotropic change in box size to reach pressure-free conditions. Minimization was carried out to a force tolerance of $1 \times 10^{-8}\,\mathrm{eV\,Å^{-1}}$.

The simulation cell for the determination of the vacancy formation energies contained 1×10^3 FCC cells for a total of 4000 lattice sites. For each sample composition 40 different random atomic arrangements were created. In each of these 40 samples, 40 separate vacancy sites per species were sampled giving 8000 vacancy samples per concentration or almost 90 000 vacancy calculations. The vacancy formation energies were calculated under static conditions using CG energy minimization. The simulation cell volume was kept constant[357] and periodic boundary conditions were applied in all dimensions. The desired force convergence was set to $1 \times 10^{-8}\,\mathrm{eV\,Å^{-1}}$.

3.9.2 Vacancy Migration Energies

Vacancy migration energies can be readily calculated from a simulation cell containing a vacancy using NEB (cf. Section 3.3). Here, the vacancy before and after the site exchange with one of its neighboring atoms are taken as start and end point of the calculation, respectively. The saddle point of the MEP obtained from CI NEB corresponds to the vacancy migration energy barrier. This process is schematically shown in Figure 3.7 (b) where the vacancy position is indicated by a square and the site exchange with a neighboring atom (circle) is indicated by an arrow. Again, the calculation of the transition path in the

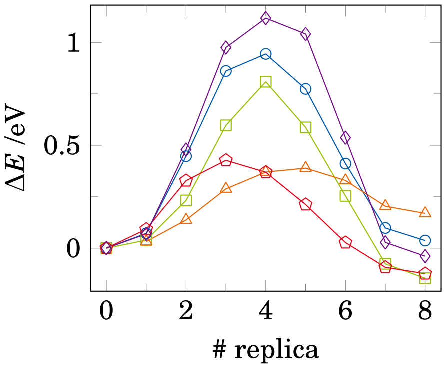

Figure 3.8: Examples of the potential energy change ΔE along the minimum energy path connecting a vacancy and a neighboring occupied lattice site in the equimolar CoCrFeMnNi Cantor alloy. Results are obtained from CI NEB so that the highest energy corresponds to the saddle point in the potential energy landscape.

simulation cell (solid lines) results in identical atomic trajectories in the periodic images (dashed lines). In concentrated alloys, the vacancy migration energy does not only scale with the atom involved in the site exchange but also the local chemical configuration. This can be seen in Figure 3.8, where five randomly selected vacancy migration energy paths in the equimolar CoCrFeMnNi alloy are shown.

Simulation Details

The vacancy migration energies along the MEP were obtained from the CI NEB method. For each concentration in the $(\mathrm{CoCrFeMn})_{1-x}\mathrm{Ni}_x$ system between 4800 and 12 200 atom-vacancy jumps were calculated leading to a total of almost 93 000 vacancy migration barriers. Note that samples where the NEB calculations did not converge were discarded. Each sample contained 1×10^3 FCC unit cells with atoms distributed randomly on the available lattice sites. A single atom was deleted to create a vacancy. This vacancy was statically relaxed on its creation site and afterwards exchanged with one of its nearest neighbors. These two states were then connected with nine NEB images (replicas) to obtain the MEP. Based on the investigation by Mishin et al.[357] all calculations were performed at constant reference volume of the defect-free single crystal. Periodic boundary conditions were applied to prevent boundary effects.

Vacancy arrangements and MEPs were minimized using the older LAMMPS implementation of the FIRE algorithm.[339] Meanwhile, an improved version has been released in early 2020.[338] Both initial and final vacancy configurations as well as the NEB images were relaxed to an energy tolerance of 1×10^{-8} eV.

3.10 Dislocations

In Chapter 5 the local pinning of isolated edged dislocations was calculated using the steps and methodology outlined in the following section. The equimolar CoCrFeMnNi HEA and all subsystems were described by the second-nearest neighbor MEAM[377] interatomic potential developed by Choi et al.[129] Other sam-

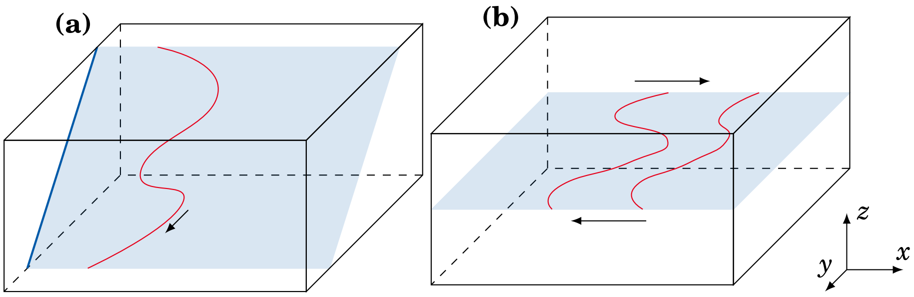

Figure 3.9: Samples used to investigate the dislocation pinning. (a) Large-scale sample used to see dislocation nucleation from a surface notch (thick blue line). Shockley partial dislocations (red line) are nucleated under the applied tensile strain (arrow) and glide on the inclined glide plane (shaded area). This sample has periodic boundary conditions along the y-direction with open boundaries along x- and z-directions mimicking experimental samples. (b) Sample geometry used to determine the critical stress for dislocation glide and the dislocation mobility. Two Shockley partial dislocations (red lines) are inserted on a central glide plane (shaded area). These start to glide under an applied shear force on the top and bottom surface (arrows). The sample has open boundaries along z-direction while the two other directions are periodic.

ples were based on the Farkas and Caro[383] or Zhou et al.[369] EAM interatomic potentials. All calculations were performed using LAMMPS.[327] Samples were prepared using ATOMSK,[381] post-processing was based on algorithms implemented in OVITO[382] and accelerated using PARALLEL.[384]

3.10.1 Virtual Samples Representing a TEM Lamella

Figure 3.9 (a) shows the geometry of the samples used for direct comparison to the experimental in situ transmission electron microscopy (TEM) deformation experiments. To mimic the experimental sample geometry a notch (dark blue line), destined as nucleation site for dislocations was cut into the sample surface. This notch was aligned with a glide plane (shaded area) at the same inclination angle as the experimental one. Uniaxial strain was applied along the periodic y-direction. This led to dislocation nucleation from the notch, which subsequently glided in x-direction to be absorbed into the opposite sample surface.

Simulation Details

The large-scale sample used for comparison with the experimental TEM measurements had initial dimensions of $101.36 \times 152.47 \times 74.62\,\mathrm{nm}^3$ filled with single crystalline FCC lattice in the orientation $[\bar{1}\bar{2}3]$, $[1\bar{2}\bar{1}]$, $[4\,1\,2]$ along x, y, and z, respectively. This gave about 1×10^8 lattice sites which were randomly filled with either CoCrFeMnNi or CoNi alloy. A surface notch with an inclination of 28.13° was cut into the y-z plane. This surface notch was aligned with a $\{1\,1\,1\}$ glide plane in the sample. To mimic the experimental conditions, the x-

and z-directions were taken as open surface boundaries, while the y-direction was set to periodic boundary conditions. The sample geometry is schematically shown in Figure 3.11 (a). After equilibration for 50 ps at 5 K or 300 K in the NVT ensemble, the sample was subjected to uniaxial strain along y up to a strain of 0.06 using an engineering strain rate of $1 \times 10^8\,\mathrm{s}^{-1}$[385] and a constant time step length of 1 fs. Dislocation lines were extracted every 5 ps during straining using the dislocation extraction algorithm (DXA).[386,387]

3.10.2 Shear of an Edge Dislocation

Figure 3.9 (b) schematically shows the sample setup used to determine the critical force to initiate dislocation glide and the dislocation mobility under constant applied shear. It contains a single perfect edge dislocation in the central glide plane (shaded area) of the sample. There are two established methods of inserting edge dislocations into crystals for simulation; Either by the manual insertion of a half plane, or by displacing the atoms according to the analytically calculated displacement field of the dislocation.[388] Inserting a half plane has the advantage of preserving periodicity along the dislocation glide direction.[389] The inserted dislocation readily dissociates into two Shockley partial dislocations (red lines). Applying a shear force to the open surfaces in z-direction (indicated by arrows in Figure 3.9 (b)) applies a Peach-Koehler force to the partial dislocations,[67]

$$\vec{F} = \left(\underline{\sigma} \cdot \vec{b}\right) \times \vec{l}, \tag{3.27}$$

where $\vec{F}$ is the force acting on the dislocation, $\underline{\sigma}$ is the local stress tensor, $\vec{b}$ is the Burgers vector, and $\vec{l}$ is the dislocation line direction. As the sample has periodic boundary conditions along the x- and y-directions, this sample geometry facilitates the simulation of an array of dislocations with infinite line length, gliding for an infinite distance.

Simulation Details

To insert a dislocation into the samples, a single half plane was inserted into a pristine FCC crystal resulting in a misfit edge dislocation following the sample geometry shown in Figure 3.9 (b).[388] The resulting dislocation had a Burgers vector $\vec{b}$ along $[1\bar{1}0]$ (corresponding to the x-direction) with a line direction of $[11\bar{2}]$ (along the y-direction). There were two different samples sizes considered for the simulation of the isolated dislocations. The smaller sample contained 477 600 atoms with periodic boundary conditions along the $[1\bar{1}0]$ (x) and $[11\bar{2}]$ (y) directions and open surfaces along the $[111]$ (z) direction. The sample was made up of $200 \times 20 \times 20$ unit cells in those directions, respectively.

The larger sample had the same crystallographic orientations, but the size was increased to $400 \times 200 \times 24$ unit cells for at total of 11.5×10^6 atoms. In both cases, the FCC lattice sites were randomly filled with the desired atomic species to create random solid solution samples. Afterwards, two more samples were prepared starting from the random CoCrFeMnNi samples. Here, 50 $L1_2$ Co_3Cr particles with radius $r = 6\,Å$ or $r = 12\,Å$ were artificially inserted in the central (1 1 1) plane of the larger sample.

The samples were annealed for 50 ps at 2 K using a 1 fs time step length. Both during this annealing and the subsequent shear simulations the surface layers were thermostatted using a Langevin thermostat,[334] while the central atoms were integrated in the microcanonical (NVE) ensemble. After equilibration, a ramping shear force was added to each atom in the outer surface layer. This force pointed in the $\pm x$-direction (Figure 3.9 (b)) and was ramped from 0 to $0.208\,\mathrm{eV}\,Å^{-1}$ over a time interval of 200 ps. From these shear ramp simulations the critical force to initiate dislocation glide F_c was determined. Once this critical force was known, a second constant force simulation was started. Here, the applied shear force was first ramped from 0 to F_c with a rate of $1 \times 10^{-6}\,\mathrm{eV}\,Å^{-1}\,\mathrm{fs}^{-1}$. Afterwards, the constant shear was applied for another 100 ps to determine the dislocation mobility. The dislocation position was extracted using the DXA method[386,387] implemented in OVITO.[382]

Simulation Details: Monte Carlo Equilibration

The aforementioned samples all resembled ideal random solid solution matrices. We were also interested in the effects of short-range order (SRO) on a gliding dislocation. The samples containing SRO were prepared using a hybrid MC/MD method. Here MD steps were performed in the isobaric-isochoric (NVT) ensemble at zero pressure and different temperatures between 600 K and 1400 K. After an initial thermalization MC trial steps were performed every 20 fs in the canonical ensemble, i.e., atoms were swapped on the lattice. During each MC step 50 swaps were attempted within each atomic pairing for 50 ps.

Since the atom swap MC method cannot be parallelized, the total number of atomic swaps that could be simulated was limited. To focus swaps on the region of interest and accelerate chemical equilibration six lattice planes in the center of the smaller dislocation sample were extracted and put in a new periodic simulation cell. These six planes were subjected to the MC simulation protocol and afterwards transplanted back into their original sample. After reinsertion into the host sample, all simulations were repeated on these SRO samples using the methodology outlined in Subsection 3.10.2 and Subsection 3.10.3. Care was taken to ensure that both the generalized stacking fault (GSF) and the glide plane of the investigated dislocation were located in the center of the MC equilibrated region.

The number of MC steps taken might seem low. Figure 3.10 (a) shows the energy over MC annealing time for the different annealing temperatures. Initially only MD steps were performed and the energy remained constant. After 30 ps the hybrid MC/MD scheme was applied and one can see a rapid

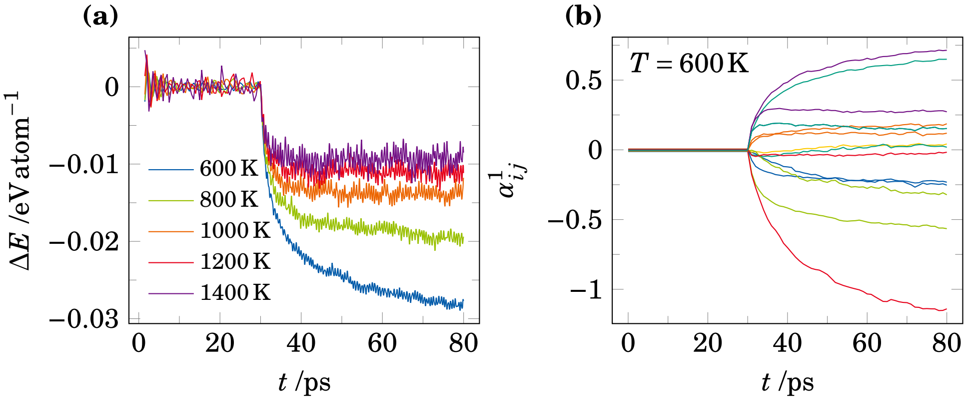

Figure 3.10: (a) Potential energy change ΔE per atom over time t for the different MC annealing temperatures. The first 30 ps are pure MD equilibration, while for the following 50 ps the full hybrid MC/MD method is employed. (b) Evolution of the WC SRO parameter α_{ij}^{1} during annealing at 600 K. Each line corresponds to a different i-j pair, for reference see Figure 5.15.

energy decrease in all samples as the SRO forms. Figure 3.10 (b) shows the temporal evolution of the Warren-Cowley SRO parameters[390] in the sample annealed at 600 K over time. These remained constant for the first 30 ps, but change rapidly thereafter. Even though, the energies were not fully converged in this sample, SRO forms. The lowest temperature sample was taken as a benchmark as convergence should be the most time-consuming given the lower MC acceptance rate at lower temperatures.

3.10.3 Generalized Stacking Fault Energy

Conventionally, the generalized stacking fault (GSF) energy is calculated based on the methodology suggested by Vitek.[251] They suggest calculating the GSF energy surface of the (111) plane in an FCC lattice by shifting two layers in this plane along the $[1\bar{1}0]$ and $[11\bar{2}]$ directions sampling the potential energy landscape. Figure 3.11 shows a schematic representation of the FCC atoms above (dashed) and below (solid) the GSF plane. The energy is sampled for all displacements within the blue rectangle. The original methodology allows for relaxation of atoms in the directions normal to the GSF plane and the planar fault energy γ is given by,[251]

$$\gamma = E - E_{\mathrm{Ref}} \quad \text{or} \quad \gamma = \frac{E - E_{\mathrm{Ref}}}{A}, \tag{3.28}$$

where E is the energy of crystal with the planar fault and E_{Ref} is the energy of the pristine single crystal. γ may then be normalized by the planar fault area A.

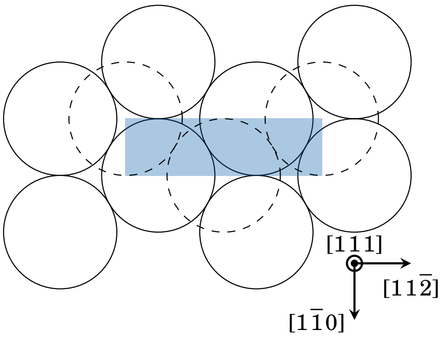

Figure 3.11: Schematic representation of the atoms in the FCC (111) plane. Calculation of the energies associated with translations of the lower (solid) against the upper (dashed) atoms within the blue rectangle gives access to the GSF energy. Adapted from Vitek.[251]

We are not only interested in the global GSF landscape calculated in this way, but also in the energy landscape experienced by any individual atom in the plane. While this number is inaccessible to experimental techniques and density functional theory (DFT) calculations, it can be calculated using LAMMPS. Here, the usage of an empirical interatomic potential gives the projected energy contributions of each atom as it interacts with the other atoms in the sample.

Simulation Details

The global and atomic GSF curves were calculated for the two differently sized samples presented in Subsection 3.10.2 prior to dislocation insertion, i.e., on the pristine FCC samples. As mentioned above, the conventional simulation methodology prevents the atomic relaxation during shifting of the two crystallites within the GSF plane. One problem that arose, applying the conventional methodology, was that the atoms in the disordered alloy relaxed in different metastable states as the two crystallites were shifted against each other. While this effect averaged out in the global GSF landscape, the resulting atomic energy landscapes were not smooth but included discontinuities when an atom relaxed into such a local metastable state. To avoid these artifacts, we decided to further constrain the atomic positions during the GSF calculations. Each atom was fixed to its ideal FCC lattice site, preventing small relaxation from the intrinsic lattice distortions (cf. Figure 3.6). During displacement, the force acting on the atoms was set to 0 along the [1$\bar{1}$0] and [11$\bar{2}$] directions, in line with conventional methodology,[251,252] while the forces normal to the GSF plane were averaged for all atoms in each crystallite. This meant that the perfect FCC lattice was preserved but the crystallites were still able to change their separation to reduce their energy. Figure 5.6 shows the difference in atomic trajectories for both relaxation methods.

To determine the GSF landscape, a 3.6 Å by 2.1 Å area was sampled with a grid spacing of 0.1 Å, corresponding to the shaded region in Figure 3.11. At each grid point, the potential energy was minimized using the latest implementation of the FIRE algorithm[338] to an energy tolerance of 1×10^{-12} eV or a force tolerance of 1×10^{-8} eV Å^{-1}. The resulting two-dimensional energy landscape for each atom was interpolated using cubic splines. The three local minima were found using the BFGS algorithm implemented in SCIPY.[391] The maximum energy gradient was calculated along a linear path connecting these three minima. Figure 5.7 shows an example of the resulting atomic energy landscape and calculated energy gradients.

3.11 Grain Boundaries

Chapter 6 provides results on the grain boundary (GB) mobility of a planar boundary in bicrystal geometry and full atomistic grain growth simulations on nanocrystalline (NC) samples. The samples and methodology employed in that chapter will be introduced in the following. The CoCuFeNi model HEA, its elemental subsystems, and Pt were described by the EAM[392] interatomic potential parametrized by Zhou et al.[369] Pd, on the other hand, was based on the EAM potential by Foiles and Hoyt.[393] The performance of the CoCuFeNi interatomic potential had already been assessed by Koch et al.[60] while the Pd interatomic potential had been characterized by Schäfer et al.[394] We also derived an avg.-atom EAM interatomic potential for the CoCuFeNi HEA following the mathematical formalism establish by Varvenne et al.[111] This method and the resulting avg.-atom interatomic potential are described in Subsection 3.7.2. Atomistic simulations were performed using LAMMPS.[327] Samples were prepared using ATOMSK[381] and post-processing was performed using OVITO.[382] Most importantly, structural identification was performed using polyhedral template matching (PTM)[395] and grain segmentation was based on an experimental algorithm.

3.11.1 Bicrystalline Σ11 Samples

The simplest sample geometry for the study of GBs is a bicrystalline sample geometry containing two differently oriented crystallites separated by a planar GB. However, in an orthogonal simulation cell with fully periodic boundary conditions only a small subset of the infinite number of possible bicrystals can be constructed. Here the two abutting grains have to form a so-called *coincidence site lattice* in the boundary plane. This allows for periodic boundary conditions in the GB plane. Moreover, as the two crystallites are connected across the periodic boundary normal to the GB plane there will always be at least two GBs in a simulation cell. In the simplest case, these two boundaries are mirror-symmetric. This sample geometry is schematically shown in Figure 3.12 (b).

We were not only interested in the equilibrium GB configuration but more importantly its mobility. Therefore, a method to drive the planar GBs in a bicrystalline sample geometry was needed. This can be achieved using so-called *synthetic driving force methods*.[398] Here, the two crystallites in a simulation cell are identified based on their local lattice orientation. A constant potential energy Δe is added to one crystallite, leading to a smooth energy gradient across the

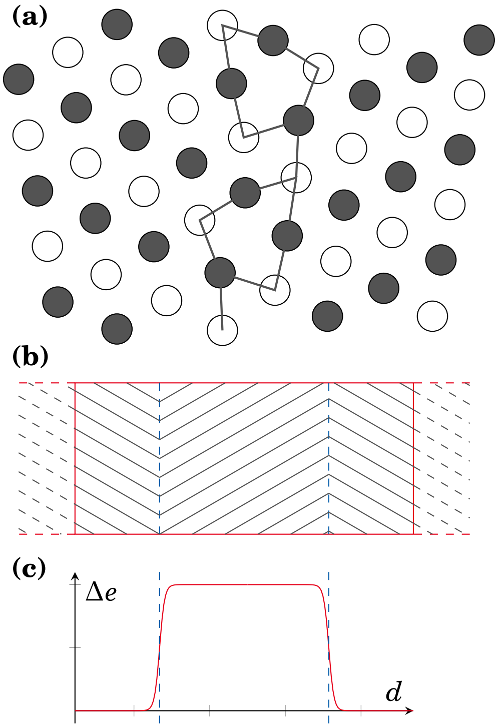

Figure 3.12: (a) 0 K equilibrium structure of the $\Sigma 11(3\,3\,2)\langle 1\,1\,0\rangle$ STGB adapted from Rittner and Seidmann.[396] Repeating structural units of the GB are connected using lines. This STGB is composed of kite-shaped E type RUs connected by linear D RUs.[396,397] Alternating lattice planes are indicated by filled and open circles. Adapted from Ref. 396. (b) Schematic representation showing how two planar STGBs (blue lines) need to be placed inside a simulation cell (red) to accommodate the periodic boundary conditions. Two neighboring periodic cells are indicated by dashed lines. Hatching directions indicate the local lattice orientations to highlight the opposite orientations in the two crystallites. (c) Sketch of the synthetic driving force Δe added to the two differently oriented crystallites shown in (b) as a function of distance d. This added potential energy gives a driving force on the planar STGB to facilitate GB migration.

GBs plane. This excess potential energy and the resulting energy gradient lead to a driving force, shrinking one grain, while the other one grows.[398] This added energy profile for the sample geometry introduced in Figure 3.12 (b) is shown (c). There are different methods of calculating the local lattice orientation and applying the synthetic excess energy. We used the method proposed by Janssen et al.[398] implemented in LAMMPS, as it is most commonly used in literature.* At the time of our simulation, there was a competing implementation by Zhou and Mohles[399] — which of the two methods is more correct has been debated by the different authors.[400,401] Mohles et al.[402,403] have also developed a third method which only became widely available in 2020 and has therefore not been an option for our simulations.

For all GB structure and mobility simulations $\Sigma 11(3\,3\,2)\langle 1\,1\,0\rangle$ symmetrical tilt grain boundary (STGB) samples were built and investigated. Here, $(3\,3\,2)$ is the boundary plane and $\langle 1\,1\,0\rangle$ is the rotation axis of the two grains forming the symmetrical tilt grain boundary. The periodic 0 K ground state structure of this STGB as proposed by Rittner and Seidmann[396] can be seen in Figure 3.12 (a). It is composed of kite-shaped E repeating structural units (RUs) that are connected by straight D RUs. Even though, this ground state was determined

---

*237 citations on Google Scholar compared to 63 for the other methods, both retrieved on May 4, 2021.

on Cu samples, it should be valid for other low stacking fault (SF) energy FCC metals.

Simulation Details

The $\Sigma 11(3\,3\,2)\langle 1\,1\,0\rangle$ STGB studied here was built with orientation $x = [\bar{1}\,\bar{1}\,3]$, $y = [\bar{1}\,1\,0]$, $z = [3\,3\,2]$. Here the y-direction corresponds to the rotation axis and z is normal to the GB plane. A second crystallite was prepared and mirrored on the x-y-plane and stacked onto of the first crystallite along the z-direction. All samples measured about 18 nm × 1 nm × 48 nm, subject to change based on element and temperature, containing 74 000 atoms. The segregation (seg.) CoCuFeNi sample had a 4 times greater thickness along y-direction as this is required by the MC algorithm. The full MC equilibration procedure is described in Section 3.11.1. All samples had periodic boundary conditions leading to two identical STGBs within each simulation cell.

The samples were first minimized to ensure that the correct minimum energy configuration, as reported by Rittner and Seidmann,[396] was reached (cf. Figure 3.12). Energy minimization was again based on the CG algorithm under pressure-free boundary conditions.

To facilitate grain growth, all samples were first equilibrated at different temperatures between 400 K and 1600 K for 10 ps in the NPT ensemble under stress-free conditions. Subsequently, a synthetic driving force[398] of 15 meV atom^{-1} was applied for 200 ps. To compensate for shear-coupling during the grain boundary migration the simulation cell was allowed to tilt. This setup corresponds to the free boundary conditions discussed by Ivanov and Mishin.[404] The time step for these simulations was set to 2 fs. Five different samples were simulated for each composition and temperature. The GB position was determined by tracking peaks in the spatial distribution of structurally unidentified atoms along the z-direction. Structural identification based on PTM.[395]

Simulation Details: Segregation to Grain Boundaries

The chemical equilibration resulting in Cu segregation to the STGB was based on the hybrid MC/MD simulations with MC steps in the variance-constraint semi-grandcanonical ensemble derived by Sadigh et al.[350] as summarized in Section 3.4. Staring from the perfectly random CoCuFeNi STGB samples, the samples were equilibrated for 40 ps at temperatures from 700 K to 1600 K, again using a 2 fs time step length. During this time MC steps were performed every 20 MD steps on 25 % of the atoms. The κ parameter was set to 1000 (cf. Koch et al.[60]) and the following chemical potential differences $\Delta\mu_{i-j}$ values were used: Cu-Co = 858.4 meV, Cu-Fe = 717.5 meV, and Cu-Ni = 906.0 meV.

The chemical potential differences discussed above were obtained from an iterative fitting process on a smaller single crystalline simulation cell. This cell contained 32 000 atoms in a fully periodic FCC lattice. This sample was then

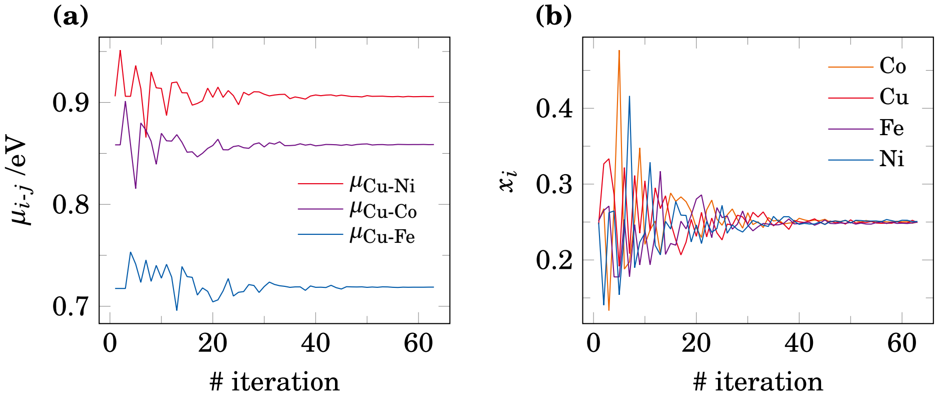

Figure 3.13: (a) Chemical potential difference in the CoCuFeNi HEA during the iterative fitting procedure. $\mu_{\text{Cu-Cu}}$ is defined to be equal to 0. (b) resulting concentrations in the sample after MC equilibration in the semi-grand canonical ensemble at 800 K.

subjected to the hybrid MC/MD simulations without variance-constraint, i.e., in the grand canonical ensemble, at 800 K. The $\Delta\mu_{i\text{-}j}$ values were taken as fit parameters for this simulation and tuned until an equimolar CoCuFeNi solid solution formed. The high temperature was chosen as it has been previously shown that this HEA forms a stable solid solution at 800 K.[60] The Nelder-Mead minimization algorithm implemented in SCIPY[391] was used, and initial values were taken from Koch et al.[60] Figure 3.13 shows the $\Delta\mu_{i\text{-}j}$ parameters (a) and resulting stable concentrations (b) in the sample as function of the iteration step. Good convergence of the concentrations can be seen.

3.11.2 Nanocrystalline Samples

It is obviously impossible to perform long time MD simulations in coarse-grained or even ultrafine microstructures usually encountered in metallurgy experiments. Therefore, atomistic simulations of microstructures usually have to resort to nanocrystalline (NC) structures with grain sizes significantly smaller than 50 nm. The initial grain geometries are commonly constructed from Voronoi tessellation.[405–408] The process will be outlined in the following, and the resulting grain structure is schematically shown in Figure 3.14. First a sample, i.e., simulation cell, volume is defined. In the next step, the center of each grain is randomly placed in this cell. These random points are taken as starting points for a space-filling Voronoi tessellation where each resulting polyhedron corresponds to an individual grain. These subvolumes are subsequently filled with the desired crystal lattice in random orientation.[409,410] This creates a set of grains separated by random GBs.

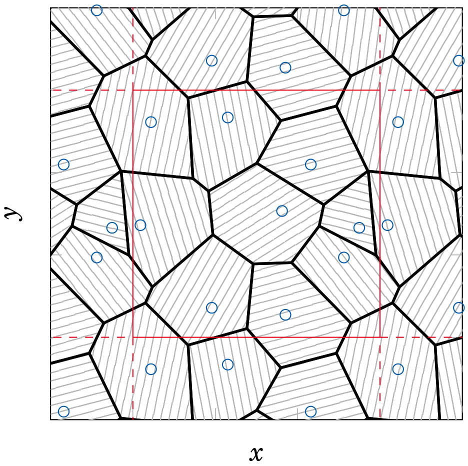

Figure 3.14: Schematic showing the Voronoi construction of a nanocrystalline sample in two dimensions. Blue circles mark the initial points for each grain and gray lines shown the resulting Voronoi tessellation.[405] Each Voronoi region corresponds to a different grain in the final microstructure and is subsequently filled with a randomly oriented crystal lattice. The red square represents the simulation cell, while dashed lines indicated surrounding periodic images.

Simulation Details

The nanocrystalline samples were cubes with an initial edge length of 26 nm containing 10 randomly oriented FCC grains with an equivalent average radius of 7.5 nm. Each simulation cell contained approximately 1.5 million atoms. These samples were equilibrated in the NPT ensemble under pressure-free conditions for 5 ns using a 2 fs time step length at different temperatures corresponding to homologous temperatures between 0.6 and 0.9.

Simulation Details: Segregation to Grain Boundaries

The segregation in the nanocrystalline CoCuFeNi sample was dialed-in using a similar methodology as in the bicrystalline sample. The same $\mu_{i\text{-}j}$ and κ values were used and MC steps were performed on 25 % of the atoms every 20 MD steps. The variance-constraint semi-grand canonical MC was run for the first 100 ps of the simulation time until the GBs were fully decorated. Afterwards, pure MD annealing was done following the random CoCuFeNi NC sample.

4 Vacancies

> *“Although being not ‘sluggish’ at all, the careful diffusion measurements discovered a lot of exciting results and the term ‘sluggish’ has to be considered with a historical respect. In fact, this myth played a key role in initiating of the enormous interest to the field.”*
>
> — S. V. Divinski *et al., 2018*[16]

The results presented in Section 4.1 are partially published in:

> “D. Utt, A. Stukowski, and K. Albe, *Thermodynamics of vacancies in concentrated solid solutions: From dilute Ni-alloys to the Cantor system*, arXiv:2104.02697 [cond-mat] (2021)’, Acta Materialia, (under review),[411]

while the results from Section 4.2 to Section 4.5 are partially published in:

> “J. Kottke, D. Utt, M. Laurent-Brocq, A. Fareed, D. Gaertner, L. Perrière, Ł. Rogal, A. Stukowski, K. Albe, S. V. Divinski, and G. Wilde, *Experimental and theoretical study of tracer diffusion in a series of (CoCrFeMn)$_{100\text{-}x}$ Ni$_x$ alloys*, Acta Materialia 194, 236–248 (2020)”.[412]

In this chapter we investigate the equimolar CoCrFeMnNi Cantor alloy and different compositions towards the Ni-rich side of its phase diagram. First, we calculate the vacancy formation energy and enthalpy. In a second step, we then calculate the vacancy migration energy in these alloys depending on the chemical environment and migrating species. Based on the harmonic transition state theory these would be sufficient to describe diffusivities in these alloys.[43,44] For comparison with tracer diffusion experiments, knowledge about the tracer correlation factors is required as well.[43,130] After successful determination of these parameters using a novel variable-barrier kinetic Monte Carlo (KMC) algorithm, the chapter concludes with a comparison of simulated and experimental tracer diffusion studies.

4.1 Thermodynamics of Vacancy Formation

For comparing the calculated vacancy migration energies to experimental tracer diffusion measurements, knowledge about the vacancy formation energy and the resulting equilibrium vacancy concentration is required. The (CoCrFeMn)$_{1-x}$

Ni_x family of high-entropy alloys (HEAs) is investigated. The free energy G_f of vacancy formation is defined as,[44]

$$\begin{aligned} G_\mathrm{f} &= G_\mathrm{Def} + \mu_i - G_\mathrm{Ref}, \\ H_\mathrm{f} + TS_\mathrm{f} &= (H_\mathrm{Def} - TS_\mathrm{Def}) + \mu_i - (H_\mathrm{Ref} - TS_\mathrm{Ref}), \end{aligned} \tag{4.1}$$

where index 'Def' denotes the sample containing the vacancy, index 'Ref' is the single crystalline reference, and μ_i is the chemical potential of the removed species i. The chemical potential depends not only on the species of the removed atom but also on the overall sample composition x_Ni. Assuming that there is no external pressure, the enthalpy H can be replaced by the inner energy U. As all following calculations are taken at a temperature of 0 K, the inner energy becomes equivalent to the potential energy E. Therefore, Equation 4.1 maybe be rewritten as:

$$E_\mathrm{f} = E_\mathrm{Def} + \mu_i - E_\mathrm{Ref}. \tag{4.2}$$

This chemical potential of i μ_i is defined as the change in free energy G resulting from a change in particle number of species i, N_i. Here we calculate μ_i at 0 K based on the following relation,[413,414]

$$\mu_i = \left(\frac{\partial G}{\partial N_i}\right)_{T,P,N_{j\neq i}} \xrightarrow[\approx]{T=0\,\mathrm{K}} \left(\frac{\partial U}{\partial N_i}\right)_{S,P,N_{j\neq i}} = \left(\frac{\partial E}{\partial N_i}\right)_{T,P,N_{j\neq i}}, \tag{4.3}$$

where N_i denotes the number of particles of type i and U is the inner energy. At 0 K, U corresponds to the potential energy E calculated by LAMMPS. The right-hand side of Equation 4.3 can be calculated numerically by changing the particle count of each species in small increments around the nominal composition and determining the energy for these configurations. To do so, we fit the energy of different quasi-binary samples of the form: $(\mathrm{ABCD})_{4N}\mathrm{E}_{N+\Delta N}$, where ΔN is some small change in the total particle number N. The slope of the resulting $\Delta E(\Delta N)$ curve corresponds to μ, under the assumption of a constant configurational entropy, since $\Delta N << N$ this condition should be fulfilled. To obtain the chemical potential for all species, species E is replaced by Co, Cr, Fe, Mn, and Ni, respectively and calculations are repeated for all desired Ni concentrations. The change in particle numbers in these samples goes without the creation of vacancies or other defects in the sample, fully periodic single crystalline samples of different sizes with different numbers of lattice sites are used. Figure 4.1 (a) shows an example of such a chemical potential calculation for the equimolar Cantor alloy. Here the number of atoms is varied by ±200 and the change in potential energy ΔE is plotted on the ordinate. For example, the Mn (purple) line corresponds to samples following the $(\mathrm{CoCrFeNi})_{4N}\mathrm{Mn}_{N+\Delta N}$ sum formula. For all samples good agreement between data and linear fit can be seen and the slope of the fits corresponds to the chemical potential μ_i. A summary of the chemical potentials not only as function of element but also of Ni concentration in the $(\mathrm{CoCrFeMn})_{1-x}\mathrm{Ni}_x$ alloys is given in Figure 4.1 (b).

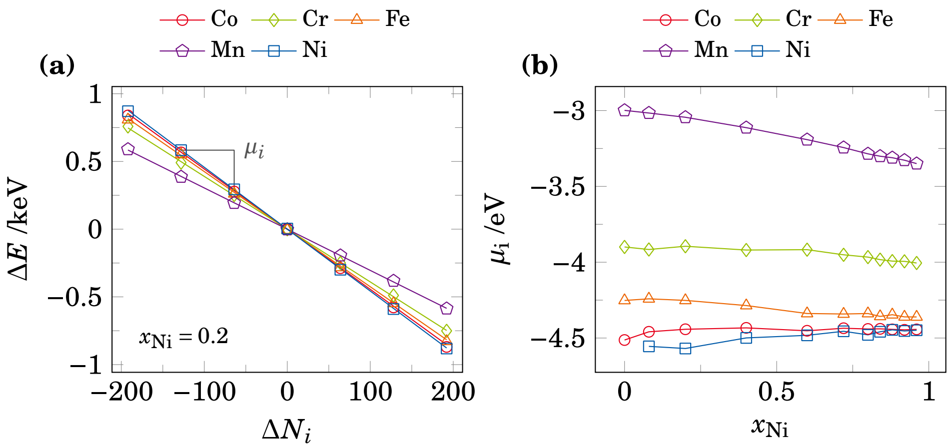

Figure 4.1: (a) Change in potential energy ΔE over the change in particle count ΔN_i for the different species in the Cantor alloy. The sample composition is changed based on the quasi-binary sum formula $(\mathrm{ABCD})_{4N}\mathrm{E}_{N+\Delta N}$. The slope of the linear fit corresponds to the chemical potential μ_i (Equation 4.3). (b) Chemical potential for each species for different samples in the $(\mathrm{CoCrFeMn})_{1-x}\mathrm{Ni}_x$ HEA. Adapted from Ref. 411.

With knowledge of the chemical potential difference, Equation 4.2 can be used to calculate the vacancy formation energy as function of x_{Ni}. Based on previous literature reports[119–123,416] we would expect the vacancy formation energies E_{f} to show a broad distribution. Figure 4.2 (a) shows the vacancy formation energy distribution for two concentrated and one dilute alloy in the $(\mathrm{CoCrFeMn})_{1-x}\mathrm{Ni}_x$ HEA family. The data is color coded based on the species of the atom removed to create the vacancy. As suggested by Ruban,[113] the vacancy formation energy is independent of the removed element and shows a distribution. For these alloys, the median of these distributions lies around 1.5 eV. The Ni-rich dilute alloy ($x_{\mathrm{Ni}} = 0.96$) features a much narrower distribution of vacancy formation energies compared to its concentrated counterparts. A summary of the results for all tested vacancy calculations by showing the median vacancy formation energies $\widetilde{E}_{\mathrm{f}}$ over the Ni concentration is given in (b). It can be seen that the vacancy formation energies remain almost constant going from the Ni-free four component alloy, via the equimolar Cantor alloy, towards the Ni-rich dilute alloys. This is not an intuitive result, as the vacancy formation energies of the pure elements in the FCC phase are very different; Co: 1.45 eV, Cr: 2.18 eV, Fe: 1.92 eV, Mn: 0.98 eV, and Ni: 1.51 eV. If one were to take a rule of mixtures based approach, one would expect the vacancy formation energy to decrease linearly from 1.63 eV for the CoCrFeMn to 1.51 eV HEA to pure Ni. Figure 4.2 (c) gives the median absolute deviation (MAD),which is more robust to outliers than the standard deviation,[417] of the vacancy formation energy distribution as a measure for the distribution width. For Ni concentrations below 0.8, i.e., highly concentrated alloys, the MAD is almost constant indicating that there

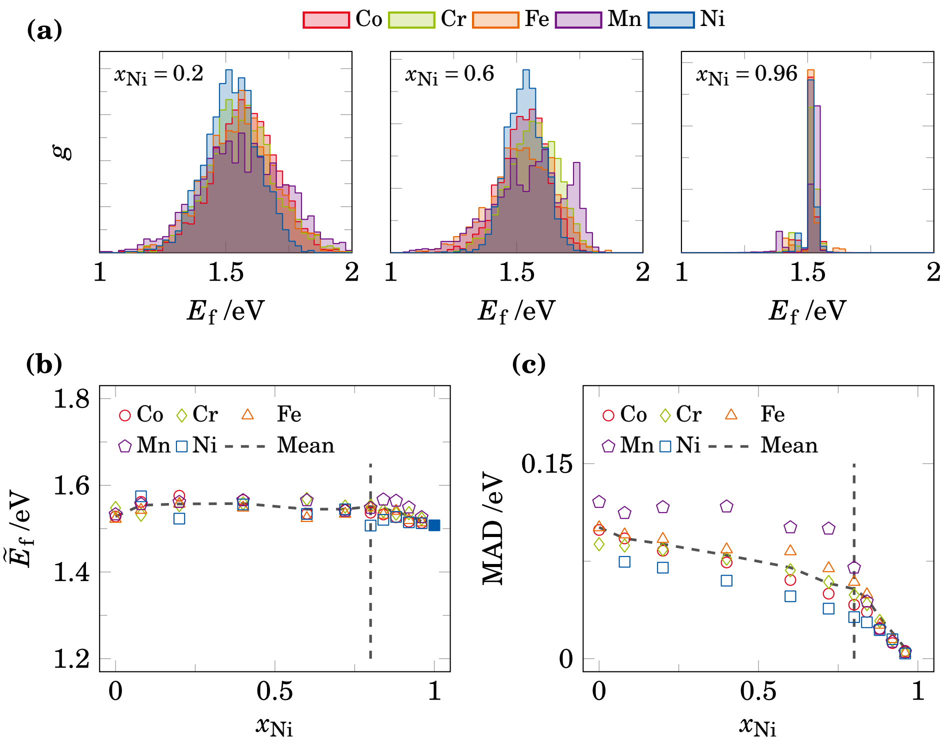

Figure 4.2: (a-c) Element specific vacancy formation energy distribution g for different $(\mathrm{CoCrFeMn})_{1-x}\mathrm{Ni}_x$ HEAs. (d) Median of the vacancy formation distributions $\widetilde{E}_{\mathrm{f}}$ and the MAD to characterize the distributions' widths (e). Dashed lines indicate the percolation threshold of the FCC lattice[415] as transition point from concentrated to dilute alloy. Partially adapted from Ref. 411.

is a vast range of different chemical environments. Each of these distinct environments leads to a slightly different vacancy formation energy spread around some median value. For Ni concentrations greater than 0.8, corresponding to more dilute solid solutions, a steadily decreasing MAD can be seen. This stems from the effect that the chemical environment of the vacancy becomes more Ni-rich and homogeneous.

A similar way to think about the transition from concentrated to dilute alloy would be in terms of percolation. In the concentrated alloy, matrix and solute atoms cannot be distinguished, and every species is bonded to all other species. The transition to a dilute alloy is marked as the point, where there is no connecting (percolating) path between solute atoms. Instead, they are always separated by, a now identifiable, solvent species. The nearest neighbor percolation threshold in the three-dimensional FCC lattice is 0.199,[415] which means that once the non-Ni concentration drops below this threshold, solutes are mostly isolated (at least along nearest neighbor bonds). Figure 4.3 confirms this statement. It gives the ratio of isolated solutes (non-Ni atoms) N_{isolated} to

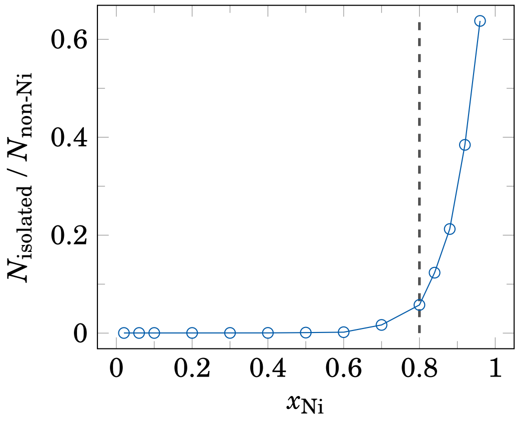

Figure 4.3: The ratio of isolated non-Ni atoms N_isolated to the total number of non-Ni atoms $N_\text{non-Ni}$ in different $(\text{CoCrFeMn})_{1-x}\text{Ni}_x$ HEA. The FCC percolation threshold[415] is indicated by a dashed line.

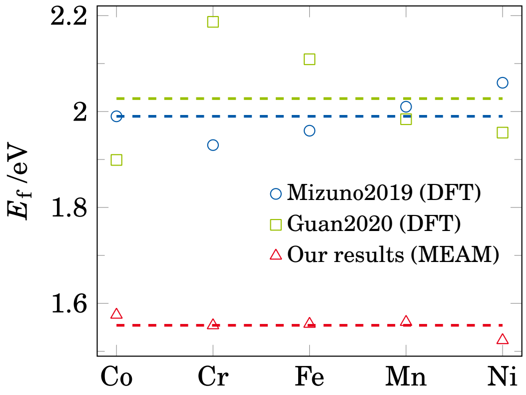

Figure 4.4: Comparison of the calculated vacancy formation energies as function of the removed element in the equimolar $(\text{CoCrFeMn})_{0.8}\text{Ni}_{0.2}$ HEA. Our results from Figure 4.2 are shown in comparison to the DFT calculations by Mizuno et al.[118] and Guan et al.[119] Symbols mark the elemental vacancy formation energies while dashed lines give the corresponding mean.

the total number of non-Ni atoms $N_\text{non-Ni}$ for different Ni concentrations. The data shows that once the percolation threshold is passed ($x_\text{Ni} > 0.8$) the fraction of isolated solute atoms rapidly increases.

Density functional theory (DFT) calculations of the vacancy formation energies are rare. They require the sampling of many vacancy sites and environments to obtain statistically relevant results. Figure 4.4 shows the DFT based vacancy formation energies calculated by Mizuno et al.[118] and Guan et al.[119] in comparison to the median vacancy formation energy we determined based on the Choi et al.[129] interatomic potential. DFT vacancy formation energies are not available for all subsystems of the Cantor alloy calculated above, but only for the five component equimolar CoCrFeMnNi Cantor alloy. Here, it can be seen that the DFT calculations do not fulfill the expected conditions of constant vacancy formation energy independent of removed species.[113] This suggests that the number of sampled simulation cells or their size is not sufficient to avoid artifacts. Moreover, it can be seen that our calculations based on the interatomic potential predict vacancy formation energies about 0.4 eV lower than the DFT calculations.

4.1.1 The Defect Dipole Tensor

While we have shown here that the vacancy formation energy is independent of the removed atom, this does not have to be true for the vacancy formation enthalpy H_f. This enthalpy depends on the defect formation volume ΔV which could depend on the size of the removed atom. This effect has not been explored for HEAs so far, and it could lead to preferential vacancies being formed by one of the elemental *sublattices* in the alloy.

The defect dipole tensor G_{ij} can be used to describe the dependency of the vacancy formation energy on an applied pressure.[418,419] It is defined as,[420]

$$G_{ij} = \left(\frac{\partial \sigma_{ij}}{\partial n} \right)_{\varepsilon} \quad \rightarrow \quad G_{ij} = V \Delta \sigma_{ij}, \tag{4.4}$$

where σ_{ij} is the stress tensor resulting from the insertion of n defects under constant strain ε. If a single defect is inserted into the simulation cell and the energy is minimized at constant volume, G_{ij} can be calculated from this volume V and the pressure difference $\Delta\sigma_{ij}$ between the defect-free reference state and the defective cell containing a vacancy. The defect formation volume ΔV can subsequently be calculated as:[419]

$$\Delta V = \frac{1}{3} B \, \mathrm{Tr}(G_{ij}), \tag{4.5}$$

with B being the bulk modulus. From here one can see that positive diagonal components of G_{ij} describe defects which expand the lattice in that direction, while a negative sign indicates the opposite.

Figure 4.5 (a) shows G_{11} in the equimolar CoCrFeMnNi alloy as an example for the calculation results. The results are obtained directly from the vacancy formation energy data set shown in Figure 4.2. Opposite to the vacancy formation energy, the distributions for the diagonal elements of G_{ij} have different medians for each atom. Moreover, the distributions are much broader with a MAD of 1.19 eV. All off-diagonal components have median G_{ij} values of zero with narrow distributions (MAD $\approx$ 0.33 eV). This is in agreement with Freedman et al.[420] who report off-diagonal components of the defect dipole tensor for vacancy formation stem from local structural relaxations or reconstructions, which disappear after averaging over all possible reconstructions. The large data set we used here seems sufficient to average out these local effects. Figure 4.5 (b) shows the median of the defect dipole tensor $\widetilde{G}_{ij}$ for the three diagonal components for each element over the whole Ni concentration range. Removal of Ni or Co is less sensitive to applied pressure, while Mn is affected the most. This in good agreement with expectations from the interatomic potential used here, where Mn (130.3 pm) has the biggest Goldschmidt radius[421] in the FCC phase. Co (125.0 pm) and Ni (124.5 pm) on the other hand are the smallest species within the alloy. There are multiple crossover points (e.g., Co and Ni at $x_\mathrm{Ni} = 0.6$) at which the preferential vacancy forming element could change.

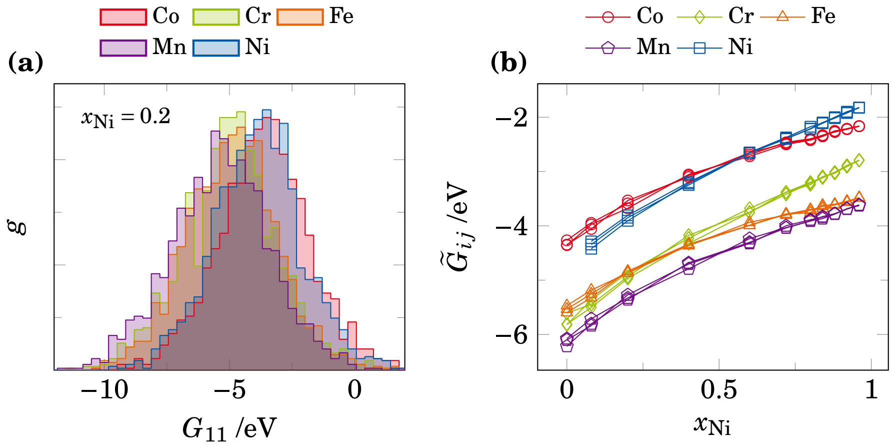

Figure 4.5: (a) Distribution g of the defect dipole tensor G_{11} for the equimolar Cantor alloy. The distributions for G_{22} and G_{33} are identical. (b) Median of the diagonal elements of the defect dipole tensor $\widetilde{G}_{ii}$ for each species at different Ni concentrations in the $(\mathrm{CoCrFeMn})_{1-x}\mathrm{Ni}_x$ HEA system. The off-diagonal elements G_{ij} are equal to 0.

To estimate the impact of G_{ij}, in the form of ΔV, on the vacancy formation enthalpy, we calculated the enthalpy change associated to a pressure p change of ±500 MPa based on the following equation,

$$H_{\mathrm{f}}(p) = E_{\mathrm{f}}(p = 0) + p\Delta V. \tag{4.6}$$

Even in this high-pressure environment the expected vacancy formation energy change is in the order of 15 meV and thereby negligibly small compared even to the effects of the width of the vacancy formation energy distribution shown in Figure 4.6.

4.1.2 Vacancy Concentration

The final step is the conversion from vacancy formation energy to vacancy concentration c_{Vac}. Two different approaches come to mind: Monte Carlo (MC) simulations in the grand-canonical ensemble[124] or analytical calculations based on the established thermodynamical models presented in Subsection 2.1.1. The three different models predict orders of magnitude different equilibrium vacancy concentrations, and we will compare their performance against MC simulations to assess which one is correct.

In the following, a short summary of the three models is presented and their main equations are rewritten using the symbols established in the previous section. Ruban[113] suggests that the configurational entropy in the HEA matrix leads to reduction of the vacancy concentration. They state that the vacancy concentration should be reduced by a factor of $1/N$ in an equimolar alloy with N

elements compared to a monoatomic metal with the same vacancy formation energy as shown in Equation 2.9,

$$c_{\mathrm{Vac,R}} = \frac{1}{N}\exp\left(\frac{S_\mathrm{f}}{k_\mathrm{B}}\right)\int g(E_\mathrm{f})\exp\left(\frac{-E_\mathrm{f}}{k_\mathrm{B}T}\right)dE_\mathrm{f}. \tag{4.7}$$

This has been disputed by Morgan and Zhang[126] who state the vacancy concentration remains independent of the configurational entropy of the host matrix and thereby the number of constituents in an alloy. Hence, the vacancy concentration for a monoatomic metal and a HEA with the same vacancy formation energy would be identical. This is reflected in the final equation derived by Morgan and Zhang.[126] Equation 2.16 once the distribution of vacancy formation energies is considered in the same way as in Equation 4.7 becomes,

$$c_{\mathrm{Vac,M}} = \exp\left(\frac{S_\mathrm{f}}{k_\mathrm{B}}\right)\int g(E_\mathrm{f})\exp\left(\frac{-E_\mathrm{f}}{k_\mathrm{B}T}\right)dE_\mathrm{f}. \tag{4.8}$$

Finally, Wang et al.[127] derive a prefactor of $\exp(N-1)/N$ for the vacancy concentration in an equimolar concentrated alloy containing N elements which increases the vacancy concentration compared to a pure metal. This factor grows fast and leads to an 11-fold increase of the vacancy concentration in a five component alloy compared to a monoatomic counterpart. They do not assume a distribution of vacancy formation energies in the HEA and instead simplify to a single average value $\Delta\overline{E}_\mathrm{f}$. Repeating Equation 2.23 from the literature review,

$$c_{\mathrm{Vac,\ W}} = \frac{\exp\left(N-1-\frac{\overline{E}_\mathrm{f}}{k_\mathrm{B}T}\right)}{N+\exp\left(N-1-\frac{\overline{E}_\mathrm{f}}{k_\mathrm{B}T}\right)}. \tag{4.9}$$

In a first step, we want to explore the effect of the vacancy formation energy distribution on the vacancy concentration under ideal circumstances. Here we investigate Equation 4.8 and neglect other entropy contributions by setting $S_\mathrm{f} = 0$. Additionally, we assume a Gaussian distribution of ΔE_Vac with different

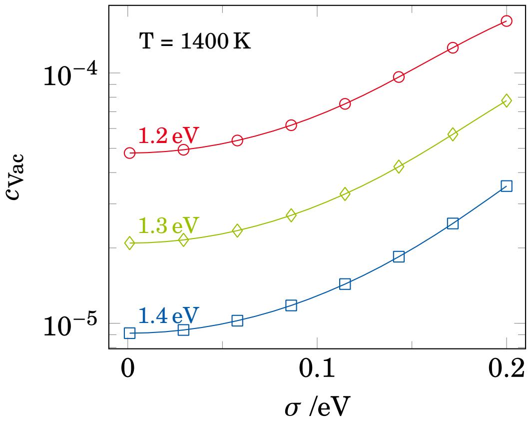

Figure 4.6: Vacancy concentration c_Vac for different mean vacancy formation energies (1.2 eV to 1.4 eV). The vacancy formation energy distribution is assumed to be Gaussian with different standard deviations σ and the resulting vacancy concentration is calculated from Equation 4.8 with the entropy prefactor set to 1 ($S_\mathrm{f} = 0$). Adapted from Ref. 411.

means μ and different widths (defined by the standard deviation σ). The temperature is kept constant at 1400 K. Figure 4.6 shows the effect of these different input parameters. The mean vacancy formation energy is varied between 1.2 eV and 1.4 eV, with standard deviations up to 0.2 eV. Both parameters have very clear implications for the resulting vacancy concentrations. While changes in μ lead to shifts in c_{Vac} by a constant factor, changes in σ lead to a smooth increase as broader distributions features a higher density of vacancy sites with a low formation energy. A change in σ of about 0.15 eV has a similar effect on the vacancy concentration as a reduction of μ by approximately 0.1 eV. Please keep this discussion in mind, as it will be revisited in Subsection 4.1.3.

Bond Counting Model

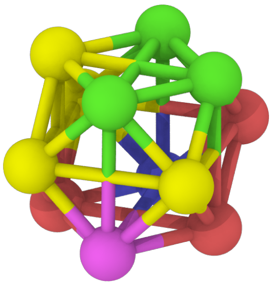

Figure 4.7: Local chemical environment around each vacancy that is included in the BC model. The nearest and next-nearest neighbor bonds are counted.

The main question, which method of vacancy concentration calculation is correct, hinges on the correct treatment of the configurational entropy of the host alloy and vacancy. This can be simulated best using MC simulations in the grand canonical ensemble. These do not require explicit knowledge of the configurational entropy of a system but instead sample it in a thermodynamically correct way. Unfortunately, the computational effort of using the full modified embedded atom method (MEAM) interatomic potential is prohibitive for this use case. As a solution, we decide to fit a simplified linear bond counting (BC) model. The model uses the first- and second-nearest neighbor bonds around a vacancy as descriptors for its formation energy. In more detail, the number of nearest ($N_{i\text{-}j,1}$) and second-nearest ($N_{i\text{-}j,2}$) i-j particles bonds between particles of type i and j around a vacancy are counted and used as descriptors. An example of such a chemical environment is shown in Figure 4.7. This is done for n different vacancies which are then used to fit the interaction parameters $\epsilon_{i\text{-}j,1}$ and $\epsilon_{i\text{-}j,2}$ for a given $(\text{CoCrFeMn})_{1-x}\text{Ni}_x$ sample to the vacancy formation energy. The interaction parameters are determined using the Moore-Penrose pseudoinverse[422] as implemented in NUMPY.[423,424] This formalism is encapsulated in the following equation:

$$\begin{bmatrix} N^1_{\text{Co-Co},1} & N^1_{\text{Co-Co},2} & N^1_{\text{Co-Cr},1} & \cdots & N^1_{\text{Ni-Ni},2} \\ N^2_{\text{Co-Co},1} & \ddots & & & \vdots \\ \vdots & & & \ddots & \vdots \\ N^n_{\text{Co-Co},1} & & \cdots & & N^n_{\text{Ni-Ni},2} \end{bmatrix} \begin{bmatrix} \epsilon_{\text{Co-Co},1} \\ \epsilon_{\text{Co-Co},2} \\ \epsilon_{\text{Co-Cr},1} \\ \vdots \\ \epsilon_{\text{Ni-Ni},2} \end{bmatrix} = \begin{bmatrix} E^1_{\text{f}} \\ E^2_{\text{f}} \\ \vdots \\ E^n_{\text{f}} \end{bmatrix}. \tag{4.10}$$

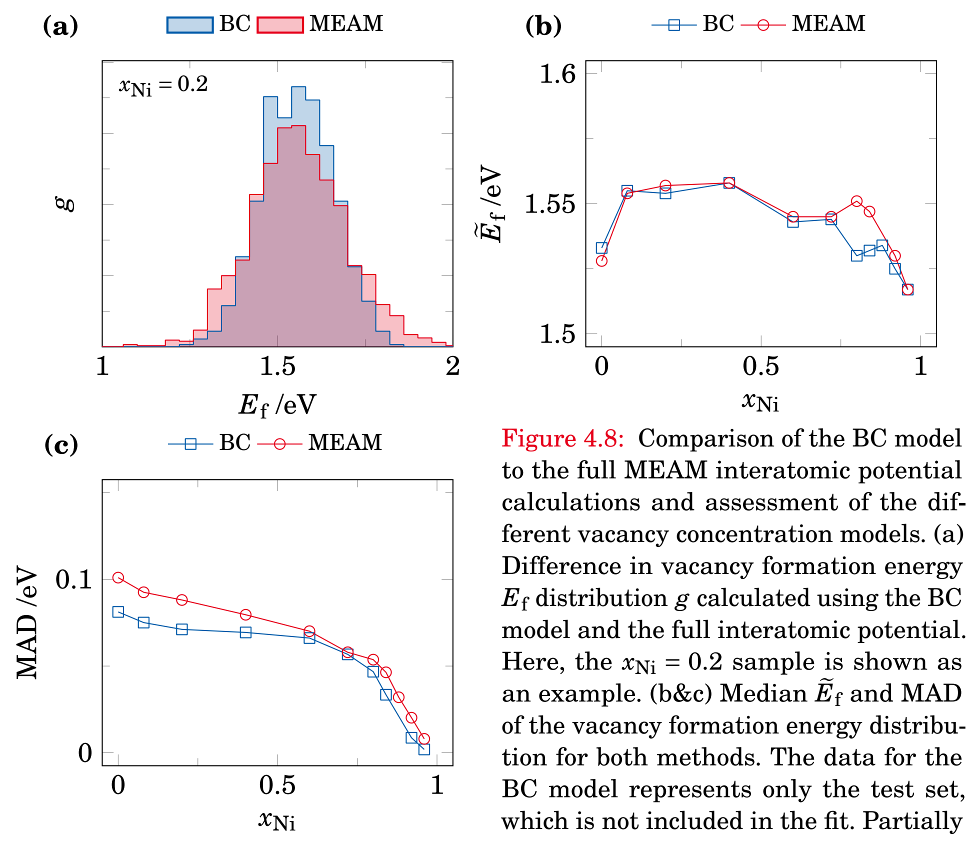

Figure 4.8: Comparison of the BC model to the full MEAM interatomic potential calculations and assessment of the different vacancy concentration models. (a) Difference in vacancy formation energy E_{f} distribution g calculated using the BC model and the full interatomic potential. Here, the $x_{\mathrm{Ni}} = 0.2$ sample is shown as an example. (b&c) Median $\widetilde{E}_{\mathrm{f}}$ and MAD of the vacancy formation energy distribution for both methods. The data for the BC model represents only the test set, which is not included in the fit. Partially adapted from Ref. 411.

For each $(\mathrm{CoCrFeMn})_{1-x}\mathrm{Ni}_x$ composition, the vacancy formation energy has already been calculated for 8000 different vacancy sites (1600 per species), as already shown in Figure 4.2. This data is then split into 80 % *training set*, used to fit $\epsilon_{i\text{-}j}$, and 20 % *test set* for validation.

Figure 4.8 (a-c) shows different characteristics of the BC model in comparison to the full MEAM interatomic potential calculations. Here the BC data shown is only obtained from the test set and thereby explicitly not included in the fit. In (a) an example for the vacancy formation energy distribution g for the equimolar Cantor alloy is given. The most obvious difference is that the BC model does not capture the full width of the distribution. This could be an indication that these vacancy energies are either associated to triplet or other longer-range configurations not captured by the model or that they have a low probability and hence the model is not sufficiently trained on these configurations. Figure 4.8 (b) presents a comparison of the median vacancy formation energy $\widetilde{E}_{\mathrm{f}}$ for all simulated Ni concentrations. This shows that there is a good agreement between BC model and full MEAM calculations. The MAD comparison shown in (c) reveals the systematic effect already seen in (a). The BC model underestimates the width of the vacancy formation energy distribution up to $x_{\mathrm{Ni}} = 0.72$, which is close to the transition from concentrated to dilute alloy at $x_{\mathrm{Ni}} \approx 0.8$ (see Figure 4.3). For the more dilute alloys, much better agreement is seen.

Monte Carlo Simulations

Now that the BC model is established and validated it can be used to set up Metropolis MC simulations in the grand-canonical ensemble.[124] During each MC trial step, a random lattice site is selected. If it is occupied, the BC model is used to determine the vacancy formation energy on this lattice site $E_{\mathrm{f},i}$ based on its chemical environment. The standard canonical Metropolis-MC acceptance probability,[321]

$$P = \min\left(1, \exp\left(\frac{-E_{\mathrm{f},i}}{k_{\mathrm{B}}T}\right)\right), \tag{4.11}$$

is used to decide whether the selected site is flipped to a vacancy. If the initial selection process picks an already vacant site, the original atom is always reinserted ($E_{\mathrm{f},i}$ always > 0). Reinsertion of the original atom was required to prevent drifts in sample composition, as the BC model was fit for each $(\mathrm{CoCrFeMn})_{1-x}\mathrm{Ni}_x$ composition separately. A set of ϵ_{ij} parameters is not transferrable across x_{Ni}. The equilibrium vacancy concentration is obtained after sufficiently long simulations. Note, that while this model does not perform atomic swaps, we did some test where we allowed for additional random site exchanges of the occupied lattice sites. This approach is technically only valid if the mixing enthalpy of the investigated HEA is sufficiently small to stabilize a random atomic arrangement at the sampling temperature. For the Cantor alloy system, this approximation is valid at the high temperatures considered in the following, where it forms a stable random solid solution.[28,29] Considering atom swaps,however, did not change the equilibrium vacancy concentration but substantially increased the number of swaps necessary converge c_{Vac}.

For each temperature between 1000 K and 1600 K 24 independent samples containing 4000 lattice sites were prepared and randomly filled with atoms in the desired $(\mathrm{CoCrFeMn})_{1-x}\mathrm{Ni}_x$ composition. These comparatively small cells were chosen to ensure that there is only one vacancy in the material at a given time as the BC model does not account for vacancy-vacancy interaction. For the lowest temperature of 1000 K 8×10^8 MC steps were required, while at higher temperatures 4×10^8 steps were sufficient. Figure 4.9 (a&b) shows the cumulative average vacancy concentration over the number of MC steps for different sample compositions at 1000 K and 1400 K, respectively.

Figure 4.9 (c) gives a comparison of the MC equilibrium vacancy concentration in the equimolar five component Cantor HEA for the three different thermodynamical models introduced in Subsection 2.1.1. Only the equation by Morgan and Zhang[126] can describe the correct vacancy concentration. For reference, their formalism corrects the derivation by Ruban[113] leading to an identical vacancy concentration for the HEA and a monoatomic metal with the same vacancy formation energy. Lastly, Figure 4.9 (d) shows the results

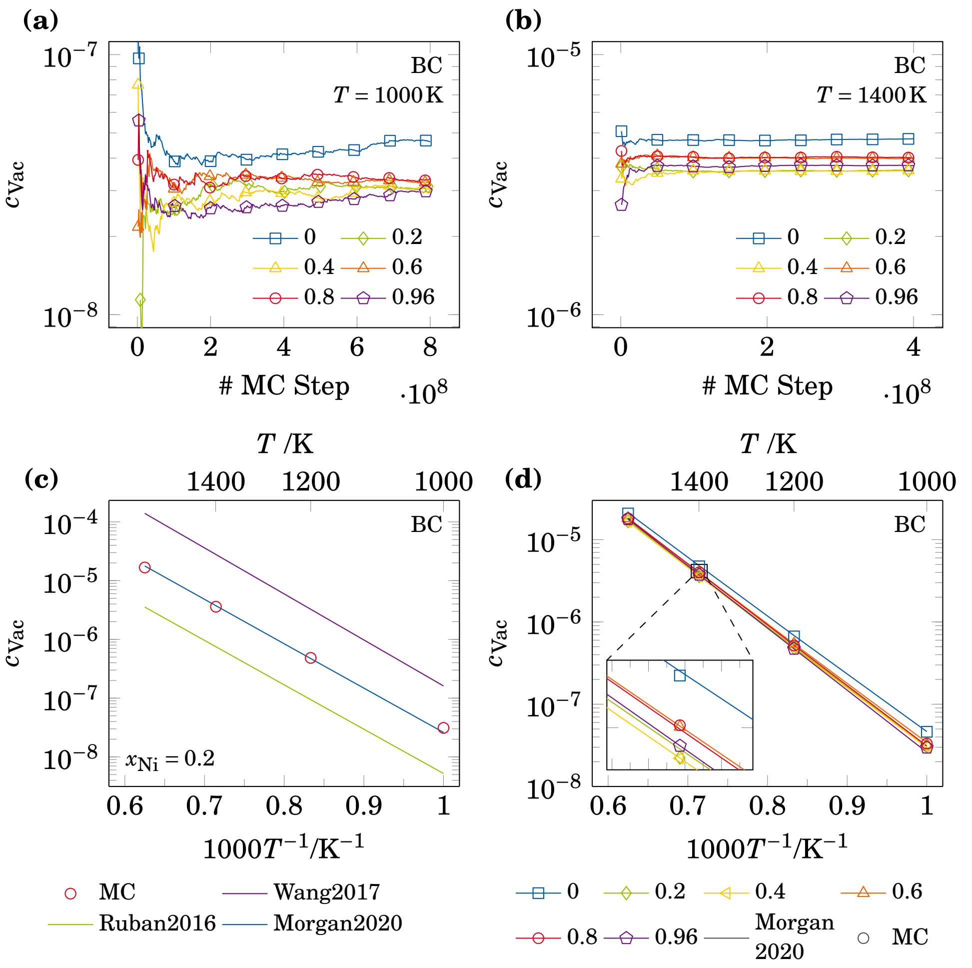

Figure 4.9: Assessment of the different vacancy concentration models. (a&b) Cumulative average vacancy concentration over the number of MC steps for different sample compositions at 1000 K and 1400 K. Only a subset of plot marks is added for clarity. All data is obtained based on the BC model. (c) Comparison of the vacancy concentration obtained from different calculation methods to our MC simulations; Wang2017 Equation 4.9,[127] Morgan2020 Equation 4.8,[126] and Ruban2016 Equation 4.7.[113] (d) Vacancy concentration calculated from equation by Morgan and Zhang[126] (Morgan2020, line) in comparison to the MC calculations (symbols). The inset shows a magnification of $T = 1400\,\mathrm{K}$. Partially adapted from Ref. 411.

of our MC simulations for different temperatures and sample compositions. Symbols correspond the MC vacancy concentrations at different temperatures, while the solid line represents the vacancy concentration calculated from the aforementioned equation by Morgan and Zhang,[126] Equation 4.8, neglecting S_{f} terms as they are omitted in the lattice MC calculations as well. Here, the vacancy formation energy distribution of the training set was used as input into the equation, as it resembles the input of the MC simulations more closely. The inset shows a magnification of the 1400 K results where one can see the almost perfect agreement between MC simulation and direct calculation for all Ni concentrations. In conclusion, it can be seen that the effect of temperature leads to a much greater variation in vacancy concentration compared to the compositional changes in $(\mathrm{CoCrFeMn})_{1-x}\mathrm{Ni}_x$ alloy system.

While omitting S_f might lead to a constant offset shifting the vacancy concentration, we do not expect substantial changes within the Ni series. Since the lattice vibrational entropy of vacancy formation is almost constant for many pure metals[425] and concentration independent for binary alloys.[426,427] The available literature data for the vibrational entropy in concentrated ternary to quinary alloys is sparse. Aziziha and Akbarshahi,[428] however, have calculated it for defect-free CoFeNi, CoCrFeNi, and CoCrFeMnNi and found the differences in the vibrational entropy of the matrix to be between $8\,k_\mathrm{B}$ and $8.4\,k_\mathrm{B}$. The concentration dependence going away from the equimolar alloys appears to be small; Ranging from $6.5\,k_\mathrm{B}$ at the edge of the phase diagram to $8.4\,k_\mathrm{B}$, with most concentrations showing a vibrational entropy greater than $7.5\,k_\mathrm{B}$. While magnetic entropy contributions have the smallest effect on the vacancy formation energy and are only relevant above 80 % of the melting temperature.[429] Therefore, this approximation should not influence the trends seen in the Ni-concentration dependent vacancy concentration.

4.1.3 Role of the vacancy formation energy distribution

The previous MC analysis has confirmed that Equation 4.8, by Morgan and Zhang,[126] correctly describes the equilibrium vacancy concentration. To conclude the investigation of the vacancy concentration we would like to revisit the parameter study of Figure 4.6 and further elucidate the role of the vacancy formation energy distribution width.

We again calculate the vacancy formation energy under the assumptions of $S_\mathrm{f} = 0$ and a Gaussian distribution of E_f with a mean value μ and a standard deviation σ. Figure 4.10 (a) shows the resulting vacancy concentrations at a temperature of 1000 K for different sets of μ and σ. Here, it can be seen that different input parameters can lead to the same equilibrium vacancy concentration as indicated by dashed lines. These show that $\mu = 1.2\,\mathrm{eV}$, $\sigma = 0\,\mathrm{eV}$ and $\mu = 1.4\,\mathrm{eV}$, $\sigma = 0.186\,\mathrm{eV}$ result in vacancy concentrations of $\approx 1 \times 10^{-6}$.

Given this initial observation one might be tempted to derive an *apparent* vacancy formation energy, a single value that replaces the vacancy formation energy distribution and results in the same vacancy concentrations. This can be seen in Figure 4.10 (b) which gives an Arrhenius plot for different sets of μ and σ. Symbols show the calculated values based on Equation 4.8 while solid lines give the best fit based on the Arrhenius equation,

$$\ln c_\mathrm{Vac} = -\frac{E_\mathrm{f}}{k_\mathrm{B} T} + c_\mathrm{Vac}^\infty, \tag{4.12}$$

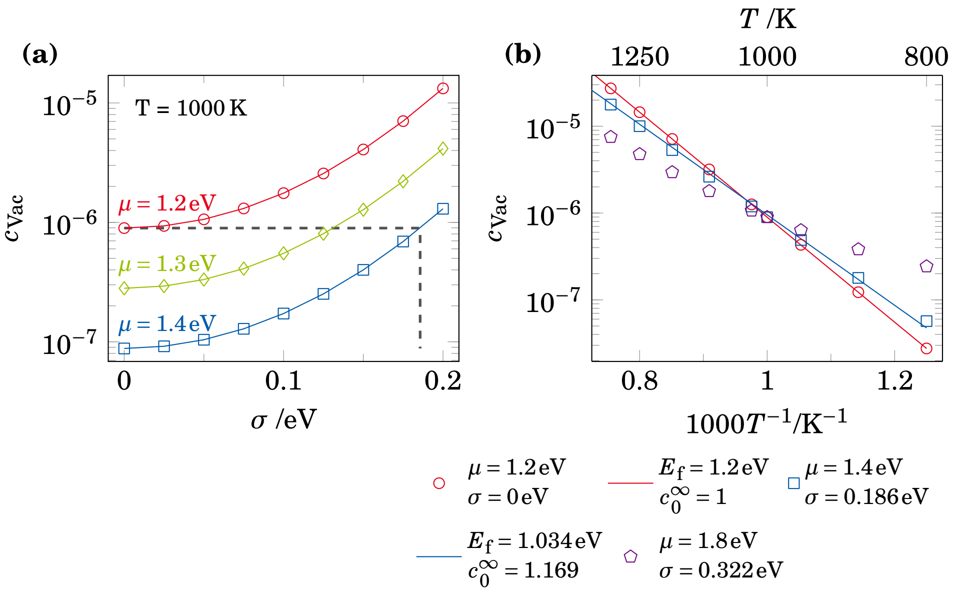

Figure 4.10: (a) Equilibrium vacancy concentration c_{Vac} as function of the vacancy formation energy distribution. The distribution is taken as a Gaussian with different means μ (1.2 eV to 1.4 eV) and standard deviations σ. The vacancy concentration is determined from Equation 4.8 with $S_{\mathrm{f}} = 0$. Different combinations of μ and σ lead to the same vacancy concentration (dashed lines). (b) Arrhenius plot of the vacancy concentration calculated for selected combinations of μ and σ. Different input parameters (symbols) can lead to the same vacancy concentration at 1000 K. Solid lines give the best fit based on Equation 4.12. They do, however, diverge for other temperatures. A wider vacancy formation energy distributions leads to a deviation from the ideal Arrhenius behavior. Adapted from Ref. 411.

where $c_{\mathrm{Vac}}^{\infty}$ is the vacancy concentration at infinite temperature. As derived from Figure 4.10 (a), the vacancy concentrations of the two data sets ($\mu = 1.2\,\mathrm{eV}$, $\sigma = 0\,\mathrm{eV}$ and $\mu = 1.4\,\mathrm{eV}$, $\sigma = 0.186\,\mathrm{eV}$) intersect at $T = 1000\,\mathrm{K}$. At higher or lower temperatures, however, the equilibrium vacancy concentrations diverge. The Arrhenius fit of the $\mu = 1.2\,\mathrm{eV}$, $\sigma = 0\,\mathrm{eV}$ data yields an $E_{\mathrm{f}} = 1.2\,\mathrm{eV}$. Fitting the second data set, on the other hand, yields a vacancy formation energy of $E_{\mathrm{f}} = 1.034\,\mathrm{eV}$ which is substantially lower than the applied μ of 1.2 eV which this effective barrier was supposed to represent. The individual data points also reveal a slight deviation from the fit line, i.e., the ideal Arrhenius behavior.

To confirm that this non-Arrhenius behavior is caused by the finite vacancy formation energy distribution width we construct a new test case with $\mu = 1.8\,\mathrm{eV}$ and $\sigma = 0.332\,\mathrm{eV}$. These parameters again lead to an equilibrium vacancy concentration of $\approx 1 \times 10^{-6}$ at 1000 K. Comparing this new sample to the previous ones reveals a much stronger deviation from the linear Arrhenius behavior showing a visible change in slope at $T = 1000\,\mathrm{K}$

In conclusion, we find that even though are infinitely many combinations of mean and standard deviation resulting in the same vacancy concentration at a given temperature these parameter sets show diverging concentrations at all other temperatures. Therefore, the distribution of vacancy formation energies cannot be approximated by a scalar effective vacancy formation energy.

4.2 Vacancy Migration Energy

The next ingredient required to understand diffusion in HEAs, is the energy barrier associated to vacancy migration, i.e., a single vacancy jump. In this section we investigate this migration energy in a wide range of CoCrFeMnNi based alloys. It is well known that the vacancy migration energy E_{Mig} strongly depends on the local chemical environment.[118,121,122,129] In the following, we will use nudged elastic band (NEB) calculations[346–349] to determine E_{Mig} in a vast number of atomic environments in the $(\text{CoCrFeMn})_{1-x}\text{Ni}_x$ HEA family.

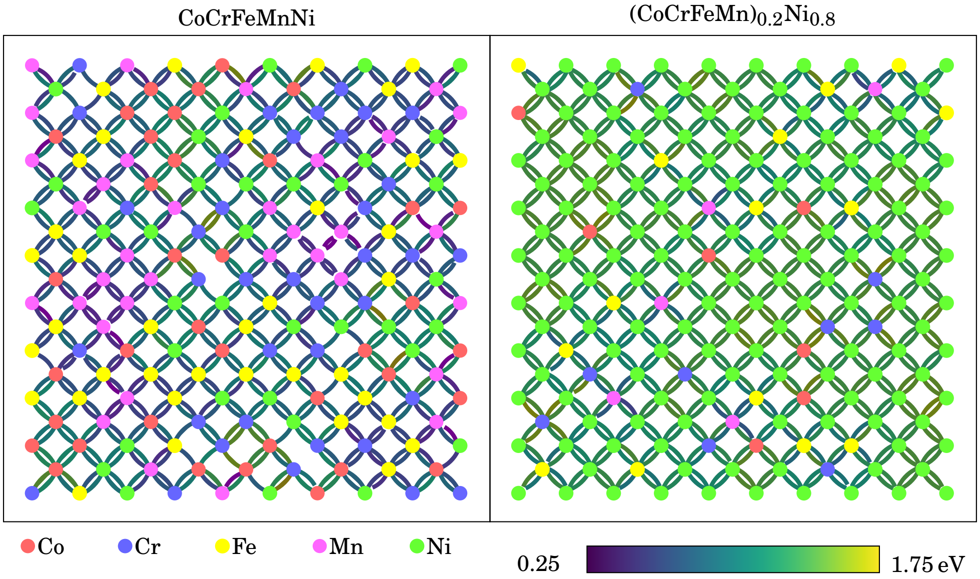

Figure 4.11: Vacancy migration barriers in the equimolar Cantor alloy and its Ni-rich $(\text{CoCrFeMn})_{0.2}\text{Ni}_{0.8}$ dilute counterpart. All nearest neighbor jumps in a [100] lattice plane are shown (unconverged calculations are omitted). Here, each lattice site is a color-coded circle denoting the species on that site, while colored lines give the migration energies for the site exchange if the neighboring site hosts a vacancy. The HEA shows a much wider spread in activation energies depending on the jumping atom and the local chemical environment. The more dilute $(\text{CoCrFeMn})_{0.2}\text{Ni}_{0.8}$ alloy has mostly homogeneous vacancy migration energies, variance can be seen for and around the solutes, which have a lower migration energy than Ni.

Figure 4.11 shows a single [1 0 0] lattice plane of the equimolar CoCrFeMnNi HEAs and the more dilute $(\mathrm{CoCrFeMn})_{0.2}\mathrm{Ni}_{0.8}$ alloy. The lattice sites are colored based on the occupying species and connecting lines denote the vacancy migration energy from one site to each adjacent one. All possible nearest neighbor jumps were calculated, missing lines correspond to unconverged calculations. When there are two differently colored lines connecting two sites, this does not mean that the forwards and backwards jump between two states has a different energy barrier (violating detailed balance). Instead, this means that an atom sitting on site A has different energy barrier jumping to a vacant position on site B compared to the atom sitting on B jumping into a vacancy on A. Looking at the equimolar HEA one can see that there is substantial variance in the energy required to move the vacancy. It scatters between 0.25 eV and 1.75 eV. The barriers itself are randomly distributed throughout the sample. In the $(\mathrm{CoCrFeMn})_{0.2}\mathrm{Ni}_{0.8}$ sample, the distribution of activation energies is much narrower and especially in the Ni-rich subvolumes, away from the solutes a fairly homogeneous energy landscape can be seen. As Ni atoms in a pure Ni matrix have the highest vacancy migration energy in this alloy system, a reduction in vacancy migration energy can be seen around each solute. While it might be easy to find a percolated, i.e., connected, low activation energy pathway through the concentrated HEA, migrating through the dilute alloy does not allow for such pathways. Therefore, one would expect diffusion to be reduced in the Ni-rich alloy compared to the concentrated HEA.

Sampling many more vacancy jumps in the different $(\mathrm{CoCrFeMn})_{1-x}\mathrm{Ni}_x$ subsystems reveals the vacancy migration energy distribution g as a function of the migrating atom. Figure 4.12 summarizes the results of the approximately 93 000 NEB calculations. In (a), the vacancy migration barrier distribution for different jumping elements in the alloy is shown. It can be seen that for the more concentrated HEA samples, $x_{\mathrm{Ni}} = 0.2$ and $x_{\mathrm{Ni}} = 0.6$, there is almost no change in the width of the individual distributions. Their mean values, on the other hand, are shifted towards higher migration energies as the Ni concentration is increased. For the most dilute sample with $x_{\mathrm{Ni}} = 0.96$ the distribution becomes very sharp with most values falling close the vacancy migration energy required for that species in pure Ni. Figure 4.12 (b&c) summarize the migration barrier distributions measured for all samples. The median migration energy barrier $\widetilde{E}_{\mathrm{Mig}}$ for each element at different Ni concentrations shown in (b). Open symbols denote results for different alloys, while the solid symbols correspond to the dilute limit, where an isolated solute atom exchanges site with an adjacent vacancy in a pure Ni matrix. The data shows that there is a linear dependency of $\widetilde{E}_{\mathrm{Mig}}$ on the Ni concentration. Note that the leftmost concentration on the graph ($x_{\mathrm{Ni}} = 0$) does not correspond to a monoatomic metal but to the four component CoCrFeMn HEA. Generally, the data shows that Fe and Mn migrate easiest through the alloy, while Co and Cr show higher vacancy migration energies. The slope for these four elements is very similar. Only Cr shows a stronger dependence of $\widetilde{E}_{\mathrm{Mig}}$ on x_{Ni}. Figure 4.12 (c) gives the corresponding

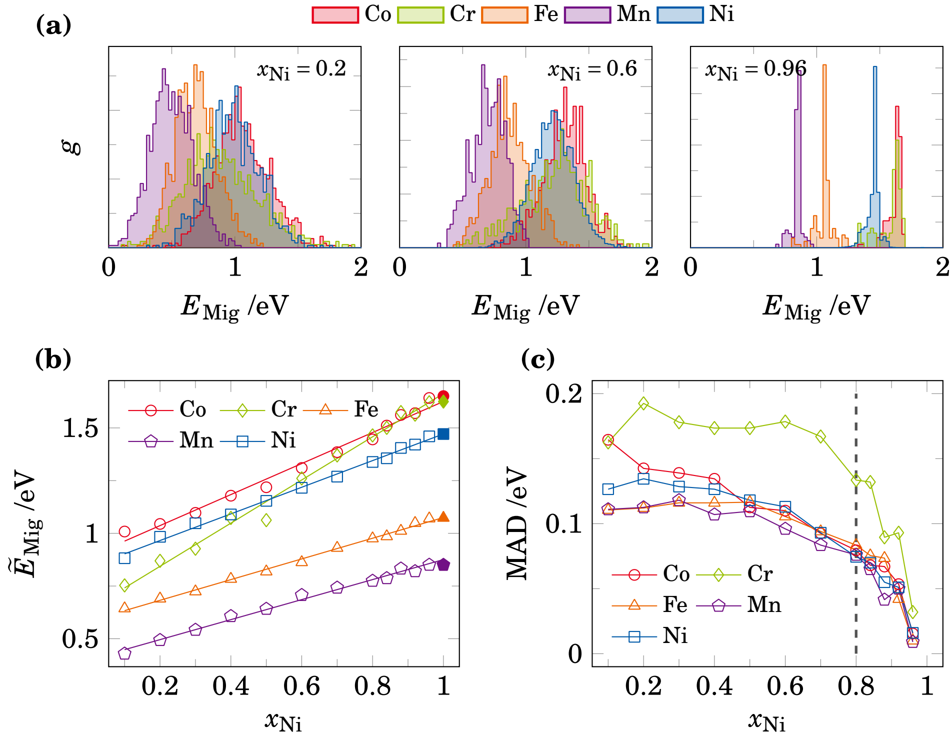

Figure 4.12: (a) Vacancy migration barrier distribution for different elements exchanging sites with a vacancy in different $(\mathrm{CoCrFeMn})_{1-x}\mathrm{Ni}_x$ HEAs. (b) Median of the vacancy migration energy distributions $\widetilde{E}_{\mathrm{Mig}}$ as a measure for the center of the distribution and MAD to characterize its width (c).[417] Different Ni concentrations from 4 component HEA ($x_{\mathrm{Ni}} = 0$), via the equimolar Cantor alloy ($x_{\mathrm{Ni}} = 0.2$) towards dilute Ni alloys ($x_{\mathrm{Ni}} \geq 0.8$) are shown. Open symbols correspond to different alloy samples, solid symbols mark the most dilute case of a single solute migrating through a pure Ni matrix. A dashed line indicates the percolation threshold of the FCC lattice[415] as transition point from concentrated to dilute alloy. Partially adapted from Ref. 412.

MAD[417] based on the calculated vacancy migration energy distributions. Here, the transition from a concentrated solid solution to a dilute Ni alloy becomes apparent. The MAD remains almost constant, indicating a constant width of the distribution up to the FCC percolation threshold of $x_{\mathrm{Ni}} \approx 0.8$, after which it rapidly decreases towards 0. This transition from concentrated HEA to dilute alloy can be attributed to the physical separation of the randomly distributed non-Ni atoms as the global Ni concentration increases, once the percolation threshold of the FCC lattice[415] is passed. This effect has already been discussed for the vacancy formation energies and their distribution in Section 4.1 (cf. Figure 4.3).

Figure 4.13 shows a graphical comparison of our vacancy migration energy barriers for the five component Cantor alloy to the two other published

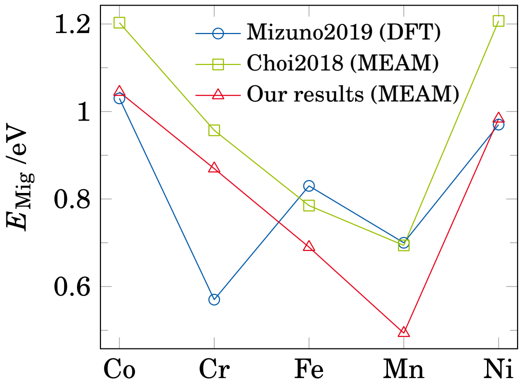

Figure 4.13: Comparison of the calculated vacancy migration barrier as function of the migrating species in the equimolar $(\mathrm{CoCrFeMn})_{0.8}\mathrm{Ni}_{0.2}$ HEA. Our results from Figure 4.12 are shown in comparison to the DFT calculations by Mizuno et al.[118] and the classical calculations by Choi et al.[129]

simulation results. Similar to Choi et al.,[129] in their original reference of the interatomic potential we employed here, we find a distribution of vacancy migration barriers in the equimolar Cantor alloy. Our calculated vacancy migration barrier distribution and elemental hierarchy are in good agreement with the original publication. Curiously, the average migration energy we find is about 0.2 eV lower for all elements. This discrepancy can most likely be attributed to the fact that Choi et al.[129] did not perform proper NEB calculations to determine the migration energy barrier but instead moved the vacancy in a straight line from one lattice site to another without structural relaxation of the intermediate states. Additionally, they calculated only 390 different vacancy jumps, which is orders of magnitude lower than the number of samples calculated here. Comparison to the DFT calculations by Mizuno et al.[118] shows a different hierarchy of elements. They find the migration energy to be lowest in Cr, followed by Mn while we find the reverse order for these two species. Due to the inherent size limitations of DFT calculations they calculated the migration barriers in special quasi-random structures,[430] where the atomic arrangement is optimized to reduce short-range order (SRO) effects in small simulation cells containing only 125 atoms. Therefore, these cells lack the more interesting atomic environments containing an excess of one species. We conjecture that these rare structures are impactful on the tails of the migration energy distribution. Moreover, they were only able to calculate 30 different vacancy jumps which appears to be insufficient to converge the distribution.

4.3 Correlation Factors in High-Entropy Alloys

Reference correlation factors based on the conventional random alloy model used for validation were provided by Josua Kottke (WWU Münster).

Going back to Section 4.2 the main assumption of the random alloy model used to determine the correlation factors in concentrated alloy is immediately challenged. There is not a single vacancy migration energy barrier for each migrating species resulting in a single jump frequency.[131,132] Instead, there is a

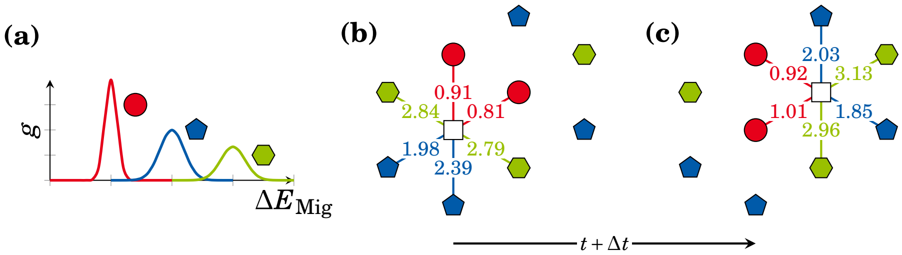

Figure 4.14: Schematic description of the variable-barrier KMC algorithm. (a) Example of the vacancy migration energy distributions for the vacancy exchange with three different atomic species. Each atom type has a different mean and standard deviation. (b) During a KMC step, each atom adjacent to the vacancy (white square) gets assigned a vacancy migration energy based on its species' energy distribution. (b → c) One jump event is randomly selected based on the KMC formalism. This event is carried out and the clock is advanced by Δt. (c) The vacancy is in a new position, new migration energies are drawn from the distribution, and the next KMC step is prepared. The numbers next to each bond correspond to the vacancy migration barrier assigned to a specific jump event during the current KMC step. Adapted from Ref. 412.

broad distribution of migration energies. An effect neglected by established literature so far.[145,150] To investigate the error introduced by this assumption, we calculate the tracer correlation factor using a single average vacancy migration energy in comparison to correlation factors obtained taking the full migration energy distribution into account.

To this end, we develop a novel simulation code based on the rejection-free KMC algorithm.[355] This code can take the variable energy barrier observed in HEAs into account. Instead of the assumption that each atomic species has a constant vacancy migration energy and hence a constant rate, the vacancy migration energies are approximated by a Gaussian distribution with means and standard deviations that depend not only on the jumping atom but also on the sample composition (cf. Figure 4.12). In the following, this approach will also be called *variable-barrier* KMC. Each variable-barrier KMC step consists of the following operations, which are also schematically illustrated in Figure 4.14,

I. For each neighbor around the vacancy a migration energy $E_{\mathrm{Mig},i}$ is drawn from its respective energy distribution.

II. Based on this energy, the rate for each neighbor swapping position with the vacancy Γ_i and the total rate Γ_{tot} is calculated as,

$$\Gamma_i = \nu_0 \exp\left(\frac{-E_{\mathrm{Mig},i}}{k_{\mathrm{B}}T}\right) \quad \text{and} \quad \Gamma_{\mathrm{tot}} = \sum_i \Gamma_i, \tag{4.13}$$

where the attempt frequency ν_0 is set to $1 \times 10^{13}\,\mathrm{s}^{-1}$.[322,431]

III. Continue at step III. of the conventional KMC algorithm outlined in Section 3.5.

Figure 4.15: Validation of the variable-barrier KMC code (*Short* and *Long*) against a reference (*Ref.*) implementation of the random alloy model. All simulations assume constant, i.e., no energy barrier distribution, jump rates of: $\Gamma_A = 10^5$, $\Gamma_B = \Gamma_C = 100$, and $\Gamma_D = \Gamma_E = 1$. *Short* corresponds to 1×10^6, *Long* to 1×10^8 simulation steps, while the reference (*Ref.*) simulation ran for 1×10^{12} steps. Adapted from Ref. 412.

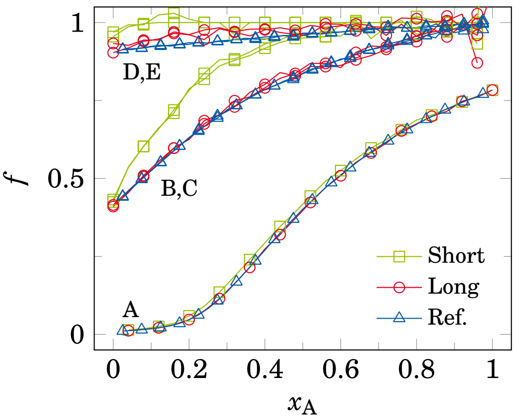

Note that this modeling approach does not account for the migration energies specific to a given chemical environment. Instead, the statistical distribution is taken as input. Therefore, detailed balance is not fulfilled for each individual atomic jump. Even the example in Figure 4.14 shows that the vacancy jump and its reversal do not share the same energy barrier. Over the long atomic trajectories studied here, this effect should average out, as the migration energy per atomic species are still drawn for the corresponding energy distribution. Moreover, as stated by Frenkel and Smit,[321] detailed balance is not strictly required to perform correct MC sampling. These KMC calculations give trajectories for each atom in the sample which can then be post-processed to calculate the correlation factor f,[130,137]

$$f = \frac{\sum_i R_i^2}{\sum_i n_i \lambda^2}, \tag{4.14}$$

here R_i is the displacement, n_i is the number of atomic jumps for each atom i, and λ is the length of a diffusional jump. This calculation treats each atom in the simulation as a tracer atom one would track in an experiment.

First, we performed validation of the variable-barrier KMC implementation against the random alloy model implementation of J. Kottke at WWU Münster. The simulations selected for comparison are on a five-component model system with quasi-binary composition $A_x(BCDE)_{1-x}$ and constant jump rates of $\Gamma_A = 10^5$, $\Gamma_B = \Gamma_C = 100$, and $\Gamma_D = \Gamma_E = 1$. For purpose of comparison, the standard deviation of the variable-barrier code was set to 1×10^{-8} to ensure constant rates, i.e., switch off the energy distribution feature. Figure 4.15 shows the calculated correlation factors after 1×10^6 (*Short*) and 1×10^8 (*Long*) simulation steps in comparison to the reference implementation after 1×10^{12} (*Ref.*) steps. The data reveals that convergence can only be achieved for the longer simulation runs. Therefore, all future calculations are run for 1×10^8 steps. The correlation factor for a monoatomic ($x_A = 1$) FCC lattice should be equal to 0.78146[432] a condition which is fulfilled by all three simulations.

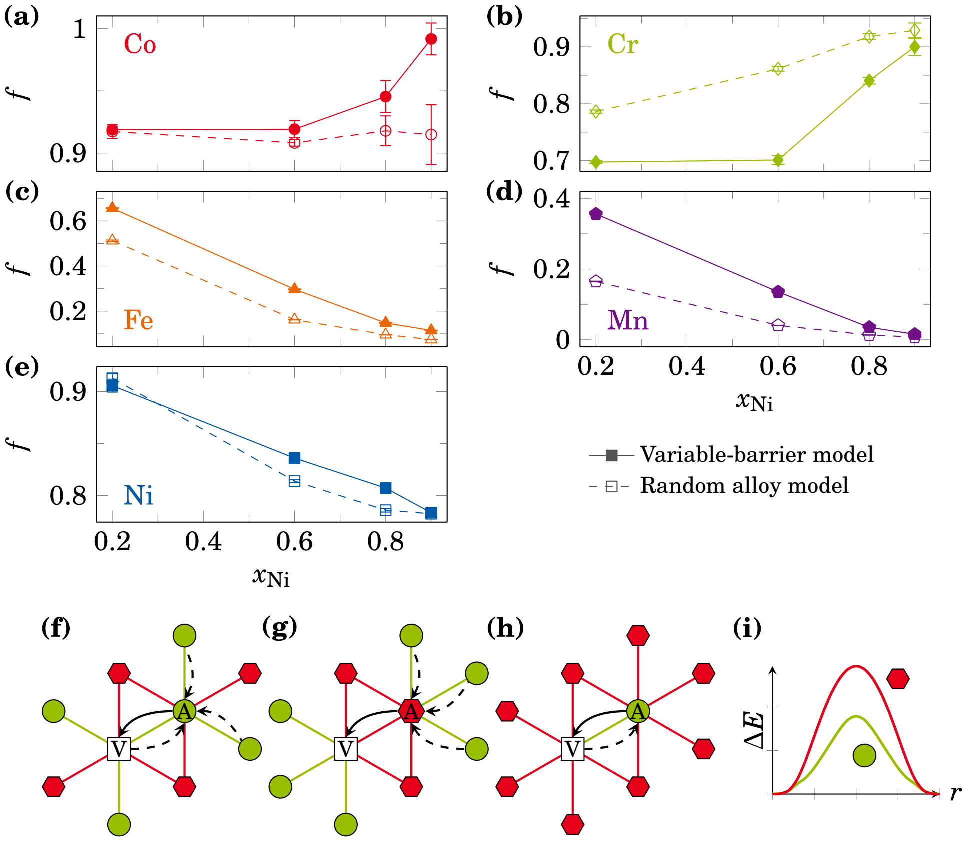

Figure 4.16: (a-e) Correlation factor f for each element in the $(\mathrm{CoCrFeMn})_{1-x}\mathrm{Ni}_x$ HEA system. Note the different intervals on the y-axis. Open symbols denote results from the conventional random alloy model, while filled symbols correspond to calculations based on the variable migration energy barrier KMC model. (f-h) Schematic overview for a system containing different concentrations of low- and high migration energy barriers (i). A solid black arrow shows the first jump, dashed arrows indicate likely secondary jumps. There are fewer correlations in the concentrated alloy (f&g), as there are multiple low energy jumps available for the vacancy from any given position. (h) In the dilute alloy, on the other hand, any jumping atom with a low activation energy barrier has a high probability of frequent back and forth jumps as it is surrounded by energetically unfavorable jumps. This leads to a much higher correlation. Adapted from Ref. 412.

After this validation, we calculate the correlation factor using a Gaussian fit of the migration barrier distributions presented in Figure 4.12 as input parameters. The resulting correlation factors are compared to the case of a constant migration energy to judge the effect of a non-zero barrier distribution width. The resulting correlation factors are shown in Figure 4.16 (a-e) as a function of Ni concentration. Here it can be seen that the two elements with the lowest migration energy barriers (Fe and Mn) show very similar trends of decreasing correlation factors as their respective concentration decreases. This effect stems from the effect that these two species can trap the vacancy into repeated forwards and backwards jumps if there are no other low energy escape paths. This effect is schematically illustrated in (f-h). For Cr, where the change in migration barrier width as the alloy transitioned from concentrated to dilute alloy was most pronounced, a strong change in f can be seen around the transition Ni-concentration. As it features the highest migration energy barrier, Co shows the smallest deviation from an ideal random walk, i.e., f close to 1. Lastly, the majority element Ni, shows a steady decrease in f from an almost ideal random walk in the HEA ($f \approx 1$) towards 0.78146, which is the expected value for a monoatomic FCC material.[432]

Comparing the differences between the variable-barrier model introduced before and the conventional random alloy model reveals most substantial differences for the fast diffusion atoms (Mn) or elements which feature a broad migration energy distribution (Cr). Slow diffusing elements with high migration energy barriers (Co or Ni) show only small differences between both methods.

Concluding, it can be seen that correlations not only introduce substantial differences between the individual constituents of the Cantor alloy, but also give rise to an additional concentration dependence. Moreover, including the vacancy migration energy barrier distribution leads to significant differences in f especially for fast diffusers and elements with a large distribution width.

4.4 Tracer Diffusion Experiments

Sample preparation, experimental measurements, and their interpretation was performed by Josua Kottke (WWU Münster).

This section will briefly outline the experimental tracer diffusion studies which form the basis of the experiment-simulation comparison shown in Section 4.5. $(\mathrm{CoCrFeMn})_{0.4}\mathrm{Ni}_{0.6}$ and $(\mathrm{CoCrFeMn})_{0.08}\mathrm{Ni}_{0.92}$ were cast and homogenized at 1373 K for 13 h. After quenching chemical homogeneity and single phase FCC structure was verified using energy dispersive X-ray spectroscopy and X-ray diffraction. Subsequently, $^{51}\mathrm{Cr}$, $^{57}\mathrm{Co}$, $^{59}\mathrm{Fe}$, and $^{54}\mathrm{Mn}$ γ-isotopes and $^{63}\mathrm{Ni}$ β-isotopes were applied to the surface. Afterwards, the samples were diffusion annealed at temperatures between 1123 K and 1273 K for 16 h to 288 h and the relative specific activity A as function of diffusion depth h into the sample was measured. The resulting profile can be fit according to the *instantaneous source* solution,[43]

$$A = \frac{M}{\sqrt{4\pi D^* t}} \exp\left(\frac{-h^2}{4D^* t}\right), \tag{4.15}$$

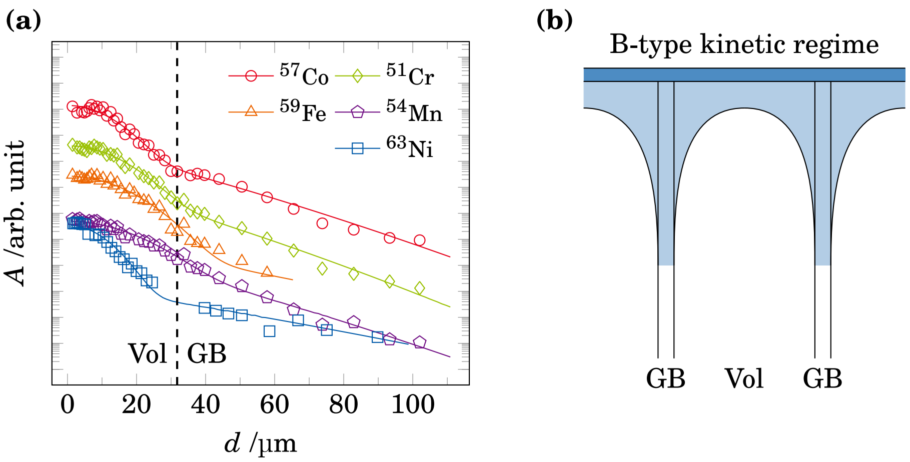

Figure 4.17: (a) Measured specific activity A over diffusion depth in the $(CoCrFeMn)_{0.4}Ni_{0.6}$ sample after annealing at 1123 K for 288 h. The data for the different tracer isotopes is offset for better readability. Marks give the individual measurements and solid lines correspond to the mathematical solution of the combined volume (Vol) and GB diffusion problem.[434] (b) Schematic representation of the B-type kinetic regime. The darker layer on top is the applied tracer source, while lightly shaded areas correspond to material into which the tracer atoms have diffused. Partially adapted from Ref. 412.

where M is the initial amount of tracer isotope and t is the annealing time. If there is still an excess amount of tracer isotope on the sample's surface after diffusion annealing, the *constant source* solution has to be used instead,[43]

$$A = A_0 \mathrm{erfc}\left(\frac{h}{4D^*t}\right). \tag{4.16}$$

Even though, we are interested in bulk diffusion and bulk diffusivities the experimental measurements contain additional grain boundary (GB) diffusion contributions. These make up the greater diffusion depths as GB diffusion is enhanced compared to the bulk.[43,149] Here, the exact solutions for the *instantaneous source* in the B-type kinetic regime has to be used[433,434]. A schematic representation of the B-type kinetic regime can be seen in Figure 4.17 (b). Here a slice through the material's surface is shown. The dark layer on top corresponds to the applied tracer element. Lightly shaded areas indicate how these atoms have diffused into the material. In this regime GB diffusion is faster than bulk diffusion, therefore tracer atoms have migrated further into the bulk along the boundaries. Hence, GBs start to act as a tracer source themselves if their tracer element concentration is increased compared to the surrounding volume. An example of such a diffusion profile can be seen in Figure 4.17 (a). Here the measured activity (symbols) for the $(CoCrFeMn)_{0.4}Ni_{0.6}$ sample after annealing at 1123 K for 288 h is shown. The different tracer elements are offset along the ordinate. Solid lines give the result for the best fit based on the combined volume

(Vol) and GB diffusion problem[434] from which the volume tracer diffusion coefficient D_i^* can be obtained for each element i. Note, the GB diffusion coefficient could be obtained as well but is out of scope for this work.

Figure 4.18 shows the obtained diffusivities for each tracer element on an inverse homologous scale T_{Melt}/T. Data for different compositions of the $(\mathrm{CoCrFeMn})_{1-x}\mathrm{Ni}_x$ alloy are shown. The data for $x = 0.6$ and $x = 0.92$ was measured specifically for the publication this chapter is based on (Ref. 412) and it is augmented by previous measurements of Kottke et al.[195] and Vaidya et al.[149,191] Additional comparison to diffusion in a pure Ni matrix is shown as well ($x = 1$). Experimental data is fit based on the Arrhenius relation,[440]

$$D_i^* = D_{i,0}^* \exp\left(\frac{-Q}{k_{\mathrm{B}}T}\right), \tag{4.17}$$

and the pre-exponential factor $D_{i,0}^*$ and the activation enthalpy for tracer diffusion Q is extracted. Comparing the different measurements, very similar trend can be seen for all tracer species. The diffusivity of each tracer element increases as the global Ni concentration in the sample increases from the equimolar HEA to the Ni-rich $x = 0.92$ dilute alloy sample. Curiously, comparing the diffusion of each element in a pure Ni matrix (corresponding to the dilute limit) reveals a reduced tracer diffusion rate leading to the following hierarchy of diffusivities in the different alloys: $(\mathrm{CoCrFeMn})_{0.08}\mathrm{Ni}_{0.92}$ > Ni > $(\mathrm{CoCrFeMn})_{0.4}\mathrm{Ni}_{0.6}$ > $(\mathrm{CoCrFeMn})_{0.8}\mathrm{Ni}_{0.2}$.

4.5 Comparison to Experimental Diffusion Measurements

Sample preparation, experimental measurements, and their interpretation was performed by Josua Kottke (WWU Münster).

In a last step, the experimentally measured diffusivities can be compared to our atomistic computer simulations. The most straight-forward way is to compare tracer diffusivities, directly. The atomic trajectories obtained from the KMC simulations allow direct calculation of D_i^* following,[321]

$$\langle R_i^2 \rangle = \frac{1}{6} D_i^* t \quad \to \quad D_i^* = 6 \frac{c_{\mathrm{Vac}}(T)}{c_{\mathrm{Vac,KMC}}} \frac{\langle R_i^2 \rangle}{t}, \tag{4.18}$$

where t is the time and $\langle R_i^2 \rangle$ is the mean squared displacement of species i. The additional factor, rescaling the simulation vacancy concentration to the experimental vacancy concentration, needs to be introduced as the KMC simulations are run with constant vacancy concentration. Here the KMC simulations were run with $c_{\mathrm{Vac,KMC}} = 1/32\,000 = 3.125 \times 10^{-5}$, corresponding to one vacancy per simulation cell, which is different from the true vacancy concentration $c_{\mathrm{Vac}}(T)$ at a given temperature T (cf. Subsection 4.1.2).

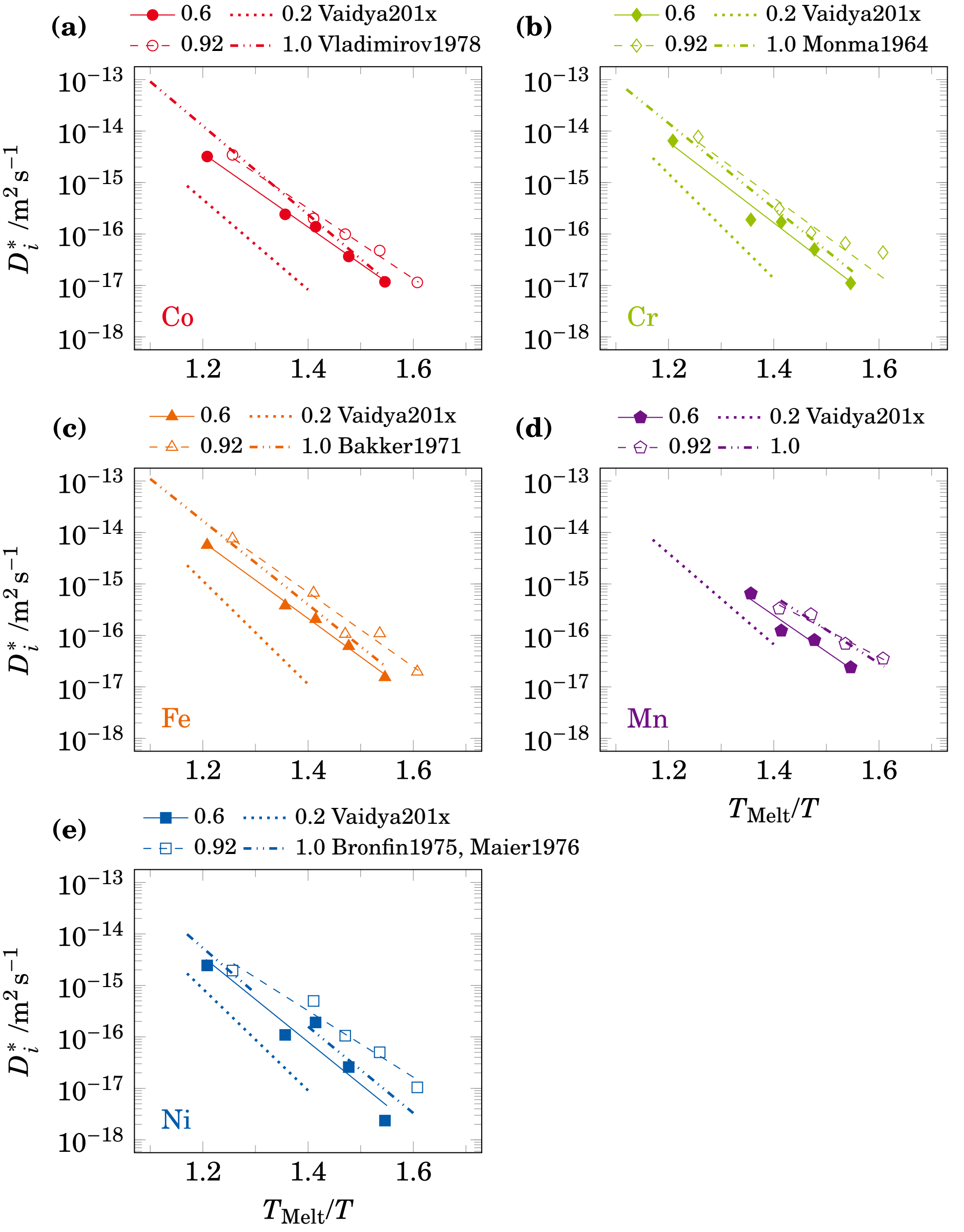

Figure 4.18: Arrhenius plot of the measured volume tracer diffusivities D_i^* normalized by the melting temperature T_{Melt}. Different alloys in the $(\mathrm{CoCrFeMn})_{1-x}\mathrm{Ni}_x$ were measured and the results are augmented with literature: Bakker1971[435], Bronfin1975[436], Kottke2019[195], Maier1976[437], Monma1964[438], Vaidya201x[149,191], Vladimirov1978[439]. Adapted from Ref. 412.

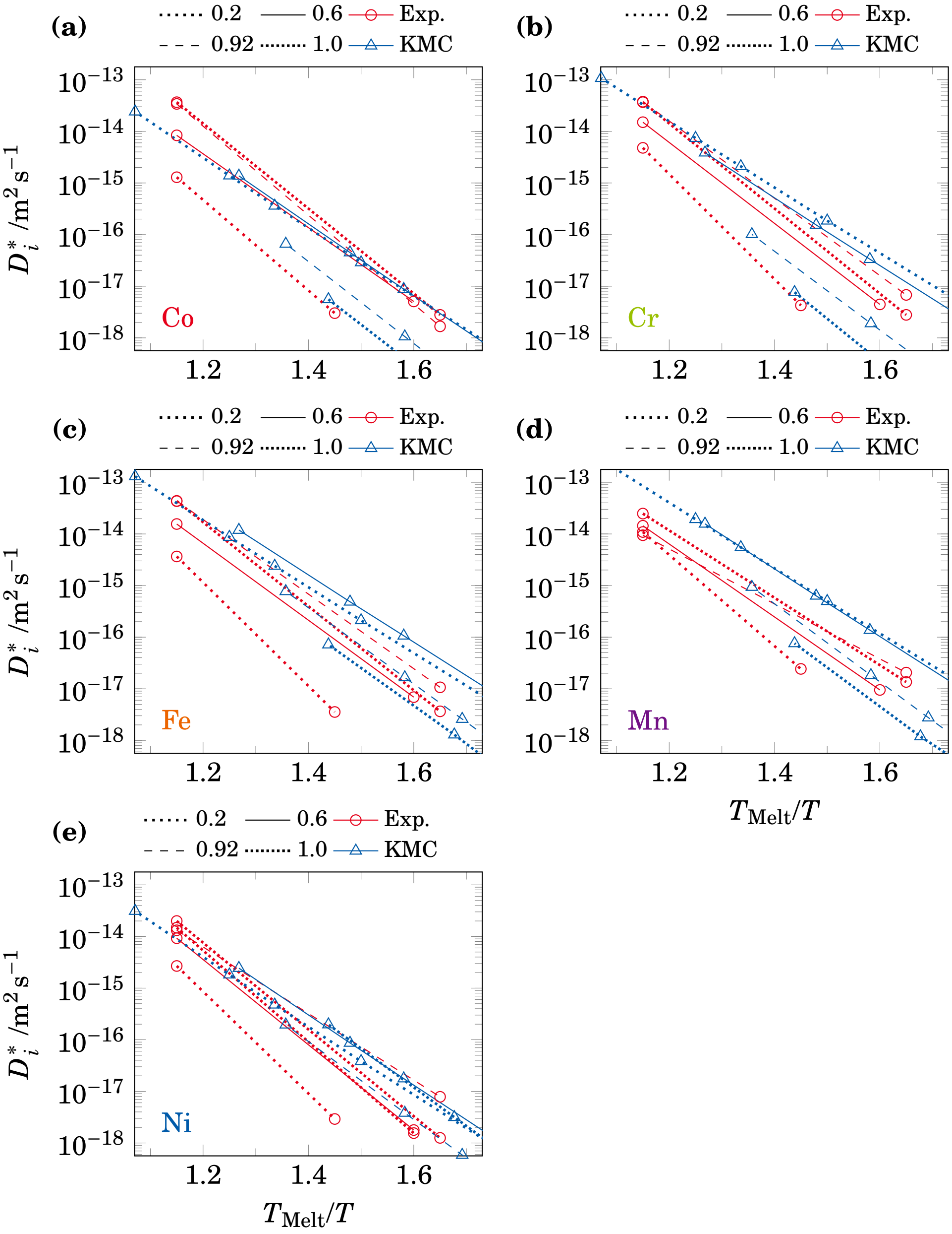

Figure 4.19: Experimentally measured tracer diffusivities (see Figure 4.18 for attribution) in the (CoCrFeMn)$_{1-x}$Ni$_x$ alloy compared to the diffusivities obtained from the variable-barrier KMC simulations (Equation 4.18). The simulation data is rescaled by the correct vacancy concentration. Partially adapted from Ref. 412.

Figure 4.19 includes the comparison of the tracer diffusivities obtained from mean squared displacements in the variable-barrier KMC simulations after rescaling with the correct vacancy concentrations. These true vacancy concentrations can be calculated from the model of Morgan and Zhang[126] and the vacancy formation energy distributions calculated previously. For more details see Subsection 4.1.2. Note, that all input parameters to the KMC simulations and the vacancy concentrations are determined based on the MEAM interatomic potential. These calculated tracer diffusivities are then compared to the experimental measurements. For comparison on the homologous temperature scale, the Ni-concentration dependent melting temperatures within the interatomic potential are calculated using standard melt-interface methodology.[375] It can be seen that the calculated diffusivities compare pretty well in magnitude for all species. But the experimental hierarchy of diffusion constants cannot be reproduced. Experimentally, the diffusivities increase from $x_{\mathrm{Ni}} = 0.2$ to $x_{\mathrm{Ni}} = 0.92$ and decrease again towards the dilute limit $x_{\mathrm{Ni}} \to 1$. The simulation results, on the other hand, predict a decreasing or constant diffusivity from $x_{\mathrm{Ni}} = 0.2$ to $x_{\mathrm{Ni}} \to 1$ for all elements except Ni. In Ni, the lowest diffusivity is calculated for $x_{\mathrm{Ni}} = 0.92$. A main problem for the direct comparison of experiments and simulations is whether the absolute vacancy formation and vacancy migration energies determined from the interatomic potential approximate their real values well. As already shown in Figure 4.13, vacancy migration energies within the interatomic potential for the CoCrFeMnNi alloy agree well with DFT calculations by Mizuno et al.[118] Vacancy formation energies, on the other hand, are systematically underestimated compared to DFT simulations (see Figure 4.4).[118,119]

In an attempt to cancel out some errors from the interatomic potential a renormalization is performed; Neglecting the vacancy migration entropy and its pressure dependence allows us to rewrite Equation 2.24 in terms of the energy of migration E_{Mig}, as already shown for the vacancy formation energies, this gives,

$$D_i^* = c_{\mathrm{Vac}} \lambda^2 \nu_{0,i} f_i \exp\left(\frac{-E_{\mathrm{Mig},i}}{k_{\mathrm{B}} T}\right), \tag{4.19}$$

where $\nu_{0,i}$ is the attempt frequency per species i while the vacancy concentration is constant within the sample and independent of the diffusing element. Note, that the migration energy $E_{\mathrm{Mig},i}$ depends on the migrating species. If one now normalizes the diffusivity of all species i by the diffusivity of Fe and assumes a constant attempt frequency the initial equation simplifies drastically,

$$\frac{D_i^*}{D_{\mathrm{Fe}}^*} = \frac{f_i}{f_{\mathrm{Fe}}} \exp\left(\frac{E_{\mathrm{Mig,Fe}} - E_{\mathrm{Mig},i}}{k_{\mathrm{B}} T}\right). \tag{4.20}$$

Not only does this cancel out errors in the interatomic potential for the vacancy formation energy, it also removes the dependence on the absolute values of E_{Mig}. The normalized diffusivities only depend on the differences of migration energies between Fe and element i which might be better represented within the interatomic potential.

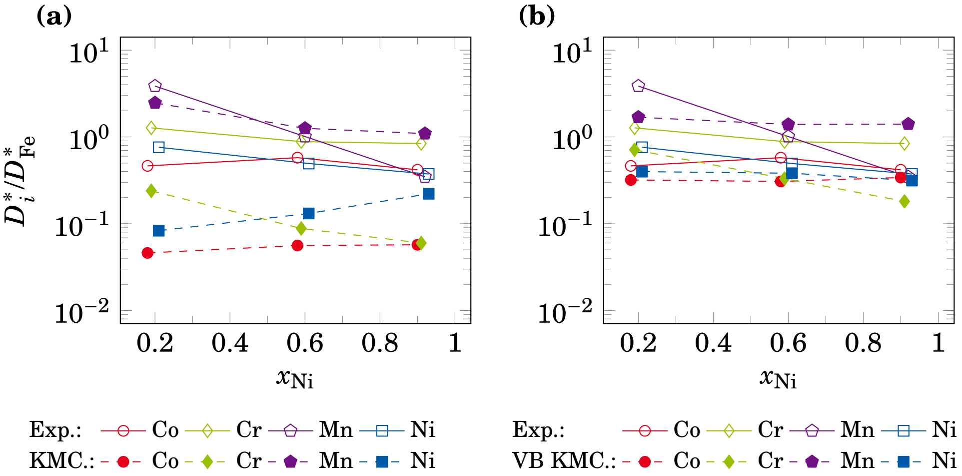

Figure 4.20: Comparison of the normalized tracer diffusivities (Equation 4.20) between experiments (Exp.) and KMC simulations. (a) Normalized diffusivities in under the assumption of constant median migration barriers without standard deviation. In (b) the same experimental data points in comparison to the variable barrier (VB) KMC calculations are shown. The samples are slightly offset in x_{Ni}. The closer these two data points are on the normalized scale the better the agreement between experiments and simulations. Partially adapted from Ref. 412.

Figure 4.20 shows this normalized tracer diffusion coefficient for the different elements obtained from the tracer correlation experiments in comparison to the ones from the KMC simulations based on the interatomic potential. The KMC simulations in (a) only considered the mean vacancy migration energy, assuming an infinitely sharp energy distribution with 0 standard deviation. This corresponds to the established random alloy model. The data in (b) is based on variable-barrier (*VB*) KMC simulations where the full vacancy migration energy distribution is considered. Direct comparison between the two models shows better performance of the random alloy model for Mn, while the variable-barrier KMC gives better agreement for Co, Cr, and Ni. For the different alloy samples reduced Co and Ni diffusivities show good agreement between experiments and simulations. For Cr and Mn, on the other hand, more pronounced differences can be seen. The good agreement for Mn at $x_{\mathrm{Ni}} = 0.6$ appears to be a coincidence.

There are still some simplifications in the calculations shown in this chapter which could be responsible for the observed differences between the simulations and the corresponding experiments. Firstly, we have neglected effects of the vibrational entropy not only to the vacancy formation but also the migration. Additionally, the attempt frequency was assumed to be a constant value independent of alloy composition and migrating species. The calculation of these quantities is rather straight forward if one knows the corresponding phonon frequencies in equilibrium and at the transition state.[351,357] In conventional materials these can be easily calculated[441] using a tool like PHONOPY.[442] However, the large simulation cells needed for a proper statistical treatment of a HEA combined with the inherent lack of symmetry lead to a situation where the phonon density of states and frequencies could not be calculated based on memory limitations of the available computer resources. Secondly, the vacancy migration energies were calculated under static conditions at 0 K under the assumption of the 0 K lattice constant. Diffusion at high temperatures happens at a larger interatomic spacing due to thermal expansion. This can either enhance diffusion as the *windows* through which the diffusion atom needs to jump increases in size,[443,444] or it can reduce diffusivities as the coordination and thereby stabilization at the transition state is reduced. Furthermore, the thermal softening of the lattice can reduce the elastic energy at the saddle point and thereby increase the diffusivity.[445] The greater atomic spacing can also lead to a new kind of diffusive jumps which are not captured by our NEB and KMC calculations.[446] Thirdly, we have only accounted for isolated vacancies in our calculations. In a real material vacancy-vacancy interactions can lead to shifts in the observed diffusivities. Even though, this error is expected to be small, especially given the good experimental Arrhenius fits shown in Figure 4.18.[447,448]

Another interesting effect not considered in our calculations is the effect of SRO. It is still unclear if and under which conditions a HEA can exist as a true random solid solution (see Subsection 2.2.5 for a review of the SRO literature in HEA). Obviously, SRO shifts the probabilities for chemical bonds and environments, modifying both the vacancy formation and migration energy distributions. As we have only investigated perfectly random alloys at very high temperatures, this effect has been neglected entirely.

4.6 Conclusion

We can now use the new insights to answer the research questions posed in Section 2.4.

I. Median vacancy formation energies are independent of the removed element and the global composition of the $(\mathrm{CoCrFeMn})_{1-x}\mathrm{Ni}_x$ alloy family. The local chemical environment influences the formation energy leading to an overall broad distribution of vacancy formation energies.

II. Estimations from the defect dipole tensor calculations show that the vacancy formation is not significantly influenced by applied pressure. Even high-pressure environments do not lead to significant vacancy formation on a given *sublattice*, i.e., for a given species.

III. We confirmed, using MC simulations, that the vacancy formation energies can be integrated directly to obtain the vacancy concentration, even in compositionally complex alloys. Confirming the works of Morgan and Zhang.[126]

IV. The width of the vacancy migration energy distribution cannot be approximated by a scalar *effective* vacancy formation energy as it leads to a non-Arrhenius type dependency of the vacancy concentration on temperature.

V. The vacancy migration energy strongly depends on the migrating element with Mn having the lowest migration energy and Co having the highest one. For all elements an almost linear increase in migration energy can be observed with increasing Ni concentration in the $(\mathrm{CoCrFeMn})_{1-x}\mathrm{Ni}_x$ alloy.

VI. Vacancy formation and migration energies show a transition from concentrated to diluted alloy at a Ni concentration of about 0.75.

VII. An extension to the conventional random alloy model is proposed to calculate the correlation factor accounting for the distribution width of the migration energies using a KMC algorithm. This extension to the model leads to pronounced changes in the correlation factor especially for fast migrating species like Mn or elements with a broad migration energy distribution like Cr.

VIII. Combining calculated vacancy concentrations with diffusivities obtained from the KMC calculations show agreement in magnitude with experimental measurements, even on the absolute scale. The concentration dependent hierarchy observed in experimental tracer diffusion measurements cannot be reproduced by the atomistic simulations.

IX. Further analysis reveals better agreement of the variable-barrier KMC simulations than the established random alloy model on a reduced diffusivity, D_i^*/D_{Fe}^*, scale. This comparison in reduced units partially compensates uncertainties from the interatomic potential.

5 Dislocations

> *"The complications in HEAs thus arise in understanding how dislocations move through the highly compositionally disordered lattice."*
>
> — E. P. George *et al., 2020*[19]

The results presented this chapter are partially published in:

"D. Utt, S. Lee, A. Stukowski, S. H. Oh, G. Dehm, and K. Albe, *Jerky motion of dislocations in high-entropy alloys: The linkage between local Peierls stress fluctuations and dislocation mobility*, arXiv:2007.11489 [cond-mat, physics:physics] (2020)", Science, (submitted).[449]

In this chapter we present transmission electron microscopy (TEM) images of gliding dislocations in a Cantor alloy sample showing non-straight dislocation lines and local pinning on atomic scale obstacles. We then perform experimental scale atomistic simulations to confirm that the computer model features similarly wavy dislocation lines pinned on local obstacles, even without a priori knowledge of their origin. After this confirmation an isolated edge dislocation is studied in detail and the individual dislocation pinning points are identified. This is not only done for the equimolar Cantor alloy but also many of its face-centered cubic (FCC) subsystems. Furthermore, different short-range order (SRO) arrangement within the Cantor alloy are investigated to establish their effect on dislocation pinning. Building on these results, the effect of the newly identified pinning point density on the critical stress for dislocation glide and dislocation mobility is established and implications for computational alloy design are discussed. Further simulations are made on the effect of larger precipitates in the Cantor alloy matrix and their influence on the dislocation line shape and its pinning.

5.1 Dislocation Pinning in the Cantor Alloy: Experiments and Simulations

Sample preparation, in situ TEM measurements, and their interpretation was performed by Dr. Subin Lee (Max-Planck-Institut für Eisenforschung GmbH, Düsseldorf).

In a first step, we confirmed that there is localized dislocation pinning in the five component Cantor alloy. To do so, a thin foil sample of the alloy is prepared and subjected to in situ tensile testing in the TEM. During mechanical loading the dislocations nucleate from a crack in the foil and glide through the sample. As they are constrained by the top and bottom surfaces, they bow out in the glide direction. In pure metals this would lead to dislocations with a constant curvature.[68] Deviations from this ideal circular behavior especially bumps or dents in the dislocation line hint at localized pinning of the dislocation line on nanoscale obstacles.

Figure 5.1 (a) shows consecutive TEM snapshots during glide. The glide direction is from left to right. While the dislocation lines are not directly visible, the stacking fault (SF) between the two Shockley partial dislocations can be seen as a darker band. The edges of this SF ribbon correspond to the two partial dislocation positions. It can be seen that the dislocations show a jerky motion of repeated pinning and depinning during glide. Therefore, the dislocation line is not a smooth round curve but shows bumps and waviness. Both observations are evidences of a strong local pinning which requires an additional force to be overcome. Even though, the images have been processed to increase contrast,[450] the frequent pinning of the dislocations during glide and their jerky motion is much easier to discern in motion (the video is available online as part of Ref. 449). To further investigate this dislocation pinning, the dislocation line shape is extracted from the TEM snapshots using Gaussian filtering and ridge detection algorithms. The extracted dislocation line shape of the first leading partial dislocation, labeled *1* in Figure 5.1 (a), are shown in (b). The line shape between extracted data points is interpolated using cubic splines,[391] from here it can be seen that the dislocation does not glide in a constant smooth motion. Instead, its segments are locally pinned on nanoscale obstacles and the line becomes wavy. This strong dislocation pinning could be the origin of the high critical shear stress reported for these samples by Lee et al.[77]

While it is easy to attribute the local pinning seen here to the random chemical fluctuations in the high-entropy alloy (HEA), there are two other explanations for the dislocation pinning observed in these samples which need to be discussed. First, SRO could lead to preferential atomic arrangements in the sample which act as obstacles for the dislocation line as their shuffling would cost additional energy.[293–295] The sample shown in Figure 5.1 (a), however, has been investigated for SRO before using atom probe tomography (APT) and scanning TEM energy-dispersive X-ray spectroscopy techniques. The authors conclude

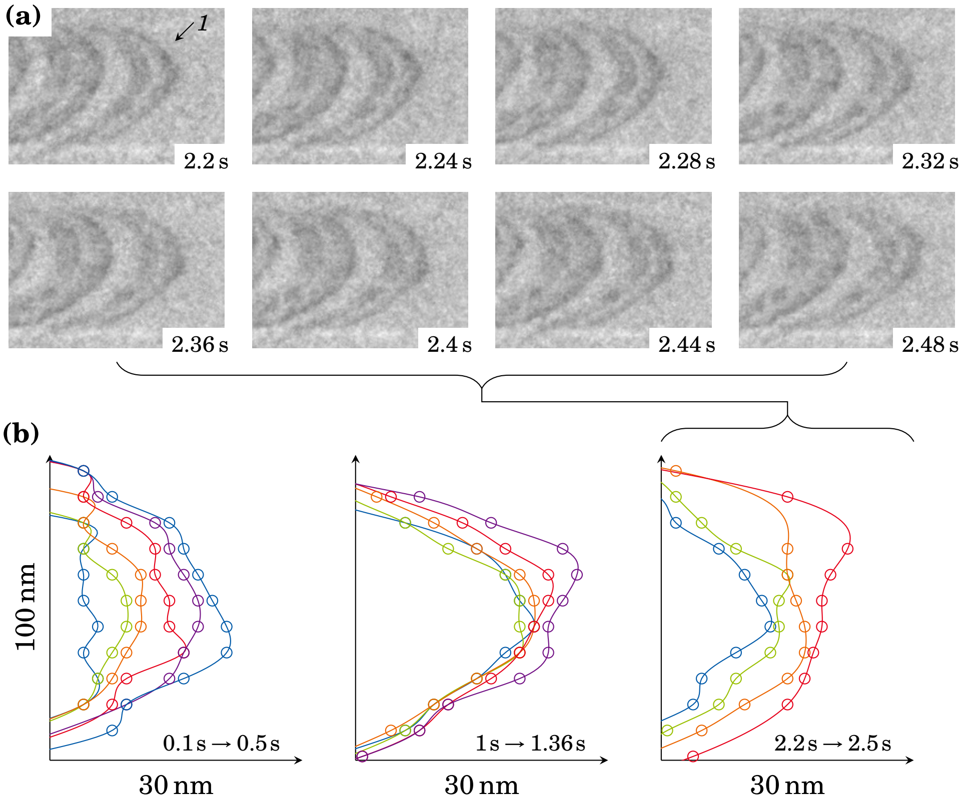

Figure 5.1: (a) Experimental TEM images showing an array of partial dislocations gliding on the $\{111\}\langle110\rangle$ glide system during in situ tensile testing. (b) Trace of the first dislocation (marked as *1* in (a)) in the array at different times during glide. Extracted from snapshots comparable to (a) using edge detection. Marked positions along the dislocation line are extracted from the TEM images, its full shape is interpolated. Partially adapted from Ref. 449.

that no SRO could be resolved, i.e., the sample is in a chemically random state.[77] As stated by Hong et al.[286] and outlined in Subsection 2.2.5 these methods are not necessarily sufficient to detect SRO on the atomic scale. Therefore, the effect of SRO cannot be excluded completely. Alternatively, one might suspect that damages from the focused ion beam preparation act as obstacles for dislocation glide. These damages accumulate close to the sample surface in depths of 5 nm to 10 nm[451,452] and may hinder dislocation glide. For reference, the TEM foil sample investigated here has a total thickness of about 100 nm, therefore, the dislocation pinning in the middle of the foil sample should not be affected by the surface damage layer.

We reproduce the experimental sample geometry in a large-scale atomistic computer model containing $\approx 1 \times 10^8$ atoms. Given the scale of all other simulations shown throughout this thesis, these newly created samples are 10 to 100 times larger to accurately replicate the experimental conditions. Figure 5.2 gives a schematic representation of the prepared sample. It contains an inclined glide plane with an aligned surface notch to ensure dislocation nucleation along said plane. The open surface on the opposite site of the notch acts as a dislocation sink. During uniaxial tensile testing, Shockley partial dislocations are emitted from this notch and travel through the material. Here we compare two alloys, namely CoCrFeMnNi and CoNi at 5 K and 300 K. The goal is to show that the atomistic simulation is able to capture the dislocation pinning observed in TEM (cf. Figure 5.1) and to confirm that the interatomic potential can resolve differences in dislocation glide between the strongly pinning Cantor alloy and the weakly pinning CoNi alloy.

Figure 5.3 shows the nucleation and glide of the first two Shockley partial dislocations in each sample, dislocation lines are shown in red and the viewing direction is normal to the glide plane (shaded blue). In all snapshots dislocations glide from left to right. In (a), the dislocation lines in the Cantor alloy gliding at 5 K are shown. The thermal energy at these temperatures is low, which reduces the thermally activated depinning of the dislocation line and leads to jagged dislocations pinned in multiple positions. The same sample shows much straighter and less meandering dislocation lines at 300 K, where thermal fluctuations assist the dislocation in crossing some of its obstacles (b). Comparing dislocations in the Cantor alloy (b) to the ones in CoNi (c) reveals a stark contrast. The dislocation lines in CoNi are almost ideally straight, and their curvature is only caused by the order of nucleation from the notch (center) or surface pinning (top and bottom in the snapshots).

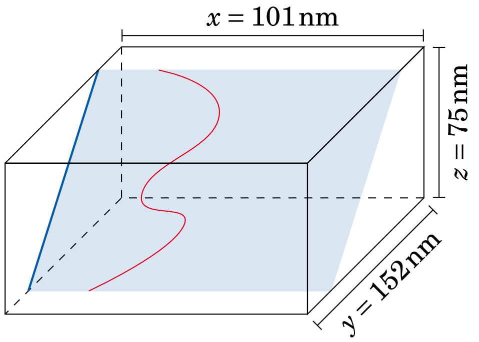

Figure 5.2: Schematic representation of the TEM sized sample used in the atomistic computer simulations. Both x and z directions are open boundaries while y is periodic. The blue plane corresponds to the inclined glide plane, following the experimentally observed tilt. A notch is cut into the sample's surface (blue line) to facilitate dislocation (red) nucleation on the desired plane. Following the experimental conditions, tensile strain is applied along y.

Inspection of the dislocation lines reveals that the atomistic simulation is not only able to produce dislocation line shapes comparable to experiment, but is also able to resolve differences between weak and strong dislocation pinning in different alloys of the same family. In the next step, we are going to use the atomistic simulations to reveal the nature of dislocation pinning points in concentrated alloys.

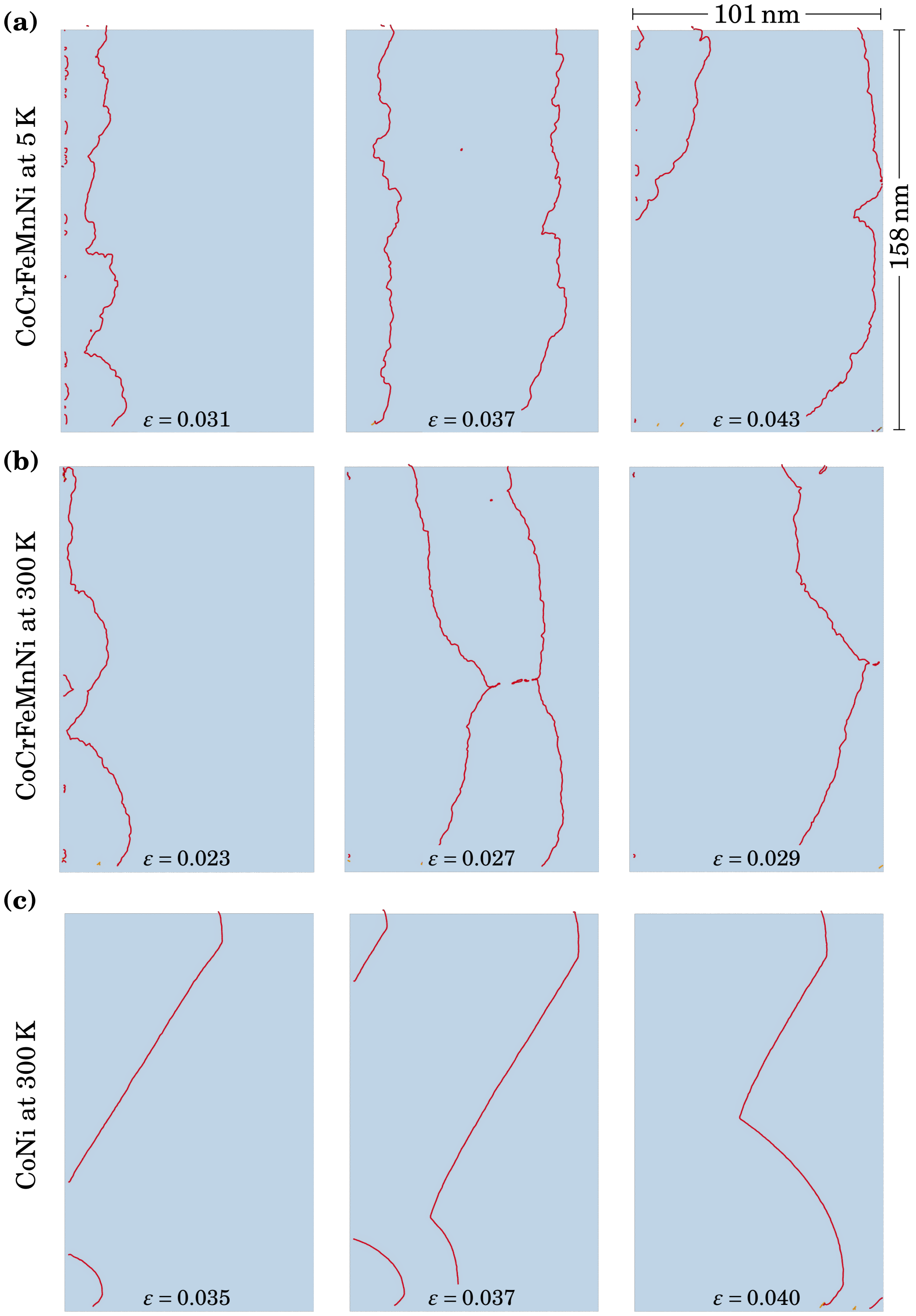

Figure 5.3: Shockley partial dislocations nucleated from a notch on the left-hand side of the sample moving across the glide plane (shaded area) to be absorbed by the open surface one the right. Each snapshot is taken at a different engineering strain ε. The engineering strain rate is a constant $1 \times 10^8\,\mathrm{s}^{-1}$. (a) Dislocations in the equimolar Cantor alloy deformed at 5 K. (b&c) Comparison of dislocation lines in the strongly pinning CoCrFeMnNi and the weakly pinning CoNi alloys deformed at ambient temperature. Partially adapted from Ref. 449.

5.2 Dislocation Pinning — An Effect on the Atomic Scale?

As stated in their recent review, George et al.[19] suggest that the strengthening in HEA cannot be a phenomenon at the atomic scale as the activation volume for dislocation glide is $70b^3$ at 77 K[285] and hence encompasses at least 100 atoms (cf. Subsection 2.2.4 for details). To investigate this claim we constructed two samples containing two distinct regions along the dislocation line (R_1 and R_2). Both samples share the same atomic configuration in R_1 but different atomic arrangements in R_2. In sample 1, R_2 is just a repetition of R_1, i.e., $R_1 = R_2$. Sample 2, on the other hand, has again the same atomic configuration in R_1 but a different random atomic arrangement in R_2. Both samples are subjected to the same constant shear stress at 2 K. The low temperature was chosen to suppress the effects of random thermal fluctuations influencing the dislocation line and activating its crossing of pinning points.

Figure 5.4 shows a metastable partial dislocation arrangements for the leading and trailing partial dislocation after about 15 ps. The dislocation line for the sample where $R_1 = R_2$ is given in red and the one where $R_1 \neq R_2$ is shown in blue. Focusing on the red dislocation first, the induced periodicity can be seen as both R_1 and R_2 feature exactly the same dislocation pinning points (highlighted by red arrows). This can be seen for both leading and trailing partials. Comparing this to the dislocations in the sample where R_2 features a different arrangement, one can see that the two main pinning points for the leading partial dislocation are still the same in R_1, while the dislocation obstacles in the shuffled region R_2 are now different (see blue arrows). As the dislocation has long-range forces acting along the dislocation line in the form

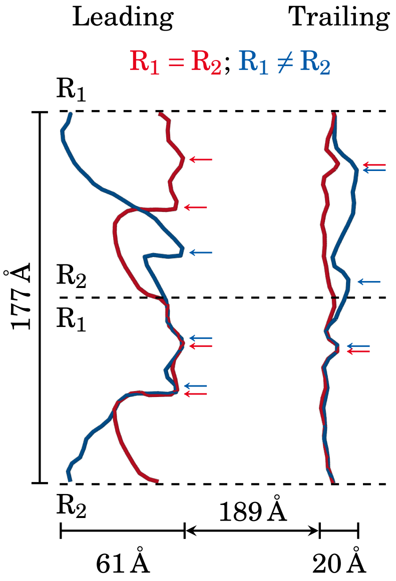

Figure 5.4: Partial dislocation configuration during glide under constant applied stress at 2 K. Two different samples are superimposed (red or blue) to compare the individual dislocation pinning points (highlighted by colored arrows). The lower (R_1) and upper (R_2) regions share the same atomic arrangement for the red dislocation lines ($R_1 = R_2$), whereas the blue dislocation lines have a different atomic configuration in the upper half ($R_1 \neq R_2$). Therefore, both samples share the same dislocation pinning points in R_1 but not in R_2. The boundary conditions along the dislocation line are periodic.

of the line tension, changes in R_2 can propagate into R_1. This explains why the advanced blue dislocation line segment in R_2 also influences the dislocation arrangement at the lower edge of R_1 across the periodic boundary.

Overall, these findings show that, even though, there are long-range interactions along the dislocation line, dislocation pinning on obstacles remains a localized process. The dislocation line shape in R_2 is vastly different for the blue and red leading partials; In R_1, however, both show the same strong pinning points. Which brings us the obvious next question — is there a descriptor for these atomic scale pinning points?

5.3 A Descriptor for Dislocation Pinning Points

Now that we confirmed that dislocation pinning is an effect on the atomic scale the question of the nature of these individual pinning points remains. Peierls[453] and Nabarro[454] have first calculated the periodic potential energy seen by a dislocation as it moves through the crystal lattice. They derived an analytical form of this displacement-potential energy relationship (also called Peierls energy). The stress required for a dislocation to cross this periodic Peierls energy landscape, i.e., for a dislocation to glide, is proportional to the maximum slope of the Peierls energy landscape.[67] In the original models, the Peierls energy is often approximated by a sinusoidal function.[67,455]

Another form of such a displacement–potential energy relationship is the generalized stacking fault (GSF) curve or landscape, formally introduced by Vítek in 1968.[251] It depicts the potential energy as two lattice planes are rigidly shifted against each other.[251,252] Calculating the GSF landscape for a $\{111\}$ plane in the FCC lattice reveals the stable FCC atomic positions as global energy minima and the intrinsic stacking fault (ISF) positions as local metastable states.[252] For the purpose of dislocation glide, the GSF landscape can be understood as a stand-in for the Peierls energy. An example of such a GSF surface can be seen in Figure 5.5 (a). The straight line displacement from one stable FCC position to an adjacent one corresponds to the displacement of a perfect $\langle 110\rangle$ dislocation ($\vec{b}_1$). It can be seen that the minimum energy path connecting two stable minima goes through the metastable ISF configuration. The displacement connecting these stable and metastable sites is the $\langle 112\rangle$ Shockley partial dislocation ($\vec{b}_2$). The corresponding planar fault energy γ line profiles are given in (b). They clearly show the much lower activation energy for the partial dislocation pathway with the metastable ISF state in the middle. This GSF surface example is for elemental Cu based on an embedded atom method interatomic potential.[456] Vítek[251] however states that for monoatomic FCC metals the overall shape of the energy landscape follows the one predicted from a hard-sphere model making it representative for this material class.

In pure metals, each atom in the GSF plane is identical, and they all see the same energy landscape. Therefore, calculation of the GSF curve allows

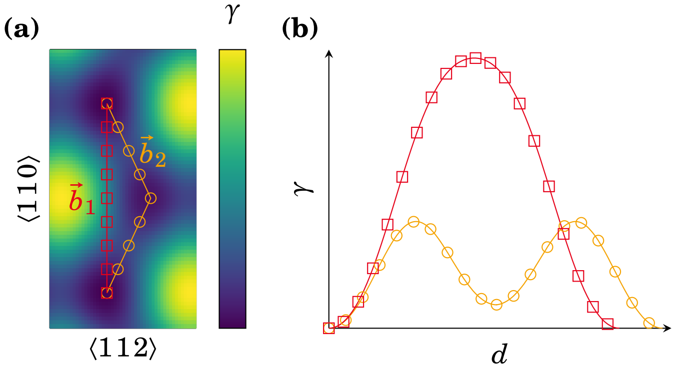

Figure 5.5: (a) Example of an FCC {111} GSF surface showing the displacement of the full dislocation ($\vec{b}_1$) or the two corresponding partial dislocations ($\vec{b}_2$). (b) GSF energy γ over displacement distance d along the two paths.

for a determination of the scalar global Peierls stress. This is not the case in concentrated solid solutions like medium-entropy alloys (MEAs) or HEAs. Here, the GSF curve strongly depends on the local chemical configuration and it becomes a spatially fluctuating quantity.[260–262] Therefore, the Peierls stress also becomes a locally varying value as it is directly related to the shape of the GSF curve. While the calculation of a local displacement–energy curve as function of the chemical environment seems daunting at first — LAMMPS allows for the determination of the energy for each atom as the sum of its interaction with all other atoms within the simulation cell. Calculating the GSF curve of an HEA using standard methodology,[251,252] but tracking the projected potential energy per atom allows for the determination of the GSF surface for every single atom. While this approach follows in the footsteps of the stochastic Peierls-Nabarro model proposed by Zhang et al.[37] and Jiang et al.,[237] we do not attempt to find a closed-form mathematical solution of the local Peierls barrier but instead measure it a priori as output of the atomistic simulation. There is one change required for the concentrated alloys compared to monoatomic materials. The standard methodology allows for relaxation of the atomic positions with respect to the direction normal to the GSF plane, to accommodate volume changes at the interface.[252] This can be seen in Figure 5.6 (a), which shows the atomic configuration at the saddle point of a SF calculation. Here, the standard methodology is employed and the atomic relaxation normal to the GSF plane can be seen in the yellow trajectory lines. In the concentrated alloys this approach cannot be taken, as it leads to discontinuous relaxations of the atoms into multiple local metastable states. To prevent these discontinuities in the energy path, the atoms are fixed to their ideal FCC lattice positions and only allowed to relax as two rigid bodies (one below and one above the GSF plane) to accommodate the interface volume changes. An example of this is given in Figure 5.6 (b), where again the SF calculation saddle point configuration is shown. This time, the atoms are not color coded based on their species, but based on the atomic energy change during the rigid shift. Note, how the trajectory lines (yellow) all run perfectly parallel, as the atoms are fixed on their FCC

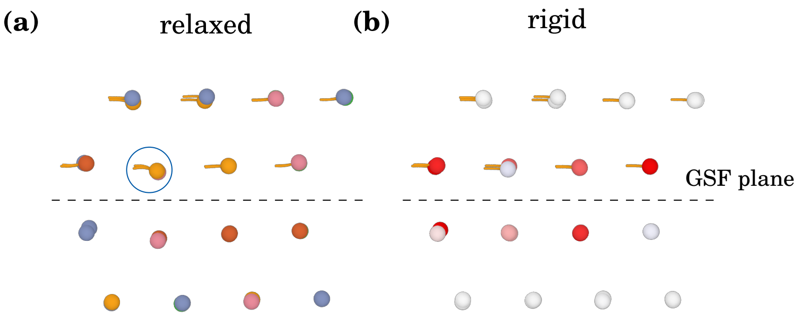

Figure 5.6: Comparison of the two different SF calculation relaxation methods. Both snapshots show the saddle point configuration which corresponds to the unstable stacking fault. Yellow lines show the full atomic trajectory starting from the ideal FCC configuration. (a) Standard methodology allowing for atomic relaxation normal to the fault plane. An atom with strong structural relaxation is highlighted. The atoms are color coded based on the species and the trajectory lines reveal atomic relaxation. (b) Proposed method, where the atoms are only allowed to perform rigid body relaxation. The atoms are color coded based on their atomic energy change during this calculation (red corresponds to an energy increase) which is subsequently used to calculate the atomic GSF curves (Figure 5.7). Here, all trajectory lines are exactly parallel.

lattice sites without individual site relaxation. To ensure comparability this methodology will be applied to all samples.

Figure 5.7 (a) shows the GSF energy surface for the equimolar Cantor alloy sample. The total energy change is normalized by the area of the GSF plane to obtain planar fault energy. Within the sampled region, there are three local minima. The two at $y \approx 0\,\text{Å}$ correspond to the two FCC lattice positions while the one in the middle at $x \approx 1\,\text{Å}$ belongs to the ISF configuration. As already shown in Figure 5.5, these three positions are connected by Shockley partial dislocation displacements. In this case the red (yellow) displacement path belongs the leading (trailing) partial dislocation. The planar fault energy γ along these two displacement paths is shown in Figure 5.7 (b). There are two main observations to make here. First, even though the alloy has a compositionally complex GSF plane both energy paths are symmetric suggesting that over the 32 000 atoms adjacent to the cut plane these local fluctuations average out. Moreover, the ISF configuration has a negative energy compared to the pristine FCC lattice indicating that the ground state phase is not the FCC but the hexagonal close-packed (HCP) phase. As outlined in the literature review (Subsection 2.2.2), the reported stable stacking fault energy in the Cantor alloy scatters widely. Density functional theory (DFT) calculations, however, seem to agree on the fact that the Cantor alloy's 0 K stable ground state phase is HCP.[257–260] Moreover, some available calculations support findings of negative ISF energy directly.[258,260,269]

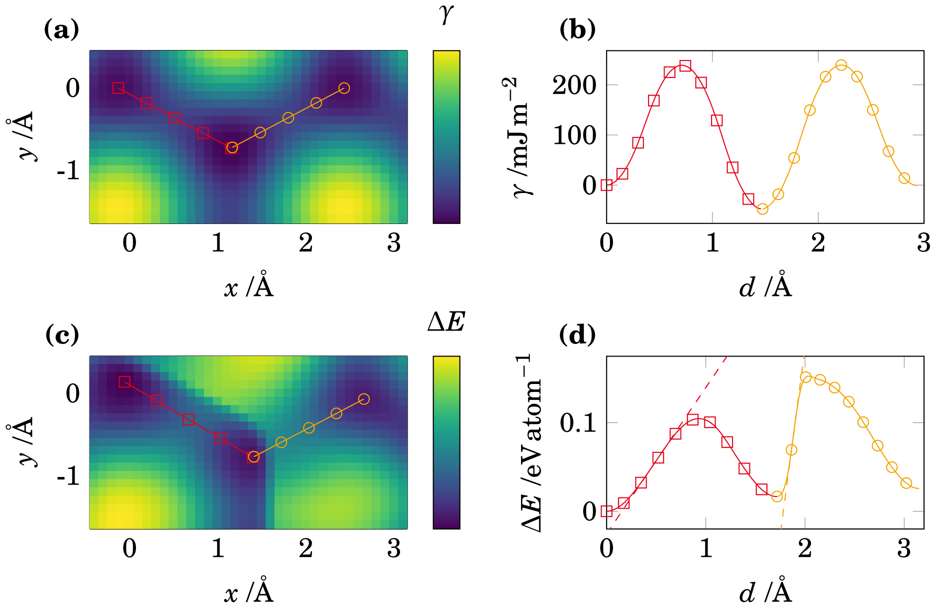

Figure 5.7: (a) GSF energy surface averaged over a whole plane in the CoNiCrFeMn HEA sample. (b) Energy profiles along the leading (red) and trailing (yellow) partial dislocations' displacements extracted from (a). (c) Energy surface shown in (a) from the perspective of a single atom in the GSF plane. (d) Energy profiles along the two displacement paths obtained from (c). Dashed lines indicate the maximum slope along both curve segments. This slope corresponds to the force F_P necessary for the atom to cross the energy barrier. Only a small fraction of plot marks are given for clarity.

In comparison, Figure 5.7 (c) shows an example of the GSF surface for a single atom in the planar fault plane. This energy cannot be normalized by an area, as the area of an atom is ill-defined. Therefore, absolute energy differences ΔE referenced to the initial FCC arrangement are given. Here it can be seen that the symmetry seen in (a) is broken if there is no averaging over numerous atoms. Moreover, the three local minima are located at slightly different coordinates compared to (a). This is because all atoms in this simulation are locked in their ideal FCC lattice positions. Therefore, the intrinsic lattice distortions lead to a shift of the minimum energy position for each atom, as the translational degrees of freedom are explored. Extracting the displacement paths of leading and trailing partial dislocation for this atom by connecting the three local minima by straight lines gives the energy profile shown in (d). It can be seen that leading and trailing partial dislocation face vastly different energy landscapes. Approximating the local Peierls stress as the slope of this local GSF curve (indicated by dashed lines) also shows how leading and trailing partial dislocation see significantly different local Peierls barriers. Note that the slope does not have units of stress but of force (eVÅ^{-1}) and will be denoted as F_P in the following. Again, this stems from the fact that we cannot normalize by an *area per atom*. It can also be seen that for this local chemical environment the ISF configuration does not correspond to the global minimum in energy but only a local one, with the initial ($d = 0$ Å) FCC configuration being more stable.

5.4 Testing the Proposed Descriptor

Now, that the local Peierls stress has been suggested as a descriptor for localized dislocation pinning and has been calculated for each atom in the GSF plane, its descriptive ability needs to be tested. Therefore, we insert a $\frac{1}{2}\langle 110\rangle$ perfect edge dislocation into the equimolar CoCrFeMnNi sample. This dislocation is inserted in the form of a misfit dislocation to ensure periodic boundary conditions in glide and line directions.[388] Care is taken to ensure that the glide plane of this inserted dislocation is aligned with the previously calculated GSF plane. This perfect dislocation dissociates into two Shockley partial dislocations which is the expected behavior for most FCC metals.[67,68] Even though, the global ISF energy is negative, these two partial dislocations remain at finite separation distance during initial energy minimization as the pinning forces acting on the dislocations are too strong.

Next, we apply a constant shear force to the dislocation to facilitate its motion at cryogenic temperatures (2 K). The low temperature is selected to reduce thermal activation boosting the dislocation across individual obstacles. During glide, the dislocation position is extracted every 10 fs using the dislocation extraction algorithm (DXA)[386,387] implemented in OVITO.[382] Figure 5.8 shows the relation between the dislocation pinning points proposed based on F_P and the observed dislocation trajectory. Panels (a-c) show the dislocation line passing over the pinning point landscape created by the spatial distribution of F_P. Initially, the pinning points of the first partial dislocation's displacement given in red in Figure 5.7 (d) are used. The slope of these atomic GSF curves has been averaged on a 3 Å×3 Å grid. Note that the discrete values have been smoothed for visualization purposes. Figure 5.8 (a) shows the initial configuration with the dislocation facing a set of glide obstacles. After 1.6 ps the dislocation has advanced under the applied shear force (b). It can be seen that the dislocation gets pinned on the obstacle with the highest F_P value and bows out significantly, as dislocation line segments away from the pinning point can glide more freely. Moreover, regions that have already been swept by the dislocation show a modified pinning point landscape, as the gliding dislocation has shifted the atoms above and below the glide plane against each other. This new pinning point landscape corresponds to the yellow curve in Figure 5.7 (d). After an additional time the dislocation has swept this whole region of the crystal and modified the entire pinning point landscape by shuffling local atomic arrangements (c). Figure 5.8 (e) shows a much larger section of the glide plane. Each plotted line corresponds to the dislocation line at a given moment, with the dislocation moving from left to right. Dislocations are shown every 250 fs for a total of 16 ps.

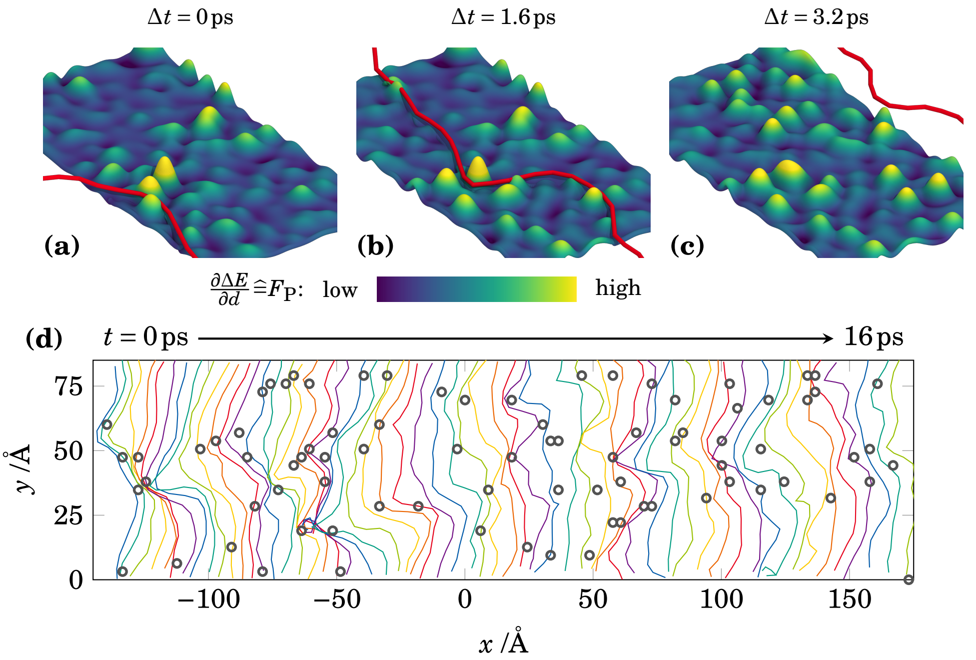

Figure 5.8: (a-c) Proposed pinning point landscape in the CoCrFeMnNi HEA sample with superimposed dislocation line. (a) Initial configuration where the dislocation faces a complex pinning point landscape determined from the atomic GSF curves similar to the one shown in Figure 5.7 (d). F_P is averaged on a $3\,\text{Å}\times3\,\text{Å}$ grid and plotted on the vertical (color) axis. (b) After some travel distance, the dislocation encounters a strong pinning point (indicated by the high peak in the pinning point landscape) and gets pinned. This pinning leads to a bowing out of the dislocation line as other line segments can advance more easily. (c) After some time, the dislocation passes over the obstacle. The pinning point landscape is modified for subsequent dislocations, as the two atomic planes have been shifted against each other. (d) Position of the leading partial dislocation extracted every 0.25 ps over a 16 ps interval. The 100 strongest proposed pinning points are indicated by circles. Note that closer dislocation lines in this graph correspond to stronger local pinning as the dislocation spends more time in a given region.

The lines are equitemporal, therefore regions where many dislocation lines are close together indicate a long dwelling time. This increase in time correlates with a strong local pinning. Gray circles highlight the spots of the 100 highest values of F_P. By eye, a correlation between these proposed pinning points and increased dislocation dwelling time can be established.

To proof that the apparent correlation between F_P and dislocation pinning points is not random chance, the Pearson product-moment correlation coefficient R is calculated. It can be used to describe the linear correlation between two variables, where $R = 1$ corresponds to a positive linear correlation and $R =$

−1 indicates a negative correlation. Non-linear correlations or uncorrelated variables have $R = 0$.[457] We average the dislocation occupation probability C for leading and trailing partial dislocation on the same 3 Å×3 Å grid as F_P. To determine C the position of the partials is tracked every 10 fs during the simulation and every grid square that is touched by the dislocation has its count incremented by one. If the dislocation remains stationary over multiple sampling steps, the respective grid square will be tallied multiple times. High dislocation probabilities correspond to high dislocation dwelling times which in turn suggest strong local pinning. The correlation coefficient for the leading partial dislocation R_leading based on $F_\mathrm{P,leading}$ and C_leading is equal to 0.14 and $R_\mathrm{trailing} = 0.16$. To put these numbers into perspective, we also calculated the correlation between the measured C and many random rearrangements of F_P. The correlation calculated for these random shuffles was found to be $R_\mathrm{leading} = R_\mathrm{trailing} = 0.00 \pm 0.02$. This confirms the correlation between proposed dislocation pinning points and measured dislocation pinning.

After showing that dislocation pinning on the atomic scale is indeed governed by F_P, the structural motives that lead strong dislocation pinning can be identified. Figure 5.9 shows the distribution g of F_P (combined for leading and trailing partial dislocations' displacement) as function of species. Here it can be seen that the strongest pinning points are exclusively Co atoms. Cr also shows increased dislocation pinning strength compared to Fe, Mn, and Ni, which only show low values of F_P. The question on what leads to this increased pinning point strength of Co immediately arises. Unfortunately, there is currently no clear answer, but there are several factors which could be investigated in the future. It could be related to the effective size of Co within a given atomic arrangement, tying our approach back to the Varvenne et al.[72] solid solution strengthening model. Another option could be the relative bond strength of Co with one of the other elements in the alloy, most likely Cr as shown later on. We can, however, conclude that the effect is caused not by an isolated Co atom but by its interaction with the local environment. Otherwise, every Co atom would

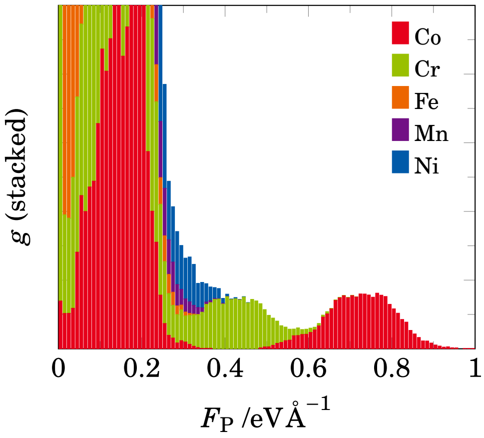

Figure 5.9: Distribution g of the maximum slope of the atomic GSF curve F_P per species of the equiatomic CoCrFeMnNi HEA. Both leading and trailing partial dislocation displacement paths were considered for the atoms in the GSF plane. For more information on F_P see Figure 5.7.

act as a dislocation pinning center. Figure 5.11 (b) and associated discussion explore the local concentrations leading to weak and strong pinning points in CoCrFeMnNi and CoCrNi in more detail. A definitive conclusion on what makes a strong pinning point can, however, not be given.

5.5 Applying the New Descriptor to Short Dislocations

After we have identified the atomic descriptor for dislocation pinning points, namely the maximum slope of atomic GSF energy curve show in Figure 5.7, we can use this descriptor for alloy design. To obtain an alloy with increased solid solution strengthening, a high density of strong dislocation pinning points is required. Based on our findings such an alloy would feature a high number of high F_P lattice sites. Applying the same methodology as for the Cantor HEA in the previous section, a large number of MEAs and HEAs are screened for F_P and compared to their resistance against dislocation glide.

To facilitate dislocation glide, a ramping shear force normal to the dislocation line direction is applied on the two surfaces parallel to the glide plane at a constant finite temperature of 2 K. Figure 5.10 (a) shows mean glide distance Δd of leading and trailing partial dislocation as function of the applied shear force F for Ni, CoCrNi, and CoCrFeMnNi. The data shows that for Ni both partials glide in tandem at very low applied forces. This is in line with expectations for single element FCC metals, where the Peierls stress is very low[69–71] and the positive ISF energy keeps both partial dislocations at roughly constant separation dis-

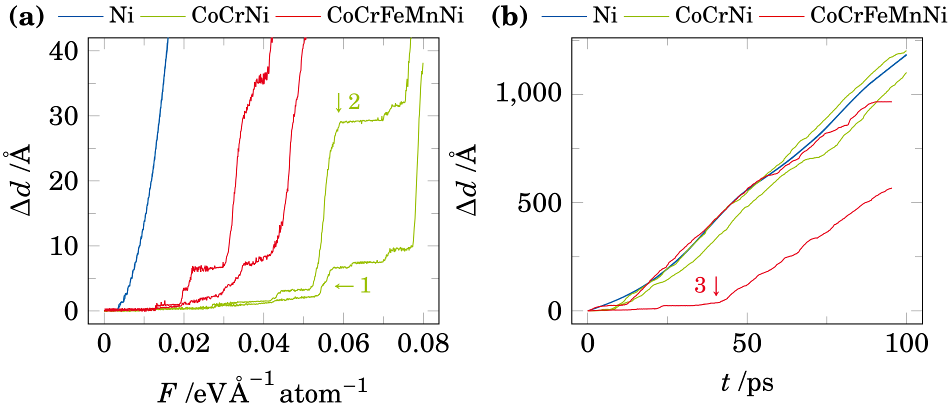

Figure 5.10: (a) Glide distance Δd of leading and trailing partial dislocation in the Ni, CoCrNi, and the CoCrFeMnNi samples under linearly increasing applied shear force at 2 K. The mean applied force where both partials have migrated for 20 Å is defined as critical force F_c. (b) Dislocation migration distance over time under constant applied shear load of F_c.

tance.[458] In both concentrated alloys, there is much more ruggedness visible in the distance–force curves. These correspond to frequent pinning and depinning of the dislocations as the applied force is increased. Once the applied force is sufficiently high, the dislocation can glide across all atomic scale obstacles at almost constant velocity. The CoCrNi sample requires the highest force to move the dislocation. The pronounced steps in its Δd–F curves are evidence that some dislocation pinning points are stronger than others. At point *1* the dislocation detaches from its current position, glides freely — shearing all lower pinning points in between, before it gets recaptured at *2*.

This re-pinning after initial dislocation glide observed here is different from the results published by Li et al.,[459] who report a sharp stress drop after yielding from their nanopillar compression simulations in different Al, Co, Cu, Fe, and Ni containing HEAs. They do not observe repinning of dislocations once they start gliding. One obvious difference is that these compression experiments do not start with dislocations in the system but require them to be nucleated heterogeneously from the sample surface. If the dislocation nucleation stress is higher than the pinning stresses, no dislocation pinning will be observed. Moreover, they used a set of embedded atom method (EAM) potentials[369] to describe their systems. In our preliminary studies of these isolated edge dislocations, we found the critical force for CoCuFeNi was about a factor of 10 lower than in the CoCrFeMnNi alloy (compare EAM based samples in Figure 5.13). This CuNiCoFe alloy is based on the same Zhou et al.[369] EAM interatomic potentials used by Li et al.[459] so there might be a difference in dislocation pinning between EAM and modified embedded atom method (MEAM) at play here. During glide, atoms in the glide plane not only change their relative distance but also their angles, therefore the added angular terms in the MEAM interatomic potential could give a better description of the atomic scale pinning point strength and shear phenomena in general.

In a next step, we apply a constant shear force to each sample and track the dislocation displacement over time t. Note that for Ni and CoCrFeMnNi this force is equal to the one required to move the leading partial dislocation by 20 Å in Figure 5.10 (a). A higher force corresponding to $\Delta d = 30$ Å was required to move the dislocations in CoCrNi for any significant distance on molecular dynamics (MD) timescales. The resulting curves are shown Figure 5.10 (b). Again, the elemental Ni behaves as one would expect, both partial dislocations glide at constant velocity leading to a linear time–displacement relation. In both the ternary and the quinary alloys the leading partial starts gliding first while the trailing partial remains stationary. This is facilitated by the negative SF energy in these alloys which provides an additional force on the leading partial dislocation, as an increase in SF area decreases the total energy of the sample. Therefore, the negative SF energy gives an additional driving force on the leading and an additional pinning force on the trailing partial. Note that this effect might or might not be comparable to the real material, Subsection 2.2.2 summarizes the disagreement about the sign of the SF energy in the Cantor

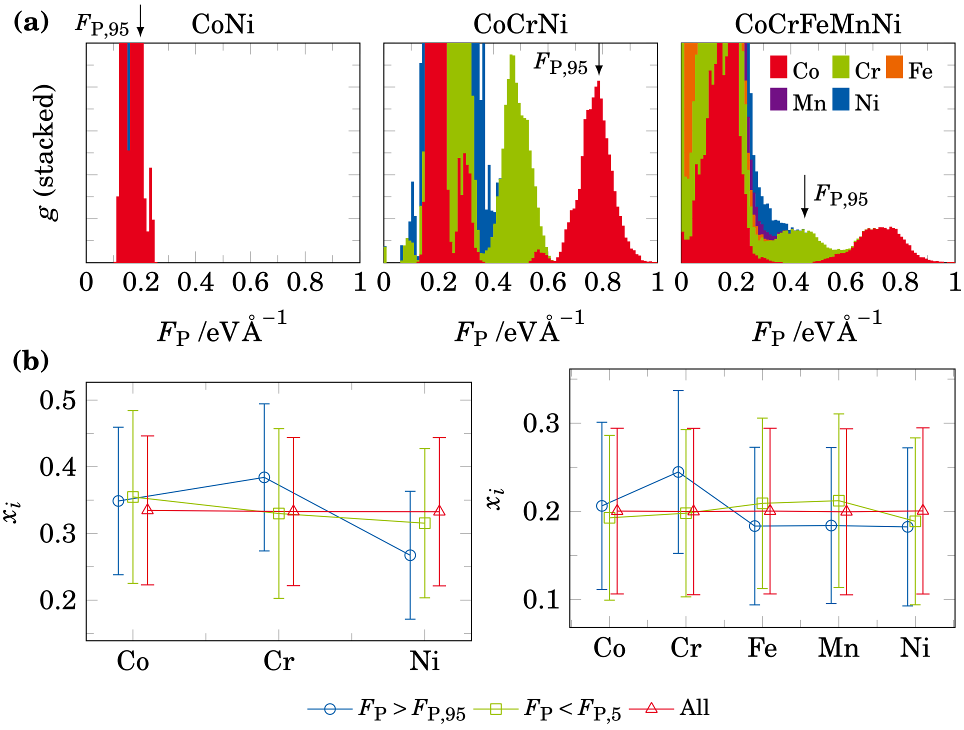

Figure 5.11: (a) Distribution g of the maximum slope of the atomic GSF curve F_P in CoNi, CoCrNi, and CoCrFeMnNi grouped by atomic species. Both leading and trailing partial dislocations' displacement paths are considered. See Figure 5.9 for further details. Arrows mark the 95.45 percentile of F_P, denoted as $F_{\mathrm{P},95}$ in the following. A measure that will be used in Figure 5.12 and thereafter. Note, the color legend applies to all three panels. (b) Composition in the first- and second-nearest neighbor shell around strong ($F_\mathrm{P} > F_{\mathrm{P},95}$) and weak ($F_\mathrm{P} < F_{\mathrm{P},5}$) pinning points in the CoCrNi and CoCrFeMnNi alloys. *All* is the average over all lattice sites which can be taken as reference. The species of the central atom is excluded in this concentration measure. Partially adapted from 449.

alloy. While this might appear problematic at first glance, the F_c value we determined already accounts for this additional driving force. Therefore, the direct comparison of F_c and later on the dislocation mobility, within the reference frame of our simulations, should be unaffected. Going back to Figure 5.10 (b), in the case of the CoCrFeMnNi sample, the trailing partial only starts moving once the leading partial has caught up with it across the periodic boundary, basically pushing it along (marked by *3*). The overall higher force in the CoCrNi sample avoids this issue even though this sample also shows a negative SF energy.

Figure 5.11 (a) shows the distribution of atomic pinning point strength F_P in a subset of the samples. Here CoNi, CoCrNi, and CoCrFeMnNi are compared. It can be seen that both the CoCrNi and CoCrFeMnNi alloy feature pinning points with F_P greater than $0.35\,\mathrm{eV\AA^{-1}}$, whereas the binary CoNi alloy has substantially smaller F_P values. The CrNi binary alloy, not shown here, has an almost identical pinning point density spectrum. Arrows indicate the position of the 95.45-percentile of F_P, denoted as $F_{\mathrm{P},95}$. This number gives a measure for the higher end of the distribution, i.e., the strength of the strongest dislocation pinning points. The fact that both CoNi and CrNi only show low values of F_P, while the two samples containing both Co and Cr show high F_P values for these two species leads us to the conclusion, that the direct interaction of Co and Cr atoms is responsible for the strong pinning points in these alloys. Moreover, we can see that the absolute number of strong pinning points is higher in CoCrNi compared to the five component CoCrFeMnNi alloy. Most likely, because the concentration of Co and Cr in the glide plane is reduced as Fe and Mn are added into the alloy. These two species only give low F_P values as shown in Figure 5.9.

Now the immediate question on the composition of the strong pinning points arises. Figure 5.11 (b) compares the concentration around the strongest 95-percentile $F_{\mathrm{P},95}$ and the weakest 5-percentile $F_{\mathrm{P},5}$ of pinning points in CoCrNi and CoCrFeMnNi. Taking into account the first- and second-nearest neighbor shells around the respective atom. This confirms the result from (a), that strong pinning points are a result of the unique interaction of Co and Cr. The strongest pinning points in both alloys are made-up exclusively of Co atoms and feature on average an enrichment in Cr atoms within their surroundings. This effect is seen in both the three and the five component alloys. Given the ideal chemical randomness of these alloys, the variance on all local concentration based measures remains high giving rise to the large error bars seen here. Nevertheless, the local concentration seen here can be used as a design guideline — *maximize the Co-Cr adjacency for more dislocation pinning*. It can, however, not be used as a tool to predict the pinning strength of a given atomic arrangement.

To assess the impact of the pinning point strength and density on the material itself, the critical force F_c for dislocation motion and the dislocation mobility M is determined for a wide range of binary, ternary, and other subsystems of the Cantor HEA. An example for the critical force determination is shown in Figure 5.10 (a). Figure 5.12 (a) shows this critical force for a wide range of binary and ternary subsystems of the Cantor alloy, as well as for the CoCrFeMnNi HEA. Here, one can see that CoCrNi, which shows the highest $F_{\mathrm{P},95}$ pinning point density descriptor, also has the highest required critical force to initiate dislocation glide. The five component HEA has intermediate F_c and $F_{\mathrm{P},95}$ values, while all other samples feature low critical force values and low dislocation pinning point strength. Additional F_c values for Cantor alloy samples containing different Ni concentrations starting from the equimolar $(\mathrm{CoCrFeMn})_{0.8}\mathrm{Ni}_{0.2}$ towards the dilute $(\mathrm{CoCrFeMn})_{0.04}\mathrm{Ni}_{0.96}$ alloy are shown as well. Here it can be seen that both $F_{\mathrm{P},95}$ and F_c decrease steadily as the alloys become more dilute. For all samples a linear correlation between F_c and $F_{\mathrm{P},95}$ can be seen. This is in

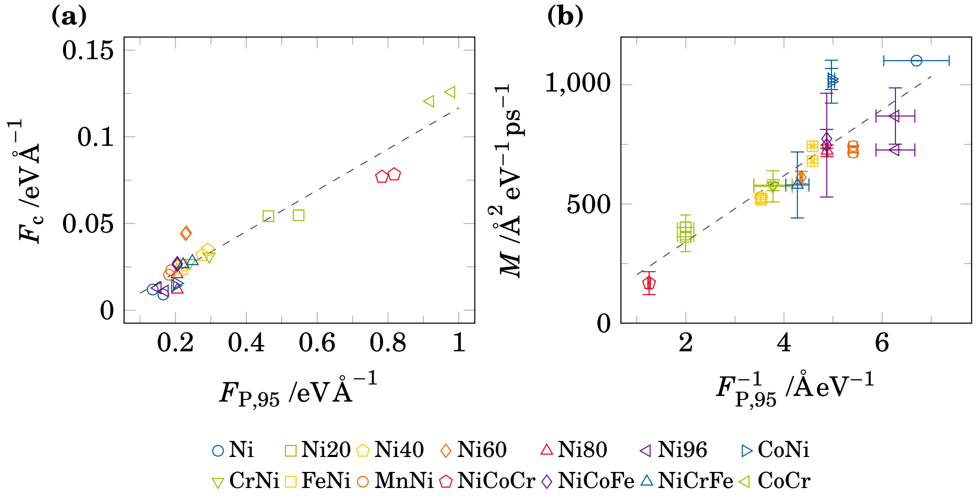

Figure 5.12: (a) Critical force F_c required to initiate dislocation glide in different binary, ternary, and other subsystems of the five component Cantor HEA. It is defined as the force required to move the dislocation by 20 Å. (b) Dislocation mobility M obtained under a constant applied shear force. Both F_c and M are shown in correlation to $F_{P,95}$ or its inverse, respectively. Figure 5.10 shows examples of the dislocation migration distance curves used as input. Samples labeled *Ni__* in the legend correspond to pseudo-binary compositions of $(\text{CoCrFeMn})_{1-x}\text{Ni}_x$, where *Ni20* is the equimolar Cantor alloy. Partially adapted from 449.

agreement with the intuition that an increased number of strong pinning points, i.e., greater $F_{P,95}$ value, requires more applied force be overcome.

The dislocation mobility is obtained from the constant force calculation in Figure 5.10 (b), where the linear regime of the displacement–time curve is fit to obtain the dislocation velocity v. The dislocation mobility can be calculated as,[67,68]

$$M = v \times F, \tag{5.1}$$

where F is the applied force. In the concentrated alloys with strong dislocation pinning, there is a substantial deviation from ideal constant velocity glide. Here only segments of linearity were fit. Figure 5.12 (b) shows the dislocation mobilities in the same set of samples. Note that these are plotted against the reciprocal of $F_{P,95}$, $F^{-1}_{P,95}$, as we intuitively expect samples with a high pinning point density and strength to feature reduced dislocation mobilities. Consequently, samples with fewer or weaker pinning points feature higher dislocation mobilities. This intuition is confirmed from the good correlation of M and the inverse of $F_{P,95}$.

5.6 Applying the New Descriptor to Long Dislocations

To limit the computational cost and allow for the screening of many alloys, rather small samples with an initial dislocation line length of 20 unit cells were simulated so far. Due to the periodic boundary conditions along the dislocation line direction, this sets an artificial limit on the maximum wavelength a dislocation line can adopt. For comparison, we construct an additional set of samples with an initial dislocation line length of 200 unit cells. For these larger samples, only a subset of the alloys shown in Figure 5.12 can be recalculated. Two additional samples, namely $Co_{0.3}Fe_{0.17}Ni_{0.37}Ti_{0.17}$ [78,369] and CoCrCuFeNi,[80,383] are added to exclude that the correlations observed previously are artifacts of the Choi et al.[129] interatomic potential. The calculations follow the same protocol: First the atomic GSF landscape is calculated, subsequently a dislocation in inserted into the GSF plane which is then subjected to ramping and constant shear. Note that in these larger samples F_c is defined as the applied force at which the dislocation has traveled 20 Å. For the dislocation mobility simulations, the force required to move the dislocation by 10 Å was chosen for all samples except for CoCrNi, which did not show long-range dislocation glide under these conditions. Here, the force to glide double that distance needed to be applied. Note that the calculation of M accounts for differences in the applied force.

Figure 5.13 shows the critical force and dislocation mobility in these newly created samples. For reference the results of the smaller samples, taken from Figure 5.12, are indicated as well. Here (a) shows that these new samples also show a linear correlation of F_c and our descriptor for pinning point density $F_{P,95}$. These longer dislocations require a reduced applied force to initiate glide compared to the smaller samples, even at a comparable pinning point strength. Looking at the dislocation mobilities M in (b), it can be clearly seen that the samples containing the longer dislocation lines also fulfill the previously established correlation with the reciprocal pinning point density descriptor. Similar to (a), the slope differs compared to the first set of samples.

Sills et al.[460] recently published their work on the dislocation line length dependent dislocation mobility. They studied the $Cr_{0.19}Fe_{0.70}Ni_{0.11}$ FCC alloy using classical MD simulations. They report that shorter dislocation lines show a reduced mobility in the solute-drag regime of glide compared to longer ones. This means that especially at low temperatures or low applied forces, long dislocation lines, in their system greater than ≈ 1200 Å, are necessary to converge the dislocation velocity. While this means that the dislocation velocities and thereby the mobilities obtained in our simulations are most likely not dislocation line length independent, comparisons at the same line length should still be valid.

Rizzardi et al.[461] measured the dislocation mobility in the FCC $Al_{0.3}$CoCrFeNi HEA and pure FCC Au samples. They report the dislocation velocities obtained from micro-compression experiments, where the force-displacement

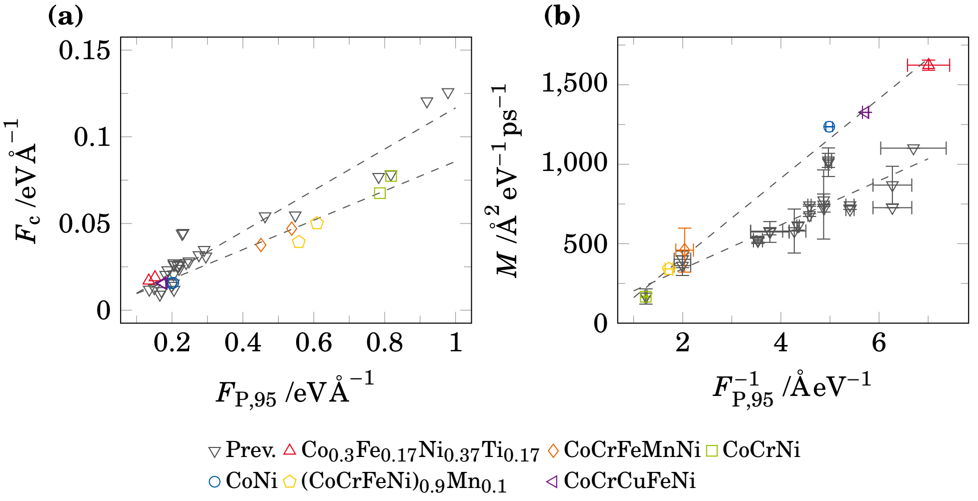

Figure 5.13: Relation of the critical force and dislocation mobility in the samples with an initial dislocation line length of 200 unit cells. Comparison to the Co$_{0.3}$Fe$_{0.17}$Ni$_{0.37}$Ti$_{0.17}$[78,369] and CoCrCuFeNi[80,383] alloys, which are described by different interatomic potentials is made. (a) Critical force F_c required to initiate dislocation glide. (b) Dislocation mobility M obtained under a constant applied shear force. Both F_c and M are shown in correlation to $F_{P,95}$ or its inverse, respectively. Results from the samples featuring a shorter dislocation lines shown in Figure 5.12 are added for reference (*Prev.*). Partially adapted from 449.

curves give insight into the number of dislocations arriving at the sample surface within a given time.[462] They draw two main conclusions from their velocity data. First, they require higher initial stresses to start dislocation glide in the HEA compared to Au. This is attributed to the much higher strength of the alloy due to solid solution strengthening. This result is in line with our findings, where the critical force for dislocation glide is much higher in CoCrFeNiMn and CoCrNi compared to the dilute Ni-alloys and pure Ni. Secondly, however, they report roughly the same maximum dislocation velocity in both, Au and Al$_{0.3}$CoCrFeNi, samples. They surmise that this stems from a *weakest-link* situation, where the dislocation starts to locally advance in regions of weaker pinning. This kink subsequently propagates along the dislocation line facilitating glide. They compare this to the HEA cross-slip model by Nöhring and Curtin,[463] which proposes a similar mechanism. Compared to our results, this would mean that the dislocation velocity, which they equate to the respective mobility, should be identical for all simulated alloys. Looking at Figure 5.13 (b) this is obviously not the case. There are two possible reasons for this difference. For one, our simulations are performed at cryogenic temperatures. Therefore, there is almost not thermal activation assisting the dislocation in passing obstacles. Thermal activation would compensate at least some observed pinning. Secondly, the experimental setup used by Rizzardi et al.[461] probes dislocation glide after homogeneous dislocation nucleation. Therefore, the acting stresses are very high. This again assists the dislocations in the HEA to glide across potential pinning obstacles. The weakest-link argument, however, explains the reason for the lower applied forces required to initiate dislocation glide in our large samples. The longer the initial dislocation line, the more likely there is a region of weaker pinning where it can disconnect from its starting position. This detached segment subsequently drags other dislocation line segments along due to the dislocation line tension. This decreases F_c and increases M for longer dislocation lines compared to shorter ones.

Li et al.[36] report that the pronounced dislocation waviness they observe in their CoCrNi samples stems from the strong interaction of Co and Cr. Here, we find a similar pattern where Co and Cr are not individually pinning the dislocation, but their interaction has a strong effect on $F_{\mathrm{P},95}$ and thereby on F_c and M. While the aforementioned authors only established a phenomenological connection, we were able to identify not only the atomic scale dislocation pinning points, but also found the origin of this pinning in the form of local fluctuations in the Peierls energy. Moreover, we find that our pinning point descriptor captures the superior strength of CoCrNi compared to CoCrFeMnNi expected from experiments and simulations.[12,244] Meanwhile, the high strength of other alloys like FeNiCo or FeNi, which have comparable strength to the five component Cantor alloy in experiments,[12] have low pinning point densities and strength within the employed interatomic potential.[129] Mind, that this direct comparison is flawed in multiple ways. SRO in experimental samples remains hard to quantify, while all samples studied here are perfectly disordered. Similarly, other experimental effects like microstructure, finite temperature, or impurities are not considered at all.

This concludes this first deep dive into dislocation pinning in concentrated HEAs. Figure 5.14 gives a schematic representation of the energy and friction force landscape encountered by a gliding dislocation. The local energy fluctuations ΔE and resulting forces F acting on a dislocation in a pure metal are negligibly small.[71] The addition of a low concentration of solutes, leading to a dilute solid solution, can either lead to local energy minima trapping the dislocation or to local energy barriers blocking the dislocation during glide. Either effect leads to a sudden change in energy and hence require a strong force to be passed. This can be seen in Figure 5.14 (a). The energy fluctuations in the HEA matrix, on the other hand, are already much higher due to the local chemical fluctuations (Figure 5.14). This leads to higher energy gradients and thereby to an increase in force required to move a dislocation through the matrix. However, as seen in Figure 5.11 there are some environments which pin the dislocation line much stronger than the surrounding matrix. These could be caused by atomic arrangements where an energy minimum sits right next to barrier (see shaded area (b)). Such an arrangement features a much steeper gradient in the local energy landscape and therefore pins the dislocation exceptionally strongly.

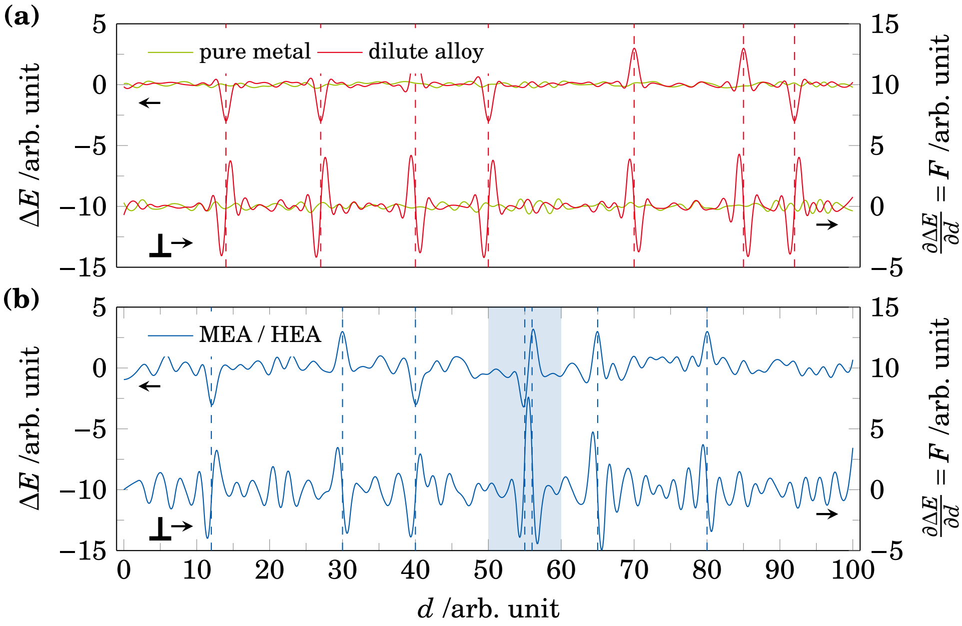

Figure 5.14: Schematic representation of the change in energy ΔE and resulting force F encountered by a dislocation as it glides for a distance d. (a) In a pure metal both energy change and resulting force are small as all chemical environments are homogeneous. The dilute solid solution behaves similarly to the pure metal far away from the solutes (indicated by dashed lines). However, close the solutes the dislocation can either be blocked by a high energy barrier or pinned by a local energy minimum, both of which lead to a stronger force acting on the dislocation. (b) shows ΔE and F in a HEA. Already a much greater variance in both quantities can be seen in the matrix, as there are many different chemical environments. Especially a combination of adjacent maxima and minima in the energy (shaded area) can lead to a much stronger local obstacle for the dislocation.

Such arrangements might also be present in dilute alloys, due to their low solute content, however, the probability for these chemical environments probably remains low.

5.7 The Effects of Short-Range Order

After the previous investigation of the perfectly random MEAs and HEAs we now want to focus on Cantor alloy samples containing different degrees of SRO. Hybrid Monte Carlo (MC)/MD equilibration with MC steps in the canonical ensemble is used to instill thermodynamically correct SRO in the samples without the need to wait for diffusive processes. Usually, the atom swap MC algorithm cannot be run on multiple processors in parallel as atoms involved in a single swap operation can be located on any two processors.[350] At the same time the parallel variance-constraint semi-grand canonical MC method[350] used in Section 6.4 cannot be used as the MEAM interatomic potential is not fully compatible at the time of writing. Therefore, the full simulation cell containing more than 4×10^5 atoms cannot be equilibrated using MC. Instead, the central region of the sample containing the GSF plane into which the dislocation will be inserted later on is cut out from the large sample and put into its own fully periodic simulation cell and subsequently MC equilibrated. These smaller samples are equilibrated at different temperatures between 600 K and 1400 K to stabilize different states between demixing and almost random configuration.

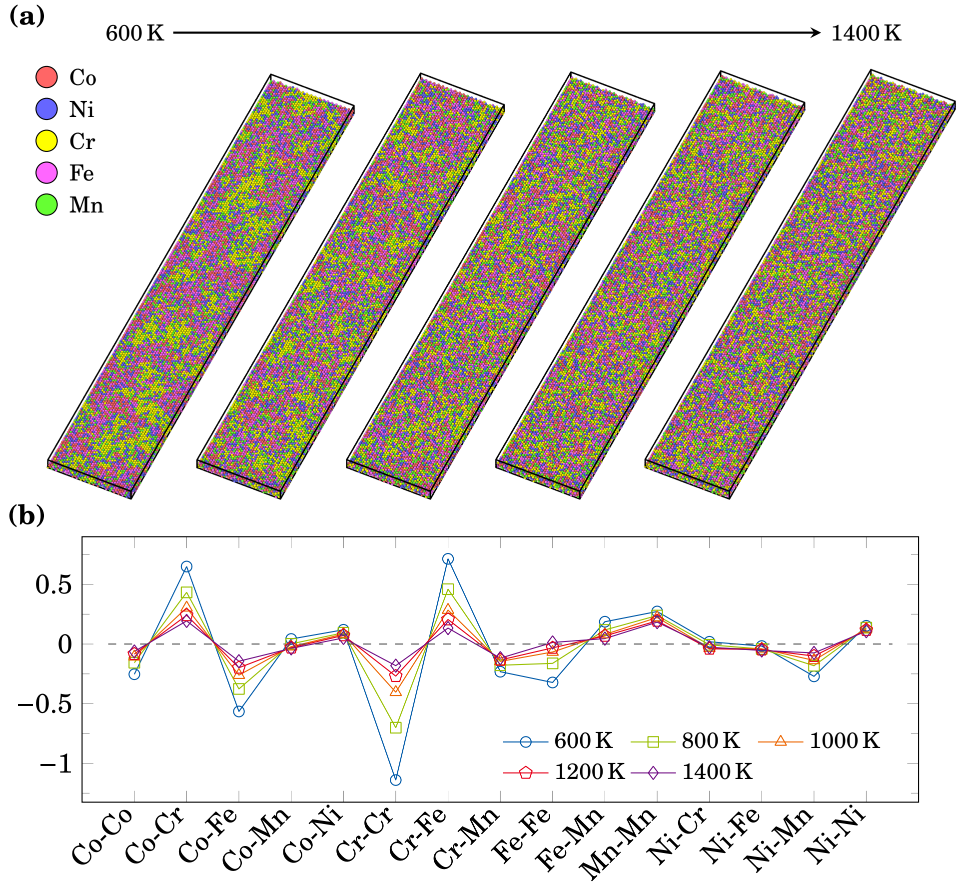

Figure 5.15: (a) Final atomic arrangements of the different CoNiCrFeMn samples after MC equilibration at different temperatures between 600 K and 1400 K. (b) Warren-Cowley SRO parameter[390] α^1_{ij} for the first neighbor shell in the MC annealed Cantor alloy. All possible i-j pairing are shown. Positive α^1_{ij} values indicate attraction while negative values correspond to repulsion between two species.

Figure 5.15 (a) gives snapshots of the final atomic configuration of the hybrid MC/MD equilibration which was subsequently reinserted into the larger samples to calculate F_P, F_c, and M. At 600 K the random solid solution is not stable and phase separation between a Co-Fe rich phase and the other species occurs. As the temperature increases, the solid solution becomes more and more homogeneous as the configurational entropy compensates the difference in mixing enthalpies.[464] To quantify the observed SRO, the Warren-Cowley SRO parameter[390] is calculated and shown in Figure 5.15 (b). The Warren-Cowley parameter α_{ij}^{n} compares the probability of finding a given pair of atomic species i and j to the expectation value for an ideal random solution. In an adapted form for multicomponent alloys it is given by,[60]

$$\alpha_{ij}^{n} = 1 - \frac{P_{ij}^{n}}{x_j} \tag{5.2}$$

where n indicates the considered neighbor shell and P_{ij}^{n} is the conditional probability of finding an atom of species j around an atom of type i. x_j is the molar fraction of species j in the alloy as this corresponds to the probability of finding an atom of type j as a neighbor of i in the random solution. A positive α value indicates a higher probability of finding two species next to each other, i.e., attraction, while a negative one indicates repulsion.

Going back to Figure 5.15 it can be seen that equilibration at low temperatures leads to prevalence of Co-Cr and Cr-Fe pairs, while Cr-Cr and to a lesser degree Co-Fe bonds are reduced in number. This is in agreement with established literature where Cr-Cr bonds have been found to be reduced in CoCrNi,[261,297] CoCrFeNi,[296] and CoCrFeMnNi[208] in equilibrium. Note that while measurements by Zhang et al.[297] indicate an increase in Co-Cr and Ni-Cr bonds, their alloy did not contain Fe hence so that the preferential Fe bonding was obviously not reported. Comparing α at different temperatures shows a reduction in SRO and a turn towards elemental randomness, $\alpha = 0$, as the effect of configurational entropy increases with increasing temperatures and starts to dominate over the mixing enthalpies.[464] Note that even the highest temperature sample, annealed at about 200 K below the melting point, is not in a perfectly random state. Comparing to the DFT MC calculations by Ren et al.,[208] who did their annealing at 1200 K, we find α values in a similar range. Based on these hybrid MC/MD simulations experimental samples, which are subjected to high temperature homogenization annealing, cannot be expected to form a perfect random solid solution on the atomic scale.

Figure 5.16 shows the distribution of atomic pinning point strength, F_P, as function of the MC annealing temperature. It can be seen that the formation of SRO at lower annealing temperatures does not change the shape of the F_P distribution. What changes is the number of high strength pinning points. Their number is much higher in the more random samples annealed at temperatures above 1000 K. This is surprising for two different reasons. Firstly, the MC

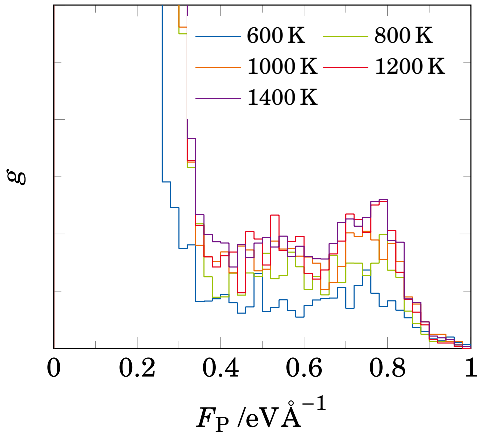

Figure 5.16: Distribution g of F_P for the samples MC annealed at different temperatures. The SRO in the GSF planes of these samples can be seen in Figure 5.15. F_P for leading and trailing partial dislocation displacements are included in each histogram.

simulation increases the number of energetically favorable bonds, which means that breaking of bonds should in turn cost more energy. One would expect to see this change in the form of higher F_P. Secondly, we previously observed a correlation of Co and Cr interaction leading to stronger pinning points. The measured SRO in these samples leads to an increase in Co-Cr bonds which should again increase F_P. It is still an open question, why this is not observed here.

If we add the new data for the different SRO samples to the F_c and M plots, as shown in Figure 5.17, it can be seen that this new data fits seamlessly into the existing data series from the random alloys samples. Curiously, the different SRO samples show a reduced strength compared to the random CoCrFeMnNi sample. This does not agree with intuition, as the theoretical works on SRO from the middle of the last century[293–295] would suggest significant strength increases from SRO formation. Note, however, that the SRO is instilled based on the energy of the atoms on their FCC lattice sites, whereas the pinning point strength is calculated based on the gradient of the GSF landscape. This corresponds to the transition state between stable lattice sites. If there is no trivial correlation between the energies of these two states, the effect of SRO on F_P becomes unclear.

The question of softening from SRO formation remains unclear. One explanation might be related to the fact that with increasing order, the solid solution strengthening is reduced. This can be seen most strongly in the samples MC annealed at 600 K which shows basically the separation into two phases. Phase one retains the 20 % Ni from the equimolar Cantor alloy but is otherwise made up mostly of Cr and Mn in a 2 : 1 ratio. The second phase contains Mn and Ni in their original HEA concentration of 20 % but shows an increase in Co and Fe in concentrations to about 30 %. Interestingly, this phase separation might be observed in a local Warren-Cowley SRO parameter, averaging over the whole glide plane, however, smoothens out Figure 5.15. While the exact strength of

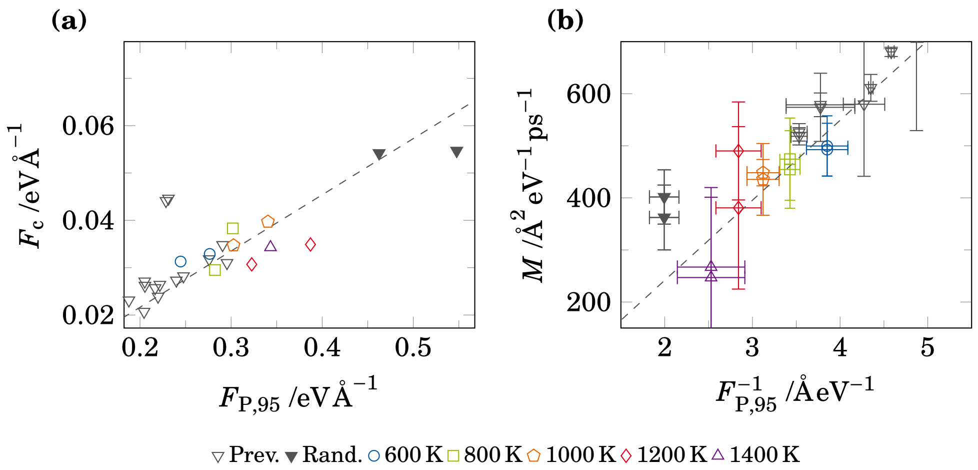

Figure 5.17: (a) Critical force F_c required to initiate dislocation motion in Cantor alloy with different degrees of SRO. Corresponding Warren-Cowley SRO parameters are given in Figure 5.15. (b) Dislocation mobility M obtained under a constant applied load of F_c at 2 K in the same samples. F_c is shown in correlation to $F_{P,95}$, while M plotted against its inverse. The data obtained for a variety of random alloys already shown in Figure 5.12 are added to each graph (*Prev.*) for comparison, dashed lines indicate the fit from this data. The random CoCrFeMnNi samples data is highlighted specifically: *Rand.*

these phases is unknown, Figure 5.12 and Figure 5.13 might be an indication that they have a lower F_c and higher M than the equimolar HEA.

This, however, cannot explain the absence of strengthening in the samples MC annealed at high temperatures, where no phase separation is observed. Looking into literature, Antillon et al.[38] reported that the effect of SRO on critical shear stress for glide of an edge dislocation in the $\mathrm{Co_{30}Fe_{16.67}Ni_{36.67}Ti_{16.67}}$ alloy is almost negligible. They attribute this to the fact that while SRO leads to a chemical strengthening, the ordering also changes the atomic misfit volumes, which are the key ingredient to solid solution strengthening model by Varvenne et al.[72] (cf. Subsection 2.2.1). In their model alloy, these two effects compensate each other the case of edge dislocations, leaving their glide stress constant after SRO formation.

5.8 Dislocation Pinning on Nano-Precipitates

Based on discussions with our experimental collaborators we also added two additional samples to investigate alternative origins of dislocation pinning. These were ideally random CoCrFeMnNi alloy containing coherent FCC nano-precipitates in the glide plane. We artificially inserted 50 spherical $L1_2$ ordered particles into the sample. Their radius was chosen to be either 6 Å or 12 Å,

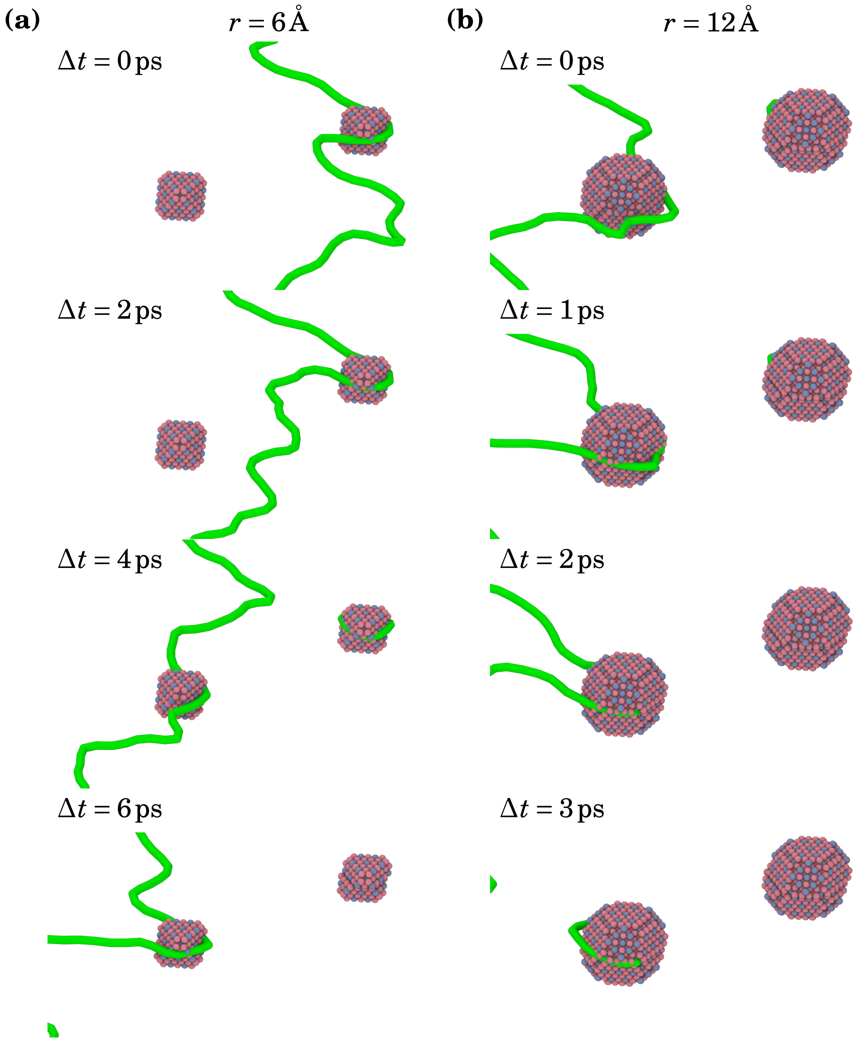

Figure 5.18: Ordered Co_3Cr $L1_2$ precipitates in a CoCrFeMnNi HEA matrix interacting with a dislocation line. The Shockley partial dislocation is shown in green, all atoms apart from the Co_3Cr particles are deleted for clarity.

as these are below the resolution limit of conventional TEM. Meaning that samples that are presumed random in the experimental context could still contain precipitates of this size. The $L1_2$ structure was filled with Co_3Cr as we expect it to have the strongest pinning effects on dislocations based on the Co-Cr interaction outlined in Section 5.5.

These new simulation cells and the dislocations therein are subjected to shear stress under the same protocol as all other simulation cells. The two samples containing precipitates show that while the smaller precipitates can be sheared by the dislocation, the larger ones have to be passed using the Orowan mechanism leaving behind Orowan loops around the particles.[68] Figure 5.18 (a) shows the dislocation in the CoCrFeMnNi sample containing the smaller ($r = 6$ Å) precipitates passing two of them. The dislocation reaches the first precipitate, bows out and easily detaches. The remaining Orowan loop immediately collapses leaving the $L1_2$ particle in a sheared state. The second precipitate experiences the same as it is passed by the dislocation. Figure 5.18 (b) shows the larger precipitates with $r = 12$ Å. Here, it can be seen that both particles are passed by the dislocation using the Orowan mechanism leaving behind an Orowan loop. For the right precipitate the line tension is sufficiently strong to annihilate said loop, while the left one persists for the remainder of the simulation.

Now we are interested in the dislocation pinning wavelength or a measure for the dislocation waviness. Naively one would determine the frequency and wavelength of the dislocation line using a Fourier transform (or a similar process, e.g., Lomb-Scargle periodogram[465]) of the dislocation coordinates. Unfortunately, this is impossible, as the dislocation line does have the required property of a function, i.e., their $y(x)$-coordinates are not unique, as the dislocation line can form loops or fold back on itself. Additionally, we tried to evaluate the roughness function for line-like manifolds to the extracted dislocation lines following the approach by Péterffy et al.[283] The small number samples and still rather short dislocation lines available to us made it impossible to obtain converged results.

In the end, we decided to use a more simplified approach measuring the ratio of observed dislocation line length l to the length of the ideal straight dislocation l_0. The greater the ratio l/l_0, the longer the dislocation line and therefore more meandering its shape. Figure 5.19 (a) gives this ratio for the long dislocation samples introduced previously and in Section 5.6. Note that only dislocation segments having a length greater than 100 Å are considered. This filters out the stable Orowan loops which form in the precipitate containing samples and shifts the focus on the waviness of the two initially inserted partial dislocations. In (b), the same analysis for the short dislocation line samples of Section 5.5. As there were no Orowan loops found in these samples, no filtering of dislocation lines needed to be performed. Comparing the random CoCrFeMnNi sample to the one containing the smaller precipitates shows that they have a very comparable increase in dislocation line length, indicating comparable bowing out of the dislocation line. The $r = 12$ Å sample, on the other hand, shows longer resulting dislocation lines as these large precipitates are more difficult to pass. Therefore, they lead to a greater bowing out of the dislocation line. There might also be an increase in line length due to imperfect filtering of the stable Orowan loops. Comparison to the other random alloy samples shows that the dislocation waviness in CoCrNi is comparable to the Cantor HEAs. At $t \gtrapprox 75$ ps, however, the dislocations CoCrNi become permanently pinned leading to a constant l/l_0. The CoCrCuFeNi alloy shows almost no dislocation pinning while the $Co_{0.3}Fe_{0.17}Ni_{0.37}Ti_{0.17}$ alloy, on the other hand, shows intermediate dislocation line length extension. This is quite surprising, as both these alloys show low critical forces to initiate dislocation glide and

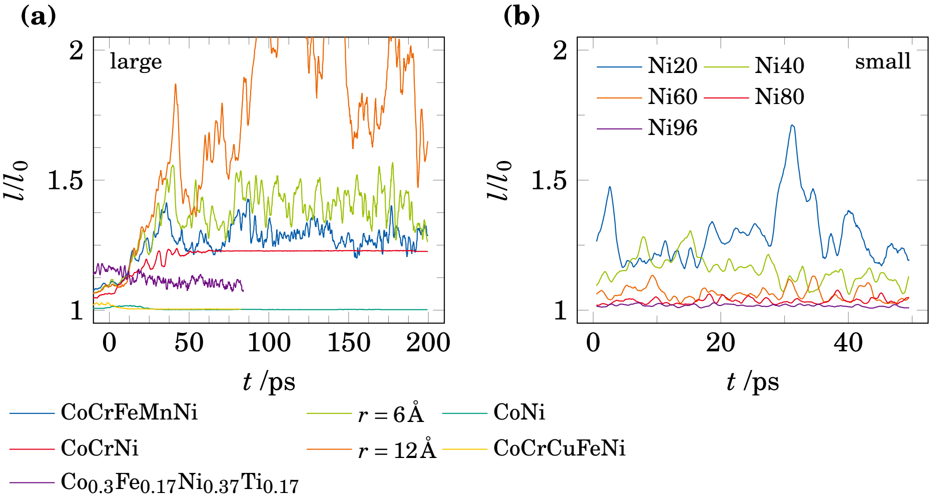

Figure 5.19: (a) Ratio of dislocation line length during glide l and the line length of the straight dislocation l_0 for different samples in the large dislocation simulation cells. r = __Å denotes the two samples containing secondary Co_3Cr $L1_2$ particles. (b) Same analysis for the different small dislocation samples prepared in the Section 5.5. Samples labeled *Ni__* in the legend correspond to pseudo-binary compositions of $(CoCrFeMn)_{1-x}Ni_x$. *Ni20* is the equimolar Cantor alloy. l/l_0 is taken as a measure for the waviness of the dislocation line, where higher values correspond to greater waviness. All data was subjected to smoothing using a moving window average of ten data points.

high dislocation mobilities. This means that the waviness of the dislocation line is not a good descriptor for either of the two. Figure 5.19 (b) shows the same analysis for the quasi-binary $(CoCrFeMn)_{1-x}Ni_x$ series of samples. Here, it can be clearly seen, how a reduction in solute concentration leads to a steady decrease in stretching of the dislocation line during glide, as the dislocation line is only weakly pinned and glides in a straighter line configuration. Comparing l/l_0 in the equimolar Cantor alloy sample (*Ni20*) for both initial dislocation line lengths reveals a very similar change in dislocation line lengthening. Therefore, the dislocation pinning is captured well, even the smaller samples. The small samples shown in (b), however, show a much larger standard deviation, as pinning in one spot, and the associated change in dislocation line length, cannot be compensated by other line segments far from the pinning site.

As already outlined in Subsection 2.2.6, strengthening in different HEA matrices due to coherent L_12 precipitates has already been studied experimentally.[33,34,207,209] They find substantial strength increases in the order of 275 MPa to 750 MPa. Our preliminary data, on the other hand, shows comparable strength and dislocation mobility between the precipitate containing and the ideally random CoCrFeMnNi samples. To create representative plots analogous to Figure 5.13, more calculations are required to obtain statistically reliable results on strength and mobility. There are two main differences between these experimental measurements and our calculations, so far. Firstly, we added a significantly lower density of precipitates. As we did not insert precipitates homogeneously in the samples, but only in the glide plane, we cannot give a meaningful volume fraction, but the area fraction within the glide plane for the $r = 6\,\text{Å}$ sample is equal to 0.63 %, while the $r = 12\,\text{Å}$ has a higher area fraction of 2.52 %. Experimental reports, on the other, hand find volume factions greater than 20 % within their samples. Secondly, the experimental reports assume shearing of the particles, which makes their strengthening independent of the precipitates' size.[309] This shearing has only been observed by Yang et al.,[207] directly. The Co_3Cr particles which we inserted into our Cantor alloy samples are not always sheared, meaning that their resistance against dislocation glide becomes size dependent, as Orowan loops need to form.[310] This could further amplify the effect of the smaller area fraction, as we do not only have fewer, but also much smaller secondary phase particles compared to these experiments.

5.9 Conclusion

After this in-depth investigation of individual edge dislocations and their interaction with the matrix of many dilute and concentrated alloys, we can now answer the research questions posed in Section 2.4.

I. The dislocation line shape in concentrated alloys is not only a local phenomenon, as the dislocation line tension limits the bowing out of the dislocation line. Nevertheless, we were able to show that samples with the same atomic arrangement in the near-field but different far-field configurations give have comparable dislocation arrangements in this near-field region.

II. We propose the slope of the atomic GSF curve as a descriptor for strong dislocation pinning sites in random concentrated alloys. A view that magnifies the established Peierls model to the atomic scale to account for the chemical fluctuations in concentrated alloys.

III. We confirm that regions of steep atomic GSF curves have longer dislocation dwell times under applied load, i.e., the dislocation line becomes pinned on these obstacles.

IV. Even though, Co-Cr rich chemical environments show a propensity for dislocation pinning, there is no unique chemical environment or structural motif that is responsible for the dislocation pinning in the Cantor alloy. Therefore, our findings suggest Labusch type weak pinning within this system. This is in line with the findings by Leyson et al.[217] and confirms the assumptions made by Varvenne et al.[72,89]

V. The strength of the strongest dislocation obstacles is a good descriptor for the critical force required for dislocation motion and dislocation mobility under constant load for a wide range of alloys.

VI. Hybrid MC/MD annealing of the Cantor alloy at different temperatures leads to phase composition into two different phases at lower annealing temperatures and partial SRO formation at higher temperatures.

VII. These partially ordered samples all show a reduced strength and increased dislocation mobility compared to the random CoCrFeMnNi alloy.

VIII. Even a comparatively small volume fraction of tiny (radius of 6 Å to 12 Å) ordered particles within the random alloy can lead to a substantial increase in dislocation line length indicating substantial waviness of the dislocation line. Therefore, particles or ordered regions invisible to TEM or APT methods can already lead to visible changes in the dislocation line shape.

6 Grain Boundaries

> *"[T]he possible discovery of new, hitherto unknown supermaterials will forever be a worthy cause."*
>
> — E. P. George *et al., 2019*[2]

The results presented sections 6.1 to 6.4 are published in:

> "D. Utt, A. Stukowski, and K. Albe, *Grain boundary structure and mobility in high-entropy alloys: A comparative molecular dynamics study on a Σ11 symmetrical tilt grain boundary in face-centered cubic CuNiCoFe*, Acta Materialia 186, 11–19 (2020)".[376]

The following chapter features the investigation of an equimolar CoCuFeNi high-entropy alloy (HEA) in comparison to its average-atom (avg.-atom)[111] counterpart and other pure metals. The change in material system from the Cantor alloy system, to this four component system is necessary as both the avg.-atom method and the semi-grand canonical Monte Carlo (MC), two key methods employed throughout this chapter, are only available for this material system.[†] First, the magnitude of the intrinsic lattice distortions is assessed in comparison to thermal vibrations. These become important in this chapter, as slight displacements of the atoms, away from their ideal lattice sites, could lead to structural differences in the equilibrium grain boundary (GB) configuration. Secondly, the structure and mobility of a high symmetry Σ11 symmetrical tilt grain boundary (STGB) is measured. Lastly, the results obtained for the one STGB will be transferred to a nanocrystalline (NC) sample containing multiple grains in random orientations. Furthermore, we will show the effect of Cu segregation to the GB on the grain growth behavior and GB mobility.

6.1 Intrinsic Lattice Distortions

The intrinsic lattice distortions are one of the four *core effects* initially postulated for HEAs.[15] and have since then been investigated thoroughly from a simulation[224,225,227,466–468] and experimental[224,226,228,229,468] standpoint. Here we determine the impact of the intrinsic lattice distortions on the CoCuFeNi

---

[†] Technically, they have only been implemented for EAM, but not MEAM interatomic potentials. The CoCrFeMnNi alloy from the previous chapters is based on an MEAM interatomic potential, while the CoCuFeNi alloy is described by an EAM potential.

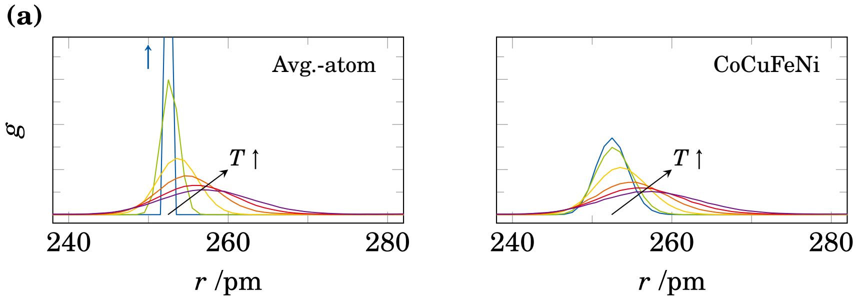

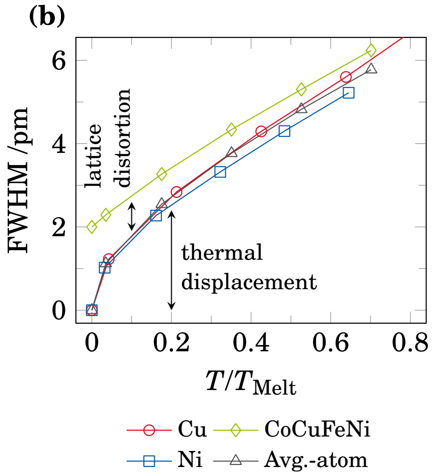

Figure 6.1: Determination of the intrinsic lattice distortions in the CoCuFeNi HEA compared to its constituents and its avg.-atom equivalent. (a) RDF g as function of the interatomic distance r for the avg.-atom and the HEA sample, respectively. (b) FWHM of g on the homologous temperature (T/T_{Melt}) scale. The difference between CoCuFeNi and avg.-atom corresponds directly to the lattice distortions. Adapted from Ref. 376.

HEA over a broad temperature range which will later be helpful in understanding grain boundary migration and grain growth. This HEA is compared to its stable face-centered cubic (FCC) constituents and a so-called avg.-atom material to compare the magnitude of the lattice distortions to the thermal vibration amplitude. The avg.-atom is a virtual element based on an interatomic potential which can be derived from an averaging of the Co, Cu, Fe, and Ni terms used for the full CoCuFeNi HEA interatomic potential.[111] This virtual element has the same long-range mechanical properties as the full HEA but it is only composed of a single species. Comparison of HEA and avg.-atom allows for the isolation of the effects caused local chemical fluctuations within the complex alloy. See Subsection 3.7.2 for a description of the method and a characterization of this specific avg.-atom material. The full width at half maximum (FWHM) of the radial distribution function (RDF) g is taken as measure for the lattice distortions. It is obtained from a Gaussian fit of g as function of the interatomic distance r. Comparison of avg.-atom and CoCuFeNi alloy allows us to separate thermal vibrations from intrinsic lattice distortions.

Figure 6.1 (a) shows $g(r)$ for the avg.-atom and the HEA sample around the FCC nearest neighbor distance at temperatures T between 0 K and 1000 K. At 0 K, $g(r)$ in the avg.-atom sample results in a Dirac delta function at $r = a_0/\sqrt{2} =$ 252 pm as all atoms sit on their ideal FCC lattice sites. In the CoCuFeNi sample, on the other hand, the atoms are evenly distributed around their ideal positions. Figure 6.1 (b) gives the resulting FWHMs for these two samples as well as for pure Cu and Ni. It shows that the intrinsic lattice distortions in the CoCuFeNi alloy amount to 2 pm at 0 K. As the temperature increases, the increase in thermal vibration amplitude leads to a broadening of $g(r)$ for all samples. Due to the significant differences in melting temperature for the samples, the data is normalized by the melting temperature T_{Melt}, which was determined using the melt-interface method.[375] For temperatures below $\approx 0.2\,T_{\text{Melt}}$ the lattice distortions in the HEA are substantially greater than the thermal vibrations. For higher temperatures the difference in FWHM between CoCuFeNi alloy and avg.-atom remains almost constant at 0.557(120) pm, while the thermal broadening of $g(r)$ steadily increases.

The overall low magnitude of the intrinsic lattice distortions compared to the thermal vibrations in the model HEA is expected given the small difference in Goldschmidt radii[421] for the four different elements in the FCC phase. They are found to be equal to; Cu:127.8 pm, Ni: 124.4 pm, Co: 125.5 pm, and Fe: 128.3 pm. Nevertheless, these differences are greater than the one found in the often studied Cantor alloy where all radii are between 124.0 pm and 125.3 pm.[225] From the perspective of the hard-sphere model, we would expect greater lattice distortions in the CoCuFeNi alloy compared to the Cantor alloy.

6.2 Structure of a Σ11 Grain Boundary

In the following section, we will investigate the 0 K and the high temperature structure of a $\Sigma 11/(3\,3\,2)\langle 1\,1\,0\rangle$ STGB in different pure metals compared to the CoCuFeNi HEA and an avg.-atom sample. Changes in the equilibrium GB structure could be facilitated by the lattice distortions in the HEA or by differences in the stacking fault (SF) energy. This specific STGB was selected as a representative example of a high angle GB. It has multiple beneficial properties for investigation. Based on the works by Rittner and Seidmann[396] on GBs in Cu it is known that this Σ11 STGB has good accessibility of the 0 K equilibrium structure and only a few metastable high temperature structures — making it a good prototype system. Moreover, it does not show structural relaxation along the rotation axis,[396] a rather uncommon effect, which would reduce the transferability of our results.

Figure 6.2 (a-f) gives the 0 K minimum energy arrangement of this STGB in different elemental metals, the avg.-atom, and the CoCuFeNi HEA samples. Only GB arrangements of constant atomic density were considered, i.e., no atoms were inserted or removed to find the minimum energy structure. All monoatomic samples (a-e) feature a regular GB structure with linear D type and kite-shaped E type repeating structural units (RUs) (cf. Figure 3.12 (a)).[396,397] Due to the difference in atomic size for the different pure metals, the interior angles of the RUs are marginally different in each sample. Nevertheless, the structure

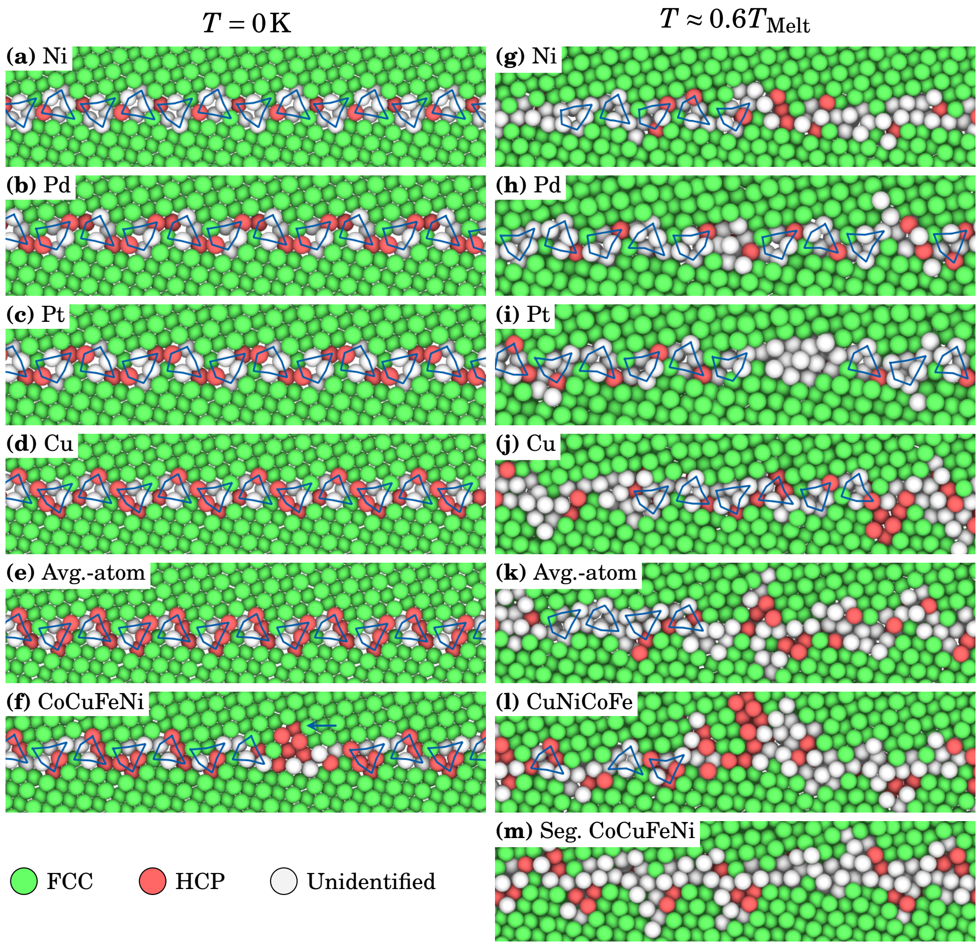

Figure 6.2: GB structure of a Σ11 STGB for the different samples at 0 K (a-f) and high temperature (g-m). Blue lines indicate the expected kite shaped *E* type RUs.[396,397] At 0 K only the CoCuFeNi sample shows strong deviations from this GB arrangement. At higher temperatures this structure changes and the emission of partial dislocations from the boundary can be seen (arrow). This change is most pronounced for the low SF energy samples (j-m). See Section 6.4 for more details on the seg. CoCuFeNi sample. Adapted from Ref. 376.

of this STGB always resembles the lowest energy arrangement reported in Cu by Rittner and Seidmann.[396] The CoCuFeNi HEA sample (f) also shows kite-shaped RUs, but instead of constant repetition over the whole GB plane, they are interrupted by a Shockley partial dislocation which is emitted from the GB (highlighted by an arrow).

We suggest two possible origins for this structural difference in the HEA sample. Either the elastic strain caused by the intrinsic lattice distortions could assist the partial dislocation emission, or local chemical fluctuations give rise to a locally reduced stable and unstable SF energy which in turn modifies the energy barrier for partial dislocation emission.[469] While we cannot provide direct evidence for this spatial variation of the SF energy, it has been reported for other HEAs[74,261,271,279] in literature or in the previous Chapter 5.

Next, molecular dynamics (MD) simulations are used to determine whether the apparent low temperature similarities between the different STGBs persist up to high temperatures. Figure 6.2 (g-m) shows the magnified GB structures after equilibration at $T \approx 0.6\,T_{\mathrm{Melt}}$. Compared to the 0 K study, we added a sample which features Cu seg. to the GB. Here a strong difference between the three metals with a high SF energy (Ni, Pd, and Pt) and the low SF energy samples can be seen. The former show mostly ordered and narrow GBs with low temperature RUs remaining somewhat intact. The other four samples show wider STGBs with frequent Shockley partial dislocation emission and overall increased disorder.

There are two main conclusions to draw from the high temperature GB structures. Firstly, the avg.-atom (k) and CoCuFeNi HEA (l) samples show very similar atomic arrangements with some remnants of the initial RUs but also frequent partial dislocation emission. This apparent similarity supports the findings of Section 6.1 where we conclude that the intrinsic lattice distortions differentiating those two sample are most important at low temperatures but overpowered by thermal vibrations at high temperatures. Moreover, the seg. CoCuFeNi sample does not show a substantially different GB structure than the perfectly random CoCuFeNi sample. Given that the GB structure appears to be strongly correlated to the SF energy, the relative similarity between the two in energy might be the root cause for their structural similarity. See Section 6.4 for more details on the seg. CoCuFeNi sample. This leads us to the initial conclusion that differences in GB mobility observed in these samples are not related to structural differences but have to be of different origin. In the next section, the aforementioned STGBs will be investigated under dynamic conditions during their migration.

6.3 Mobility of a $\Sigma 11$ Grain Boundary

After the detailed investigation of the GB structure of the chosen $\Sigma 11/(332)\langle 110\rangle$ STGB we investigate its mobility and migration mechanism. To drive the migration of the planar STGB, the synthetic driving force method derived by Janssens et al.[398] is used, cf. Section 3.11 for more details. The goal of this section is to establish, whether the grain boundary mobility in HEAs is intrinsically reduced compared to similar monoatomic metals.

In the bicrystalline sample geometry, the synthetic driving force method adds a potential energy Δe to each atom belonging to one of the two grains. This results in an energy gradient at the GB which in turn leads to a driving force for the atoms to change grain allegiance and thereby facilitates GB migration.[398]

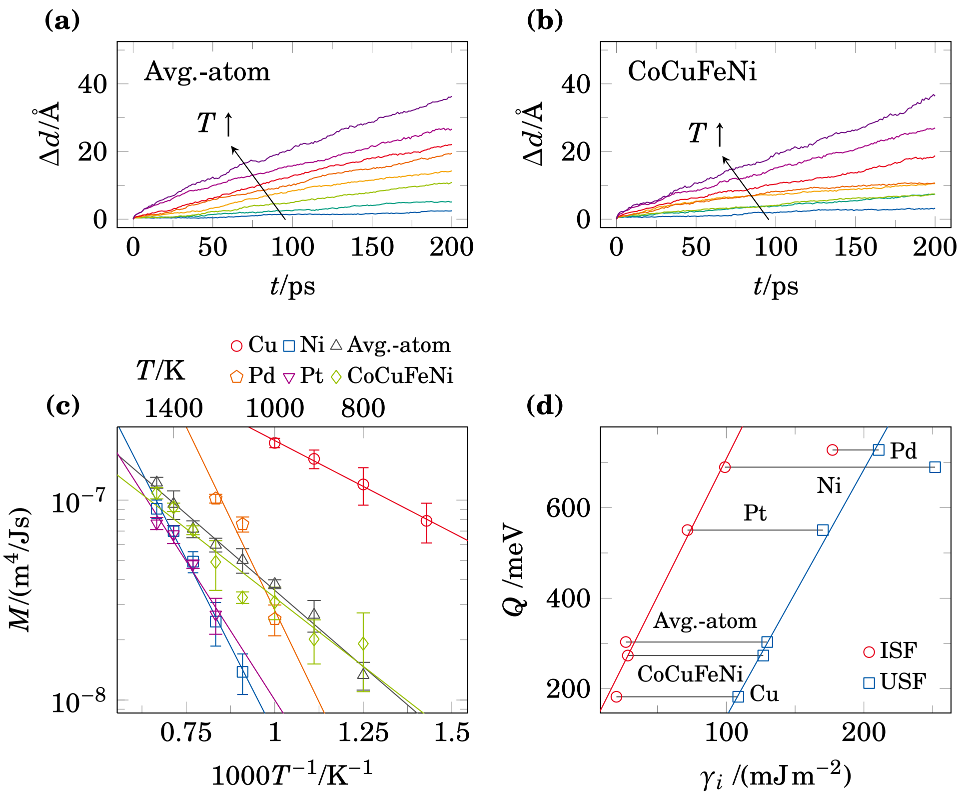

Figure 6.3: Migration of a Σ11 STGB under applied synthetic driving force[398] $\Delta e = 15\,\mathrm{meV}$ and resulting GB mobilities. (a&b) Direct comparison of the GB migration distance Δd as function of time t in the avg.-atom and the CoCuFeNi sample. Increasing temperatures between 700 K and 1400 K are shown. (c) Arrhenius plot showing the GB mobility M over the inverse temperature T for all studied samples. (d) Correlation of the GB migration activation energy to the ISF and USF planar fault energies γ. Partially adapted from Ref. 376.

Physically, this added potential energy is comparable to excess energy stored in grains from an increased defect density or increased elastic energy.[470]

In the following, we apply a constant Δe of 15 meV per atom. Figure 6.3 (a&b) show the GB migration distance Δd averaged over ten independent simulations over the simulation time t. Different lines correspond to increasing temperatures between 700 K and 1400 K. The GB velocity v can be obtained from a linear fit of $\Delta d(t)$. Both, avg.-atom and CoCuFeNi sample show approximately the same GB velocity. Since the avg.-atom sample only contains a single species but features otherwise similar material properties as the CoCuFeNi alloy this implies that the chemical fluctuations in the HEA do not strongly pin this STGB.

The GB mobility M can be calculated directly from v and Δe using Equation 6.1,

$$M = \frac{v\Omega}{\Delta e}, \tag{6.1}$$

where Ω is the atomic volume.[398] The temperature dependence of M can be described by an Arrhenius type equation,[471]

$$M(T) = M^{\infty} \exp\left(\frac{-Q}{k_{\mathrm{B}}T}\right), \tag{6.2}$$

where Q is the activation energy for thermally activated GB migration, M^{∞} is an exponential prefactor corresponding to the GB mobility at infinitely high temperature and $k_{\mathrm{B}}T$ has its usual meaning. Both, M^{∞} and Q may be obtained from a linear fit of the temperature dependent mobility data.

Figure 6.3 (c) shows the measured mobility for the Σ11 STGB in different pure metals, the avg.-atom sample, and the CoCuFeNi alloy. It can be seen that while all samples show an Arrhenius type (Equation 6.2) behavior, the activation energy is vastly different. Cu, CoCuFeNi, and avg.-atom show low activation energies, while Ni, Pd, and Pt show comparatively high Q values. There are two main conclusions to be drawn from this data. Firstly, the avg.-atom and the HEA sample both show, within the margin of error, the same GB mobility and activation energy over the whole temperature range. Supporting the previous statement that neither the intrinsic lattice distortions nor solute drag caused by the local chemical fluctuations in the HEA lead to a substantial reduction in GB mobility. Secondly, the activation energy for GB migration correlates strongly with the intrinsic stacking fault (ISF) and unstable stacking fault (USF) energies. Figure 6.3 (d) shows Q for the different samples over the two (ISF and USF) planar fault energies γ_i, which were calculated using the standard procedure.[252]

The origin of this linear relationship can be understood in terms of the migration mechanism for this STGB. The energy barrier to nucleate a partial dislocation from a defect like a GB is proportional to γ_{ISF} and γ_{USF}[469] therefore the observed correlation points at a migration mode based on repeated partial dislocation nucleation and absorption of the GB. Figure 6.4 shows an example of such a process in the CoCuFeNi sample at 1100 K. Starting from the initial STGB structure (a), Shockley partial dislocations are first emitted from the GB and the boundary plane advances (b&c). Afterwards, the GB arrives in its new position with partial dislocations mostly retracted into the boundary (d). Now, the boundary plane has advanced compared to its initial position (marked by a dashed line). As stated earlier, the $\Sigma 11/(3\,3\,2)\langle 1\,1\,0\rangle$ studied here consists of kite-shaped E and linear D type RUs[396]. Especially the E type RUs have been found to be preferential sites for partial dislocation nucleation during tensile loading of GBs, due to their comparatively large free volume[472,473].

In conclusion, comparing the mobility of a Σ11 STGB in a CoCuFeNi HEA and its avg.-atom counterpart, we find that neither the local chemical fluctu-

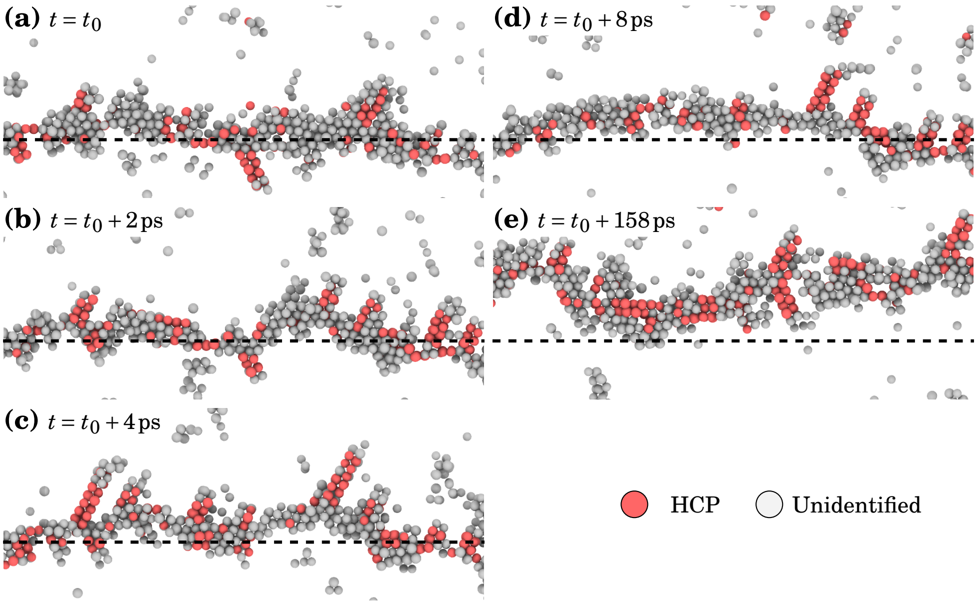

Figure 6.4: Grain boundary migration mechanism for a Σ11 STGB in the CoCuFeNi HEA at 1100 K under an applied synthetic driving force. (a) initial GB position (b&c) partial dislocation emission and GB advancement. (d) configuration in forward position with mostly reabsorbed partial dislocations. (e) GB configuration after a longer time interval shows its progress from the initial position. The initial STGB plane is marked by a dashed line in all figures, the grain growth direction always points up. Adapted from Ref. 376.

ations nor the intrinsic lattice distortions lead to a reduction in GB mobility. Instead, the mobility correlates with the ISF and USF energy based on the observed GB migration mechanism.

6.4 Influence of GB Segregation

Another possible reason for the immobilization of GBs in HEAs could be GB segregation. It has been established that most HEAs are not thermodynamically stable but are instead kinetically trapped in a metastable solid solution state.[9] Therefore many HEAs show phase separation during annealing.[24–29] We studied the effect of GB segregation using a hybrid MC/MD equilibration scheme to find the thermodynamic equilibrium configuration of atoms in the sample.[350] The MC algorithm allows for a fast rearrangement of atoms in the sample without the need to wait for slow diffusive processes. In each MC trial move, a lattice site is selected, and its atom is swapped against one of the other species in the alloy taken from an infinite reservoir. The chemical potential of this reservoir depends on the two distinct species which are swapped and the global concentration.

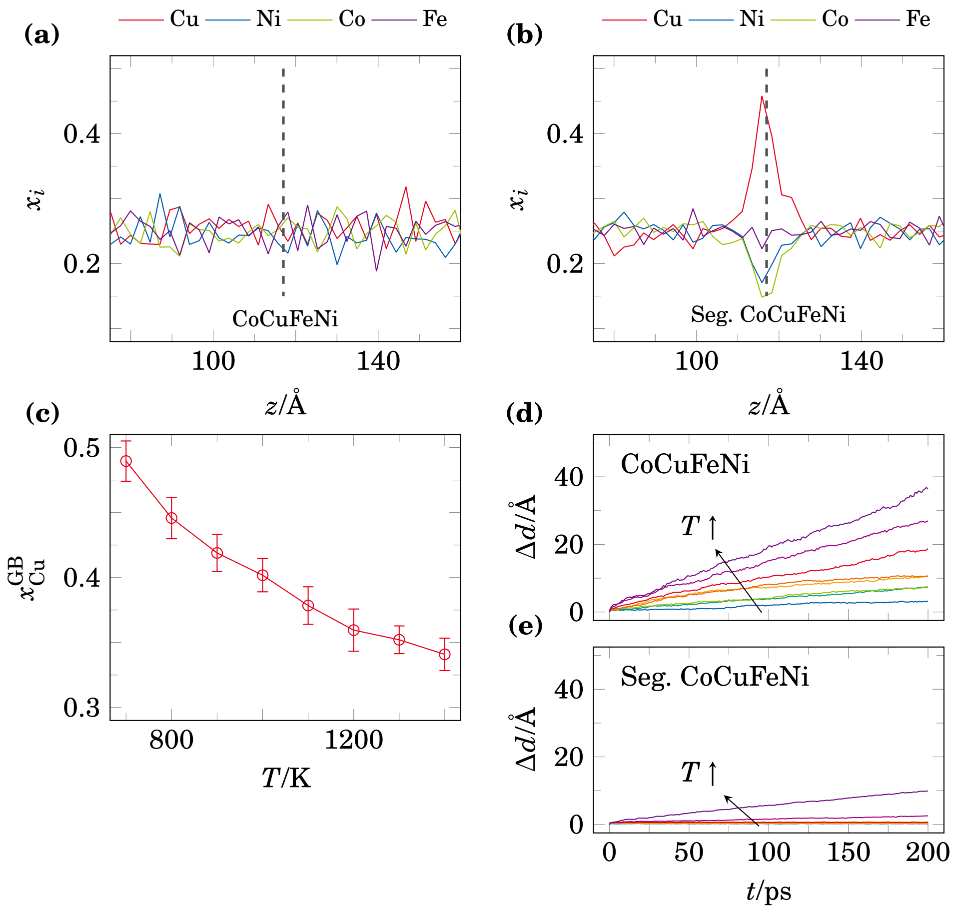

Figure 6.5: Segregation to a Σ11 STGB and its impact on GB mobility. Concentration x of species i around the initial GB position (marked by a dashed line) in the perfectly random HEA (a) and the seg. HEA sample after hybrid MC/MD equilibration (b). This chemical equilibration leads to a pronounced increase in Cu around the GB. Both concentration profiles are taken at 800 K. (c) Mean increase in Cu around the STGB as function of the annealing temperature. (d&e) comparison of the GB migration distance Δd over time t in the random CoCuFeNi sample (cf. Figure 6.3) and the seg. CoCuFeNi sample, respectively. Each line corresponds to increasing temperatures between 700 K and 1400 K. Partially adapted from Ref. 376.

For further information see Section 3.4.[350] This leads to a fast redistribution of atomic species throughout the sample in a thermodynamically coherent manner. We know from our previous work[60] that Cu accumulates around volume defects[474] in the crystalline HEA. Hence, Cu is expected to segregate to the Σ11 STGB as well. The insolubility of Cu in different HEA matrices observed in a variety of experimental studies as well.[24,30,163,165,172,475–477]

Figure 6.5 (a&b) show the elemental distribution normal to the STGB plane in the perfectly random and the seg. CoCuFeNi HEA samples, respectively. Here the concentration profiles at 800 K are shown and the GB position is marked by a dashed line. While the local chemical fluctuations in the random alloy remain minor, the seg. sample shows a strong increase of Cu in the vicinity of the GB. This increase in Cu corresponds to a reduction in Ni and Co, while the Fe concentration remains constant. Figure 6.5 (c) gives the peak Cu concentration around the GB in the seg. CoCuFeNi samples annealed at different temperatures. As the temperature increases, the configurational entropy starts to dominate over the GB segregation enthalpy leading to the observed decrease in Cu enrichment at the STGB. This trend is in line with analytical GB segregation models developed for conventional alloys[478] and expectations from the Lupis-Elliot rule.[464] Koch et al.[60] have previously shown for this interatomic potential that there is strong clustering of Cu in single crystalline samples at 400 K. This clustering, however, mostly disappears after high temperature annealing at 800 K. Therefore, the still substantial Cu segregation observed at temperatures above 800 K seen in the bicrystalline samples cannot only be attributed to a positive mixing enthalpy in the bulk HEA *pushing* Cu out of the matrix. There is an additional GB segregational enthalpy attracting Cu to the boundaries.

The GB migration distance Δd measured in the random CoCuFeNi alloy and its segregated counterpart are presented in Figure 6.5 (d&e). Grain growth is stipulated using the synthetic driving force method with $\Delta e = 15\,\mathrm{meV}$ (compare Section 6.3). Comparing both HEA samples reveals that for all temperatures between 700 K and 1400 K the Cu solute cloud leads to a strong pinning of the STGB. While in the random CoCuFeNi sample, the GB starts migrating for temperatures above 800 K, the Cu solute cloud prevents all GB motion up to 1300 K in the seg. HEA.

To further quantify the binding energy between the Cu solute cloud and the STGB a very high driving force of 100 meV is applied to the Cu decorated GBs. This driving force is sufficient to move the STGB away from its original position, into the other crystallite. As the boundary is moved from its preferred chemical environment into a random chemical environment, its energy increases. We determine this energy difference to be in the order of $285\,\mathrm{mJ\,m^{-2}}$ and suggest this number as an approximation for the Cu-GB interaction.

In this section, we report the strong pinning force exerted by Cu atoms segregated to a $\Sigma 11$ STGB. This pinning force stems from a reduction of the GB energy after Cu decoration which effectively pins this boundary up to temperatures of 1300 K. It is impossible to observe diffusion of the Cu solute cloud alongside the GB on timescales accessible by MD simulations. Nevertheless, one could envision that at sufficiently high temperatures and longer timescales, STGB and solute cloud start diffusing in tandem through the material. In this case the grain growth kinetics would be expected to follow the diffusion kinetics of the solute cloud. This corresponds to the high impurity concentration or low driving force situation described by Cahn.[313] Moreover, this would be an explanation for the comparable activation energies for diffusion and GB migration found in experiments, e.g., $288\,\mathrm{kJ\,mol^{-1}}$ to $318\,\mathrm{kJ\,mol^{-1}}$ and $321.7\,\mathrm{kJ\,mol^{-1}}$, respectively, in the Cantor alloy.[45,97,100]

One open question that remains is whether the diffusion kinetics in real samples would be sufficiently fast to allow for segregation of one species to the GBs. At high temperatures, diffusion is fast, but the driving force for segregation is low, as the effect of the configurational entropy is strong. Lower temperatures increase the driving force for segregation but the kinetics become exponentially slower. Here one should remember that required diffusion distances to saturate GBs in HEAs are shorter, compared to conventional dilute alloys. This comes from the fact that the segregating species is dispersed in high concentration throughout the sample.[94] The required calculations to determine the exact temperature and cooling conditions for a given alloy to instill the optimum GB segregation profile in a sample are out of scope for this study but are required for real-world applications. Examples from literature show both, GB segregation[100,102] or chemically homogeneous GBs[100,191] with an obvious dependence on the material system and processing route.

This previous section has looked at a single high symmetry tilt GB and found that its mobility strongly depends on its migration mechanism. Obviously, this limits our understanding to GBs following the same migration mechanism. Instead of sampling many more boundaries, as Olmsted et al.[479,480] did, we decided to study larger nanocrystalline samples instead. These contain multiple grains in random orientations separated by GBs of random orientations. Therefore, these simulations are not limited to high symmetry bicrystals fitting into a periodic simulation cell.

6.5 Grain Growth in Nanocrystalline High-Entropy Alloys

Previously, we showed GB mobility results on a single high symmetry STGB and the impact of Cu segregation on GB pinning. In the following we will present results on grain growth in large-scale NC samples to determine if the previously determined GB mobilities can be generalized for random GBs.

To ensure comparability between the different samples, they all start from the same initial microstructure containing 10 grains with an average equivalent radius $\overline{r} \approx 75\,\text{Å}$ (depending on the lattice constant). The FCC lattice sites in this structure are filled with the different pure elements studied for the STGB, the CoCuFeNi HEA, and its avg.-atom counterpart. Levo et al.[63] have shown that the collapse of nanocrystalline grain structures to the single crystalline state, albeit under irradiation conditions, strongly depends on the initial grain sizes and orientations. Our samples are subjected to isothermal annealing at temperatures ranging from $0.6\,T_{\mathrm{Melt}}$ to $0.9\,T_{\mathrm{Melt}}$ for 5 ns. During post-processing, the nanocrystal is divided into individual grains using an experimental grain segmentation algorithm included in OVITO.[382] The latter algorithm is based on

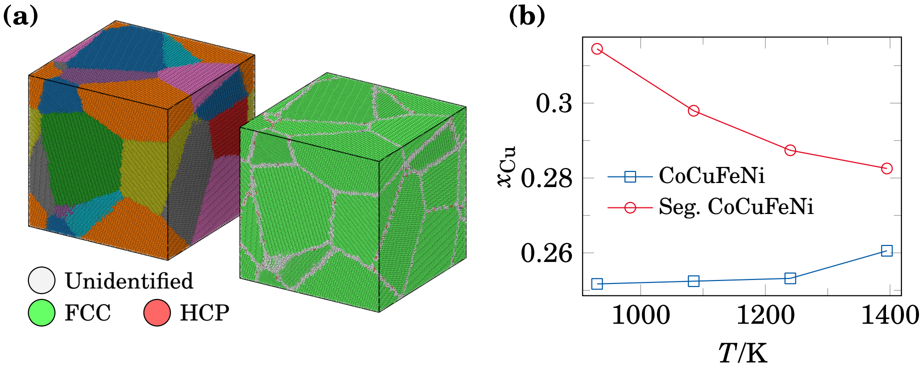

Figure 6.6: (a) Initial grain structure in the NC sample the atoms are color coded based on their local structure type or their grain association. (b) Cu concentration of the GB and its adjacent atomic layer in the seg. and the random CoCuFeNi HEA samples over annealing temperature.

a formulation by Panzarino and Rupert,[481] but featured improved structural detection accuracy and speed. It outputs the number of atoms belonging to each grain N_i.

Figure 6.6 (a) shows the initial NC sample color coded based on the local structure type determined from polyhedral template matching (PTM)[395] and each atom colored based on its grain identity. It can be seen that the experimental grain segmentation algorithm successfully separates the grains at their GBs. GBs can be seen in the PTM color coding as planar regions of *unidentified* atoms. In (b), the Cu concentration of the GB and its adjacent atomic layer is shown as function of the annealing temperature, highlighting the difference between the perfectly random CoCuFeNi sample and its seg. counterpart. Similar to the STGB sample studied before, the competition between segregational enthalpy and configurational entropy leads to a decrease in Cu accumulation at the GBs with increasing annealing temperature (Figure 6.5).[478] Compared to the bicrystalline samples, the maximum excess Cu concentration at the boundaries is reduced. This could be caused by the structural differences between the randomly oriented GBs in the nanocrystal compared to the high symmetry boundary studied in the previous section. It could also be a trivial artifact of the different methods of calculating the excess Cu concentration. While the concentration profile in the STGB sample can be extracted easily using so-called *spatial binning* normal to the GB plane, the meandering GBs in the NC sample require us to use a different approach. Here we select GB atoms and their neighbors based on the PTM results and extract their concentration.

The mean grain size $\overline{N}$ is calculated as a number-weighted average combined with the temperature dependent atomic volume Ω, of a single crystalline

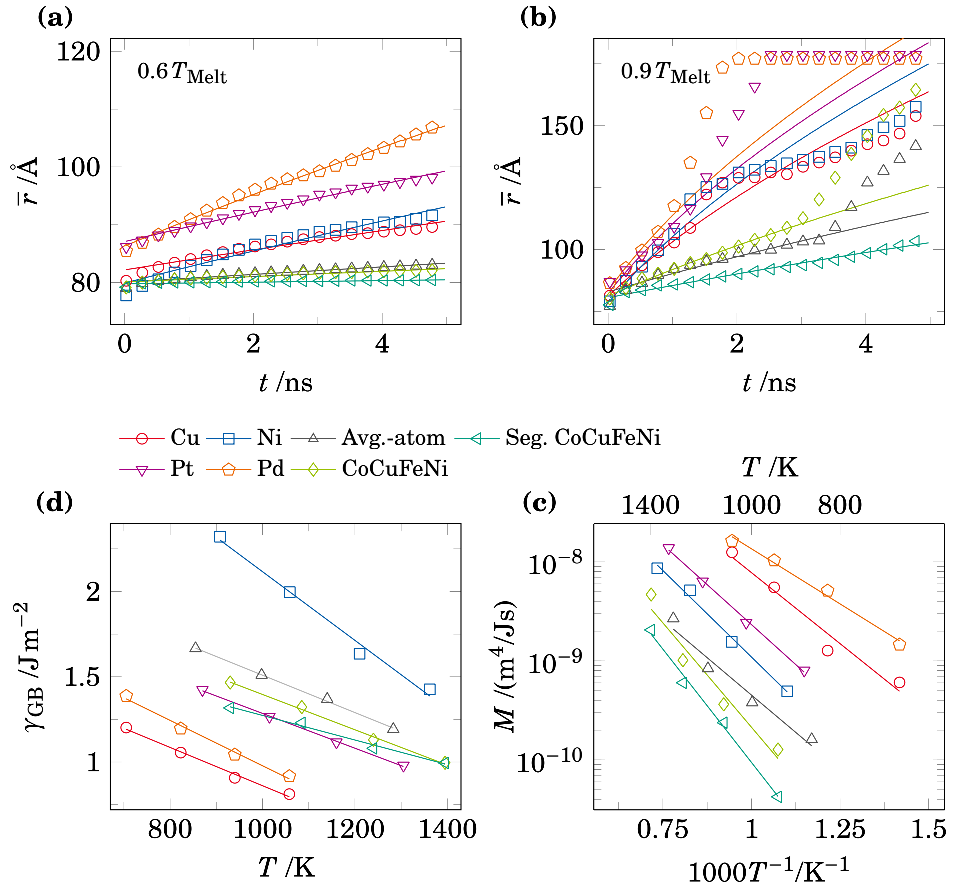

Figure 6.7: Grain size evolution and GB mobility in the NC samples annealed for 5 ns at temperatures between 0.6 T_Melt and 0.9 T_Melt. (a&b) Evolution of the mean grain radius $\overline{r}$ over time (Equation 6.3). Markers show the extracted grain size, while solid lines represent the best fit based on Equation 6.4 (every tenth marker is shown). Only the initial growth regime is included in the fit. Note, the different scale for $\overline{r}$. (c) Temperature dependent GB energy calculated from Equation 6.5. (d) Arrhenius plot of the GB mobility for all samples.

reference sample, the mean radius of an equivalent spherical grain can be calculated,

$$\overline{r} = \left(\frac{3}{4}\frac{\overline{N}\Omega}{\pi}\right)^{\frac{1}{3}} \quad \text{with} \quad \overline{N} = \sum_i \frac{N_i}{N} N_i. \tag{6.3}$$

Figure 6.7 (a&b) gives this mean radius as function of the annealing time t. Here (a) shows the lowest temperature, while (b) corresponds to the highest one. While the grain size is calculated every 25 ps only every tenth data point is shown for clarity. Solid lines show a fit based on the established Burke-Turnbull law,[470,482]

$$r^2 - r_0^2 = kt \quad \text{with} \quad k = 4\gamma_{\mathrm{GB}} M, \tag{6.4}$$

where r is the current radius, r_0 is the initial radius, and k is a rate constant. This rate constant is proportional to the GB energy γ_{GB} and the GB mobility M. At the higher temperature, only the initial parabolic growth regime is fit with this law.

At the lower temperature Pd and Pt show the greatest grain growth rate, while Ni and Cu feature intermediate growth rates. The average grain size in the three HEA adjacent (CoCuFeNi, seg. CoCuFeNi, and avg.-atom) samples appears to be almost constant. The measured grain size evolution is described well by Equation 6.4. Going to the highest annealing temperature, we can see that all four elemental samples (Pd, Pt, Cu, and Ni) immediately show rapid grain coarsening. After one grain has reached a critical size, the nanostructure quickly collapses to the single crystalline state. For these four samples, the critical radius appears to be around 125 Å. The CoCuFeNi and avg.-atom samples show comparatively slower initial grain growth rates, but the onset of rapid grain coalescence happens at smaller sizes of ≈ 100 Å. Only the seg. CoCuFeNi sample does not reach this state of this rapid coarsening. While the initial stages of growth can be described with Equation 6.4, the second regime, with its much higher growth rate could not be fit.

In the previous section, we made conclusions based on the mobility of a STGB, there is currently one ingredient missing to calculate the average GB mobility in the NC samples. The GB energy is needed to determine the average driving force acting on each GB. As the exact GB area A_{GB} is unknown, we need to approximate it,

$$\gamma_{\mathrm{GB}} = \frac{E_{\mathrm{NC}} - E_{\mathrm{Ref}}}{A_{\mathrm{GB}}} \quad \text{with} \quad A_{\mathrm{GB}} \approx \frac{N_{\mathrm{GB}}\Omega}{w_{\mathrm{GB}}}, \tag{6.5}$$

where E_{NC} is the energy of the NC sample and E_{Ref} is the energy of a single crystalline sample containing the same number of atoms. Note that for the seg. CoCuFeNi sample, the random CoCuFeNi HEA has to be used as reference. N_{GB} is the number of structurally unidentified atoms, which are used as a surrogate for the number of atoms located at the GBs and w_{GB} is the width of the GB, which is taken as 10 Å. The calculated GB energy is a function of time and temperature. During the first regime of growth, where Equation 6.4 could be used to describe the change in $\bar{r}$, this energy remains almost constant per sample and temperature. The obtained mean GB energies are plotted in Figure 6.7 (c). It can be seen that for all samples the GB energy decreases with temperature, which is in agreement with some reports on pure metals.[483,484] Sun and Singh, on the other hand, report constant GB energies over a wide temperature window ($T < 0.8\,T_{\mathrm{Melt}}$) with a strong increase at higher temperatures.[485] Their data also suggests that the assumption of a constant GB width might be inappropriate at temperatures above $0.8\,T_{\mathrm{Melt}}$.

Nevertheless, it can be seen that Ni has the highest GB energy, while Cu has the lowest one. Further, the avg.-atom sample has a slightly higher GB energy compared to the multicomponent CoCuFeNi HEA. Comparing the seg. CoCuFeNi alloy to its random counterpart shows that the Cu segregation the boundaries decreases the GB energy measurably, especially at lower annealing temperatures where the amount of Cu segregated to the boundary is higher (cf. Figure 6.6). This can be attributed to the increased Cu concentration at the GBs as Cu is the pure element with the lowest GB energy included in the HEA. Due to the high annealing temperatures and overall unordered GB structures in these samples, a direct structural comparison as done for the STGB samples (cf. Figure 6.2) is impossible.

The resulting GB mobilities calculated based on Equation 6.4, are given in Figure 6.7 (d). The figure shows that the four elemental metals (Pd, Cu, Pt, and Ni) have the highest GB mobilities in the NC samples. Moreover, avg.-atom and CoCuFeNi sample show comparable mobilities at high temperature, but the avg.-atom sample has increased mobility at lower temperatures. Lastly, the seg. HEA has the lowest GB mobility at all tested temperatures. Again, pointing at the strong pinning exerted by the solute cloud on the GBs.

If we now compare the mobilities in the NC samples to the STGB samples investigated initially, shown in Figure 6.3, there are some interesting differences. Cu, which has the highest STGB mobility by a substantial margin only shows the second-highest mobility in the NC samples, while Pd has the highest one. Ni and Pt have the lowest STGB mobilities, less than HEA and avg.-atom samples, albeit show greater GB mobilities than those two in the NCs. These differences in hierarchy can most likely be attributed to a difference in GB migration mechanisms. While the STGB featured one well-defined migration mechanism with a clear indication of its rate defining step, the migration mechanisms for the random GBs in the NC samples are less clear and potentially different. Lastly, as already shown for the STGB samples, the mobility of the seg. CoCuFeNi sample is lower than the one of the chemically random HEA and the avg.-atom samples. Nevertheless, the GB migration in these samples could not be prevented entirely. One reason for this might be the higher driving force acting on the NC GB compared to the low and well-defined artificial driving force applied to the STGBs.

Figure 6.8 presents snapshots of all samples during annealing at $T = 0.9\,T_{\mathrm{Melt}}$. Each sample is shown in two color codings, once based on the local crystal structure type determined by PTM and once based on the grain segmentation algorithm. It can also be seen that the NC grain structure collapses first in Pd and Pt, while both Cu and Ni have two elongated cylindrical grains which persist for significantly longer times, even though the remainder of the structure has already evolved to the single crystalline state. The increased resistance against grain growth for the avg.-atom, CoCuFeNi, and seg. CoCuFeNi samples can be clearly seen. The first two still feature distinct grains after 3.75 ns, while the seg. HEA sample remains in that state up to 5 ns. The

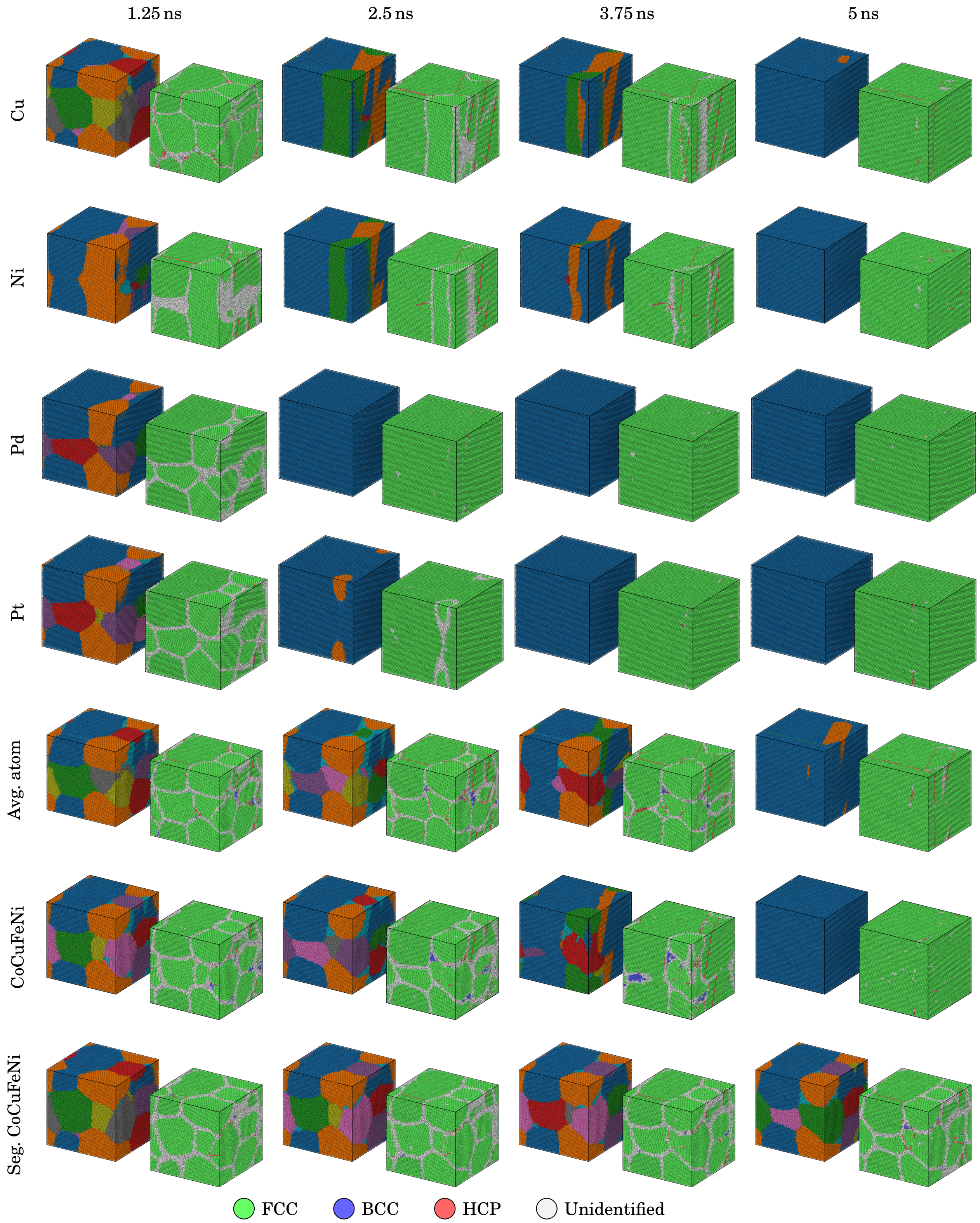

Figure 6.8: Snapshots of the microstructure evolution in all samples at the highest annealing temperature of $0.9\,T_{\mathrm{Melt}}$. Both, results of the grain segmentation algorithm and local crystal structure identification using PTM are shown. Atomic positions are averaged over consecutive time intervals to compensate thermal vibrations. The color coding for the grain association is based on the grain size, therefore some grains might change color in consecutive snapshots.

avg.-atom sample shows the formation of body-centered cubic (BCC) phase along some GBs and triple junctions. The CoCuFeNi sample also shows BCC phase formation at similar positions within the sample suggesting a geometric origin, independent of the local chemical fluctuations. Additionally, the HEA sample shows a full FCC to BCC phase transition of a single small grain. Details on this phase instability, while interesting are out of scope here. The seg. CoCuFeNi sample, on the other hand, does not show the formation of BCC phase, which can be attributed to the increase in Cu at the GBs stabilizing the FCC phase. Since both CoCuFeNi, and avg.-atom samples show some grain growth at this very high temperature it seems to be unlikely that the secondary BCC phase stabilizes the grain structure by means of Zener pinning.[315]

6.6 Conclusion

To answer the research questions raised in Section 2.4:

I. Intrinsic lattice distortions in this model HEA are measurable at 0 K, but their magnitude is small compared to the thermal vibration amplitude at higher temperatures.

II. In line with these findings, we observe slight structural differences between HEA and avg.-atom sample for the $\Sigma 11$ STGB at 0 K which disappear at high temperatures.

III. Both the CoCuFeNi alloy and its avg.-atom counterpart show substantially reduced GB mobilities compared to the investigated pure metals. This cannot be attributed to a solute drag effect or other effects relying on the chemical disorder in HEAs, as this is absent in the monoatomic avg.-atom sample, but instead this has to be caused by a long-range material property.

IV. In the case of the investigated STGB we find that the reduced GB mobility is linked to the migration mechanism of the $\Sigma 11$ STGB which relies on repeated emission and reincorporation of Shockley partial dislocations from and into the boundary.

V. Cu segregation to the GBs strongly inhibits the migration of the STGB and prevents grain growth in the NC sample up to very high temperatures of $0.9\,T_{\mathrm{Melt}}$.

VI. The general GB mobility hierarchy of the elemental metals investigated here differs between the bicrystalline and NC samples. This is most likely caused by a difference in GB migration mechanism and acting driving force.

7 Summary & Outlook

> *"During this last decade we have made much progress, but it is very clear that we have still only just scratched the surface."*
>
> — B. Cantor, 2020[14]

7.1 Summary

In this thesis we investigated different face-centered cubic (FCC) $3d$ transition metal high-entropy alloys (HEAs) with a focus on the interaction of different defects with the complex matrix. Here we focused on vacancies, dislocations, and grain boundaries (GBs), respectively.

Vacancies

In Chapter 4, *'Vacancies'*, we have investigated zero-dimensional point defects within the matrix of the Cantor alloy system. First, we calculated the vacancy formation energies in the pseudo-binary $(\mathrm{CoCrFeMn})_{1-x}\mathrm{Ni}_x$ system. The vacancy formation energies followed an approximately Gaussian distribution based on the local chemical environment of the vacancy site. There was, however, no significant dependence on the removed atom's species or the alloy composition. The vacancy formation energy remained around 1.54(2) eV. The width of this Gaussian distribution, however, was found to be roughly constant for concentrated alloys but decreased rapidly once the FCC site percolation threshold[415] was reached.

The vacancy formation energy was only an intermediate quantity used to calculate the equilibrium vacancy concentration in a given system at a given temperature. Currently, there are three different thermodynamic models relating the vacancy formation energy to the vacancy concentration. They differ in the way they treat the configurational entropy of the HEA matrix.[113,126,127] We calculated the vacancy concentration from all three models based on the previously determined vacancy formation energy distributions and compared them to direct grand-canonical Monte Carlo (MC) simulations. These simulations confirmed that the vacancy concentration only depends on the mean vacancy formation energy and its distribution's width, but is independent of the configurational entropy of the host matrix. Moreover, we determined it impossible to approximate the vacancy formation energy distribution by a scalar *effective* vacancy formation energy. In conclusion, the equilibrium vacancy concentration in this alloy system changes strongly with temperature but shows only a weak dependence on the alloy composition.

In a second step, we calculated the vacancy migration energies within the complex $(\mathrm{CoCrFeMn})_{1-x}\mathrm{Ni}_x$ matrix. This revealed that the migration energies depend on both, the species of the exchanging atom and the chemical environment of the vacancy-atom pair. The former led to a shift in mean vacancy migration energy between 0.5 eV and 1 eV in the equimolar Cantor alloy. The latter gave rise to an approximately Gaussian distribution of migration energies around the aforementioned mean value. Again, the width of this distribution only changed once the alloy was too dilute for secondary elements to percolate. Moreover, we found an almost linear increase in vacancy migration energies for all species as the alloy composition changed from equimolar towards Ni-rich.

Conventionally, kinetic Monte Carlo (KMC) simulations within the random alloy model[131,132] approximation are used to model tracer diffusion in HEA. In this model, each atomic species has a single-valued migration energy. As discussed above, these migration energies actually followed a Gaussian distribution. Therefore, we built a novel variable-barrier KMC simulation code, which could account for this distribution. We used this code and the previously calculated vacancy concentrations to determine the tracer diffusion coefficients for the different Cantor alloy systems. Comparison to tracer diffusion experiments showed an improved agreement of the new KMC method compared to the random alloy model based KMC simulations.

There are, however, some remaining differences between simulation and experiment. These could be attributed to simplifications made in our calculations. We have neglected the effects of vibrational entropy on both the vacancy formation and vacancy migration energies. Moreover, all our calculations were made within the framework of the interatomic potential. While we were able to show reasonable agreement of this potential with established density functional theory (DFT) calculations, some quantitative deviations remain. Lastly, the simulations operated under the assumption of a perfectly random HEA matrix. While the high temperatures used in the experiment promote a random mixing within the HEA, they also enable ordering as they accelerate diffusion.

7.1.1 Dislocations

In Chapter 5, *'Dislocations'*, we investigated the interaction of line defects in the form of dislocations with the random matrix of different concentrated alloys. Wavy dislocations, compared to the rather straight ones expected in monoatomic metals, have long been observed in concentrated alloys. They are commonly attributed to solid solution strengthening, which pins some dislocation segments more than others leading to a jagged line shape (strong Fleischer type pinning). The wavy dislocation lines could also be caused by the local chemical fluctuations in HEAs giving rise to energetically beneficial environments to which the dislocation line conforms in equilibrium (Labusch type weak pinning).

Initially, we compared transmission electron microscopy (TEM) observations of dislocations in the Cantor alloy showing local pinning and waviness to similarly sized atomistic simulations. This confirmed that the interatomic potential could reproduce the experimentally observed dislocation pinning. The origin of this dislocation pinning, however, remained elusive. In this chapter, we proposed the local Peierls barrier as the root cause for dislocation pinning on the atomic scale. This descriptor is not only in line with established metallurgy theory established over the past 80 years,[453] but it can also be readily calculated. Conventionally, the Peierls barrier is taken as the maximum gradient of the generalized stacking fault (GSF) energy curve. In a concentrated alloy, however, this GSF energy landscape is not uniquely defined. Instead, it varies for each atom in the glide plane, leading to a distinct pinning force exerted by each atom on a passing dislocation.

First, we calculated the local pinning point strength for different concentrated subsystems of the Cantor alloy and found that CoNi showed almost no strong pinning points, while CoCrNi showed a very high density of strongly pinning Co and Cr atoms. This led us to the conclusion that the high strength of CoCrNi often reported in literature[12,244] stems from the unique interaction between Co and Cr atoms. The full five component Cantor alloy also showed the strongest pinning on Co and Cr atoms. However, the strong pinning point density was reduced compared to the three component alloy as the Co and Cr concentration is lower. Comparing dislocations during glide in these three samples showed almost ideally straight dislocations in CoNi, as there was no pinning, while both CoCrNi and CoCrFeMnNi showed wavy dislocations with pronounced local pinning. Spatially correlating the observed dislocation pinning to the local Peierls stress descriptor showed satisfactory agreement, given that there were other factors, for example the dislocation line tension, influencing the dislocation line shape.

Even though, our findings support the notion of dislocation pinning in Co-Cr rich environments, we could not point a single structural arrangement of atoms that always pinned the dislocation. Therefore, our simulations support the results by Leyson et al.[217] and Varvenne et al.[72,89], stating that Labusch type pinning is dominating in concentrated alloys.

Next, we extended our simulations to many other equimolar or Ni-rich subsystems of the Cantor alloy — calculating the pinning point density, critical force to initiate dislocation glide, and dislocation mobility under constant applied load. Here we found that in all samples the critical force for dislocation glide was proportional to the density of strong pinning points. Similarly, the dislocation mobility was inversely proportional to the pinning point density, as a higher density of strong pinning points led to a reduction in the average dislocation mobility. We also inserted other obstacles, e.g., short-range order (SRO) or ordered precipitates, into the Cantor alloy matrix and repeated the simulations outlined above. Here all samples confirmed the expectations from our pining point descriptor. Moreover, we found that even small ordered precipitates, below the resolution limit of TEM or atom probe tomography (APT), could already lead to substantial pinning of the dislocation, significantly altering its shape.

7.1.2 Grain Boundaries

In Chapter 6, *'Grain Boundaries'*, we studied the migration of a symmetrical tilt grain boundary (STGB) and grain growth in nanocrystalline samples to understand GB pinning in HEAs.

First, we studied the mobility of a $\Sigma 11/(332)\langle 110\rangle$ STGB using the synthetic driving force method.[398] Here different pure metals, a model CoCuFeNi HEA, and its average-atom (avg.-atom) counterpart were compared. This avg.-atom sample was made up of a virtual element which possesses the same long-range properties as the concentrated HEA but contained only a single atomic species.[111] Comparison of the full alloy and this avg.-atom sample allowed for the identification of effects caused by the local chemical fluctuations within the HEA.

In the STGB sample, we found that the HEA and the aforementioned avg.-atom sample shared almost identical GB mobilities and GB migration activation energies. This led to the conclusion that the mobility of this STGB was mostly independent of the local chemical fluctuations. Detailed inspection of the atomic trajectories during STGB migration revealed that its migration relies on repeated emission and absorption of Shockley partial dislocations. We proposed that this is the rate-limiting step of GB migration, as the activation energy for migration was proportional to the stable and unstable stacking fault (SF) energy in all samples.

Using MC annealing a substantial amount of Cu could be segregated to this STGB from the HEA matrix. This solute cloud in turn led to a pronounced pinning of the boundary up to very high temperatures. This pinning was driven by a reduction of the GB energy in the vicinity of the Cu solute cloud.

To generalize the previously obtained results, nanocrystalline (NC) samples were built from each material investigated previously. These were subjected to high temperature annealing to facilitate grain growth. In this case, there were different, randomly oriented GBs in the sample subjected to a driving force from the finite GB energy. In this situation, the grain growth rate and GB mobility in the random HEA and its avg.-atom counterpart differed slightly. This could be caused by the respective differences in GB energies or could point at effects caused by the local chemical fluctuations. The strong GB pinning effect caused by the Cu solute cloud up to very high temperatures observed in the STGB sample could be reproduced for the NC samples. The GBs between the randomly oriented grains in the nanocrystal did not migrate based on the partial dislocation mechanism observed for the STGB. Therefore, differences in mobility hierarchy between the STGB and nanocrystalline samples could be explained by differences in migration mechanism.

7.2 Outlook

7.2.1 Accuracy and Statistics in Atomistic High-Entropy Alloy Simulation

One problem for computational research in the field of HEAs is the difficulty of obtaining statistically representative results. This can be seen in Chapter 4 where we calculated almost 1×10^5 vacancy formation energies and vacancy migration energies, respectively. While a smaller number might be sufficient to converge the Gaussian distributions, many independent calculations are required to sample the vast number of possible chemical environments. For example, a single FCC vacancy has 12 nearest neighbors leading to $5^{12} = 244140625$ distinct permutations of 5 chemical species on these 12 sites.[*] This means that computationally costly methods like DFT are difficult to apply. Their cost limits the number of independent structures which can be calculated for statistical purposes. Moreover, DFT only allows for the calculation of small, i.e., fewer than 500 atoms, periodic simulation cells. Even if special-quasi random structures are used,[430] this introduces a degree of artificial SRO into the presumably random alloys. Classical empirical interatomic potentials, on the other hand, are able to tackle problems this size more easily as they can be evaluated orders of magnitude faster than DFT. The results, however, are always subject to uncertainties from the fitting process and inherent limitations of the functional form. An emerging technology which is able to overcome both issues are *machine learning interatomic potentials* which promise DFT accuracy at a fraction of the cost.[362] To date, no machine learning interatomic potential for HEAs has been published.

7.2.2 A Cantor Alloy Average-Atom Interatomic Potential

While this new method could increase the accuracy of our empirical interatomic potential based calculations by simply applying the same methodology, there are other directions which could be explored as well. These go beyond increased accuracy in the hope of providing increased physical understanding of HEAs. Immediately the development of an avg.-atom potential for the Cantor alloy comes to mind. Varvenne et al.[111] state in their original embedded atom method (EAM) avg.-atom publication that an extension to the modified embedded atom method (MEAM) formalism would be possible. However, no further steps in this direction have been reported. Firstly, a Cantor alloy avg.-atom could help understand the results obtained on point defects and diffusion in HEAs in Chapter 4. Obviously, the point defect energies in such an average material should be of scalar value, similar to a monoatomic metal. While this is not useful initially, the avg.-atom can be augmented with solutes,[111] describing the interaction of specific species with the average HEA matrix. This approach could be used to

---

[*] (excluding symmetry)

selectively add solutes around the diffusing atom-vacancy pair to understand, how the chemical environment influences the migration energy. We have already attempted to understand the effect of chemical environment on the migration energies by fixing the atomic configuration outside the nearest neighbor shell away from the vacancy-atom pair, while sampling many configurations inside this shell. So far, the statistical noise in migration energies has been still too large to fully understand the role of each species or structural motive. If one could replace the background matrix by the homogeneous avg.-atom matrix, this would hopefully curb this noise.

Alongside this migration study, different solutes could be added around a vacancy, to see the effect of chemical environment on the vacancy formation energy. While the bond counting model can already give some insights into the effects different atomic arrangements have on the formation energy, a more isolated approach would again be beneficial to understand the effects of each solute.

If the diffusive mass transport in the avg.-atom sample differs substantially from the corresponding random HEA this would hint at the importance of percolation paths for diffusion in HEAs.

7.2.3 The Effects of Vibrational Entropy on Diffusion

Going away from the avg.-atom approach, our calculations so far have neglected effects of the vibrational entropy on the vacancy formation and vacancy migration energies. In principle, the calculation of the vibrational free energies using tools like PHONOPY[442] is relatively straight forward. In particular, if the costly force calculations are done based on an interatomic potential instead of DFT. Unfortunately, there are substantial computational post-processing requirements due to the intrinsically low symmetry of the HEA simulation cells. So far, these limitations in time and computer memory have stopped us from further pursuing this issue, but it remains an obvious task for the future. Here, modern tools of phonon calculations like ALAMODE[486] or HIPHIVE[487] could help accelerate the process.

7.2.4 Dislocations in FCC High-Entropy Alloys

For the dislocations discussed in Chapter 5, an obvious follow-up task springs to mind. For now, only the pinning of a dissociated edge dislocation was studied at low temperatures. Other relevant dislocation types and elevated temperatures are obviously of interest and could be investigated in the same way. Secondly, visual comparison of TEM images showing the dislocation lines in the Cantor alloy and our similarly scaled simulations do not show agreement in the pinning point density and ruggedness of the dislocation line. Due to experimental limitations, the TEM images show fewer details and lower resolution. To facilitate comparison between experiment and simulation, the simulated dislocations could be put into an image simulation to simulate the corresponding TEM image and confirm their similarity. While we have started working on these image simulations using the methodology presented by Tessmer,[488] the results are still actively evolving and not ready for publication and discussion.

Moreover, while physically motivated, the proposed pinning point model is only based on indirect evidence. Pinning points are proposed, and the observed pinning of the dislocation line correlates nicely. More direct evidence could be obtained following the methodology by Antillon et al.[489] who propose a method of directly measuring the energy landscape seen by the dislocation during glide. Comparing the resulting energy landscape with the proposed pinning point strength can provide direct evidence and thereby nicely augment the presented results.

So far, the pinning points can only be calculated from classical potentials, as the potential energy per atom is required. They are inaccessible to other calculation methods, where only the total energy of a given simulation cell can be obtained. We tried different methods, to reconstruct the pinning point distributions shown in Chapter 5 from small cell GSF calculations. While the gradient of the total energy–displacement curves in these smaller simulations also showed discrete peaks, we were unable to align the pinning point strength observed in the large samples based on the per-atom energies to these smaller ones. This means that there is currently no way of obtaining the pinning point strength of an alloy from ab initio methods which would be necessary to guide future alloy design.

Finally, this third chapter could be improved by a more realistic Cantor alloy potential. The current potential always produces a negative SF energy as the hexagonal close-packed (HCP) phase is more stable than the FCC phase. While this is in agreement with DFT calculations at lower temperatures, it is currently estimated that the Cantor alloy transitions from stable HCP to stable FCC phase at about 300 K.[257] Obviously, the SF energy and therefore the HCP–FCC free energy differences are essential for the behavior of Shockley partial dislocations. Hence, an interatomic potential that is able to reproduce this phase stability hierarchy more accurately would be desirable for future simulations.

7.2.5 Grain Growth in the Cantor Alloy

Our original GB mobility study was performed on the CoCuFeNi model HEA system. This has multiple reasons. Firstly, it was started before the Choi et al.[129] Cantor alloy MEAM interatomic potential became available in December 2018. Secondly, as it is described by an EAM interatomic potential it allows for MC simulations in the variance-constrained semi-grand canonical ensemble, which is currently not implemented for MEAM interatomic potentials in LAMMPS. Unfortunately, the canonical, atom swap, MC method is too slow to replicate the segregation study shown in Chapter 6. Similarly, having an avg.-atom potential would be desirable before undertaking this study to see the effect of the local chemical fluctuations, following the reasoning shown in the respective chapter.

Another straight forward, but not necessarily exciting, extension of the current work presented in Chapter 6 would be a repetition of the grain growth studies for differently oriented STGBs, following the work of Olmsted et al.[479,480] This would give confirmation that the GB mobilities found here readily extend to other STGBs. Moreover, if other STGB configurations rely on different mechanisms for migration, these could be revealed and their mobility hierarchy could be assessed.

While these atomistic grain boundary migration studies are great to investigate the kinetics of grain growth, the thermodynamics can be investigated more easily using a different and more efficient method. Chookajorn et al.[319,490] proposed a lattice MC algorithm, where each lattice site does not only have information about the occupying atomic species but also its grain allegiance. The energy in this model is then parametrized in the form of inter- and intra-granular pair interactions. Originally, this model only accounts for nearest-neighbor interactions. With this approach, however, we were not able to reproduce the thermodynamics of the Cantor alloy (based on the MEAM reference). Based on our findings in Chapter 4, where second-nearest neighbors were necessary for the vacancy formation energy bond counting model, an extension to second-nearest neighbors might be necessary. This step would be a worthwhile endeavor to determine the equilibrium grain structure of HEAs, accounting not only for the configurational entropy, but also for potential SRO, and even segregation, much faster and more efficiently than molecular dynamics (MD) simulations.

Curriculum Vitæ

Research Experience

since 05/2021	Scientific staff member (*Wissenschaftlicher Mitarbeiter*) Materials modeling group Prof. Dr. rer. nat. Karsten Albe, Technische Universität Darmstadt, Germany ‘*NHR for Computational Engineering Sciences NHR4CRS*’
11/2017 - 04/2021	Scientific staff member (*Wissenschaftlicher Mitarbeiter*) Materials modeling group Prof. Dr. rer. nat. Karsten Albe, Technische Universität Darmstadt, Germany DFG Priority Program ‘*Compositionally Complex Alloys — High Entropy Alloys (CCA-HEA)*’
04/2019 - 06/2019	Visiting scientist Ghazisaeidi group The Ohio State University, USA

Education

10/2017	Master of Science in Materials Science FAME Master Program Technische Universität Darmstadt, Germany
09/2015 - 08/2016	FAME Master Program Institut Polytechnique de Grenoble, France
08/2015	Bachelor of Science in Materials Science Technische Universität Darmstadt, Germany
06/2012	Secondary education (*Abitur*) Heinrich-von-Kleist Schule, Eschborn, Germany

Peer Reviewed Articles

T. Keil, D. Utt, E. Bruder, A. Stukowski, K. Albe, and K. Durst, *Solid solution hardening in CrMnFeCoNi-based high entropy alloy systems studied by a combinatorial approach*, Journal of Materials Research (2021)

D. Utt, A. Stukowski, and M. Ghazisaeidi, *The effect of solute cloud formation on the second order pyramidal to basal transition of* $\langle c + a \rangle$ *edge dislocations in Mg-Y solid solutions*, Scripta Materialia 182, 53–56 (2020)

F. Thiel, D. Utt, A. Kauffmann, K. Nielsch, K. Albe, M. Heilmaier, and J. Freudenberger, *Breakdown of Varvenne scaling in (AuNiPdPt) 1 - x Cu high-entropy alloys*, Scripta Materialia 181, 15–18 (2020)

J. Kottke, D. Utt, M. Laurent-Brocq, A. Fareed, D. Gaertner, L. Perrière, Ł. Rogal, A. Stukowski, K. Albe, S. V. Divinski, and G. Wilde, *Experimental and theoretical study of tracer diffusion in a series of* $(CoCrFeMn)_{100\text{-}x}\,Ni_x$ *alloys*, Acta Materialia 194, 236–248 (2020)

D. Utt, A. Stukowski, and K. Albe, *Grain boundary structure and mobility in high-entropy alloys: A comparative molecular dynamics study on a* $\Sigma 11$ *symmetrical tilt grain boundary in face-centered cubic CuNiCoFe*, Acta Materialia 186, 11–19 (2020)

F. Thiel, D. Geissler, K. Nielsch, A. Kauffmann, S. Seils, M. Heilmaier, D. Utt, K. Albe, M. Motylenko, D. Rafaja, and J. Freudenberger, *Origins of strength and plasticity in the precious metal based high-entropy alloy AuCuNiPdPt*, Acta Materialia 185, 400–411 (2020)

E. Levo, F. Granberg, D. Utt, K. Albe, K. Nordlund, and F. Djurabekova, *Radiation stability of nanocrystalline single-phase multicomponent alloys*, Journal of Materials Research 34, 854–866 (2019)

H. Henck, J. Avila, Z. Ben Aziza, D. Pierucci, J. Baima, B. Pamuk, J. Chaste, D. Utt, M. Bartos, K. Nogajewski, B. A. Piot, M. Orlita, M. Potemski, M. Calandra, M. C. Asensio, F. Mauri, C. Faugeras, and A. Ouerghi, *Flat electronic bands in long sequences of rhombohedral-stacked graphene*, Physical Review B 97, 245421 (2018)

L. Koch, F. Granberg, T. Brink, D. Utt, K. Albe, F. Djurabekova, and K. Nordlund, *Local segregation versus irradiation effects in high-entropy alloys: Steady-state conditions in a driven system*, Journal of Applied Physics 122, 105106 (2017)

Submitted Articles

D. Utt, A. Stukowski, and K. Albe, *Thermodynamics of vacancies in concentrated solid solutions: From dilute Ni-alloys to the Cantor system*, arXiv:2104.02697 [cond-mat] (2021), Acta Materialia

D. Utt, S. Lee, A. Stukowski, S. H. Oh, G. Dehm, and K. Albe, *Jerky motion of dislocations in high-entropy alloys: The linkage between local Peierls stress fluctuations and dislocation mobility*, arXiv:2007.11489 [cond-mat, physics:physics] (2020), Science

Oral Presentations at International Conferences

09/2020 MSE Congress, Darmstadt, Germany, '*Diffusion in Ni–CoCrFeMn alloys: Experimental and theoretical study on the transition from dilute solid solution to high-entropy alloy*', D. Utt, J. Kottke, S. V. Divinskiy, A. Stukowski, G. Wilde, K. Albe

07/2020 (postponed to 06/2021) DSL, St. Julian's, Malta '*Experimental and theoretical study of tracer diffusion in the Ni–CoCrFeMn alloys*', D. Utt, J. Kottke, S. V. Divinskiy, A. Stukowski, G. Wilde, K. Albe

05/2020 (postponed to 05/2021), THERMEC, Vienna, Austria, '*Variation of atomic diffusion and mechanical strength with composition in the Cantor alloy system: Experiments and computer modelling*', D. Utt, T. Keil, J. Kottke, E. Bruder, S. V. Divinski, A. Stukowski, K. Albe, K. Durst, G. Wilde

03/2020 (cancelled), DPG-Frühjahrstagung, Regensburg, Germany, '*Variation of mechanical strength with composition in the Cantor alloy system: Experiments and modeling*', D. Utt, T. Keil, A. Stukowski, E. Bruder, K. Albe, K. Durst

09/2019, EUROMAT, Stockholm, Sweden, '*Grain boundary migration in high entropy alloys*', D. Utt, A. Stukowski, and K. Albe

09/2018 MSE Congress, Darmstadt, Germany, '*Grain Boundary Effects in High Entropy Alloys: Insights from Atomistic Computer Simulations*', D. Utt, A. Stukowski, and K. Albe

03/2018, DPG-Frühjahrstagung, Berlin, Germany, '*Grain Boundary Effects in High Entropy Alloys: Insights from Atomistic Computer Simulations*', D. Utt, A. Stukowski, and K. Albe

Bibliography

[1] W. Steurer, *Single-phase high-entropy alloys – A critical update*, Materials Characterization 162, 110179 (2020).

[2] E. P. George, D. Raabe, and R. O. Ritchie, *High-entropy alloys*, Nature Reviews Materials 4, 515–534 (2019).

[3] H. Long, S. Mao, Y. Liu, Z. Zhang, and X. Han, *Microstructural and compositional design of Ni-based single crystalline superalloys — A review*, Journal of Alloys and Compounds 743, 203–220 (2018).

[4] A. Williams, *The knight and the blast furnace: A history of the metallurgy of armour in the Middle Ages & the early modern period*, History of Warfare, no. v. 12, Brill, Leiden ; Boston, 2003.

[5] B. Cantor, I. Chang, P. Knight, and A. Vincent, *Microstructural development in equiatomic multicomponent alloys*, Materials Science and Engineering: A 375-377, 213–218 (2004).

[6] J.-W. Yeh, S.-K. Chen, S.-J. Lin, J.-Y. Gan, T.-S. Chin, T.-T. Shun, C.-H. Tsau, and S.-Y. Chang, *Nanostructured High-Entropy Alloys with Multiple Principal Elements: Novel Alloy Design Concepts and Outcomes*, Advanced Engineering Materials 6, 299–303 (2004).

[7] J.-W. Yeh, S.-J. Lin, T.-S. Chin, J.-Y. Gan, S.-K. Chen, T.-T. Shun, C.-H. Tsau, and S.-Y. Chou, *Formation of simple crystal structures in Cu-Co-Ni-Cr-Al-Fe-Ti-V alloys with multiprincipal metallic elements*, Metallurgical and Materials Transactions A 35, 2533–2536 (2004).

[8] E. J. Pickering and N. G. Jones, *High-entropy alloys: A critical assessment of their founding principles and future prospects*, International Materials Reviews 61, 183–202 (2016).

[9] S. A. Kube and J. Schroers, *Metastability in high entropy alloys*, Scripta Materialia 186, 392–400 (2020).

[10] D. Miracle and O. Senkov, *A critical review of high entropy alloys and related concepts*, Acta Materialia 122, 448–511 (2017).

[11] Z. Wu, H. Bei, F. Otto, G. Pharr, and E. George, *Recovery, recrystallization, grain growth and phase stability of a family of FCC-structured multi-component equiatomic solid solution alloys*, Intermetallics 46, 131–140 (2014).

[12] Z. Wu, H. Bei, G. Pharr, and E. George, *Temperature dependence of the mechanical properties of equiatomic solid solution alloys with face-centered cubic crystal structures*, Acta Materialia 81, 428–441 (2014).

[13] K. Biswas, J.-W. Yeh, P. P. Bhattacharjee, and J. T. DeHosson, *High entropy alloys: Key issues under passionate debate*, Scripta Materialia 188, 54–58 (2020).

[14] B. Cantor, *Multicomponent high-entropy Cantor alloys*, Progress in Materials Science, 100754 (2020).

[15] J.-W. Yeh, *Recent progress in high-entropy alloys*, Annales de Chimie Science des Matériaux 31, 633–648 (2006).

[16] S. V. Divinski, A. V. Pokoev, N. Esakkiraja, and A. Paul, *A Mystery of "Sluggish Diffusion" in High-Entropy Alloys: The Truth or a Myth?*, Diffusion Foundations 17, 69–104 (2018).

[17] S. Ranganathan, *Alloyed pleasures: Multimetallic cocktails*, Current science 85, 1404–1406 (2003).

[18] D. Raabe, C. C. Tasan, H. Springer, and M. Bausch, *From High-Entropy Alloys to High-Entropy Steels*, steel research international 86, 1127–1138 (2015).

[19] E. P. George, W. A. Curtin, and C. C. Tasan, *High entropy alloys: A focused review of mechanical properties and deformation mechanisms*, Acta Materialia 188, 435–474 (2020).

[20] M. C. Gao, D. B. Miracle, D. Maurice, X. Yan, Y. Zhang, and J. A. Hawk, *High-entropy functional materials*, Journal of Materials Research 33, 3138–3155 (2018).

[21] X. Yan and Y. Zhang, *Functional properties and promising applications of high entropy alloys*, Scripta Materialia 187, 188–193 (2020).

[22] W. Nöhring and W. Curtin, *Design using randomness: A new dimension for metallurgy*, Scripta Materialia 187, 210–215 (2020).

[23] J. Chen, X. Zhou, W. Wang, B. Liu, Y. Lv, W. Yang, D. Xu, and Y. Liu, *A review on fundamental of high entropy alloys with promising high–temperature properties*, Journal of Alloys and Compounds 760, 15–30 (2018).

[24] A. Manzoni, H. Daoud, S. Mondal, S. van Smaalen, R. Völkl, U. Glatzel, and N. Wanderka, *Investigation of phases in Al23Co15Cr23Cu8Fe15Ni16 and Al8Co17Cr17Cu8Fe17Ni33 high entropy alloys and comparison with equilibrium phases predicted by Thermo-Calc*, Journal of Alloys and Compounds 552, 430–436 (2013).

[25] F. Otto, Y. Yang, H. Bei, and E. George, *Relative effects of enthalpy and entropy on the phase stability of equiatomic high-entropy alloys*, Acta Materialia 61, 2628–2638 (2013).

[26] J. He, C. Zhu, D. Zhou, W. Liu, T. Nieh, and Z. Lu, *Steady state flow of the FeCoNiCrMn high entropy alloy at elevated temperatures*, Intermetallics 55, 9–14 (2014).

[27] B. Schuh, F. Mendez-Martin, B. Völker, E. George, H. Clemens, R. Pippan, and A. Hohenwarter, *Mechanical properties, microstructure and thermal stability of a nanocrystalline CoCrFeMnNi high-entropy alloy after severe plastic deformation*, Acta Materialia 96, 258–268 (2015).

[28] F. Otto, A. Dlouhý, K. Pradeep, M. Kuběnová, D. Raabe, G. Eggeler, and E. George, *Decomposition of the single-phase high-entropy alloy CrMnFeCoNi after prolonged anneals at intermediate temperatures*, Acta Materialia 112, 40–52 (2016).

[29] E. Pickering, R. Muñoz-Moreno, H. Stone, and N. Jones, *Precipitation in the equiatomic high-entropy alloy CrMnFeCoNi*, Scripta Materialia 113, 106–109 (2016).

[30] V. K. Soni, S. Sanyal, and S. Sinha, *Microstructure and mechanical properties of non equiatomic FeCoNiCuMo high entropy systems*, Advances in Materials and Processing Technologies, 1–14 (2020).

[31] B. Ren, Z. Liu, B. Cai, M. Wang, and L. Shi, *Aging behavior of a CuCr2Fe2NiMn high-entropy alloy*, Materials & Design 33, 121–126 (2012).

[32] J. He, H. Wang, H. Huang, X. Xu, M. Chen, Y. Wu, X. Liu, T. Nieh, K. An, and Z. Lu, *A precipitation-hardened high-entropy alloy with outstanding tensile properties*, Acta Materialia 102, 187–196 (2016).

[33] Y. Zhao, T. Yang, Y. Tong, J. Wang, J. Luan, Z. Jiao, D. Chen, Y. Yang, A. Hu, C. Liu, and J.-J. Kai, *Heterogeneous precipitation behavior and stacking-fault-mediated deformation in a CoCrNi-based medium-entropy alloy*, Acta Materialia 138, 72–82 (2017).

[34] Y.-J. Liang, L. Wang, Y. Wen, B. Cheng, Q. Wu, T. Cao, Q. Xiao, Y. Xue, G. Sha, Y. Wang, Y. Ren, X. Li, L. Wang, F. Wang, and H. Cai, *High-content ductile coherent nanoprecipitates achieve ultrastrong high-entropy alloys*, Nature Communications 9, 4063 (2018).

[35] Y.-T. Chen, Y.-J. Chang, H. Murakami, T. Sasaki, K. Hono, C.-W. Li, K. Kakehi, J.-W. Yeh, and A.-C. Yeh, *Hierarchical microstructure strengthening in a single crystal high entropy superalloy*, Scientific Reports 10, 12163 (2020).

[36] Q.-J. Li, H. Sheng, and E. Ma, *Strengthening in multi-principal element alloys with local-chemical-order roughened dislocation pathways*, Nature Communications 10, 3563 (2019).

[37] L. Zhang, Y. Xiang, J. Han, and D. J. Srolovitz, *The effect of randomness on the strength of high-entropy alloys*, Acta Materialia 166, 424–434 (2019).

[38] E. Antillon, C. Woodward, S. Rao, B. Akdim, and T. Parthasarathy, *Chemical short range order strengthening in a model FCC high entropy alloy*, Acta Materialia 190, 29–42 (2020).

[39] R. Zhang, S. Zhao, J. Ding, Y. Chong, T. Jia, C. Ophus, M. Asta, R. O. Ritchie, and A. M. Minor, *Short-range order and its impact on the CrCoNi medium-entropy alloy*, Nature 581, 283–287 (2020).

[40] C. S. Jayanth and P. Nash, *Factors affecting particle-coarsening kinetics and size distribution*, Journal of Materials Science 24, 3041–3052 (1989).

[41] T. J. Carter, *Common failures in gas turbine blades*, Engineering Failure Analysis 12, 237–247 (2005).

[42] J. Fiala, L. Kloc, and J. Čadek, *Creep in metals at intermediate temperatures and low stresses: A review*, Materials Science and Engineering: A 137, 163–172 (1991).

[43] R. W. Balluffi, S. M. Allen, W. C. Carter, and R. A. Kemper, *Kinetics of materials*, J. Wiley & Sons, Hoboken, N.J, 2005.

[44] Z. Cai, G. Jin, X. Cui, Y. Li, Y. Fan, and J. Song, *Experimental and simulated data about microstructure and phase composition of a NiCrCoTiV high-entropy alloy prepared by vacuum hot-pressing sintering*, Vacuum 124, 5–10 (2016).

[45] K.-Y. Tsai, M.-H. Tsai, and J.-W. Yeh, *Sluggish diffusion in Co–Cr–Fe–Mn–Ni high-entropy alloys*, Acta Materialia 61, 4887–4897 (2013).

[46] J. Dąbrowa and M. Danielewski, *State-of-the-Art Diffusion Studies in the High Entropy Alloys*, Metals 10, 347 (2020).

[47] S.-Q. Xia, Z. Wang, T.-F. Yang, and Y. Zhang, *Irradiation Behavior in High Entropy Alloys*, Journal of Iron and Steel Research, International 22, 879–884 (2015).

[48] T. Egami, W. Guo, P. D. Rack, and T. Nagase, *Irradiation Resistance of Multicomponent Alloys*, Metallurgical and Materials Transactions A 45, 180–183 (2014).

[49] S. Q. Xia, X. Yang, T. F. Yang, S. Liu, and Y. Zhang, *Irradiation Resistance in AlxCoCrFeNi High Entropy Alloys*, JOM 67, 2340–2344 (2015).

[50] Y. Zhang, G. M. Stocks, K. Jin, C. Lu, H. Bei, B. C. Sales, L. Wang, L. K. Béland, R. E. Stoller, G. D. Samolyuk, M. Caro, A. Caro, and W. J. Weber, *Influence of chemical disorder on energy dissipation and defect evolution in concentrated solid solution alloys*, Nature Communications 6, 8736 (2015).

[51] K. Jin, C. Lu, L. M. Wang, J. Qu, W. J. Weber, Y. Zhang, and H. Bei, *Effects of compositional complexity on the ion-irradiation induced swelling and hardening in Ni-containing equiatomic alloys*, Scripta Materialia 119, 65–70 (2016).

[52] Y. Zhang, K. Jin, H. Xue, C. Lu, R. J. Olsen, L. K. Beland, M. W. Ullah, S. Zhao, H. Bei, D. S. Aidhy, G. D. Samolyuk, L. Wang, M. Caro, A. Caro, G. M. Stocks, B. C. Larson, I. M. Robertson, A. A. Correa, and W. J. Weber, *Influence of chemical disorder on energy dissipation and defect evolution in advanced alloys*, Journal of Materials Research 31, 2363–2375 (2016).

[53] F. Granberg, K. Nordlund, M. W. Ullah, K. Jin, C. Lu, H. Bei, L. M. Wang, F. Djurabekova, W. J. Weber, and Y. Zhang, *Mechanism of Radiation Damage Reduction in Equiatomic Multicomponent Single Phase Alloys*, Physical Review Letters 116, 135504 (2016).

[54] T. Yang, S. Xia, S. Liu, C. Wang, S. Liu, Y. Fang, Y. Zhang, J. Xue, S. Yan, and Y. Wang, *Precipitation behavior of Al x CoCrFeNi high entropy alloys under ion irradiation*, Scientific Reports 6, 32146 (2016).

[55] M. W. Ullah, D. S. Aidhy, Y. Zhang, and W. J. Weber, *Damage accumulation in ion-irradiated Ni-based concentrated solid-solution alloys*, Acta Materialia 109, 17–22 (2016).

[56] N. A. P. K. Kumar, C. Li, K. J. Leonard, H. Bei, and S. J. Zinkle, *Microstructural stability and mechanical behavior of FeNiMnCr high entropy alloy under ion irradiation*, Acta Materialia 113, 230–244 (2016).

[57] C. Lu, L. Niu, N. Chen, K. Jin, T. Yang, P. Xiu, Y. Zhang, F. Gao, H. Bei, S. Shi, M.-R. He, I. M. Robertson, W. J. Weber, and L. Wang, *Enhancing radiation tolerance by controlling defect mobility and migration pathways in multicomponent single-phase alloys*, Nature Communications 7, 13564 (2016).

[58] F. Granberg, F. Djurabekova, E. Levo, and K. Nordlund, *Damage buildup and edge dislocation mobility in equiatomic multicomponent alloys*, Nuclear Instruments and Methods in Physics Research Section B: Beam Interactions with Materials and Atoms 393, 114–117 (2017).

[59] E. Levo, F. Granberg, C. Fridlund, K. Nordlund, and F. Djurabekova, *Radiation damage buildup and dislocation evolution in Ni and equiatomic multicomponent Ni-based alloys*, Journal of Nuclear Materials 490, 323–332 (2017).

[60] L. Koch, F. Granberg, T. Brink, D. Utt, K. Albe, F. Djurabekova, and K. Nordlund, *Local segregation versus irradiation effects in high-entropy alloys: Steady-state conditions in a driven system*, Journal of Applied Physics 122, 105106 (2017).

[61] M. W. Ullah, H. Xue, G. Velisa, K. Jin, H. Bei, W. J. Weber, and Y. Zhang, *Effects of chemical alternation on damage accumulation in concentrated solid-solution alloys*, Scientific Reports 7, 4146 (2017).

[62] G. Velisa, M. W. Ullah, H. Xue, K. Jin, M. L. Crespillo, H. Bei, W. J. Weber, and Y. Zhang, *Irradiation-induced damage evolution in concentrated Ni-based alloys*, Acta Materialia 135 (2017).

[63] E. Levo, F. Granberg, D. Utt, K. Albe, K. Nordlund, and F. Djurabekova, *Radiation stability of nanocrystalline single-phase multicomponent alloys*, Journal of Materials Research 34, 854–866 (2019).

[64] D. I. R. Norris, *Voids in irradiated metals (Part I)*, Radiation Effects 14, 1–37 (1972).

[65] L. K. Mansur, *Void Swelling in Metals and Alloys Under Irradiation: An Assessment of the Theory*, Nuclear Technology 40, 5–34 (1978).

[66] F. Garner, *Radiation Damage in Austenitic Steels*, Comprehensive Nuclear Materials, Elsevier, 2012, pp. 33–95.

[67] J. P. Hirth and J. Lothe, *Theory of dislocations*, 2nd ed ed., Wiley, New York, 1982.

[68] D. Hull and D. J. Bacon, *Introduction to dislocations*, vol. 37, Elsevier, 2011.

[69] F. W. Young, *Elastic-Plastic Transition in Copper Crystals as Determined by an Etch-Pit Technique*, Journal of Applied Physics 32, 1815–1820 (1961).

[70] P. Haasen, *Plastic deformation of nickel single crystals at low temperatures*, The Philosophical Magazine: A Journal of Theoretical Experimental and Applied Physics 3, 384–418 (1958).

[71] J. J. Gilman, *The "Peierls stress" for pure metals (evidence that it is negligible)*, Philosophical Magazine 87, 5601–5606 (2007).

[72] C. Varvenne, A. Luque, and W. A. Curtin, *Theory of strengthening in fcc high entropy alloys*, Acta Materialia 118, 164–176 (2016).

[73] E. Ma, *Unusual dislocation behavior in high-entropy alloys*, Scripta Materialia 181, 127–133 (2020).

[74] T. Smith, M. Hooshmand, B. Esser, F. Otto, D. McComb, E. George, M. Ghazisaeidi, and M. Mills, *Atomic-scale characterization and modeling of 60° dislocations in a high-entropy alloy*, Acta Materialia 110, 352–363 (2016).

[75] X. Xu, P. Liu, Z. Tang, A. Hirata, S. Song, T. Nieh, P. Liaw, C. Liu, and M. Chen, *Transmission electron microscopy characterization of dislocation structure in a face-centered cubic high-entropy alloy Al0.1CoCrFeNi*, Acta Materialia 144, 107–115 (2018).

[76] Z. Zhang, M. M. Mao, J. Wang, B. Gludovatz, Z. Zhang, S. X. Mao, E. P. George, Q. Yu, and R. O. Ritchie, *Nanoscale origins of the damage tolerance of the high-entropy alloy CrMnFeCoNi*, Nature Communications 6, 10143 (2015).

[77] S. Lee, M. J. Duarte, M. Feuerbacher, R. Soler, C. Kirchlechner, C. H. Liebscher, S. H. Oh, and G. Dehm, *Dislocation plasticity in FeCoCrMnNi high-entropy alloy: Quantitative insights from* in situ *transmission electron microscopy deformation*, Materials Research Letters 8, 216–224 (2020).

[78] S. Rao, C. Woodward, T. Parthasarathy, and O. Senkov, *Atomistic simulations of dislocation behavior in a model FCC multicomponent concentrated solid solution alloy*, Acta Materialia 134, 188–194 (2017).

[79] P. Wang, Y. Wu, J. Liu, and H. Wang, *Impacts of atomic scale lattice distortion on dislocation activity in high-entropy alloys*, Extreme Mechanics Letters 17, 38–42 (2017).

[80] R. Pasianot and D. Farkas, *Atomistic modeling of dislocations in a random quinary high-entropy alloy*, Computational Materials Science 173, 109366 (2020).

[81] R. Gröger, V. Vitek, and A. Dlouhy, *Effective pair potential for random fcc CoCrFeMnNi alloys*, Modelling and Simulation in Materials Science and Engineering (2020).

[82] W. Li, S. I. Rao, Q. Wang, H. Fan, J. Yang, and J. A. El-Awady, *Core structure and mobility of edge dislocations in face-centered-cubic chemically complex NiCoFe and NiCoFeCu equiatomic solid-solution alloys*, Materialia 9, 100628 (2020).

[83] R. Fleischer, *Solution hardening*, Acta Metallurgica 9, 996–1000 (1961).

[84] R. Fleischer, *Substitutional solution hardening*, Acta Metallurgica 11, 203–209 (1963).

[85] J. Friedel, *Dislocations*, Elsevier, 1964.

[86] N. F. Mott, *CXVII. A theory of work-hardening of metal crystals*, The London, Edinburgh, and Dublin Philosophical Magazine and Journal of Science 43, 1151–1178 (1952).

[87] R. Labusch, *A Statistical Theory of Solid Solution Hardening*, physica status solidi (b) 41, 659–669 (1970).

[88] R. Labusch, *Statistische theorien der mischkristallhärtung*, Acta Metallurgica 20, 917–927 (1972).

[89] C. Varvenne, G. Leyson, M. Ghazisaeidi, and W. Curtin, *Solute strengthening in random alloys*, Acta Materialia 124, 660–683 (2017).

[90] M. Dao, L. Lu, R. Asaro, J. Dehosson, and E. Ma, *Toward a quantitative understanding of mechanical behavior of nanocrystalline metals*, Acta Materialia 55, 4041–4065 (2007).

[91] M. Rose, A. G. Balogh, and H. Hahn, *Instability of irradiation induced defects in nanostructured materials*, Nuclear Instruments and Methods in Physics Research Section B: Beam Interactions with Materials and Atoms 127-128, 119–122 (1997).

[92] O. El-Atwani, J. A. Hinks, G. Greaves, J. P. Allain, and S. A. Maloy, *Grain size threshold for enhanced irradiation resistance in nanocrystalline and ultrafine tungsten*, Materials Research Letters 5, 343–349 (2017).

[93] O. El-Atwani, E. Esquivel, M. Efe, E. Aydogan, Y. Wang, E. Martinez, and S. Maloy, *Loop and void damage during heavy ion irradiation on nanocrystalline and coarse grained tungsten: Microstructure, effect of dpa rate, temperature, and grain size*, Acta Materialia 149, 206–219 (2018).

[94] P. Bhattacharjee, G. Sathiaraj, M. Zaid, J. Gatti, C. Lee, C.-W. Tsai, and J.-W. Yeh, *Microstructure and texture evolution during annealing of equiatomic CoCrFeMnNi high-entropy alloy*, Journal of Alloys and Compounds 587, 544–552 (2014).

[95] P. Thirathipviwat, G. Song, J. Jayaraj, J. Bednarcik, H. Wendrock, T. Gemming, J. Freudenberger, K. Nielsch, and J. Han, *A comparison study of dislocation density, recrystallization and grain growth among nickel, FeNiCo ternary alloy and FeNiCoCrMn high entropy alloy*, Journal of Alloys and Compounds 790, 266–273 (2019).

[96] G. Sathiaraj and P. Bhattacharjee, *Effect of starting grain size on the evolution of microstructure and texture during thermo-mechanical processing of CoCrFeMnNi high entropy alloy*, Journal of Alloys and Compounds 647, 82–96 (2015).

[97] W. Liu, Y. Wu, J. He, T. Nieh, and Z. Lu, *Grain growth and the Hall–Petch relationship in a high-entropy FeCrNiCoMn alloy*, Scripta Materialia 68, 526–529 (2013).

[98] N. Zhou, T. Hu, J. Huang, and J. Luo, *Stabilization of nanocrystalline alloys at high temperatures via utilizing high-entropy grain boundary complexions*, Scripta Materialia 124, 160–163 (2016).

[99] F. Otto, N. Hanold, and E. George, *Microstructural evolution after thermomechanical processing in an equiatomic, single-phase CoCrFeMnNi high-entropy alloy with special focus on twin boundaries*, Intermetallics 54, 39–48 (2014).

[100] G. Liu, D. H. Lu, X. W. Liu, F. C. Liu, Q. Yang, H. Du, Q. Hu, and Z. T. Fan, *Solute segregation effect on grain boundary migration and Hall–Petch relationship in CrMnFeCoNi high-entropy alloy*, Materials Science and Technology, 1–9 (2019).

[101] B. Gwalani, R. Salloom, T. Alam, S. G. Valentin, X. Zhou, G. Thompson, S. G. Srinivasan, and R. Banerjee, *Composition-dependent apparent activation-energy and sluggish grain-growth in high entropy alloys*, Materials Research Letters 7, 267–274 (2019).

[102] M. Annasamy, N. Haghdadi, A. Taylor, P. Hodgson, and D. Fabijanic, *Static recrystallization and grain growth behaviour of Al0.3CoCrFeNi high entropy alloy*, Materials Science and Engineering: A 754, 282–294 (2019).

[103] S. Praveen, J. Basu, S. Kashyap, and R. S. Kottada, *Exceptional resistance to grain growth in nanocrystalline CoCrFeNi high entropy alloy at high homologous temperatures*, Journal of Alloys and Compounds 662, 361–367 (2016).

[104] P. Sathiyamoorthi, J. Basu, S. Kashyap, K. Pradeep, and R. S. Kottada, *Thermal stability and grain boundary strengthening in ultrafine-grained CoCrFeNi high entropy alloy composite*, Materials & Design 134, 426–433 (2017).

[105] N. Stepanov, D. Shaysultanov, R. Chernichenko, D. Ikornikov, V. Sanin, and S. Zherebtsov, *Mechanical properties of a new high entropy alloy with a duplex ultra-fine grained structure*, Materials Science and Engineering: A 728, 54–62 (2018).

[106] M. Vaidya, A. Anupam, J. V. Bharadwaj, C. Srivastava, and B. Murty, *Grain growth kinetics in CoCrFeNi and CoCrFeMnNi high entropy alloys processed by spark plasma sintering*, Journal of Alloys and Compounds 791, 1114–1121 (2019).

[107] M. Klimova, D. Shaysultanov, S. Zherebtsov, and N. Stepanov, *Effect of second phase particles on mechanical properties and grain growth in a CoCrFeMnNi high entropy alloy*, Materials Science and Engineering: A 748, 228–235 (2019).

[108] D. Farkas, *Grain boundary structure in high-entropy alloys*, Journal of Materials Science 55, 9173–9183 (2020).

[109] K. Shiotani, T. Niiyama, and T. Shimokawa, *Dislocation Emission from Grain Boundaries in High-Entropy Alloys: Influence of Atomic Composition at Grain Boundaries*, MATERIALS TRANSACTIONS 61, 1272–1279 (2020).

[110] F. Tan, J. Li, H. Feng, Q. Fang, C. Jiang, Y. Liu, and P. K. Liaw, *Entropy-induced transition on grain-boundary migration in multi-principal element alloys*, 36 (2021).

[111] C. Varvenne, A. Luque, W. G. Nöhring, and W. A. Curtin, *Average-atom interatomic potential for random alloys*, Physical Review B 93, 104201 (2016).

[112] J. Wang, S. Niu, T. Guo, H. Kou, and J. Li, *The FCC to BCC phase transformation kinetics in an Al0.5CoCrFeNi high entropy alloy*, Journal of Alloys and Compounds 710, 144–150 (2017).

[113] A. V. Ruban, *Thermal vacancies in random alloys in the single-site mean-field approximation*, Physical Review B 93, 134115 (2016).

[114] E.-W. Huang, H.-S. Chou, K. N. Tu, W.-S. Hung, T.-N. Lam, C.-W. Tsai, C.-Y. Chiang, B.-H. Lin, A.-C. Yeh, S.-H. Chang, Y.-J. Chang, J.-J. Yang, X.-Y. Li, C.-S. Ku, K. An, Y.-W. Chang, and Y.-L. Jao, *Element Effects on High-Entropy Alloy Vacancy and Heterogeneous Lattice Distortion Subjected to Quasi-equilibrium Heating*, Scientific Reports 9, 14788 (2019).

[115] R. O. Simmons and R. W. Balluffi, *Measurements of Equilibrium Vacancy Concentrations in Aluminum*, Physical Review 117, 52–61 (1960).

[116] K. Sugita, N. Matsuoka, M. Mizuno, and H. Araki, *Vacancy formation enthalpy in CoCrFeMnNi high-entropy alloy*, Scripta Materialia 176, 32–35 (2020).

[117] T. Abe, *Thermal Vacancies in High-Entropy Alloys*, MATERIALS TRANSACTIONS 61, 610–615 (2020).

[118] M. Mizuno, K. Sugita, and H. Araki, *Defect energetics for diffusion in CrMnFeCoNi high-entropy alloy from first-principles calculations*, Computational Materials Science 170, 109163 (2019).

[119] H. Guan, S. Huang, J. Ding, F. Tian, Q. Xu, and J. Zhao, *Chemical environment and magnetic moment effects on point defect formations in CoCrNi-based concentrated solid-solution alloys*, Acta Materialia 187, 122–134 (2020).

[120] W. Chen, X. Ding, Y. Feng, X. Liu, K. Liu, Z. Lu, D. Li, Y. Li, C. Liu, and X.-Q. Chen, *Vacancy formation enthalpies of high-entropy FeCoCrNi alloy via first-principles calculations and possible implications to its superior radiation tolerance*, Journal of Materials Science & Technology 34, 355–364 (2018).

[121] S. Zhao, T. Egami, G. M. Stocks, and Y. Zhang, *Effect of* d *electrons on defect properties in equiatomic NiCoCr and NiCoFeCr concentrated solid solution alloys*, Physical Review Materials 2, 013602 (2018).

[122] C. Li, J. Yin, K. Odbadrakh, B. C. Sales, S. J. Zinkle, G. M. Stocks, and B. D. Wirth, *First principle study of magnetism and vacancy energetics in a near equimolar NiFeMnCr high entropy alloy*, Journal of Applied Physics 125, 155103 (2019).

[123] S. Middleburgh, D. King, G. Lumpkin, M. Cortie, and L. Edwards, *Segregation and migration of species in the CrCoFeNi high entropy alloy*, Journal of Alloys and Compounds 599, 179–182 (2014).

[124] A. Van der Ven and G. Ceder, *Vacancies in ordered and disordered binary alloys treated with the cluster expansion*, Physical Review B 71, 054102 (2005).

[125] W. Cai, W. D. Nix, and Materials Research Society, *Imperfections in crystalline solids*, 2016.

[126] D. Morgan and Y. Zhang, *Comment on "Thermal vacancies in random alloys in the single-site mean-field approximation"*, Physical Review B 101, 136101 (2020).

[127] Z. Wang, C. T. Liu, and P. Dou, *Thermodynamics of vacancies and clusters in high-entropy alloys*, Physical Review Materials 1, 043601 (2017).

[128] R. Abbaschian, L. Abbaschian, and R. E. Reed-Hill, *Physical metallurgy principles*, 4th ed ed., Cengage Learning, Stamford, CT, 2009.

[129] W.-M. Choi, Y. H. Jo, S. S. Sohn, S. Lee, and B.-J. Lee, *Understanding the physical metallurgy of the CoCrFeMnNi high-entropy alloy: An atomistic simulation study*, npj Computational Materials 4, 1 (2018).

[130] G. E. Murch and Z. Qin, *Tracer and Collective Correlation Factors in Solid State Diffusion*, Defect and Diffusion Forum 109-110, 1–18 (1994).

[131] J. R. Manning, *Diffusion Kinetics for Atoms in Crystals*, Van Nostrand, 1968.

[132] J. R. Manning, *Correlation Factors for Diffusion in Nondilute Alloys*, Physical Review B 4, 1111–1121 (1971).

[133] H. J. de Bruin, G. E. Murch, H. Bakker, and L. P. Van der Mey, *Diffusion correlation in random alloys*, Thin Solid Films 25, 47–62 (1975).

[134] N. A. Stolwijk and H. Bakker, *On computer simulation for the calculation of correlation factors for diffusion*, physica status solidi (b) 79, K1–K4 (1977).

[135] H. J. D. Buin, H. Bakker, and L. P. V. D. Mey, *Diffusion Correlation in Random Primitive Cubic Alloys*, physica status solidi (b) 82, 581–588 (1977).

[136] G. E. Murch, *An expression for the vacancy-wind effect in diffusion in a binary substitutional alloy*, Philosophical Magazine A 46, 151–159 (1982).

[137] G. E. Murch, *Diffusion correlation and isotope effects in high-defect-content solids*, Philosophical Magazine A 49, 21–29 (1984).

[138] A. R. Allnatt and E. L. Allnatt, *Computer simulation of phenomenological coefficients for atom transport in a random alloy*, Philosophical Magazine A 49, 625–635 (1984).

[139] N. El-Meshad and R. A. Tahir-Kheli, *Diffusion in mixed A-B alloys in two and three dimensions*, Physical Review B 32, 6176–6183 (1985).

[140] L. K. Moleko, A. R. Allnatt, and E. L. Allnatt, *A self-consistent theory of matter transport in a random lattice gas and some simulation results*, Philosophical Magazine A 59, 141–160 (1989).

[141] P. Franke and R. Dieckmann, *Correlation factors for diffusion in binary random alloys with fcc structure*, Journal of Applied Physics 70, 787–792 (1991).

[142] Z. Qin and G. E. Murch, *Collective correlation effects in solid-state diffusion*, Philosophical Magazine A 66, 957–973 (1992).

[143] I. V. Belova and G. E. Murch, *Tracer correlation factors in the random alloy*, Philosophical Magazine A 80, 1469–1479 (2000).

[144] I. V. Belova and G. E. Murch, *Collective diffusion in the binary random alloy*, Philosophical Magazine A 80, 599–607 (2000).

[145] T. R. Paul, I. V. Belova, and G. E. Murch, *Random alloy diffusion kinetics for the application to multicomponent alloy systems*, Philosophical Magazine 96, 1228–1244 (2016).

[146] D. L. Beke and G. Erdélyi, *On the diffusion in high-entropy alloys*, Materials Letters 164, 111–113 (2016).

[147] A. R. Allnatt, T. R. Paul, I. V. Belova, and G. E. Murch, *A high accuracy diffusion kinetics formalism for random multicomponent alloys: Application to high entropy alloys*, Philosophical Magazine 96, 2969–2985 (2016).

[148] M. Vaidya, S. Trubel, B. S. Murty, G. Wilde, and S. V. Divinski, *Ni tracer diffusion in CoCrFeNi and CoCrFeMnNi high entropy alloys*, Journal of Alloys and Compounds 688, 994–1001 (2016).

[149] M. Vaidya, K. Pradeep, B. Murty, G. Wilde, and S. Divinski, *Bulk tracer diffusion in CoCrFeNi and CoCrFeMnNi high entropy alloys*, Acta Materialia 146, 211–224 (2018).

[150] D. Gaertner, J. Kottke, Y. Chumlyakov, F. Hergemöller, G. Wilde, and S. V. Divinski, *Tracer diffusion in single crystalline CoCrFeNi and CoCrFeMnNi high-entropy alloys: Kinetic hints towards a low-temperature phase instability of the solid-solution?*, Scripta Materialia 187, 57–62 (2020).

[151] P.-K. Huang, J.-W. Yeh, T.-T. Shun, and S.-K. Chen, *Multi-Principal-Element Alloys with Improved Oxidation and Wear Resistance for Thermal Spray Coating*, Advanced Engineering Materials 6, 74–78 (2004).

[152] C.-J. Tong, Y.-L. Chen, J.-W. Yeh, S.-J. Lin, S.-K. Chen, T.-T. Shun, C.-H. Tsau, and S.-Y. Chang, *Microstructure characterization of Al x CoCrCuFeNi high-entropy alloy system with multiprincipal elements*, Metallurgical and Materials Transactions A 36, 881–893 (2005).

[153] H.-W. Chang, P.-K. Huang, J.-W. Yeh, A. Davison, C.-H. Tsau, and C.-C. Yang, *Influence of substrate bias, deposition temperature and post-deposition annealing on the structure and properties of multi-principal-component (AlCrMoSiTi)N coatings*, Surface and Coatings Technology 202, 3360–3366 (2008).

[154] M.-H. Tsai, J.-W. Yeh, and J.-Y. Gan, *Diffusion barrier properties of AlMoNbSiTaTiVZr high-entropy alloy layer between copper and silicon*, Thin Solid Films 516, 5527–5530 (2008).

[155] C. Ng, S. Guo, J. Luan, S. Shi, and C. T. Liu, *Entropy-driven phase stability and slow diffusion kinetics in an Al0.5CoCrCuFeNi high entropy alloy*, Intermetallics 31, 165–172 (2012).

[156] C. Ng, S. Guo, J. Luan, Q. Wang, J. Lu, S. Shi, and C. T. Liu, *Phase stability and tensile properties of Co-free Al0.5CrCuFeNi2 high-entropy alloys*, Journal of Alloys and Compounds 584, 530–537 (2014).

[157] D.-H. Lee, M.-Y. Seok, Y. Zhao, I.-C. Choi, J. He, Z. Lu, J.-Y. Suh, U. Ramamurty, M. Kawasaki, T. G. Langdon, and J.-i. Jang, *Spherical nanoindentation creep behavior of nanocrystalline and coarse-grained CoCrFeMnNi high-entropy alloys*, Acta Materialia 109, 314–322 (2016).

[158] M.-R. Chen, S.-J. Lin, J.-W. Yeh, M.-H. Chuang, S.-K. Chen, and Y.-S. Huang, *Effect of vanadium addition on the microstructure, hardness, and wear resistance of Al0.5CoCrCuFeNi high-entropy alloy*, Metallurgical and Materials Transactions A 37, 1363–1369 (2006).

[159] Y. P. Wang, B. S. Li, M. X. Ren, C. Yang, and H. Z. Fu, *Microstructure and compressive properties of AlCrFeCoNi high entropy alloy*, Materials Science and Engineering: A 491, 154–158 (2008).

[160] K. B. Zhang, Z. Y. Fu, J. Y. Zhang, J. Shi, W. M. Wang, H. Wang, Y. C. Wang, and Q. J. Zhang, *Annealing on the structure and properties evolution of the CoCrFeNiCuAl high-entropy alloy*, Journal of Alloys and Compounds 502, 295–299 (2010).

[161] T.-T. Shun, C.-H. Hung, and C.-F. Lee, *The effects of secondary elemental Mo or Ti addition in Al0.3CoCrFeNi high-entropy alloy on age hardening at 700°C*, Journal of Alloys and Compounds 495, 55–58 (2010).

[162] K. Zhang and Z. Fu, *Effects of annealing treatment on phase composition and microstructure of CoCrFeNiTiAlx high-entropy alloys*, Intermetallics 22, 24–32 (2012).

[163] M.-H. Tsai, H. Yuan, G. Cheng, W. Xu, K.-Y. Tsai, C.-W. Tsai, W. W. Jian, C.-C. Juan, W.-J. Shen, M.-H. Chuang, J.-W. Yeh, and Y. T. Zhu, *Morphology, structure and composition of precipitates in Al0.3CoCrCu0.5FeNi high-entropy alloy*, Intermetallics 32, 329–336 (2013).

[164] U. Roy, H. Roy, H. Daoud, U. Glatzel, and K. K. Ray, *Fracture toughness and fracture micromechanism in a cast AlCoCrCuFeNi high entropy alloy system*, Materials Letters 132, 186–189 (2014).

[165] N. G. Jones, J. W. Aveson, A. Bhowmik, B. D. Conduit, and H. J. Stone, *On the entropic stabilisation of an Al0.5CrFeCoNiCu high entropy alloy*, Intermetallics 54, 148–153 (2014).

[166] N. G. Jones, A. Frezza, and H. J. Stone, *Phase equilibria of an Al0.5CrFeCoNiCu High Entropy Alloy*, Materials Science and Engineering: A 615, 214–221 (2014).

[167] J. Y. He, W. H. Liu, H. Wang, Y. Wu, X. J. Liu, T. G. Nieh, and Z. P. Lu, *Effects of Al addition on structural evolution and tensile properties of the FeCoNiCrMn high-entropy alloy system*, Acta Materialia 62, 105–113 (2014).

[168] D. Choudhuri, T. Alam, T. Borkar, B. Gwalani, A. S. Mantri, S. G. Srinivasan, M. A. Gibson, and R. Banerjee, *Formation of a Huesler-like L21 phase in a CoCrCuFeNiAlTi high-entropy alloy*, Scripta Materialia 100, 36–39 (2015).

[169] N. G. Jones, K. A. Christofidou, and H. J. Stone, *Rapid precipitation in an Al0.5CrFeCoNiCu high entropy alloy*, Materials Science and Technology 31, 1171–1177 (2015).

[170] E. J. Pickering, H. J. Stone, and N. G. Jones, *Fine-scale precipitation in the high-entropy alloy Al0.5CrFeCoNiCu*, Materials Science and Engineering: A 645, 65–71 (2015).

[171] H. Zhang, Y. Pan, and Y.-Z. He, *Synthesis and characterization of FeCoNiCrCu high-entropy alloy coating by laser cladding*, Materials & Design 32, 1910–1915 (2011).

[172] X. D. Xu, P. Liu, S. Guo, A. Hirata, T. Fujita, T. G. Nieh, C. T. Liu, and M. W. Chen, *Nanoscale phase separation in a fcc-based CoCrCuFeNiAl0.5 high-entropy alloy*, Acta Materialia 84, 145–152 (2015).

[173] P. F. Yu, H. Cheng, L. J. Zhang, H. Zhang, M. Z. Ma, G. Li, P. K. Liaw, and R. P. Liu, *Nanotwin's formation and growth in an AlCoCuFeNi high-entropy alloy*, Scripta Materialia 114, 31–34 (2016).

[174] Z. Tang, T. Yuan, C.-W. Tsai, J.-W. Yeh, C. D. Lundin, and P. K. Liaw, *Fatigue behavior of a wrought Al0.5CoCrCuFeNi two-phase high-entropy alloy*, Acta Materialia 99, 247–258 (2015).

[175] D. Li and Y. Zhang, *The ultrahigh charpy impact toughness of forged AlxCoCrFeNi high entropy alloys at room and cryogenic temperatures*, Intermetallics 70, 24–28 (2016).

[176] J. Dąbrowa, W. Kucza, G. Cieślak, T. Kulik, M. Danielewski, and J.-W. Yeh, *Interdiffusion in the FCC-structured Al-Co-Cr-Fe-Ni high entropy alloys: Experimental studies and numerical simulations*, Journal of Alloys and Compounds 674, 455–462 (2016).

[177] K. Jin, C. Zhang, F. Zhang, and H. Bei, *Influence of compositional complexity on interdiffusion in Ni-containing concentrated solid-solution alloys*, Materials Research Letters 6, 293–299 (2018).

[178] J. Dąbrowa, M. Zajusz, W. Kucza, G. Cieślak, K. Berent, T. Czeppe, T. Kulik, and M. Danielewski, *Demystifying the sluggish diffusion effect in high entropy alloys*, Journal of Alloys and Compounds 783, 193–207 (2019).

[179] A. Brown and M. Ashby, *Correlations for diffusion constants*, Acta Metallurgica 28, 1085–1101 (1980).

[180] A. Paul, *Comments on "Sluggish diffusion in Co–Cr–Fe–Mn–Ni high-entropy alloys" by K.Y. Tsai, M.H. Tsai and J.W. Yeh, Acta Materialia 61 (2013) 4887–4897*, Scripta Materialia 135, 153–157 (2017).

[181] K.-Y. Tsai, M.-H. Tsai, and J.-W. Yeh, *Reply to comments on "Sluggish diffusion in Co-Cr-Fe-Mn-Ni high-entropy alloys" by K.Y. Tsai, M.H. Tsai and J.W. Yeh, Acta Materialia 61 (2013) 4887-4897*, Scripta Materialia 135, 158–159 (2017).

[182] K. Kulkarni and G. P. S. Chauhan, *Investigations of quaternary interdiffusion in a constituent system of high entropy alloys*, AIP Advances 5, 097162 (2015).

[183] V. Verma, A. Tripathi, and K. N. Kulkarni, *On Interdiffusion in FeNiCoCrMn High Entropy Alloy*, Journal of Phase Equilibria and Diffusion 38, 445–456 (2017).

[184] C. Zhang, F. Zhang, K. Jin, H. Bei, S. Chen, W. Cao, J. Zhu, and D. Lv, *Understanding of the Elemental Diffusion Behavior in Concentrated Solid Solution Alloys*, Journal of Phase Equilibria and Diffusion 38, 434–444 (2017).

[185] W. Chen and L. Zhang, *High-Throughput Determination of Interdiffusion Coefficients for Co-Cr-Fe-Mn-Ni High-Entropy Alloys*, Journal of Phase Equilibria and Diffusion 38, 457–465 (2017).

[186] Q. Li, W. Chen, J. Zhong, L. Zhang, Q. Chen, and Z.-K. Liu, *On Sluggish Diffusion in Fcc Al–Co–Cr–Fe–Ni High-Entropy Alloys: An Experimental and Numerical Study*, Metals 8, 16 (2018).

[187] R. Wang, W. Chen, J. Zhong, and L. Zhang, *Experimental and numerical studies on the sluggish diffusion in face centered cubic Co-Cr-Cu-Fe-Ni high-entropy alloys*, Journal of Materials Science & Technology 34, 1791–1798 (2018).

[188] M. Vaidya, G. Mohan Muralikrishna, S. Divinski, and B. Murty, *Experimental assessment of the thermodynamic factor for diffusion in CoCrFeNi and CoCrFeMnNi high entropy alloys*, Scripta Materialia 157, 81–85 (2018).

[189] W. Kucza, J. Dąbrowa, G. Cieślak, K. Berent, T. Kulik, and M. Danielewski, *Studies of "sluggish diffusion" effect in Co-Cr-Fe-Mn-Ni, Co-Cr-Fe-Ni and Co-Fe-Mn-Ni high entropy alloys; determination of tracer diffusivities by combinatorial approach*, Journal of Alloys and Compounds 731, 920–928 (2018).

[190] S. Chen, Q. Li, J. Zhong, F. Xing, and L. Zhang, *On diffusion behaviors in face centered cubic phase of Al-Co-Cr-Fe-Ni-Ti high-entropy superalloys*, Journal of Alloys and Compounds 791, 255–264 (2019).

[191] M. Vaidya, K. G. Pradeep, B. S. Murty, G. Wilde, and S. V. Divinski, *Radioactive isotopes reveal a non sluggish kinetics of grain boundary diffusion in high entropy alloys*, Scientific Reports 7, 12293 (2017).

[192] V. Nadutov, V. F. Mazanko, and S. Y. Makarenko, *Tracer Diffusion of Cobalt in High-Entropy Alloys* $Al_xFeNiCoCuCr$, Metallofizika i Noveishie Tekhnologii 39, 337–348 (2017).

[193] D. Gaertner, J. Kottke, G. Wilde, S. V. Divinski, and Y. Chumlyakov, *Tracer diffusion in single crystalline CoCrFeNi and CoCrFeMnNi high entropy alloys*, Journal of Materials Research 33, 3184–3191 (2018).

[194] D. Gaertner, K. Abrahams, J. Kottke, V. A. Esin, I. Steinbach, G. Wilde, and S. V. Divinski, *Concentration-dependent atomic mobilities in FCC CoCrFeMnNi high-entropy alloys*, Acta Materialia 166, 357–370 (2019).

[195] J. Kottke, M. Laurent-Brocq, A. Fareed, D. Gaertner, L. Perrière, Ł. Rogal, S. V. Divinski, and G. Wilde, *Tracer diffusion in the Ni–CoCrFeMn system: Transition from a dilute solid solution to a high entropy alloy*, Scripta Materialia 159, 94–98 (2019).

[196] A. Durand, L. Peng, G. Laplanche, J. Morris, E. George, and G. Eggeler, *Interdiffusion in Cr–Fe–Co–Ni medium-entropy alloys*, Intermetallics 122, 106789 (2020).

[197] Y. N. Osetsky, L. K. Béland, A. V. Barashev, and Y. Zhang, *On the existence and origin of sluggish diffusion in chemically disordered concentrated alloys*, Current Opinion in Solid State and Materials Science 22, 65–74 (2018).

[198] D. B. Miracle, *Critical Assessment 14: High entropy alloys and their development as structural materials*, Materials Science and Technology 31, 1142–1147 (2015).

[199] Y. Deng, C. Tasan, K. Pradeep, H. Springer, A. Kostka, and D. Raabe, *Design of a twinning-induced plasticity high entropy alloy*, Acta Materialia 94, 124–133 (2015).

[200] Z. Li, K. G. Pradeep, Y. Deng, D. Raabe, and C. C. Tasan, *Metastable high-entropy dual-phase alloys overcome the strength–ductility trade-off*, Nature 534, 227–230 (2016).

[201] Z. Li, C. C. Tasan, H. Springer, B. Gault, and D. Raabe, *Interstitial atoms enable joint twinning and transformation induced plasticity in strong and ductile high-entropy alloys*, Scientific Reports 7, 40704 (2017).

[202] M. Wang, Z. Li, and D. Raabe, *In-situ SEM observation of phase transformation and twinning mechanisms in an interstitial high-entropy alloy*, Acta Materialia 147, 236–246 (2018).

[203] W. Lu, C. H. Liebscher, G. Dehm, D. Raabe, and Z. Li, *Bidirectional Transformation Enables Hierarchical Nanolaminate Dual-Phase High-Entropy Alloys*, Advanced Materials 30, 1804727 (2018).

[204] C. Slone, S. Chakraborty, J. Miao, E. George, M. Mills, and S. Niezgoda, *Influence of deformation induced nanoscale twinning and FCC-HCP transformation on hardening and texture development in medium-entropy CrCoNi alloy*, Acta Materialia 158, 38–52 (2018).

[205] C. Slone, J. Miao, E. George, and M. Mills, *Achieving ultra-high strength and ductility in equiatomic CrCoNi with partially recrystallized microstructures*, Acta Materialia 165, 496–507 (2019).

[206] B. C. De Cooman, K.-g. Chin, and J. Kim, *High Mn TWIP Steels for Automotive Applications*, New Trends and Developments in Automotive System Engineering (M. Chiaberge, ed.), InTech, 2011.

[207] T. Yang, Y. L. Zhao, Y. Tong, Z. B. Jiao, J. Wei, J. X. Cai, X. D. Han, D. Chen, A. Hu, J. J. Kai, K. Lu, Y. Liu, and C. T. Liu, *Multicomponent intermetallic nanoparticles and superb mechanical behaviors of complex alloys*, Science 362, 933–937 (2018).

[208] X. Ren, B. Yao, T. Zhu, Z. Zhong, Y. Wang, X. Cao, S. Jinno, and Q. Xu, *Effect of irradiation on randomness of element distribution in CoCrFeMnNi equiatomic high-entropy alloy*, Intermetallics 126, 106942 (2020).

[209] Y. Qi, Y. Wu, T. Cao, L. He, F. Jiang, and J. sun, *L21-strengthened face-centered cubic high-entropy alloy with high strength and ductility*, Materials Science and Engineering: A 797, 140056 (2020).

[210] N. R. Rathod and J. V. Menghani, *Influence of precipitation hardening in aluminum based systems: A literature review*, PROCEEDINGS OF THE 14TH ASIA-PACIFIC PHYSICS CONFERENCE (Kuching, Malaysia), 2021, p. 020035.

[211] J.-F. Nie, *Precipitation and Hardening in Magnesium Alloys*, Metallurgical and Materials Transactions A 43, 3891–3939 (2012).

[212] Y. Wu, F. Zhang, X. Yuan, H. Huang, X. Wen, Y. Wang, H. Wu, X. Liu, H. Wang, S. Jiang, and Z. Lu, *Short-range ordering and its effects on mechanical properties of high-entropy alloys*, Journal of Materials Science & Technology, S1005030220306083 (2020).

[213] C. R. LaRosa, M. Shih, C. Varvenne, and M. Ghazisaeidi, *Solid solution strengthening theories of high-entropy alloys*, Materials Characterization 151, 310–317 (2019).

[214] Ł. Rogal, D. Kalita, and L. Litynska-Dobrzynska, *CoCrFeMnNi high entropy alloy matrix nanocomposite with addition of Al 2 O 3*, Intermetallics 86, 104–109 (2017).

[215] Ł. Rogal, D. Kalita, A. Tarasek, P. Bobrowski, and F. Czerwinski, *Effect of SiC nano-particles on microstructure and mechanical properties of the CoCrFeMnNi high entropy alloy*, Journal of Alloys and Compounds 708, 344–352 (2017).

[216] A. Zhang, J. Han, B. Su, P. Li, and J. Meng, *Microstructure, mechanical properties and tribological performance of CoCrFeNi high entropy alloy matrix self-lubricating composite*, Materials & Design 114, 253–263 (2017).

[217] G. Leyson and W. Curtin, *Friedel vs. Labusch: The strong/weak pinning transition in solute strengthened metals*, Philosophical Magazine 93, 2428–2444 (2013).

[218] G. P. M. Leyson, W. A. Curtin, L. G. Hector, and C. F. Woodward, *Quantitative prediction of solute strengthening in aluminium alloys*, Nature Materials 9, 750–755 (2010).

[219] G. P. M. Leyson, L. G. Hector, and W. A. Curtin, *Solute strengthening from first principles and application to aluminum alloys*, Acta Materialia 60, 3873–3884 (2012).

[220] O. Senkov, J. Scott, S. Senkova, D. Miracle, and C. Woodward, *Microstructure and room temperature properties of a high-entropy TaNbHfZrTi alloy*, Journal of Alloys and Compounds 509, 6043–6048 (2011).

[221] I. Toda-Caraballo and P. E. Rivera-Díaz-del-Castillo, *Modelling solid solution hardening in high entropy alloys*, Acta Materialia 85, 14–23 (2015).

[222] I. Toda-Caraballo, *A general formulation for solid solution hardening effect in multicomponent alloys*, Scripta Materialia 127, 113–117 (2017).

[223] I. Toda-Caraballo, J. S. Wróbel, S. L. Dudarev, D. Nguyen-Manh, and P. E. J. Rivera-Díaz-del-Castillo, *Interatomic spacing distribution in multicomponent alloys*, Acta Materialia 97, 156–169 (2015).

[224] H. Oh, D. Ma, G. Leyson, B. Grabowski, E. Park, F. Körmann, and D. Raabe, *Lattice Distortions in the FeCoNiCrMn High Entropy Alloy Studied by Theory and Experiment*, Entropy 18, 321 (2016).

[225] N. L. Okamoto, K. Yuge, K. Tanaka, H. Inui, and E. P. George, *Atomic displacement in the CrMnFeCoNi high-entropy alloy – A scaling factor to predict solid solution strengthening*, AIP Advances 6, 125008 (2016).

[226] Y. Tong, G. Velisa, T. Yang, K. Jin, C. Lu, H. Bei, J. Y. P. Ko, D. C. Pagan, R. Huang, Y. Zhang, L. Wang, and F. X. Zhang, *Probing local lattice distortion in medium- and high-entropy alloys*, arXiv:1707.07745 [cond-mat] (2017).

[227] H. Song, F. Tian, Q.-M. Hu, L. Vitos, Y. Wang, J. Shen, and N. Chen, *Local lattice distortion in high-entropy alloys*, Physical Review Materials 1, 023404 (2017).

[228] L. Owen, E. Pickering, H. Playford, H. Stone, M. Tucker, and N. Jones, *An assessment of the lattice strain in the CrMnFeCoNi high-entropy alloy*, Acta Materialia 122, 11–18 (2017).

[229] Y. Tong, K. Jin, H. Bei, J. Ko, D. Pagan, Y. Zhang, and F. Zhang, *Local lattice distortion in NiCoCr, FeCoNiCr and FeCoNiCrMn concentrated alloys investigated by synchrotron X-ray diffraction*, Materials & Design 155, 1–7 (2018).

[230] K. Jin, Y. Gao, and H. Bei, *Intrinsic properties and strengthening mechanism of monocrystalline Ni-containing ternary concentrated solid solutions*, Materials Science and Engineering: A 695, 74–79 (2017).

[231] F. G. Coury, K. D. Clarke, C. S. Kiminami, M. J. Kaufman, and A. J. Clarke, *High Throughput Discovery and Design of Strong Multicomponent Metallic Solid Solutions*, Scientific Reports 8, 8600 (2018).

[232] F. G. Coury, T. Butler, K. Chaput, A. Saville, J. Copley, J. Foltz, P. Mason, K. Clarke, M. Kaufman, and A. Clarke, *Phase equilibria, mechanical properties and design of quaternary refractory high entropy alloys*, Materials & Design 155, 244–256 (2018).

[233] S. Yoshida, T. Ikeuchi, T. Bhattacharjee, Y. Bai, A. Shibata, and N. Tsuji, *Effect of elemental combination on friction stress and Hall-Petch relationship in face-centered cubic high / medium entropy alloys*, Acta Materialia 171, 201–215 (2019).

[234] M. Walbrühl, D. Linder, J. Ågren, and A. Borgenstam, *Modelling of solid solution strengthening in multicomponent alloys*, Materials Science and Engineering: A 700, 301–311 (2017).

[235] A. Shafiei, *Simple approach to model the strength of solid-solution high entropy alloys in Co-Cr-Fe-Mn-Ni system*, arXiv:2005.07948 [cond-mat] (2020).

[236] G. Bracq, M. Laurent-Brocq, C. Varvenne, L. Perrière, W. Curtin, J.-M. Joubert, and I. Guillot, *Combining experiments and modeling to explore the solid solution strengthening of high and medium entropy alloys*, Acta Materialia 177, 266–279 (2019).

[237] T. Jiang, Y. Xiang, and L. Zhang, *Stochastic Peierls-Nabarro Model for Dislocations in High Entropy Alloys*, arXiv:2004.09375 [cond-mat] (2020).

[238] M. Laurent-Brocq, L. Perrière, R. Pirès, F. Prima, P. Vermaut, and Y. Champion, *From diluted solid solutions to high entropy alloys: On the evolution of properties with composition of multi-components alloys*, Materials Science and Engineering: A 696, 228–235 (2017).

[239] C. Varvenne and W. A. Curtin, *Strengthening of high entropy alloys by dilute solute additions: CoCrFeNiAl x and CoCrFeNiMnAl x alloys*, Scripta Materialia 138, 92–95 (2017).

[240] C. Varvenne and W. A. Curtin, *Predicting yield strengths of noble metal high entropy alloys*, Scripta Materialia 142, 92–95 (2018).

[241] M. P. Agustianingrum, I. Ondicho, D. E. Jodi, N. Park, and U. Lee, *Theoretical evaluation of solid solution interaction in Fe (CoCrMnNi)100- medium- and high-entropy alloys*, Materials Science and Engineering: A 759, 633–639 (2019).

[242] B. Yin and W. A. Curtin, *First-principles-based prediction of yield strength in the RhIrPdPtNiCu high-entropy alloy*, npj Computational Materials 5, 14 (2019).

[243] B. Yin and W. A. Curtin, *Origin of high strength in the CoCrFeNiPd high-entropy alloy*, Materials Research Letters 8, 209–215 (2020).

[244] B. Yin, S. Yoshida, N. Tsuji, and W. A. Curtin, *Yield strength and misfit volumes of NiCoCr and implications for short-range-order*, Nature Communications 11, 2507 (2020).

[245] B. Yin, F. Maresca, and W. Curtin, *Vanadium is an optimal element for strengthening in both fcc and bcc high-entropy alloys*, Acta Materialia 188, 486–491 (2020).

[246] G. I. Taylor, *Plastic strain in metals*, J. Inst. Metals 62, 307–324 (1938).

[247] S. Nag and W. A. Curtin, *Effect of solute-solute interactions on strengthening of random alloys from dilute to high entropy alloys*, Acta Materialia 200, 659–673 (2020).

[248] F. Thiel, D. Geissler, K. Nielsch, A. Kauffmann, S. Seils, M. Heilmaier, D. Utt, K. Albe, M. Motylenko, D. Rafaja, and J. Freudenberger, *Origins of strength and plasticity in the precious metal based high-entropy alloy AuCuNiPdPt*, Acta Materialia 185, 400–411 (2020).

[249] F. Thiel, D. Utt, A. Kauffmann, K. Nielsch, K. Albe, M. Heilmaier, and J. Freudenberger, *Breakdown of Varvenne scaling in (AuNiPdPt) 1 - x Cu high-entropy alloys*, Scripta Materialia 181, 15–18 (2020).

[250] T. Keil, D. Utt, E. Bruder, A. Stukowski, K. Albe, and K. Durst, *Solid solution hardening in CrMnFeCoNi-based high entropy alloy systems studied by a combinatorial approach*, Journal of Materials Research (2021).

[251] V. Vítek, *Intrinsic stacking faults in body-centred cubic crystals*, Philosophical Magazine 18, 773–786 (1968).

[252] J. A. Zimmerman, H. Gao, and F. F. Abraham, *Generalized stacking fault energies for embedded atom FCC metals*, Modelling and Simulation in Materials Science and Engineering 8, 103–115 (2000).

[253] L. M. Brown, *The self-stress of dislocations and the shape of extended nodes*, Philosophical Magazine 10, 441–466 (1964).

[254] D. J. H. Cockayne, I. L. F. Ray, and M. J. Whelan, *Investigations of dislocation strain fields using weak beams*, Philosophical Magazine 20, 1265–1270 (1969).

[255] R. P. Reed and R. E. Schramm, *Relationship between stacking-fault energy and x-ray measurements of stacking-fault probability and microstrain*, Journal of Applied Physics 45, 4705–4711 (1974).

[256] X. Sun, S. Lu, R. Xie, X. An, W. Li, T. Zhang, C. Liang, X. Ding, Y. Wang, H. Zhang, and L. Vitos, *Can experiment determine the stacking fault energy of metastable alloys?*, Materials & Design 199, 109396 (2021).

[257] D. Ma, B. Grabowski, F. Körmann, J. Neugebauer, and D. Raabe, *Ab initio thermodynamics of the CoCrFeMnNi high entropy alloy: Importance of entropy contributions beyond the configurational one*, Acta Materialia 100, 90–97 (2015).

[258] S. Zhao, G. M. Stocks, and Y. Zhang, *Stacking fault energies of face-centered cubic concentrated solid solution alloys*, Acta Materialia 134, 334–345 (2017).

[259] Z. Dong, S. Schönecker, W. Li, D. Chen, and L. Vitos, *Thermal spin fluctuations in CoCrFeMnNi high entropy alloy*, Scientific Reports 8, 12211 (2018).

[260] C. Niu, C. R. LaRosa, J. Miao, M. J. Mills, and M. Ghazisaeidi, *Magnetically-driven phase transformation strengthening in high entropy alloys*, Nature Communications 9, 1363 (2018).

[261] J. Ding, Q. Yu, M. Asta, and R. O. Ritchie, *Tunable stacking fault energies by tailoring local chemical order in CrCoNi medium-entropy alloys*, Proceedings of the National Academy of Sciences 115, 8919–8924 (2018).

[262] Y. Ikeda, F. Körmann, I. Tanaka, and J. Neugebauer, *Impact of Chemical Fluctuations on Stacking Fault Energies of CrCoNi and CrMnFeCoNi High Entropy Alloys from First Principles*, Entropy 20, 655 (2018).

[263] N. L. Okamoto, S. Fujimoto, Y. Kambara, M. Kawamura, Z. M. T. Chen, H. Matsunoshita, K. Tanaka, H. Inui, and E. P. George, *Size effect, critical resolved shear stress, stacking fault energy, and solid solution strengthening in the CrMnFeCoNi high-entropy alloy*, Scientific Reports 6, 35863 (2016).

[264] S. Liu, Y. Wu, H. Wang, J. He, J. Liu, C. Chen, X. Liu, H. Wang, and Z. Lu, *Stacking fault energy of face-centered-cubic high entropy alloys*, Intermetallics 93, 269–273 (2018).

[265] A. J. Zaddach, C. Niu, C. C. Koch, and D. L. Irving, *Mechanical Properties and Stacking Fault Energies of NiFeCrCoMn High-Entropy Alloy*, JOM 65, 1780–1789 (2013).

[266] L. Patriarca, A. Ojha, H. Sehitoglu, and Y. I. Chumlyakov, *Slip nucleation in single crystal FeNiCoCrMn high entropy alloy*, Scripta Materialia 112, 54–57 (2016).

[267] M. Beyramali Kivy and M. Asle Zaeem, *Generalized stacking fault energies, ductilities, and twinnabilities of CoCrFeNi-based face-centered cubic high entropy alloys*, Scripta Materialia 139, 83–86 (2017).

[268] S. Alkan, A. Ojha, and H. Sehitoglu, *Determination of latent hardening response for FeNiCoCrMn for twin-twin interactions*, Acta Materialia 147, 149–164 (2018).

[269] H. Huang, X. Li, Z. Dong, W. Li, S. Huang, D. Meng, X. Lai, T. Liu, S. Zhu, and L. Vitos, *Critical stress for twinning nucleation in CrCoNi-based medium and high entropy alloys*, Acta Materialia 149, 388–396 (2018).

[270] G. Laplanche, A. Kostka, C. Reinhart, J. Hunfeld, G. Eggeler, and E. P. George, *Reasons for the superior mechanical properties of medium-entropy CrCoNi compared to high-entropy CrMnFeCoNi*, Acta Materialia 128, 292–303 (2017).

[271] Y. Zhang, Y. Zhuang, A. Hu, J. Kai, and C. Liu, *The origin of negative stacking fault energies and nano-twin formation in face-centered cubic high entropy alloys*, Scripta Materialia 130, 96–99 (2017).

[272] Z. Zhang, H. Sheng, Z. Wang, B. Gludovatz, Z. Zhang, E. P. George, Q. Yu, S. X. Mao, and R. O. Ritchie, *Dislocation mechanisms and 3D twin architectures generate exceptional strength-ductility-toughness combination in CrCoNi medium-entropy alloy*, Nature Communications 8, 14390 (2017).

[273] F. Otto, A. Dlouhý, C. Somsen, H. Bei, G. Eggeler, and E. George, *The influences of temperature and microstructure on the tensile properties of a CoCrFeMnNi high-entropy alloy*, Acta Materialia 61, 5743–5755 (2013).

[274] G. Laplanche, A. Kostka, O. Horst, G. Eggeler, and E. George, *Microstructure evolution and critical stress for twinning in the CrMnFeCoNi high-entropy alloy*, Acta Materialia 118, 152–163 (2016).

[275] F. C. Frank, *On the Equations of Motion of Crystal Dislocations*, Proceedings of the Physical Society. Section A 62, 131 (1949).

[276] J.-H. Zhai and M. Zaiser, *Properties of dislocation lines in crystals with strong atomic-scale disorder*, Materials Science and Engineering: A 740-741, 285–294 (2019).

[277] H. Suzuki, *Chemical interaction of solute atoms with dislocations*, Sci. Rep. Res. Inst. Tohoku Univ. A 4, 455–463 (1952).

[278] H. Suzuki, *Segregation of Solute Atoms to Stacking Faults*, Journal of the Physical Society of Japan 17, 322–325 (1962).

[279] Y. Zeng, X. Cai, and M. Koslowski, *Effects of the stacking fault energy fluctuations on the strengthening of alloys*, Acta Materialia 164, 1–11 (2019).

[280] V. V. Bulatov and W. Cai, *Computer simulations of dislocations*, reprinted ed., Oxford Series on Materials Modelling, no. 3, Oxford Univ. Press, Oxford, 2008.

[281] S.-D. Kim, J. Y. Park, S.-J. Park, J. hoon Jang, J. Moon, H.-Y. Ha, C.-H. Lee, J.-Y. Kang, J.-H. Shin, and T.-H. Lee, *Direct observation of dislocation plasticity in high-Mn lightweight steel by in-situ TEM*, Scientific Reports 9, 15171 (2019).

[282] J. Kacher, G. S. Liu, and I. M. Robertson, *In situ and tomographic observations of defect free channel formation in ion irradiated stainless steels*, Micron 43, 1099–1107 (2012).

[283] G. Péterffy, P. D. Ispánovity, M. E. Foster, X. Zhou, and R. B. Sills, *Length scales and scale-free dynamics of dislocations in dense solid solutions*, Materials Theory 4, 6 (2020).

[284] S. S. Sohn, A. K. da Silva, Y. Ikeda, F. Körmann, W. Lu, W. S. Choi, B. Gault, D. Ponge, J. Neugebauer, and D. Raabe, *Ultrastrong Medium-Entropy Single-Phase Alloys Designed via Severe Lattice Distortion*, Advanced Materials 31, 1807142 (2019).

[285] G. Laplanche, J. Bonneville, C. Varvenne, W. Curtin, and E. George, *Thermal activation parameters of plastic flow reveal deformation mechanisms in the CrMnFeCoNi high-entropy alloy*, Acta Materialia 143, 257–264 (2018).

[286] S. I. Hong, J. Moon, S. K. Hong, and H. S. Kim, *Thermally activated deformation and the rate controlling mechanism in CoCrFeMnNi high entropy alloy*, Materials Science and Engineering: A 682, 569–576 (2017).

[287] V. Maier-Kiener, B. Schuh, E. P. George, H. Clemens, and A. Hohenwarter, *Nanoindentation testing as a powerful screening tool for assessing phase stability of nanocrystalline high-entropy alloys*, Materials & Design 115, 479–485 (2017).

[288] V. Maier-Kiener, B. Schuh, E. P. George, H. Clemens, and A. Hohenwarter, *Insights into the deformation behavior of the CrMnFeCoNi high-entropy alloy revealed by elevated temperature nanoindentation*, Journal of Materials Research 32, 2658–2667 (2017).

[289] Y. Xiao, Y. Zou, A. S. Sologubenko, R. Spolenak, and J. M. Wheeler, *Size-dependent strengthening in multi-principal element, face-centered cubic alloys*, Materials & Design 193, 108786 (2020).

[290] Y. Zhao and T. Nieh, *Correlation between lattice distortion and friction stress in Ni-based equiatomic alloys*, Intermetallics 86, 45–50 (2017).

[291] S. Yoshida, T. Bhattacharjee, Y. Bai, and N. Tsuji, *Friction stress and Hall-Petch relationship in CoCrNi equi-atomic medium entropy alloy processed by severe plastic deformation and subsequent annealing*, Scripta Materialia 134, 33–36 (2017).

[292] W. G. Nöhring and W. Curtin, *Correlation of microdistortions with misfit volumes in High Entropy Alloys*, Scripta Materialia 168, 119–123 (2019).

[293] P. Flinn, *Solute hardening of close-packed solid solutions*, Acta Metallurgica 6, 631–635 (1958).

[294] J. Fisher, *On the strength of solid solution alloys*, Acta Metallurgica 2, 9–10 (1954).

[295] J. Cohen and M. E. Fine, *Some aspects of short-range order*, Journal de Physique et le Radium 23, 749–762 (1962).

[296] C. Niu, A. J. Zaddach, A. A. Oni, X. Sang, J. W. Hurt, J. M. LeBeau, C. C. Koch, and D. L. Irving, *Spin-driven ordering of Cr in the equiatomic high entropy alloy NiFeCrCo*, Applied Physics Letters 106, 161906 (2015).

[297] F. X. Zhang, S. Zhao, K. Jin, H. Xue, G. Velisa, H. Bei, R. Huang, J. Y. P. Ko, D. C. Pagan, J. C. Neuefeind, W. J. Weber, and Y. Zhang, *Local Structure and Short-Range Order in a NiCoCr Solid Solution Alloy*, Physical Review Letters 118, 205501 (2017).

[298] B. Schönfeld, C. R. Sax, J. Zemp, M. Engelke, P. Boesecke, T. Kresse, T. Boll, T. Al-Kassab, O. E. Peil, and A. V. Ruban, *Local order in Cr-Fe-Co-Ni: Experiment and electronic structure calculations*, Physical Review B 99, 014206 (2019).

[299] A. Tamm, A. Aabloo, M. Klintenberg, M. Stocks, and A. Caro, *Atomic-scale properties of Ni-based FCC ternary, and quaternary alloys*, Acta Materialia 99, 307–312 (2015).

[300] E. A. Meshkov, I. I. Novoselov, A. V. Yanilkin, S. V. Rogozhkin, A. A. Nikitin, A. A. Khomich, A. S. Shutov, B. A. Tarasov, S. E. Danilov, and V. L. Arbuzov, *Experimental and Theoretical Study of the Atomic Structure Evolution of High-Entropy Alloys Based on Fe, Cr, Ni, Mn, and Co upon Thermal and Radiation Aging*, Physics of the Solid State 62, 389–400 (2020).

[301] Z. Pei, R. Li, M. C. Gao, and G. M. Stocks, *Statistics of the NiCoCr medium-entropy alloy: Novel aspects of an old puzzle*, npj Computational Materials 6, 122 (2020).

[302] V. Gerold and H. Karnthaler, *On the origin of planar slip in f.c.c. alloys*, Acta Metallurgica 37, 2177–2183 (1989).

[303] C. C. Tasan, Y. Deng, K. G. Pradeep, M. J. Yao, H. Springer, and D. Raabe, *Composition Dependence of Phase Stability, Deformation Mechanisms, and Mechanical Properties of the CoCrFeMnNi High-Entropy Alloy System*, JOM 66, 1993–2001 (2014).

[304] M. Yao, K. Pradeep, C. Tasan, and D. Raabe, *A novel, single phase, non-equiatomic FeMnNiCoCr high-entropy alloy with exceptional phase stability and tensile ductility*, Scripta Materialia 72-73, 5–8 (2014).

[305] Z. Wu, Y. F. Gao, and H. Bei, *Single crystal plastic behavior of a single-phase, face-center-cubic-structured, equiatomic FeNiCrCo alloy*, Scripta Materialia 109, 108–112 (2015).

[306] M. Laurent-Brocq, A. Akhatova, L. Perrière, S. Chebini, X. Sauvage, E. Leroy, and Y. Champion, *Insights into the phase diagram of the CrMnFeCoNi high entropy alloy*, Acta Materialia 88, 355–365 (2015).

[307] R. Marceau, A. Ceguerra, A. Breen, M. Palm, F. Stein, S. Ringer, and D. Raabe, *Atom probe tomography investigation of heterogeneous short-range ordering in the 'komplex' phase state (K-state) of Fe–18Al (at.%)*, Intermetallics 64, 23–31 (2015).

[308] R. Marceau, A. Ceguerra, A. Breen, D. Raabe, and S. Ringer, *Quantitative chemical-structure evaluation using atom probe tomography: Short-range order analysis of Fe–Al*, Ultramicroscopy 157, 12–20 (2015).

[309] A. J. Ardell, *Precipitation hardening*, Metallurgical Transactions A 16, 2131–2165 (1985).

[310] T. Gladman, *Precipitation hardening in metals*, Materials Science and Technology 15, 30–36 (1999).

[311] C. E. Krill, H. Ehrhardt, and R. Birringer, *Thermodynamic stabilization of nanocrystallinity*, Zeitschrift für Metallkunde 96, 1134–1141 (2005).

[312] C. C. Koch, R. O. Scattergood, K. A. Darling, and J. E. Semones, *Stabilization of nanocrystalline grain sizes by solute additions*, Journal of Materials Science 43, 7264–7272 (2008).

[313] J. W. Cahn, *The impurity-drag effect in grain boundary motion*, Acta Metallurgica 10, 789–798 (1962).

[314] R. Brook, *The impurity-drag effect and grain growth kinetics*, Scripta Metallurgica 2, 375–378 (1968).

[315] E. Nes, N. Ryum, and O. Hunderi, *On the Zener drag*, Acta Metallurgica 33, 11–22 (1985).

[316] C. M. Barr, J. E. Nathaniel, K. A. Unocic, J. Liu, Y. Zhang, Y. Wang, and M. L. Taheri, *Exploring radiation induced segregation mechanisms at grain boundaries in equiatomic CoCrFeNiMn high entropy alloy under heavy ion irradiation*, Scripta Materialia 156, 80–84 (2018).

[317] J. Weissmüller, *Alloy effects in nanostructures*, Nanostructured Materials 3, 261–272 (1993).

[318] R. Kirchheim, *Grain coarsening inhibited by solute segregation*, Acta Materialia 50, 413–419 (2002).

[319] T. Chookajorn, H. A. Murdoch, and C. A. Schuh, *Design of Stable Nanocrystalline Alloys*, Science 337, 951–954 (2012).

[320] E. B. Tadmor and R. E. Miller, *Modeling materials: Continuum, atomistic, and multiscale techniques*, Cambridge University Press, Cambridge ; New York, 2011.

[321] D. Frenkel and B. Smit, *Understanding molecular simulation: From algorithms to applications*, second ed., Computational Science Series, no. 1, Academic Press, San Diego, 2002.

[322] A. F. Voter, *Introduction to the Kinetic Monte Carlo Method*, Radiation Effects in Solids (K. E. Sickafus, E. A. Kotomin, and B. P. Uberuaga, eds.), vol. 235, Springer Netherlands, Dordrecht, 2007, pp. 1–23.

[323] M. Born and R. Oppenheimer, *Zur Quantentheorie der Molekeln*, Annalen der Physik 389, 457–484 (1927).

[324] A.-T. Petit and P.-L. Dulong, *Recherches sur quelques points importants de la Théorie de la Chaleur*, Annales de Chimie et de Physique, 395–413 (1819).

[325] M. E. Tuckerman, Ab Initio *molecular dynamics: Basic concepts, current trends and novel applications*, Journal of Physics: Condensed Matter 14, R1297–R1355 (2002).

[326] J. Hafner, Ab-Initio *simulations of materials using VASP: Density-functional theory and beyond*, Journal of Computational Chemistry 29, 2044–2078 (2008).

[327] S. Plimpton, *Fast parallel algorithms for short-range molecular dynamics*, Tech. Report SAND–91-1144, 10176421, 1993.

[328] M. Herlihy and N. Shavit, *The Art of Multiprocessor Programming, Revised Reprint.*, Elsevier Science, Burlington, 2012.

[329] L. Verlet, *Computer "Experiments" on Classical Fluids. I. Thermodynamical Properties of Lennard-Jones Molecules*, Physical Review 159, 98–103 (1967).

[330] W. C. Swope, H. C. Andersen, P. H. Berens, and K. R. Wilson, *A computer simulation method for the calculation of equilibrium constants for the formation of physical clusters of molecules: Application to small water clusters*, The Journal of Chemical Physics 76, 637–649 (1982).

[331] E. Hairer, C. Lubich, and G. Wanner, *Geometric numerical integration illustrated by the Störmer–Verlet method*, Acta Numerica 12, 399–450 (2003).

[332] S. Nosé, *A unified formulation of the constant temperature molecular dynamics methods*, The Journal of Chemical Physics 81, 511–519 (1984).

[333] W. G. Hoover, *Canonical dynamics: Equilibrium phase-space distributions*, Physical Review A 31, 1695–1697 (1985).

[334] T. Schneider and E. Stoll, *Molecular-dynamics study of a three-dimensional one-component model for distortive phase transitions*, Physical Review B 17, 1302–1322 (1978).

[335] B. Dünweg and W. Paul, *Brownian Dynamics Simulations without Gaussian random Numbers*, International Journal of Modern Physics C 02, 817–827 (1991).

[336] M. Parrinello and A. Rahman, *Polymorphic transitions in single crystals: A new molecular dynamics method*, Journal of Applied Physics 52, 7182–7190 (1981).

[337] W. Shinoda, M. Shiga, and M. Mikami, *Rapid estimation of elastic constants by molecular dynamics simulation under constant stress*, Physical Review B 69, 134103 (2004).

[338] J. Guénolé, W. G. Nöhring, A. Vaid, F. Houllé, Z. Xie, A. Prakash, and E. Bitzek, *Assessment and optimization of the fast inertial relaxation engine (fire) for energy minimization in atomistic simulations and its implementation in lammps*, Computational Materials Science 175, 109584 (2020).

[339] E. Bitzek, P. Koskinen, F. Gähler, M. Moseler, and P. Gumbsch, *Structural Relaxation Made Simple*, Physical Review Letters 97, 170201 (2006).

[340] M. R. Hestenes and E. Stiefel, *Methods of conjugate gradients for solving linear systems*, Journal of Research of the National Bureau of Standards 49, 409–436 (1952).

[341] E. Polak and G. Ribiére, *Note sur la convergence de méthodes de directions conjuguées*, ESAIM: Mathematical Modelling and Numerical Analysis - Modélisation Mathématique et Analyse Numérique 3, 35–43 (1969). MR 255025

[342] D. M. Himmelblau, *Applied nonlinear programming*, McGraw-Hill, New York, 1972.

[343] H. H. Rosenbrock, *An Automatic Method for Finding the Greatest or Least Value of a Function*, The Computer Journal 3, 175–184 (1960).

[344] G. Mills and H. Jónsson, *Quantum and thermal effects in H 2 dissociative adsorption: Evaluation of free energy barriers in multidimensional quantum systems*, Physical Review Letters 72, 1124–1127 (1994).

[345] G. Mills, H. Jónsson, and G. K. Schenter, *Reversible work transition state theory: Application to dissociative adsorption of hydrogen*, Surface Science 324, 305–337 (1995).

[346] G. Henkelman, B. P. Uberuaga, and H. Jónsson, *A climbing image nudged elastic band method for finding saddle points and minimum energy paths*, The Journal of Chemical Physics 113, 9901–9904 (2000).

[347] G. Henkelman and H. Jónsson, *Improved tangent estimate in the nudged elastic band method for finding minimum energy paths and saddle points*, The Journal of Chemical Physics 113, 9978–9985 (2000).

[348] A. Nakano, *A space–time-ensemble parallel nudged elastic band algorithm for molecular kinetics simulation*, Computer Physics Communications 178, 280–289 (2008).

[349] E. Maras, O. Trushin, A. Stukowski, T. Ala-Nissila, and H. Jónsson, *Global transition path search for dislocation formation in Ge on Si(001)*, Computer Physics Communications 205, 13–21 (2016).

[350] B. Sadigh, P. Erhart, A. Stukowski, A. Caro, E. Martinez, and L. Zepeda-Ruiz, *Scalable parallel Monte Carlo algorithm for atomistic simulations of precipitation in alloys*, Physical Review B 85, 184203 (2012).

[351] G. H. Vineyard, *Frequency factors and isotope effects in solid state rate processes*, Journal of Physics and Chemistry of Solids 3, 121–127 (1957).

[352] P. Hanggi, P. Talkner, and M. Borkovec, *Reaction-rate theory: Fifty years after Kramers*, Rev. Mod. Phys. 62, 92 (1990).

[353] D. T. Gillespie, *A general method for numerically simulating the stochastic time evolution of coupled chemical reactions*, Journal of Computational Physics 22, 403–434 (1976).

[354] A. B. Bortz, M. H. Kalos, and J. L. Lebowitz, *A new algorithm for Monte Carlo simulation of Ising spin systems*, Journal of Computational Physics 17, 10–18 (1975).

[355] K. A. Fichthorn and W. H. Weinberg, *Theoretical foundations of dynamical Monte Carlo simulations*, The Journal of Chemical Physics 95, 1090–1096 (1991).

[356] Y. Shibuta, S. Sakane, E. Miyoshi, S. Okita, T. Takaki, and M. Ohno, *Heterogeneity in homogeneous nucleation from billion-atom molecular dynamics simulation of solidification of pure metal*, Nature Communications 8, 10 (2017).

[357] Y. Mishin, M. R. S⊘rensen, and A. F. Voter, *Calculation of point-defect entropy in metals*, Philosophical Magazine A 81, 2591–2612 (2001).

[358] D. Marx and J. Hutter, *Ab Initio Molecular Dynamics: Basic Theory and Advanced Methods*, Cambridge University Press, Cambridge, 2009.

[359] A. Carlsson, *Beyond Pair Potentials in Elemental Transition Metals and Semiconductors*, Solid State Physics, vol. 43, Elsevier, 1990, pp. 1–91.

[360] G. Bonny and L. Malerba, *Overview of interatomic potentials*, Tech. Report 1379-2407, Belgium, 2005.

[361] J. Behler, *Perspective: Machine learning potentials for atomistic simulations*, The Journal of Chemical Physics 145, 170901 (2016).

[362] V. L. Deringer, M. A. Caro, and G. Csányi, *Machine Learning Interatomic Potentials as Emerging Tools for Materials Science*, Advanced Materials 31, 1902765 (2019).

[363] P. Hohenberg and W. Kohn, *Inhomogeneous Electron Gas*, Physical Review 136, B864–B871 (1964).

[364] M. J. Stott and E. Zaremba, *Quasiatoms: An approach to atoms in nonuniform electronic systems*, Physical Review B 22, 1564–1583 (1980).

[365] J. K. Nørskov and N. D. Lang, *Effective-medium theory of chemical binding: Application to chemisorption*, Physical Review B 21, 2131–2136 (1980).

[366] M. S. Daw and M. I. Baskes, *Semiempirical, Quantum Mechanical Calculation of Hydrogen Embrittlement in Metals*, Physical Review Letters 50, 1285–1288 (1983).

[367] M. S. Daw and M. I. Baskes, *Embedded-atom method: Derivation and application to impurities, surfaces, and other defects in metals*, Physical Review B 29, 6443–6453 (1984).

[368] R. A. Johnson, *Alloy models with the embedded-atom method*, Physical Review B 39, 12554–12559 (1989).

[369] X. W. Zhou, R. A. Johnson, and H. N. G. Wadley, *Misfit-energy-increasing dislocations in vapor-deposited CoFe/NiFe multilayers*, Physical Review B 69, 144113 (2004).

[370] R. W. Smith and G. S. Was, *Application of molecular dynamics to the study of hydrogen embrittlement in Ni-Cr-Fe alloys*, Physical Review B 40, 10322–10336 (1989).

[371] R. J. Elliott, J. A. Krumhansl, and P. L. Leath, *The theory and properties of randomly disordered crystals and related physical systems*, Reviews of Modern Physics 46, 465–543 (1974).

[372] J. Faulkner, *The modern theory of alloys*, Progress in Materials Science 27, 1–187 (1982).

[373] M. Grujicic and X. Zhou, *Analysis of Fe-Ni-Cr-N austenite using the Embedded-Atom Method*, Calphad 17, 383–413 (1993).

[374] J. F. Nye, *Physical properties of crystals: Their representation by tensors and matrices*, 1st published in pbk. with corrections, 1984 ed., Clarendon Press ; Oxford University Press, Oxford [Oxfordshire] : New York, 1984.

[375] F. Ercolessi, O. Tomagnini, S. Iarlori, and E. Tosatti, *Molecular Dynamics Simulations of Metal Surfaces: Surface Melting and Non-Melting, and Tip-Surface Interactions*, Nanosources and Manipulation of Atoms Under High Fields and Temperatures: Applications (V. T. Binh, N. Garcia, and K. Dransfeld, eds.), Springer Netherlands, Dordrecht, 1993, pp. 185–205.

[376] D. Utt, A. Stukowski, and K. Albe, *Grain boundary structure and mobility in high-entropy alloys: A comparative molecular dynamics study on a $\Sigma 11$ symmetrical tilt grain boundary in face-centered cubic CuNiCoFe*, Acta Materialia 186, 11–19 (2020).

[377] B.-J. Lee and M. I. Baskes, *Second nearest-neighbor modified embedded-atom-method potential*, Physical Review B 62, 8564–8567 (2000).

[378] B.-J. Lee, M. Baskes, H. Kim, and Y. Koo Cho, *Second nearest-neighbor modified embedded atom method potentials for bcc transition metals*, Physical Review B 64, 184102 (2001).

[379] M. I. Baskes, *Application of the Embedded-Atom Method to Covalent Materials: A Semiempirical Potential for Silicon*, Physical Review Letters 59, 2666–2669 (1987).

[380] M. I. Baskes, J. S. Nelson, and A. F. Wright, *Semiempirical modified embedded-atom potentials for silicon and germanium*, Physical Review B 40, 6085–6100 (1989).

[381] P. Hirel, *Atomsk: A tool for manipulating and converting atomic data files*, Computer Physics Communications 197, 212–219 (2015).

[382] A. Stukowski, *Visualization and analysis of atomistic simulation data with OVITO–the Open Visualization Tool*, Modelling and Simulation in Materials Science and Engineering 18, 015012 (2010).

[383] D. Farkas and A. Caro, *Model interatomic potentials and lattice strain in a high-entropy alloy*, Journal of Materials Research 33, 3218–3225 (2018).

[384] O. Tange, *GNU parallel - the command-line power tool*, ;login: The USENIX Magazine 36, 42–47 (2011).

[385] C. Brandl, P. M. Derlet, and H. Van Swygenhoven, *Strain rates in molecular dynamics simulations of nanocrystalline metals*, Philosophical Magazine 89, 3465–3475 (2009).

[386] A. Stukowski and K. Albe, *Extracting dislocations and non-dislocation crystal defects from atomistic simulation data*, Modelling and Simulation in Materials Science and Engineering 18, 085001 (2010).

[387] A. Stukowski, V. V. Bulatov, and A. Arsenlis, *Automated identification and indexing of dislocations in crystal interfaces*, Modelling and Simulation in Materials Science and Engineering 20, 085007 (2012).

[388] Y. N. Osetsky and D. J. Bacon, *An atomic-level model for studying the dynamics of edge dislocations in metals*, Modelling and Simulation in Materials Science and Engineering 11, 427–446 (2003).

[389] V. V. Bulatov and W. Cai, *Computer simulations of dislocations*, Oxford Series on Materials Modelling, no. 3, Oxford University Press, Oxford ; New York, 2006.

[390] J. M. Cowley, *An Approximate Theory of Order in Alloys*, Physical Review 77, 669–675 (1950).

[391] P. Virtanen, R. Gommers, T. E. Oliphant, M. Haberland, T. Reddy, D. Cournapeau, E. Burovski, P. Peterson, W. Weckesser, J. Bright, S. J. van der Walt, M. Brett, J. Wilson, K. J. Millman, N. Mayorov, A. R. J. Nelson, E. Jones, R. Kern, E. Larson, C. J. Carey, İ. Polat, Y. Feng, E. W. Moore, J. VanderPlas, D. Laxalde, J. Perktold, R. Cimrman, I. Henriksen, E. A. Quintero, C. R. Harris, A. M. Archibald, A. H. Ribeiro, F. Pedregosa, and P. van Mulbregt, *SciPy 1.0: Fundamental algorithms for scientific computing in Python*, Nature Methods 17, 261–272 (2020).

[392] S. M. Foiles, M. I. Baskes, and M. S. Daw, *Embedded-atom-method functions for the fcc metals Cu, Ag, Au, Ni, Pd, Pt, and their alloys*, Physical Review B 33, 7983–7991 (1986).

[393] S. M. Foiles and J. J. Hoyt, *Computer Simulation of Bubble Growth in Metals Due to He*, Tech. report, Sandia National Laboratories, 2001.

[394] J. Schäfer, A. Stukowski, and K. Albe, *Plastic deformation of nanocrystalline Pd–Au alloys: On the interplay of grain boundary solute segregation, fault energies and grain size*, Acta Materialia 59, 2957–2968 (2011).

[395] P. M. Larsen, S. Schmidt, and J. Schiøtz, *Robust Structural Identification via Polyhedral Template Matching*, Modelling and Simulation in Materials Science and Engineering 24, 055007 (2016).

[396] J. D. Rittner and D. N. Seidman, *$\langle 110 \rangle$ symmetric tilt grain-boundary structures in fcc metals with low stacking-fault energies*, Physical Review B 54, 6999–7015 (1996).

[397] R. Balluffi and P. Bristowe, *On the structural unit/grain boundary dislocation model for grain boundary structure*, Surface Science 144, 28–43 (1984).

[398] K. G. F. Janssens, D. Olmsted, E. A. Holm, S. M. Foiles, S. J. Plimpton, and P. M. Derlet, *Computing the mobility of grain boundaries*, Nature Materials 5, 124–127 (2006).

[399] J. Zhou and V. Mohles, *Towards realistic molecular dynamics simulations of grain boundary mobility*, Acta Materialia 59, 5997–6006 (2011).

[400] E. A. Holm, S. M. Foiles, E. R. Homer, and D. L. Olmsted, *Comment on "Toward realistic molecular dynamics simulations of grain boundary mobility" by Zhou and Mohles*, Scripta Materialia 66, 714–716 (2012).

[401] V. Mohles and J. Zhou, *Response to the comment by Holm, Foiles, Homer and Olmsted on "Towards realistic molecular dynamics simulations of grain boundary mobility" by Zhou and Mohles*, Scripta Materialia 66, 717–719 (2012).

[402] F. Ulomek, C. J. O'Brien, S. M. Foiles, and V. Mohles, *Energy conserving orientational force for determining grain boundary mobility*, Modelling and Simulation in Materials Science and Engineering 23, 025007 (2015).

[403] A. A. Schratt and V. Mohles, *Efficient calculation of the ECO driving force for atomistic simulations of grain boundary motion*, Computational Materials Science 182, 109774 (2020).

[404] V. A. Ivanov and Y. Mishin, *Dynamics of grain boundary motion coupled to shear deformation: An analytical model and its verification by molecular dynamics*, Physical Review B 78, 064106 (2008).

[405] F. Aurenhammer, *Voronoi diagrams—a survey of a fundamental geometric data structure*, ACM Computing Surveys 23, 345–405 (1991).

[406] G. Voronoi, *Nouvelles applications des paramètres continus à la théorie des formes quadratiques. Premier mémoire. Sur quelques propriétés des formes quadratiques positives parfaites.*, Journal für die reine und angewandte Mathematik (Crelles Journal) 1908, 97–102 (1908).

[407] G. Voronoi, *Nouvelles applications des paramètres continus à la théorie des formes quadratiques. Deuxième mémoire. Recherches sur les parallélloèdres primitifs.*, Journal für die reine und angewandte Mathematik (Crelles Journal) 1908, 198–287 (1908).

[408] G. Voronoi, *Nouvelles applications des paramètres continus à théorie des formes quadratiques. Deuxième Mémoire. Recherches sur les paralléloèdres primitifs.*, Journal für die reine und angewandte Mathematik 1909, 67–182 (1909).

[409] J. Schiøtz, T. Vegge, F. D. Di Tolla, and K. W. Jacobsen, *Atomic-scale simulations of the mechanical deformation of nanocrystalline metals*, Physical Review B 60, 11971–11983 (1999).

[410] H. Van Swygenhoven, M. Spaczer, A. Caro, and D. Farkas, *Competing plastic deformation mechanisms in nanophase metals*, Physical Review B 60, 22–25 (1999).

[411] D. Utt, A. Stukowski, and K. Albe, *Thermodynamics of vacancies in concentrated solid solutions: From dilute Ni-alloys to the Cantor system*, arXiv:2104.02697 [cond-mat] (2021).

[412] J. Kottke, D. Utt, M. Laurent-Brocq, A. Fareed, D. Gaertner, L. Perrière, Ł. Rogal, A. Stukowski, K. Albe, S. V. Divinski, and G. Wilde, *Experimental and theoretical study of tracer diffusion in a series of (CoCrFeMn)$_{100\text{-}x}$ Ni$_x$ alloys*, Acta Materialia 194, 236–248 (2020).

[413] G. Cook and R. H. Dickerson, *Understanding the chemical potential*, American Journal of Physics 63, 737–742 (1995).

[414] R. Baierlein, *The elusive chemical potential*, American Journal of Physics 69, 423–434 (2001).

[415] D. S. Gaunt and M. F. Sykes, *Series study of random percolation in three dimensions*, Journal of Physics A: Mathematical and General 16, 783–799 (1983).

[416] H. Zhang, W. Xu, Y. Xu, Z. Lu, and D. Li, *The thermal-mechanical behavior of WTaMoNb high-entropy alloy via selective laser melting (SLM): Experiment and simulation*, The International Journal of Advanced Manufacturing Technology 96, 461–474 (2018).

[417] C. Leys, C. Ley, O. Klein, P. Bernard, and L. Licata, *Detecting outliers: Do not use standard deviation around the mean, use absolute deviation around the median*, Journal of Experimental Social Psychology 49, 764–766 (2013).

[418] G. Leibfried and N. Breuer, *Point Defects in Metals I*, Springer Tracts in Modern Physics 81, vol. 81, Springer-Verlag, Berlin/Heidelberg, 1978.

[419] M. J. Gillan, *The elastic dipole tensor for point defects in ionic crystals*, Journal of Physics C: Solid State Physics 17, 1473–1488 (1984).

[420] D. A. Freedman, D. Roundy, and T. A. Arias, *Elastic effects of vacancies in strontium titanate: Short- and long-range strain fields, elastic dipole tensors, and chemical strain*, Physical Review B 80, 064108 (2009).

[421] V. M. Goldschmidt, *Die Gesetze der Krystallochemie*, Die Naturwissenschaften 14, 477–485 (1926).

[422] G. Strang, *Linear algebra and its applications*, 3rd ed., Harcourt, Brace, Jovanovich, Publishers, San Diego, 1988.

[423] S. van der Walt, S. C. Colbert, and G. Varoquaux, *The NumPy Array: A Structure for Efficient Numerical Computation*, Computing in Science & Engineering 13, 22–30 (2011).

[424] T. E. Oliphant, *Guide to NumPy*, Continuum Press, Austin, Tex., 2015.

[425] J. J. Burton, *Vacancy-Formation Entropy in Cubic Metals*, Physical Review B 5, 2948–2957 (1972).

[426] K. Mosig, J. Wolff, J.-E. Kluin, and T. Hehenkamp, *Investigation of the equilibrium concentration of lattice vacancies in silver and dilute silver-tin alloys with a differential dilatometer*, Journal of Physics: Condensed Matter 4, 1447–1458 (1992).

[427] T. Hehenkamp, P. Scholz, B. Köhler, and R. Kerl, *Vacancy Formation and Diffusion in FeAl-Alloys*, Defect and Diffusion Forum 194-199, 389–396 (2001).

[428] M. Aziziha and S. Akbarshahi, *Vibrational Entropy Investigation in High Entropy Alloys*, arXiv:2008.03338 [cond-mat] (2020).

[429] Y. Gong, B. Grabowski, A. Glensk, F. Körmann, J. Neugebauer, and R. C. Reed, *Temperature dependence of the Gibbs energy of vacancy formation of fcc Ni*, Physical Review B 97, 214106 (2018).

[430] A. Zunger, S.-H. Wei, L. G. Ferreira, and J. E. Bernard, *Special quasirandom structures*, Physical Review Letters 65, 353–356 (1990).

[431] F. Montalenti and A. F. Voter, *Applying Accelerated Molecular Dynamics to Crystal Growth*, 8 (2001).

[432] G. Murch, *The haven ratio in fast ionic conductors*, Solid State Ionics 7, 177–198 (1982).

[433] J. C. Fisher, *Calculation of Diffusion Penetration Curves for Surface and Grain Boundary Diffusion*, Journal of Applied Physics 22, 74–77 (1951).

[434] T. Suzuoka, *Exact Solutions of Two Ideal Cases in Grain Boundary Diffusion Problem and the Application to Sectioning Method*, Journal of the Physical Society of Japan 19, 839–851 (1964).

[435] H. Bakker, J. Backus, and F. Waals, *A Curvature in the Arrhenius Plot for the Diffusion of Iron in Single Crystals of Nickel in the Temperature Range from 1200 to 1400°C*, physica status solidi (b) 45, 633–638 (1971).

[436] M. Bronfin, G. Bulatov, and I. Drugova, *Study of Nickel self-diffusion in intermetallide Ni3Al and pure Nickel*, Fizika Metallov I Metallovedenie 40, 363–366 (1975).

[437] K. Maier, H. Mehrer, E. Lessmann, and W. Schüle, *Self-diffusion in nickel at low temperatures*, physica status solidi (b) 78, 689–698 (1976).

[438] K. Monma, H. Suto, and H. Oikawa, *Diffusion of Ni^{63} and Cr^{51} in Nickel-Chromium Alloys (On the Relation between High-Temperature Creep and Diffusion in Nickel Base Solid Solutions. I)*, Journal of the Japan Institute of Metals 28, 188–192 (1964).

[439] A. Vladimirov, V. Kaigorodov, S. Klotsman, and I. Trakhtenberg, *The volume and intercrystalline diffusion of silver in nickel*, Fizika Metallov i Metallovedenie 45, 1015–1023 (1978).

[440] H. Mehrer, *Diffusion in Solids*, Springer Series in Solid-State Sciences, vol. 155, Springer Berlin Heidelberg, Berlin, Heidelberg, 2007.

[441] K. Parlinski, Z. Q. Li, and Y. Kawazoe, *First-Principles Determination of the Soft Mode in Cubic ZrO_2*, Physical Review Letters 78, 4063–4066 (1997).

[442] A. Togo and I. Tanaka, *First principles phonon calculations in materials science*, Scripta Materialia 108, 1–5 (2015).

[443] R. Swalin, *A model for solute diffusion in metals based on elasticity concepts*, Acta Metallurgica 5, 443–448 (1957).

[444] Y. Feng, M. Liu, Y. Shi, H. Ma, D. Li, Y. Li, L. Lu, and X. Chen, *High-throughput modeling of atomic diffusion migration energy barrier of fcc metals*, Progress in Natural Science: Materials International 29, 341–348 (2019).

[445] C. P. Flynn, *Atomic Migration in Monatomic Crystals*, Physical Review 171, 682–698 (1968).

[446] G. de Lorenzi and F. Ercolessi, *Multiple Jumps and Vacancy Diffusion in a Face-Centered-Cubic Metal*, Europhysics Letters (EPL) 20, 349–355 (1992).

[447] H. Bakker, *A Curvature in the InD versus 1/T Plot for Self-Diffusion in Nickel at Temperatures from 980 to 1400°C*, Physica Status Solidi (b) 28, 569–576 (1968).

[448] A. Seeger, *The mechanisms of diffusion in metals and alloys*, Journal of the Less Common Metals 28, 387–418 (1972).

[449] D. Utt, S. Lee, A. Stukowski, S. H. Oh, G. Dehm, and K. Albe, *Jerky motion of dislocations in high-entropy alloys: The linkage between local Peierls stress fluctuations and dislocation mobility*, arXiv:2007.11489 [cond-mat, physics:physics] (2020).

[450] S. van der Walt, J. L. Schönberger, J. Nunez-Iglesias, F. Boulogne, J. D. Warner, N. Yager, E. Gouillart, and T. Yu, *Scikit-image: Image processing in Python*, PeerJ 2, e453 (2014).

[451] J. Mayer, L. A. Giannuzzi, T. Kamino, and J. Michael, *TEM Sample Preparation and FIB-Induced Damage*, MRS Bulletin 32, 400–407 (2007).

[452] D. Kiener, C. Motz, M. Rester, M. Jenko, and G. Dehm, *FIB damage of Cu and possible consequences for miniaturized mechanical tests*, Materials Science and Engineering: A 459, 262–272 (2007).

[453] R. Peierls, *The size of a dislocation*, Proceedings of the Physical Society 52, 34–37 (1940).

[454] F. R. N. Nabarro, *Dislocations in a simple cubic lattice*, Proceedings of the Physical Society 59, 256–272 (1947).

[455] C. H. Woo and M. P. Puls, *The Peierls mechanism in MgO*, Philosophical Magazine 35, 1641–1652 (1977).

[456] J. B. Adams, S. M. Foiles, and W. G. Wolfer, *Self-diffusion and impurity diffusion of fcc metals using the five-frequency model and the Embedded Atom Method*, Journal of Materials Research 4, 102–112 (1989).

[457] P. Schober, C. Boer, and L. A. Schwarte, *Correlation Coefficients: Appropriate Use and Interpretation*, Anesthesia & Analgesia 126, 1763–1768 (2018).

[458] T. Byun, *On the stress dependence of partial dislocation separation and deformation microstructure in austenitic stainless steels*, Acta Materialia 51, 3063–3071 (2003).

[459] W. Li, H. Fan, J. Tang, Q. Wang, X. Zhang, and J. A. El-Awady, *Effects of alloying on deformation twinning in high entropy alloys*, Materials Science and Engineering: A 763, 138143 (2019).

[460] R. B. Sills, M. E. Foster, and X. W. Zhou, *Line-length-dependent dislocation mobilities in an FCC stainless steel alloy*, International Journal of Plasticity 135, 102791 (2020).

[461] Q. Rizzardi, G. Sparks, and R. Maaß, *Fast Slip Velocity in a High-Entropy Alloy*, JOM 70, 1088–1093 (2018).

[462] G. Sparks, P. S. Phani, U. Hangen, and R. Maaß, *Spatiotemporal slip dynamics during deformation of gold micro-crystals*, Acta Materialia 122, 109–119 (2017).

[463] W. G. Nöhring and W. Curtin, *Cross-slip of long dislocations in FCC solid solutions*, Acta Materialia 158, 95–117 (2018).

[464] G. Kaptay, *On the Tendency of Solutions to Tend Toward Ideal Solutions at High Temperatures*, Metallurgical and Materials Transactions A 43, 531–543 (2012).

[465] J. T. VanderPlas, *Understanding the Lomb–Scargle Periodogram*, The Astrophysical Journal Supplement Series 236, 16 (2018).

[466] S. Qiu, X.-C. Zhang, J. Zhou, S. Cao, H. Yu, Q.-M. Hu, and Z. Sun, *Influence of lattice distortion on stacking fault energies of CoCrFeNi and Al-CoCrFeNi high entropy alloys*, Journal of Alloys and Compounds, 156321 (2020).

[467] C.-C. Yen, G.-R. Huang, Y.-C. Tan, H.-W. Yeh, D.-J. Luo, K.-T. Hsieh, E.-W. Huang, J.-W. Yeh, S.-J. Lin, C.-C. Wang, C.-L. Kuo, S.-Y. Chang, and Y.-C. Lo, *Lattice distortion effect on elastic anisotropy of high entropy alloys*, Journal of Alloys and Compounds 818, 152876 (2020).

[468] Y. Tong, S. Zhao, K. Jin, H. Bei, J. Ko, Y. Zhang, and F. Zhang, *A comparison study of local lattice distortion in Ni80Pd20 binary alloy and FeCoNiCrPd high-entropy alloy*, Scripta Materialia 156, 14–18 (2018).

[469] J. R. Rice, *Dislocation nucleation from a crack tip: An analysis based on the Peierls concept*, Journal of the Mechanics and Physics of Solids 40, 239–271 (1992).

[470] D. A. Porter, K. E. Easterling, and M. Y. Sherif, *Phase transformations in metals and alloys*, 3rd ed ed., CRC Press, Boca Raton, FL, 2009.

[471] G. N. Gottstein, D. A. Molodov, and L. S. Shvindlerman, *Grain Boundary Migration in Metals: Recent Developments*, 16 (1998).

[472] D. Spearot, M. Tschopp, K. Jacob, and D. Mcdowell, *Tensile strength of ⟨100⟩ and ⟨110⟩ tilt bicrystal copper interfaces*, Acta Materialia 55, 705–714 (2007).

[473] D. E. Spearot, *Evolution of the E structural unit during uniaxial and constrained tensile deformation*, Mechanics Research Communications 35, 81–88 (2008).

[474] L. E. Murr, *Volume Defects: 3D Imperfections in Crystals*, pp. 1–11, Springer International Publishing, Cham, 2014.

[475] C.-W. Tsai, M.-H. Tsai, J.-W. Yeh, and C.-C. Yang, *Effect of temperature on mechanical properties of Al0.5CoCrCuFeNi wrought alloy*, Journal of Alloys and Compounds 490, 160–165 (2010).

[476] L. Liu, J. Zhu, C. Zhang, J. Li, and Q. Jiang, *Microstructure and the properties of FeCoCuNiSnx high entropy alloys*, Materials Science and Engineering: A 548, 64–68 (2012).

[477] L. Liu, J. Zhu, L. Li, J. Li, and Q. Jiang, *Microstructure and tensile properties of FeMnNiCuCoSnx high entropy alloys*, Materials & Design 44, 223–227 (2013).

[478] E. D. Hondros and M. P. Seah, *The theory of grain boundary segregation in terms of surface adsorption analogues*, Metallurgical Transactions A 8, 1363–1371 (1977).

[479] D. L. Olmsted, S. M. Foiles, and E. A. Holm, *Survey of computed grain boundary properties in face-centered cubic metals: I. Grain boundary energy*, Acta Materialia 57, 3694–3703 (2009).

[480] D. L. Olmsted, E. A. Holm, and S. M. Foiles, *Survey of computed grain boundary properties in face-centered cubic metals—II: Grain boundary mobility*, Acta Materialia 57, 3704–3713 (2009).

[481] J. F. Panzarino and T. J. Rupert, *Tracking Microstructure of Crystalline Materials: A Post-Processing Algorithm for Atomistic Simulations*, JOM 66, 417–428 (2014).

[482] J. Burke and D. Turnbull, *Recrystallization and grain growth*, Progress in Metal Physics 3, 220–292 (1952).

[483] H. Miura, M. Kato, and T. Mori, *Temperature dependence of the energy of Cu [110] symmetrical tilt grain boundaries*, Journal of Materials Science Letters 13, 46–48 (1994).

[484] S. M. Foiles, *Temperature dependence of grain boundary free energy and elastic constants*, Scripta Materialia 62, 231–234 (2010).

[485] H. Sun and C. V. Singh, *Temperature dependence of grain boundary excess free volume*, Scripta Materialia 178, 71–76 (2020).

[486] T. Tadano, Y. Gohda, and S. Tsuneyuki, *Anharmonic force constants extracted from first-principles molecular dynamics: Applications to heat transfer simulations*, Journal of Physics: Condensed Matter 26, 225402 (2014).

[487] F. Eriksson, E. Fransson, and P. Erhart, *The Hiphive Package for the Extraction of High-Order Force Constants by Machine Learning*, Advanced Theory and Simulations 2, 1800184 (2019).

[488] J. N. Tessmer, *Simulation of S/TEM Images for Discrete DislocationDynamics and Molecular Dynamics*, Ph.D. thesis, Carnegie Mellon University, Pittsburgh, PA, 2020.

[489] E. Antillon, C. Woodward, S. Rao, B. Akdim, and T. Parthasarathy, *A molecular dynamics technique for determining energy landscapes as a dislocation percolates through a field of solutes*, Acta Materialia 166, 658–676 (2019).

[490] T. Chookajorn, *Enhancing Stability of Powder-Route Nanocrystalline Tungsten-Titanium via Alloy Thermodynamics*, Ph.D. thesis, Carnegie Mellon University, 2014.

[491] D. Utt, A. Stukowski, and M. Ghazisaeidi, *The effect of solute cloud formation on the second order pyramidal to basal transition of* $\langle c + a \rangle$ *edge dislocations in Mg-Y solid solutions*, Scripta Materialia 182, 53–56 (2020).

[492] H. Henck, J. Avila, Z. Ben Aziza, D. Pierucci, J. Baima, B. Pamuk, J. Chaste, D. Utt, M. Bartos, K. Nogajewski, B. A. Piot, M. Orlita, M. Potemski, M. Calandra, M. C. Asensio, F. Mauri, C. Faugeras, and A. Ouerghi, *Flat electronic bands in long sequences of rhombohedral-stacked graphene*, Physical Review B 97, 245421 (2018).